THÈSE

En vue de l'obtention du

DOCTORAT DE L'UNIVERSITÉ DE TOULOUSE

Délivré par : *l'Université Toulouse 3 Paul Sabatier (UT3 Paul Sabatier)*

Présentée et soutenue le *26/05/2021* **par :**

Carlos Conejero García

Impact du changement climatique sur la circulation océanique dans les Systèmes d'Upwelling de Bord Est de l'hémisphère Sud.

JURY

Patrick Marchesiello	Directeur de Recherche IRD-LEGOS, Toulouse	Président du Jury
Sang-Wook Yeh	Professeur d'Université Hanyang University, Korea	Rapporteur
Oscar Pizarro	Professeur d'Université Universidad de Concepción, Chile	Rapporteur
Catalina Aguirre	Professeur d'Université Universidad de Valparaíso, Chile	Examinatrice
Emilia Sanchez-Gomez	Directrice de Recherche CERFACS, Toulouse	Examinatrice
Myriam Khodri	Directrice de Recherche IRD-LOCEAN, Paris	Examinatrice
Boris Dewitte	Directeur de Recherche IRD-LEGOS, Toulouse	Directeur de thèse
Véronique Garçon	Directrice de Recherche CNRS-LEGOS, Toulouse	Co-Directrice de thèse

---

École doctorale et spécialité :
SDU2E : Océan, Atmosphère et Surfaces Continentales

Unité de Recherche :
Laboratoire d'Études en Géophysique et Océanographie Spatiales (UMR 5566)

Directeur(s) de Thèse :
Boris Dewitte (LEGOS) et *Véronique Garçon (LEGOS)*

Rapporteurs :
Sang-Wook Yeh et *Oscar Pizarro*

THÈSE

En vue de l'obtention du

DOCTORAT DE L'UNIVERSITÉ DE TOULOUSE

Délivré par : *l'Université Toulouse 3 Paul Sabatier (UT3 Paul Sabatier)*

Présentée et soutenue le *26/05/2021* **par :**

Carlos Conejero García

Impact of climate change on the oceanic circulation in the Eastern Boundary Upwelling Systems of the South Hemisphere.

JURY

Patrick Marchesiello	Directeur de Recherche IRD-LEGOS, Toulouse	Président du Jury
Sang-Wook Yeh	Professeur d'Université Hanyang University, Korea	Rapporteur
Oscar Pizarro	Professeur d'Université Universidad de Concepción, Chile	Rapporteur
Catalina Aguirre	Professeur d'Université Universidad de Valparaíso, Chile	Examinatrice
Emilia Sanchez-Gomez	Directrice de Recherche CERFACS, Toulouse	Examinatrice
Myriam Khodri	Directrice de Recherche IRD-LOCEAN, Paris	Examinatrice
Boris Dewitte	Directeur de Recherche IRD-LEGOS, Toulouse	Directeur de thèse
Véronique Garçon	Directrice de Recherche CNRS-LEGOS, Toulouse	Co-Directrice de thèse

---

École doctorale et spécialité :
SDU2E : Océan, Atmosphère et Surfaces Continentales

Unité de Recherche :
Laboratoire d'Études en Géophysique et Océanographie Spatiales (UMR 5566)

Directeur(s) de Thèse :
Boris Dewitte (LEGOS) et *Véronique Garçon (LEGOS)*

Rapporteurs :
Sang-Wook Yeh et *Oscar Pizarro*

Abstract

Among the world oceans, the Eastern Boundary Upwelling Systems (EBUS) are of particular interest because they connect the tropical ocean basins with the mid-latitudes and so are subject to large fluctuations associated with both the natural climate variability and the anthropogenic forcing. Understanding how global warming will modify the oceanic circulation and the marine ecosystems in the EBUS remains a scientific challenge due to the complex of processes at play. Current generation of Coupled General Circulation Models (CGCMs) still suffers limitations associated to not resolving realistically some aspects of the coastal upwelling dynamics and mesoscale circulation. Still they remain powerful tools to better understand the formation of climate change patterns in a key region of the world for the Earth's radiation budget. In this thesis, we have investigated processes of formation of the climate change pattern and of natural variability in the EBUS of the South Hemisphere, with particular emphasis in the South Eastern Pacific (SEP). We take advantage on latest generation resources to the community for studying climate change in the presence of internal climate variability, including the CESM Large Ensemble performed by NCAR and mesoscale-resolving global climate long-term simulations performed at the IBS Center for Climate Physics. Assuming quasi-equilibrium between the radiative external forcing and mixed layer and upper-ocean processes, oceanic and atmospheric processes responsible for the SST trend over the period 2006-2100 are derived. It is first shown that the latitudinal location of the minimum warming in the SEP deviates significantly from that predicted by theory for which maximum evaporative cooling is controlled by the pattern of mean climatological latent heat/precipitation. The explicit heat budget of the CESM-LE simulations reveals that advection forms the El Niño-like warming pattern in the equatorial region and along the coast of Peru and Chile, while the minimum warming center is mostly determined by the relative cooling of both latent heat and solar radiation, partly compensated by meridional advection. Details in the warming trend along the coast of Peru and Chile are also shown to result from a balance between advection induced by both change in Ekman currents and geostrophic compensation. The results also reveal that the SST climate change pattern has a significant projection on the patterns of natural variability in the SEP (i.e. El Niño and the South Pacific Meridional Mode), suggesting that it can be off-set by natural variability. In a suite

of high-resolution model simulations we investigate the ENSO oceanic teleconnection along the coast of Peru and Chile on the turbulent flow, considered here as a source of natural variability in the SEP. It is shown in particular that ENSO can fuel energy in the circulation at decadal timescales along the coast of Peru and Chile through modulating instabilities in the coastal current system. Overall, the thesis illustrates the complex of processes associated to the equatorial teleconnection in the SEP at different timescales, which are not yet accessible from the current too-short observing system.

Résumé

Parmi les océans du monde, les Systèmes d'Upwelling de Bord Est (EBUS, de l'anglais « Eastern Boundary Upwelling Systems ») présentent un intérêt particulier car ils relient les bassins océaniques tropicaux aux latitudes moyennes et sont donc soumis à de fortes fluctuations associées à la fois à la variabilité naturelle du climat et au forçage anthropique. Comprendre comment le réchauffement climatique modifie la circulation océanique et les écosystèmes marins dans les EBUS reste un défi scientifique en raison de la complexité des processus en jeu. La génération actuelle de modèles couplés de circulation générale souffre encore des limitations associées à la non prise en compte de manière réaliste de certains aspects de la dynamique des upwellings côtiers et de la circulation à méso-échelle. Dans cette thèse, nous avons étudié les processus de formation du pattern de changement climatique et de la variabilité naturelle dans le Pacifique Sud-Est (SEP, de l'anglais « South East Pacific ») sur la base de simulations numériques de dernière génération mises à disposition de la communauté pour étudier le changement climatique en présence de la variabilité climatique interne. Ces ressources incluent le CESM Large Ensemble (CESM-LENS) modèle réalisé par le NCAR aux Etats Unis et des simulations à long terme du climat mondial résolvant la méso-échelle réalisées au Centre IBS Center for Climate Physics (ICCP) en Corée du sud. En supposant un quasi-équilibre entre le forçage radiatif externe et les processus de couche de mélange de la circulation de l'océan de surface, il est possible d'identifier les processus océaniques et atmosphériques responsables de la tendance de la température de surface de la mer (SST, de l'anglais « Sea Surface temperature ») sur la période 2006-2100. Nous montrons tout d'abord que la localisation latitudinale du réchauffement minimum de la SST dans le SEP s'écarte significativement de celle prédite par la théorie pour laquelle le refroidissement évaporatif maximum est contrôlé par le pattern de chaleur latente climatologique (précipitations moyennes). Le bilan de chaleur des simulations CESM-LENS révèle que l'advection océanique est responsable du pattern de réchauffement de type El Niño dans la région équatoriale et le long des côtes du Pérou et du Chili. Le centre de la zone de réchauffement minimum est principalement déterminé par le refroidissement relatif du flux de chaleur latente et le rayonnement solaire, partiellement compensé par l'advection méridienne de l'océan.

Les détails de la tendance au réchauffement le long des côtes du Pérou et du Chili résultent également d'un équilibre entre l'advection induite à la fois par le changement des courants d'Ekman et la compensation géostrophique. Les résultats révèlent également que le pattern de changement climatique de la SST a une projection significative sur les modes de variabilité naturelle dans le SEP, ce qui suggère qu'il peut être compensé par la variabilité naturelle. Dans une suite de simulations de modèles à haute résolution, nous étudions la téléconnection océanique d'ENSO (de l'anglais « El Niño Southern Oscillation ») le long des côtes du Pérou et du Chili sur le flux turbulent, considéré ici comme une source de variabilité naturelle dans le SEP. Nous avons montré en particulier que l'ENSO peut alimenter l'énergie de la circulation à des échelles de temps décennales le long des côtes du Pérou et du Chili en modulant les instabilités du système de courants côtiers. Globalement, la thèse illustre la complexité des processus associés à la téléconnection équatoriale dans le SEP à différentes échelles de temps, qui ne sont pas encore accessibles à partir du système d'observations actuel trop court.

Contents

Chapter 1

Introduction

Weather and climate variability on planet Earth emerge fundamentally from both differential radiative heating and the transport of energy through the dynamic ocean-atmosphere components. These fluids can move heat and moisture owing to advective processes by atmospheric winds and ocean currents, including eddies, large-scale atmospheric jet streams and convection. In particular, ocean circulation plays a fundamental role in regulating climate and supporting marine life by transporting freshwater, heat, carbon, oxygen, and nutrients throughout the world's ocean. Anthropogenic forcing, in turn, can influence global ocean circulation as a consequence that the ocean absorbs most of the excess heat from greenhouse gas emissions, leading to rising ocean temperatures which enhance ocean stratification. From this perspective, numerical models of the Earth system are a powerful tool to figure out the past, present, and future variability of the climate. However, one of the main issues in ocean modeling, and subsequently its role in the climate, is accounting for the broad range of spatial and temporal scales in which the ocean circulation transfers physical, chemical and biological properties around the globe. Thereby, understanding how the global warming will modify the oceanic circulation and their potential impact on the sea surface temperature (SST) pattern as well as biogeochemical properties of upwelled waters over the ecosystems remains a scientific challenge. In this context, the present work focuses on two goals based on the latest regional-to-global oceanic modeling tools: i) the coupled ocean-atmosphere processes involved in the future SST pattern formation in the tropical/subtropical oceans of the South Hemisphere, and ii) the influence of the natural variability to modulate the mesoscale activity in the South East Pacific. The present chapter provides a brief synthesis of the key aspects of the circulation for understanding the formation of the climate change and the role of mesoscale activity in the EBUS. This introductory chapter concludes with the presentation of the scientific objectives of the present work.

1.1 Global ocean circulation

The global ocean circulation is an important component of the Earth's climate system. The ocean circulation in its simplest form is the movement of sea water, which transfers physical, chemical and biological properties, from one region to another. Oceans cover more than 70% of the Earth's surface, receiving the most part of the solar radiation. In certain perspective, the Earth seems as a near-perfect "aquaplanet". In this regard, the strong heat capacity of water leads the ocean to play a major role in the storage and transport of the solar heat over long periods of time around the globe. Indeed, the ocean holds more heat in the uppermost 3 meters that the entire atmosphere. The general circulation of the world ocean is mainly driven by the atmosphere–ocean fluxes via the transfer of momentum, heat and freshwater to the ocean with a distinct spatial distribution (see Figure 1.1).

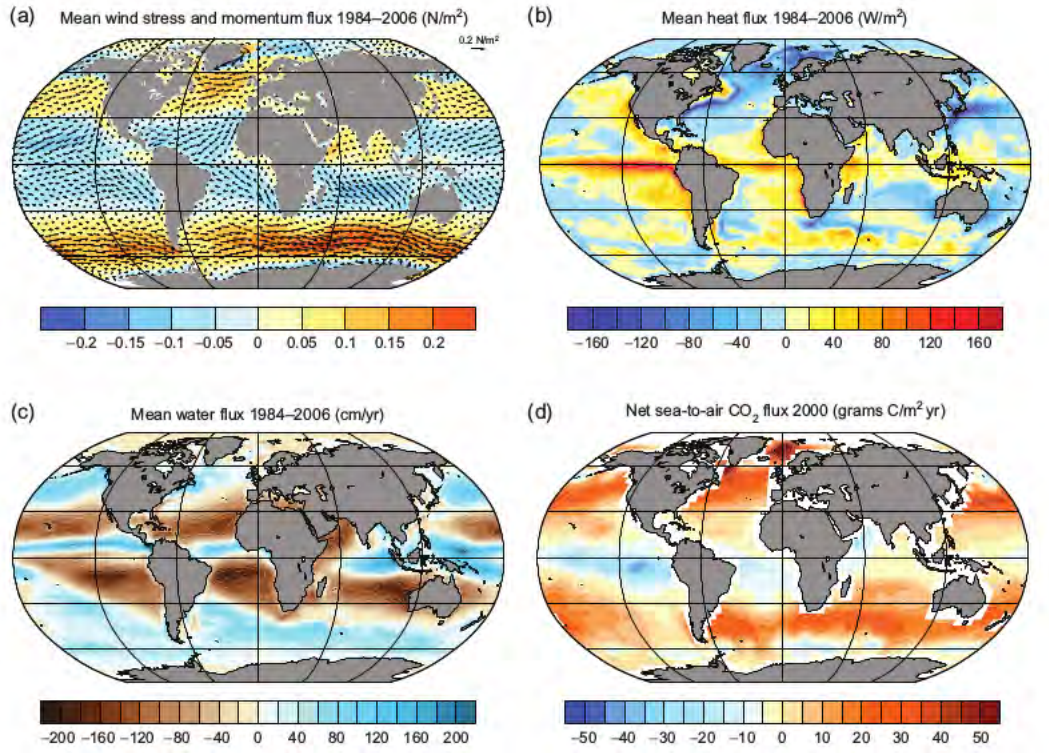

Figure 1.1: *Major drivers of ocean processes and ocean circulation from various data sources. Shown are time-averaged quantities: (a) wind stress (arrows) and atmosphere-to-ocean momentum flux (colors); (b) net atmosphere-to-ocean heat flux; (c) net freshwater flux excluding river runoff, that is, precipitation minus evaporation, and (d) net atmosphere-to-ocean carbon flux in the year 2000, indicating a large imbalance caused by the uptake of anthropogenic carbon by the ocean. Momentum flux is everywhere into the ocean; positive (negative) values indicate that this flux is caused by a westerly (easterly) wind stress. In panels (b–d), fluxes are positive when they are from the atmosphere to the ocean. After Stocker, 2013.*

The large-scale atmospheric circulation induces surface wind stress on the ocean surface, which is partly influenced by air–sea fluxes (i.e., heat and water vapor). On a global scale, the zonal component of the wind stress is stronger than the meridional component (Figure 1.1a), pointed out by the westerly wind belt of the Southern Ocean. In the equatorial region (20°S-20°N) the ocean gains heat, while outside this area heat is released (Figure 1.1b), meaning that the ocean must transport heat away from the equator, specially throughout the western boundaries. The freshwater balance on the ocean surface is carried out principally by precipitation and evaporation, with a largely zonal structure on a global scale (Figure 1.1c). This is characterized by net freshwater gain in both narrow equatorial band and higher latitudes, and net freshwater loss in the subtropical dry zones. At the same time, the air-to-sea flux of carbon illustrates the large imprint of the natural carbon cycle at the ocean surface (Figure 1.1d). In the mid-latitudes the surface ocean takes carbon, while in the tropics and Southern ocean the carbon is released. The spatial distribution of these fluxes is conducted throughout global ocean circulation, which is dominated by two major processes: 1) Wind-driven circulation, forced by wind stress on the sea surface (i.e., momentum exchange), and 2) Thermohaline circulation, driven by differences in temperature and salinity within the ocean (i.e., buoyancy exchange). These two circulation types are not fully independent, since the sea-air buoyancy and momentum exchange are dependent on wind speed. Figure 1.2 shows a conceptual picture of the global ocean circulation.

On one hand, winds on the sea surface constitute a dominant source of energy responsible for motions in the upper ocean over broad spatial-temporal variability, from small-scale turbulent fluctuations to large-scale oceanic currents. They are directly linked to the base of the atmospheric boundary layer, where their pattern reflects the overall structure of the atmospheric general circulation. Its surface flow is characterized by basin-wide gyre circulations in the Atlantic, Pacific, and Indian oceans. The wind-driven circulation can be divided roughly into three major phenomena from: polar/subpolar gyres (e.g., Antarctic Circumpolar current), subtropical gyres (including both Eastern and Western Boundary currents) and mainly zonal equatorial current systems (Figure 1.2a). The wind stress induces a circulation pattern that share many commonalities between ocean basins. As the winds blow above the ocean surface, the upper ocean moves in a balance of frictional and Coriolis forces known as Ekman transport. This mechanism drives a net transport of water that is perpendicular to the wind. This transport results in areas of divergence and convergence that lead, respectively, to upwelling (i.e. upward motion of interior waters) and downwelling (i.e. sinking of surface waters). On the other hand, the Thermohaline circulation (THC) is that part of the ocean circulation which is driven by the joint effect of heat fluxes

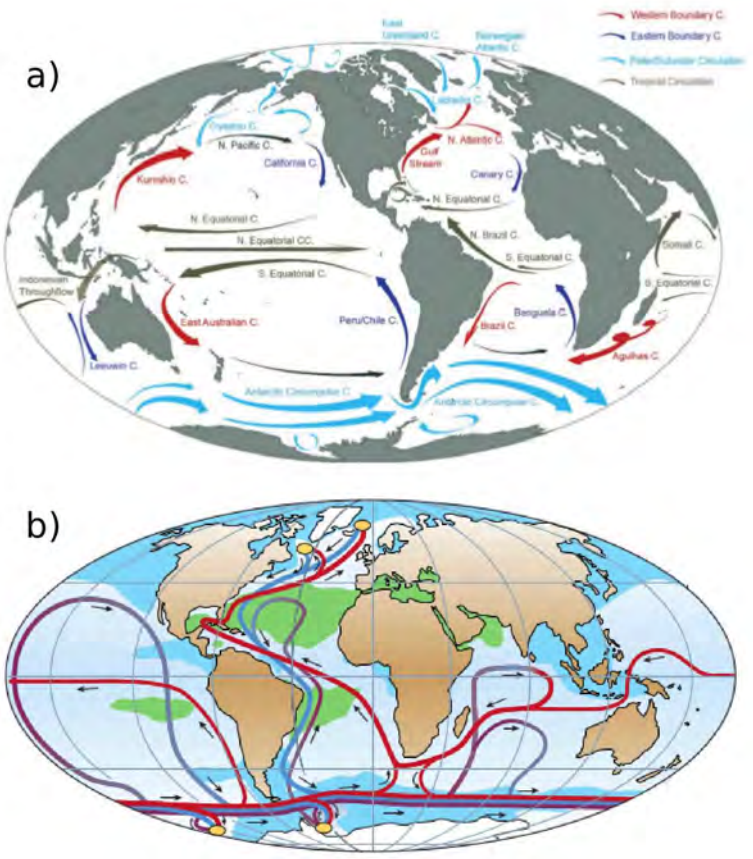

Figure 1.2: *a) Wind-driven surface ocean circulation. Driven by winds, the surface currents form the main subtropical and subpolar gyres and the tropical/equatorial circulation. After Delorme and Eddebbar, 2016. b) Thermohaline circulation. Near-surface waters (red lines) flow towards three main deep-water formation regions (yellow ovals) — in the northern North Atlantic, the Ross Sea and the Weddell Sea — and recirculate at depth (deep currents shown in blue, bottom currents in purple; green shading indicates salinity above 36%, blue shading indicates salinity below 34%). After Rahmstorf, 2002.*

and freshwater throughout the sea surface and subsequent interior mixing of heat and salt (see Figure 1.2b). Therefore, the THC consists of cooling-induced deep convection and sinking at high latitudes, upwelling at lower latitudes, and the horizontal currents feeding the vertical flows. As a consequence, thermohaline and wind-driven currents interact in non-linear forms that cannot be isolated by oceanographic measurements. For this reason, there are two unequivocal forcing mechanisms rather than two individual circulations.

1.1.1 Climate system and global energy budget

The climate system is an interactive system that can be usefully divided into several parts: Atmosphere, Hydrosphere, Cryosphere, Biosphere, Lithosphere, Pedosphere, or

Anthroposphere (e.g., Figure 1.3a). However, the Earth's components are not fully disconnected, because they are physically coupled through exchange fluxes of energy, momentum, and matter. Numerous physical and biogeochemical processes occur among the components of the climate system on a broad range of spatio-temporal scales, making the system extraordinarily complex. For example, as part of the hydrological cycle, the atmosphere and the oceans exchange, among others, water vapour and heat through evaporation, which leads to condensation, cloud formation, precipitation and runoff. On the other hand, the wind-driven circulation can impact the biogeochemical processes through exchange fluxes of substances such as carbon, nitrogen, oxygen, and many others. Another example is the biosphere that regulates the carbon dioxide concentration by photosynthesis and respiration, which in turn is influenced by climate change.

In this respect, the climate system is dominated by various external forcing mechanisms, the most important of which is the radiation from the Sun. Incoming radiant energy may be scattered and reflected by clouds and aerosols or absorbed in the atmosphere (e.g., Kiehl and Trenberth, 1997; Trenberth et al., 2009). For a stable climate, the global budget of the Earth's system is composed by the balance between the input and output radiation from the Sun and the Earth, respectively. Thus, for the climate system to be in equilibrium, the planetary radiation balance must be zero. The difference between both input and output radiations corresponds to the Earth's Energy Imbalance (EEI, see Figure 1.3b-c). As a consequence of the EEI, the climate system stores energy. The positive EEI is mostly produced by human activity, through the greenhouse effect. This is caused by the small percentage of greenhouse gases (GHG) that kept in our atmosphere reduce the rate at which Earth reflects energy back into space. GHG include: water vapor (H_2O), carbon dioxide (CO_2), ozone (O_3), methane (CH_4), and nitrous oxide (N_2O). Furthermore, the positive EEI is responsible of the climate change in the Earth's system, including rises in surface temperature, ocean heat content, ocean mass, global mean sea level, atmospheric temperature and moisture, drought, flooding and erosion, increased extreme events, and evaporation-precipitation (E-P), as well as decreases in land and sea ice, snow cover and glaciers (Schuckmann et al., 2016). A substantial portion of this energy warms the ocean (93%), due to its large heat capacity, while a minor part is warming the land, atmosphere and melting ice. In this sense, the energy budget at the sea surface is a combination of the net shortwave and longwave radiation and net latent and sensible heat flux (see Figure 1.1b). Loss of energy from the ocean through sensible and latent heat fluxes reduces the magnitude of the net radiation. Without oceanic transport of energy from the equator to the poles, the global energy balance could not be maintained. Therefore, the ocean is the likely source of

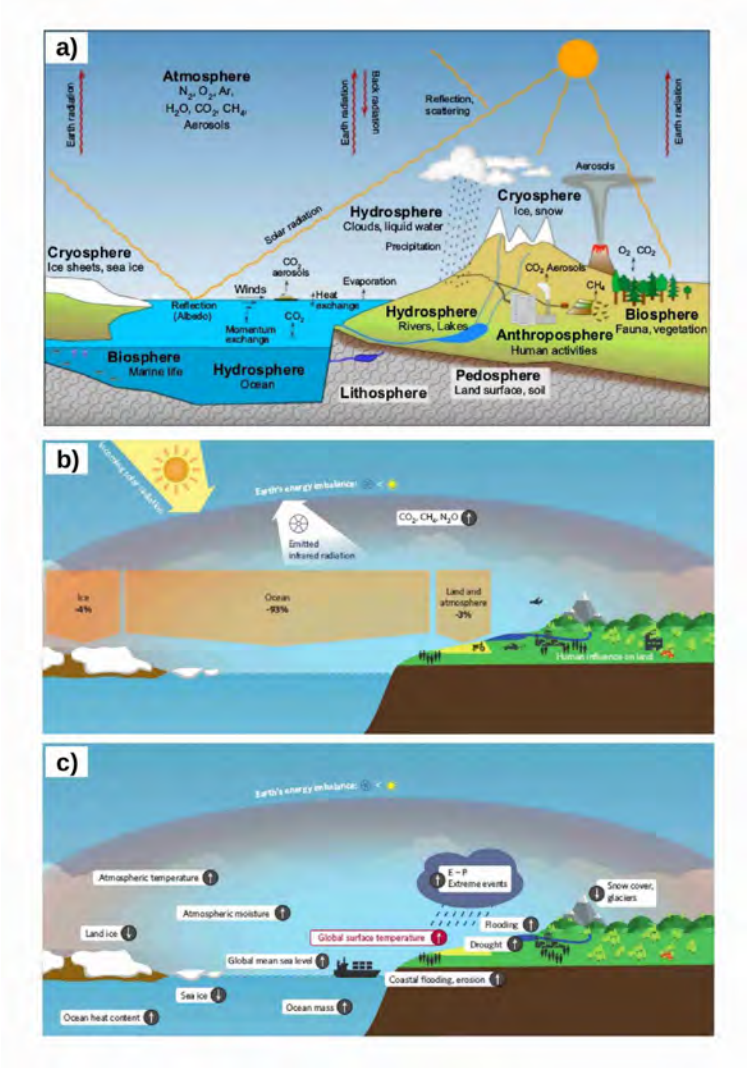

Figure 1.3: *a) Illustration of the Earth System components, which are intertwined and physically coupled through exchange fluxes of energy, momentum, and matter, and biogeochemically coupled through fluxes of carbon and other substances. After Stocker, 2013. b-c) Schematic representations of the flow and storage of energy in the Earth's climate system and related consequences. b) Earth's Energy Imbalance (EEI) as a result of human activities. The global ocean is the major heat reservoir, with about 90% of EEI stored there. The rest goes into warming the land and atmosphere, as well as melting ice (as indicated). c) 'Symptoms' of positive EEI, including rises in Earth's surface temperature, ocean heat content, ocean mass, global mean sea level, atmospheric temperature and moisture, drought, flooding and erosion, increased extreme events, and evaporation-precipitation (E-P), as well as a decrease in land and sea ice, snow cover and glaciers. After Schuckmann et al., 2016.*

natural long-term climate variability. Consequently, the oceans can impact the surface temperature directly, through surface fluxes of heat, or indirectly, by altering the atmospheric circulation and impacting the distribution of clouds and water vapor. The

global ocean therefore has a key role in the regulation and control of the climate fluctuations. However, our understanding of how the ocean impacts the global mean surface temperature (GMST) is strongly limited by available observations.

1.1.2 Change in future mean state

The GMST at the Earth's surface corresponds to both externally imposed forcing, i.e. anthropogenic GHG-induced and natural modes of variability internal to the climate system (see Figure 1.4).

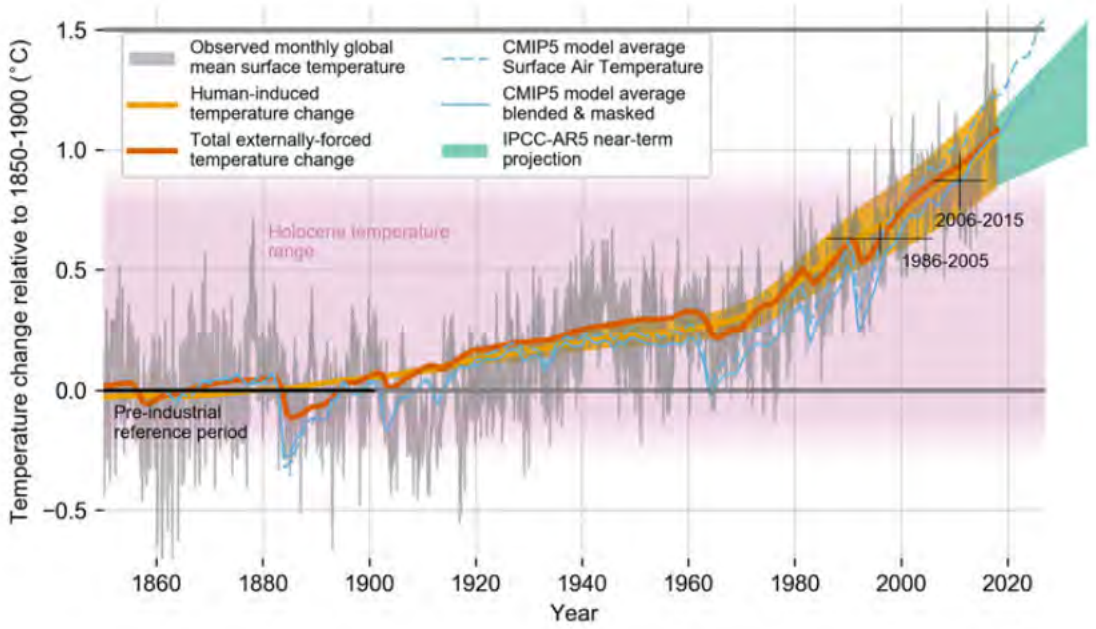

Figure 1.4: *Evolution of global mean surface temperature (GMST) over the period of instrumental observations. After M. Allen et al., 2018. Grey-shaded line shows monthly mean GMST in the HadCRUT4, NOAAGlobalTemp, GISTEMP and Cowtan-Way datasets, expressed as departures from 1850 to 1900, with varying grey line thickness indicating inter-dataset range. All observational datasets shown represent GMST as a weighted average of near-surface air temperature over land and sea surface temperature over oceans. Human-induced (yellow) and total (human and naturally forced, orange) contributions to these GMST changes are shown calculated following Otto et al., (2015) and Haustein et al., (2017). Fractional uncertainty in the level of human-induced warming in 2017 is set equal to 20% based on multiple lines of evidence. Thin blue lines show the modelled global mean surface air temperature (dashed) and blended surface air and sea surface temperature accounting for observational coverage (solid) from the CMIP5 historical ensemble average extended with RCP8.5 forcing. The pink shading indicates a range for temperature fluctuations over the Holocene (Marcott et al., 2013). Light green plume shows the AR5 prediction for average GMST over 2016–2035 (Kirtman et al., 2013).*

Historical records of GMST extend back farther than any other global instrumental timeseries. Thereby, the GMST has a crucial importance to understanding the patterns and magnitude of natural climate variations and distinguishing them from anthropogenic forcing. Unfortunately, human activities since the industrial revolution have caused a massive increase of the concentrations of the major GHG in the atmosphere. This is considered the main cause of GMST rise observed during the last decades and are projected to accelerate the rate of global warming (Meehl et al., 2007). The Fifth Assessment Report published by the Intergovernmental Panel on Climate Change (IPCC) in 2013 revealed that the ocean had absorbed more than 93% of the excess heat from GHG emissions since the 1970s. During the last few decades, there have been numerous efforts to understand what mechanisms are driving the future mean state of the climate system using current Coupled Global Climate Models (CGCMs). For example, increasing the GHG concentrations for the future climate, the hydrological cycle is expected to be modified through an increase in global mean temperature and the water vapor content of the atmosphere (M. R. Allen and Ingram, 2002; Held and Soden, 2006; Meehl et al., 2007). Indeed, taking into account different scenarios of GHG-induced in CGCMs, notable general agreements have been achieved, such as: global mean sea level rise (J. Church et al., 2013; Nicholls and Cazenave, 2010; Vermeer and Rahmstorf, 2009), increase of precipitation over the tropics and high latitudes with a decline over the subtropics (Chou et al., 2009; Held and Soden, 2006; P. Huang et al., 2013), weakening of tropical circulation (Chou and Chen, 2010; He and Soden, 2015; Vecchi and Soden, 2007; Vecchi et al., 2006), or the Hadley cell expansion (Kang and J. Lu, 2012; J. Lu et al., 2007; Nguyen et al., 2015). Figure 1.5 represents the future change in average from some variables of the climate system considering two different scenarios of increased GHG concentrations. While climate change is global, the regional response of each variable is not expected to be uniform across the planet. For instance, Arctic temperatures are rising much faster than the global average (Stocker, 2013), and rates of sea-level rise vary significantly across the world (J. Church et al., 2013). Nevertheless, both natural and human-induced SST change have large influences in the climate system in terms of amount, intensity or frequency on rainfall (droughts and floods), sea level, favorable upwelling winds, tropical cyclone development, monsoons circulation, storms tracks, and so on. More details of the change in mean state of the climate system are discussed in Chapter 3.

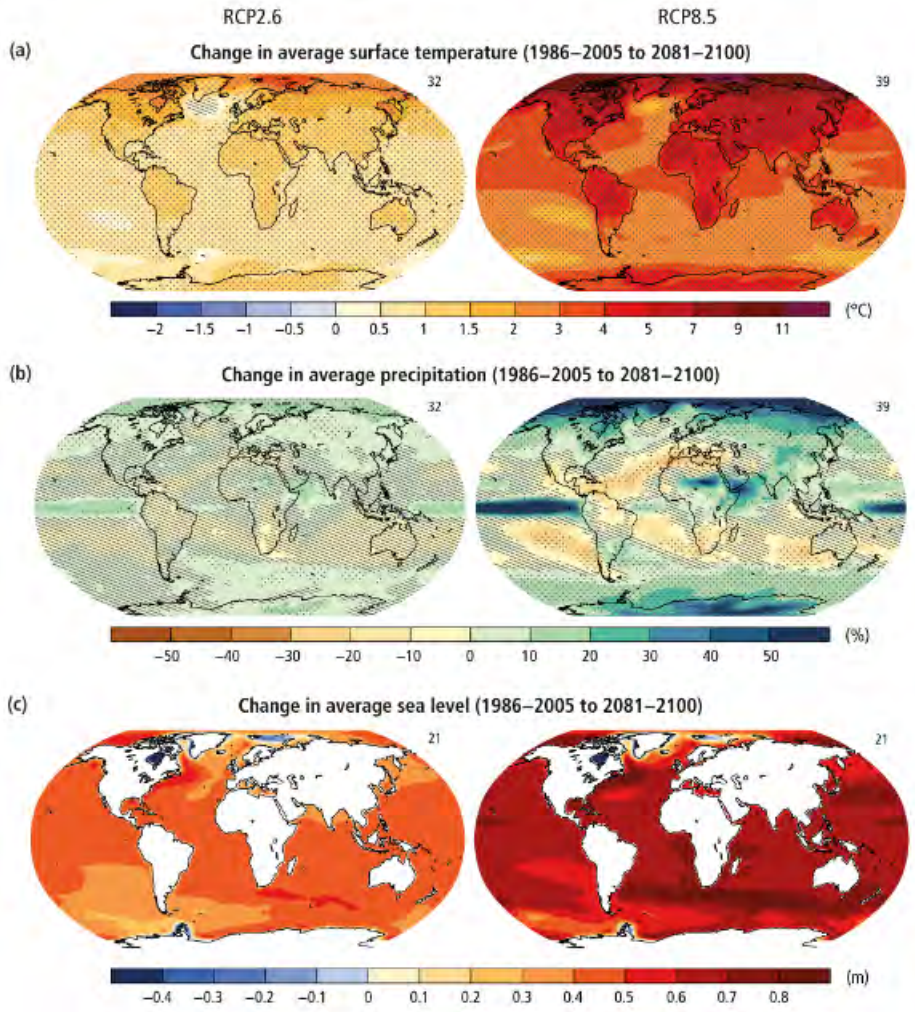

Figure 1.5: *Coupled Model Intercomparison Project Phase 5 (CMIP5) multi-model mean projections (i.e., the average of the model projections available) for the 2081–2100 period under the RCP2.6 (left) and RCP8.5 (right) scenarios for (a) change in annual mean surface temperature and (b) change in annual mean precipitation, in percentages, and (c) change in average sea level. Changes are shown relative to the 1986–2005 period. The number of CMIP5 models used to calculate the multi-model mean is indicated in the upper right corner of each panel. Stippling (dots) on (a) and (b) indicates regions where the projected change is large compared to natural internal variability (i.e., greater than two standard deviations of internal variability in 20-year means) and where 90% of the models agree on the sign of change. Hatching (diagonal lines) on (a) and (b) shows regions where the projected change is less than one standard deviation of natural internal variability in 20-year means. After IPCC, 2013.*

1.2 Natural modes of variability

The concept of "climate mode" represents a useful tool for reducing the complexity of Earth system variability. A mode can be defined as a set of physical processes characterized by coherent large-scale variations and a quasiperiodic evolution in time. These fluctuations on the climate variables (i.e., SST, rainfall, surface pressure, winds,

etc) are known as natural variability, which corresponds to the variation in climate parameters caused by nonhuman forces. There are two types of natural variability: i) external, mostly associated to changes in the sun, volcanic eruptions or in the orbit of the Earth, and ii) internal, as a result from interactions between the atmosphere and ocean. They have been identified through statistical analysis, from observations to numerical models, and commonly described by a distinctive spatial pattern and its associated time series (Christensen et al., 2013). Natural modes of variability affect global and regional climates on different spatio-temporal scales, and they have important impacts on human activities and ecosystems. In this sense, we have noted that the oceans play an important role in the climate system owing in part to their large heat-storage capacity, where SST operates as a source to regulate the climate system and its variability. Moreover, slow variations in SST contribute to climate fluctuations predictability on timescales of seasons and longer (Deser et al., 2010). However, a leading paradigm from atmospheric forcing patterns of SST variability has been considered during previous investigations: the stochastic climate model (Frankignoul and Hasselmann, 1977). The ocean mixed-layer temperature anomalies are forced by random atmospheric variability via surface energy fluxes and Ekman currents, and decay by damping back to the atmosphere via turbulent energy and longwave radiative fluxes. The simple stochastic climate model has been widely adopted as the leading paradigm for the "null hypothesis" of SST variability in middle and high latitudes where random fluctuations in the atmospheric circulation give rise to a low-frequency SST response. Examples include SST fluctuations from extra-tropics such as the Southern Annular Mode (Limpasuvan and D. L. Hartmann, 1999), the North Atlantic Oscillation (Marshall et al., 2001), the Pacific Decadal Oscillation (Mantua et al., 1997) or Interdecadal Pacific Oscillation (Power et al., 1999). Nevertheless, in this work we focused on patterns of nonseasonal SST variability that result from coupled ocean-atmosphere interactions in the tropical-subtropical oceans of the South Hemisphere, described below (see Figure 1.6).

1.2.1 El Niño Southern Oscillation

El Niño-Southern Oscillation (ENSO) is the largest source of interannual climate variability on a global scale, and arises from ocean-atmosphere interactions in the tropical Pacific through the Bjerknes feedback (Bjerknes, 1969). The positive phase of ENSO is called El Niño (see Figure 1.6b). Given a warm SST anomaly in the equatorial eastern Pacific, the east–west SST gradient in the tropical Pacific is reduced. The atmospheric response is a reduction of the east–west gradient of sea level pressure, and consequently results in a weakening of the Walker circulation and the easterly trade

winds. The weakening of the easterly trade winds causes a reduction in upwelling of cooler subsurface waters in the eastern and central equatorial Pacific ocean. In addition, warm waters from the western Pacific warm pool move eastward, enhancing the initial warm SST anomaly in the equatorial eastern Pacific. This Bjerknes feedback continues to amplify and enhance initial SST perturbations into a large-scale warming in

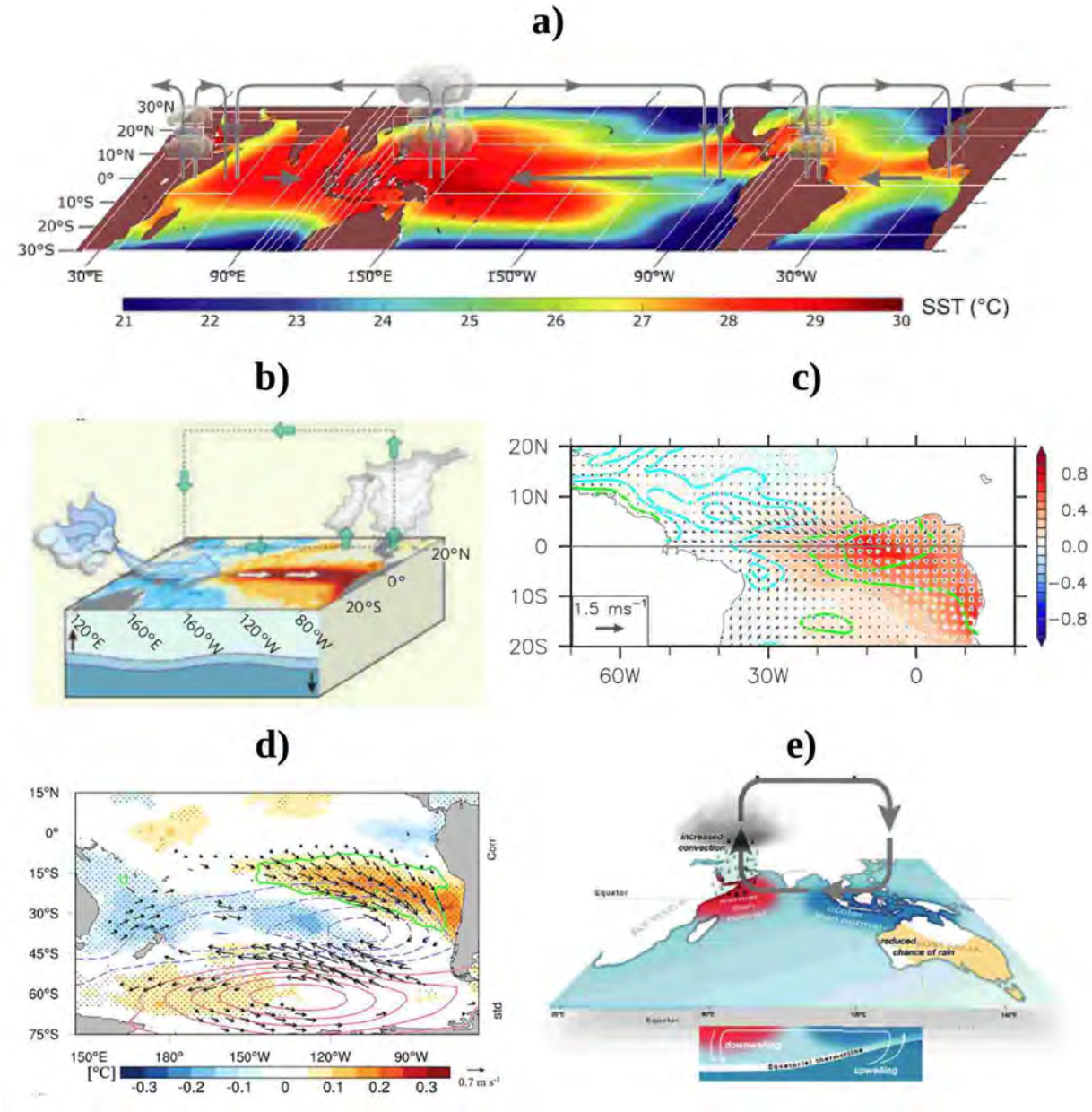

Figure 1.6: *a) Background mean state of the sea surface temperature (shading) and Walker circulation (arrows). After Cai et al., 2019. b) mature phase of El Niño events in the equatorial Pacific. After Ashok and Yamagata, 2009. c) mature phase of the Atlantic El Niño events. After Vallès-Casanova et al., 2020. d) positive phase of the South Pacific Meridional Mode. After You and Furtado, 2018. e) positive phase of the Indian Ocean Dipole mode. Source: Australian Bureau of Meteorology (http://www.bom.gov.au/climate/iod/).*

the tropical eastern Pacific. The eastward shift in the Walker circulation enhances the atmospheric convection and increase precipitation to the central Pacific ocean. This reorganization of large-scale atmospheric circulation further enhances central and eastern Pacific warming and leads to profound shifts in temperature and precipitation patterns across many regions of the world via atmospheric teleconnections. During the negative phase of ENSO (La Niña events), a strengthening of the Pacific trade winds drives increased upwelling resulting in cooler ocean surface temperatures, with a set of global climate impacts that are largely opposite to those of El Niño events. However, the spatial pattern and temporal evolution of ENSO events vary markedly among them, producing a wide diversity and complexity (e.g., Capotondi et al., 2015; Timmermann et al., 2018).

1.2.2 Atlantic El Niño

The dominant mode of interannual variability in the equatorial Atlantic ocean is usually described by a zonal mode over the east-west equatorial band (Zebiak, 1993). The dynamics of the Atlantic El Niño are somewhat similar to those of a Pacific El Niño, which results from ocean-atmosphere interactions and equatorial wave dynamics through the Bjerknes feedback (see Figure 1.6c and more details in section 2.4). However, other processes have also been suggested to contribute in the development of those events: i) off-equatorial Rossby waves being reflected into equatorial Kelvin waves at the western boundary (Foltz and McPhaden, 2010; Lübbecke and McPhaden, 2012), ii) meridional advection by temperature anomalies from north of the equator (Richter et al., 2013), iii) anomalous air-sea heat fluxes (Polo et al., 2015a), iv) forcing from the deep ocean by equatorial deep jets that propagate their energy upwards and thereby perturb the SST (Brandt et al., 2011), or v) thermodynamics feedbacks excited by stochastic atmospheric perturbations (Nnamchi et al., 2015). These could potentially lead to different flavors of Atlantic Niños/Niñas, alike the ENSO diversity (e.g., Vallès-Casanova et al., 2020).

1.2.3 South Pacific Meridional Mode

Generally, the "Meridional Mode" corresponds to subtropical ocean–atmosphere processes in which extratropical atmospheric variability impinges into the tropics, modifying from seasonal to longer timescales the tropical climate variability. The Meridional Mode has been identified in the North Atlantic (Chang et al., 1997), the North Pacific (Chiang and Vimont, 2004), and more recently the South Pacific (You and Furtado, 2018; H. Zhang et al., 2014a,b) basin. These modes share a similar spatial pattern

characterized with subtropical SST warming (cooling) and the corresponding weakening (strengthening) of the trade winds. Over the Pacific ocean, observational and modeling studies have been highlighted that the Meridional Mode may contribute as a potential ENSO diversity precursor (M. A. Alexander et al., 2010; R. Ding et al., 2015; Min et al., 2017; Vimont et al., 2014), although the South Pacific Meridional Mode (SPMM, see Figure 1.6d) has a larger equatorial signature than its northern counterpart for the same amount of extratropical variability, particularly in the central to eastern equatorial Pacific (H. Zhang et al., 2014a,b). During a positive (negative) phase of the SPMM, a weakening (strengthening) of the subtropical trade winds, triggered by mid-to-high latitude atmospheric variability, warms (cools) the local SST by modifying evaporation through the turbulent latent heat flux, where the anomalous SST signal propagates along the direction of the climatological trade winds via the wind-evaporation-SST (WES) feedback mechanism (Xie and S. G. H. Philander, 1994), and consequently warms (cools) the tropical SST.

1.2.4 Indian Ocean Dipole

In the tropical Indian Ocean, a basin-wide mode of variability associated to strong ocean–atmosphere interactions has been established as the Indian Ocean Dipole mode (IOD, Saji et al., 1999; Webster et al., 1999). The physical mechanism driving the IOD is similar to that driving ENSO, i.e., related to the Bjerknes feedback (see Figure 1.6e). During its positive phase, the SST off the coast off Sumatra is colder, while the western Indian Ocean exhibits anomalously warm waters. The colder temperatures of Sumatra generate atmospheric subsidence and stronger easterly winds along the equator, reinforcing the upwelling. The opposite happens throughout their negative phase. The IOD causes worldwide impacts, from an increase fire risk (Cai et al., 2009) to the worst droughts in Australia (Ummenhofer et al., 2009), severe wildfires and habitat destruction in Indonesia (Abram et al., 2003), or floods and disease outbreaks in East Africa (Webster et al., 1999).

1.2.5 Atmospheric bridges and oceanic pathways

All these natural modes of variability are connected through atmospheric bridges and oceanic tunnels (see Figure 1.7). The atmospheric bridges indicate atmospheric processes or patterns that can connect and link two or more sites far away, principally through the Hadley and Walker circulations. Because the three tropical basins are connected via the atmospheric circulation (M. A. Alexander et al., 2002; Latif and Barnett, 1995) any change in the SST trend magnitude across the tropical ocean leads to an

inter-basin SST gradient that drives changes in atmospheric and oceanic circulations from interannual to decadal timescales (Cai et al., 2019). For example, the occurrence of an El Niño event in the Pacific redistributes atmospheric heating sources and then changes atmospheric convection and circulation, resulting in changes of atmospheric wind, humidity, cloud cover and so on. These changes in turn influence surface heat fluxes, wind and ocean circulation. In this sense, the oceanic pathways of the Indonesian throughflow, the Tasman leakage and the Agulhas leakage are also important for connecting climate variability over the three oceans. Moreover, the Indian ocean can modify both Pacific and Atlantic oceans. The propagations of atmospheric Kelvin waves from a warm Indian ocean can increase equatorial easterly wind anomalies in the western Pacific and thus cool the SST in the eastern Pacific. On the other hand, the Indian ocean impacts the Atlantic ocean by atmospheric bridge and the oceanic Agulhas leakage south of Africa. At the same time, recent studies hypothesized that the equatorial Atlantic variability is able to kick off a tropical-wide teleconnection (X. Li et al., 2016), with Atlantic Niños (Niñas) inducing easterly (westerly) surface wind anomalies over the western equatorial Pacific, via changes in the Walker circulation and atmospheric waves trains, triggering upwelling (downwelling) equatorial Kelvin waves and favoring the development of a Pacific La Niña (El Niño) event (H. Ding et al., 2012; Losada et al., 2010; Polo et al., 2015b; Rodríguez-Fonseca et al., 2009). Thus, interactions among the Pacific, Atlantic and Indian Oceans through ocean-atmosphere coupling processes can initiate and/or modulate climate variability.

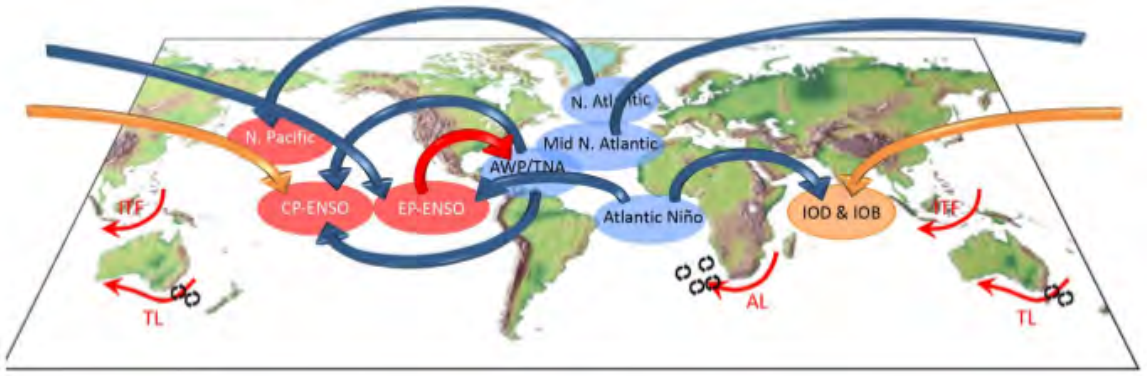

Figure 1.7: *Schematic diagram summarizing three-ocean interaction processes. Atmospheric bridge processes are represented by thick bending arrows. One-way bending arrow indicates one-way influenced process. Two-way bending arrow means that two oceans can affect each other. The oceanic pathways of inter-ocean interactions are the Indonesian throughflow (ITF), the Agulhas leakage (AL), and the Tasman leakage (TL), which are drawn and shown by red arrows. AWP and TNA stand for the Atlantic warm pool and the tropical North Atlantic, respectively. After C. Wang, 2019.*

1.3 Earth System Models

Climate models are an essential tool for studying the past, present and future climate change, including the anthropogenic forcing and natural variability. Their usefulness, however, depends on how realistically they simulate the statistics of present-day, including the mean state, trend, extreme events and variability of the observed climate system. The models used in climate research range from simple energy balance models to complex Earth System Models (ESMs) requiring state of the art high-performance computing. Rigorous and extensive tests are elaborated to determine the quality of the models, principally whether they can conserve mass or simulate the natural variability of the climate system (e.g., ENSO). However, although models reach an agreement with observations, there is no confidence that their predictions will be faithful due to the sensitivity of the climate to future anthropogenic forcing (present skill does not equal future skill). In addition, even the observations against which the models are to be checked are sometimes of questionable quality. In order to simulate the complex phenomena of natural variability, climate models must to able to represent efficiently processes such as deep convection, wind strength, short-wave radiation and cloud feedbacks, especially over the tropical Pacific to reproduce correctly the ENSO features (Bellenger et al., 2014; Capotondi et al., 2006; Guilyardi, 2006; Guilyardi et al., 2012, 2009; Leloup et al., 2008). In this sense, climate models can be tuned to fit twentieth-century global mean temperatures by adjusting interdependent parameters governing radiative forcing by aerosols and climate sensitivity (Knutti, 2008). Thus, climate models may simulate observed patterns of warming but for very different reasons (Crook and Forster, 2011).

1.3.1 Control runs

A control run is basically an integration of a climate model in which all forcing have a repeating annual cycle or are kept constant in time. The forcing can include concentrations of GHG or aerosols (e.g., from present-day conditions) that affect the atmosphere radiation balance. These simulations can be compared with recent observations. However, the present-day climate is not in equilibrium because important forcing (GHG and aerosols) has been increasing rather fast. Therefore, an alternative control run is made for "pre-industrial" conditions, when it is assumed that the climate was in equilibrium. Preindustrial is often chosen to be 1850, with a very small increase in CO_2. Most climate modeling groups focus on having the globally averaged heat imbalance less than 0.1 W/m^2, considering that it is difficult to get such an imbalance very close to zero. Still, selecting an 1850 control run is not totally truthful because the

global ocean observations (including sea ice and land states) are not available for 1850 (e.g., P. R. Gent, 2013; Kay et al., 2015). In general terms, the control run simulation allows to document the internal variability of the climate model. For example, it has been demonstrated that ENSO exhibits decadal to centennial variability in a 2000 years control run simulation (see Figure 1.8a).

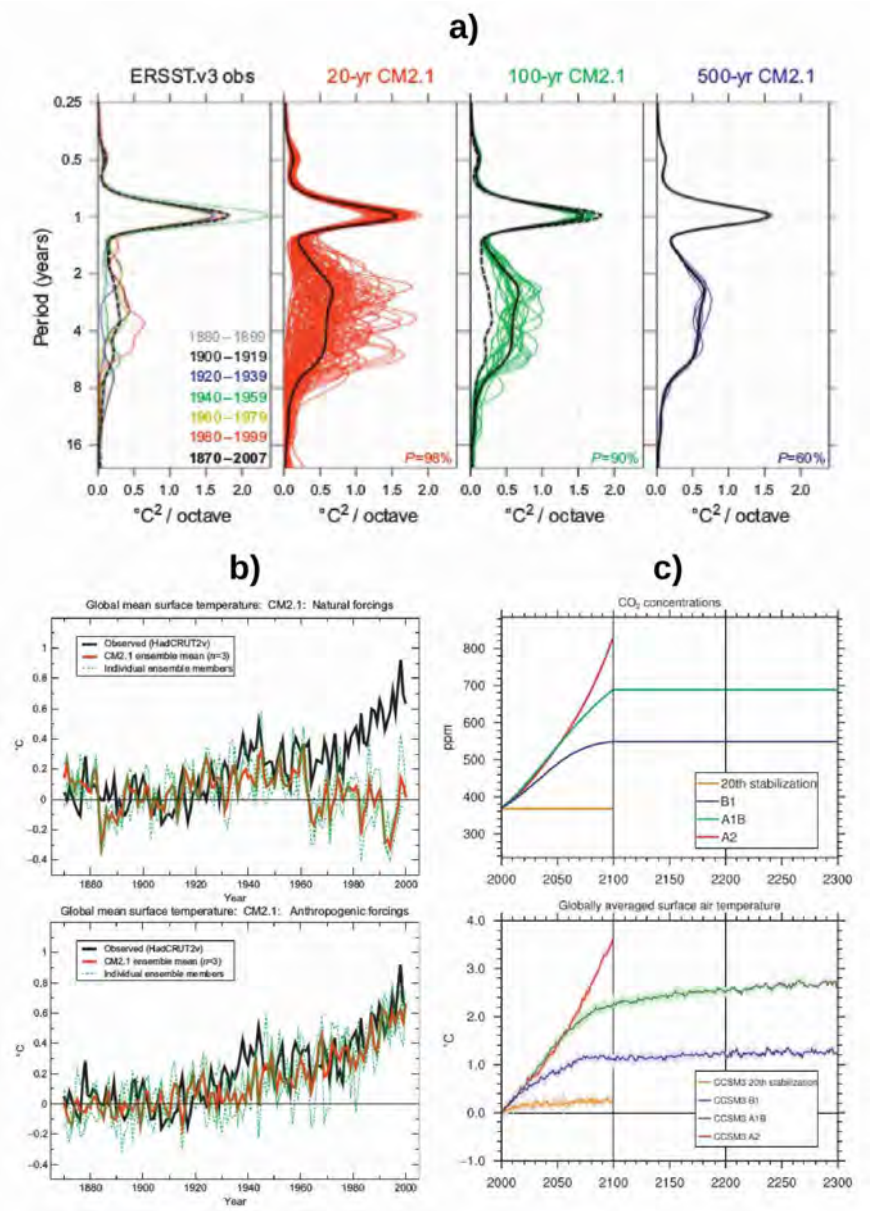

Figure 1.8: *a) Power spectra of NINO3 SSTs as a function of the period in octaves of the annual cycle from ERSST observations and the CM2.1 preindustrial control run. After Wittenberg, 2009. b) Globally averaged surface temperature 1870–2000 from observations, and ensembles of all natural forcing runs (upper panel) and anthropogenic forcings runs (lower panel) using the GFDL CM2.1. After Knutson et al., 2006. c) CO_2 concentrations from four future scenarios (upper panel) and the resulting globally averaged surface temperature increase (lower panel) from runs using the CCSM3. After Meehl et al., 2006.*

1.3.2 Historical simulations

The Historical simulations (also called "twentieth century runs") are forced, as initial conditions, by different climate variables from control runs experiments, such as atmospheric CO_2 concentrations, level of solar output, natural aerosols (e.g., volcanic eruptions), man-made aerosols, changes in land, etc. Commonly, these initial conditions are chosen after a few hundred years of the control run, when the climate system is in equilibrium. Then, Historical simulations must reproduce properly the observed changes in the climate system over the last 150 years (e.g., SST, Figure 1.4). One of the most fascinating objectives that the research community achieved with this kind of global climate simulations is to determine the cause of the global warming. For example, considering two experiments from historical climate simulations (all the natural forcing and GHGs are retained at their preindustrial values versus just the anthropogenic forcing allowed to vary) it was demonstrated that the accelerated warming since 1975 is caused by anthropogenic forcing (see Figure 1.8b). Nevertheless, the uncertainty of these climate simulations through the parameterization of clouds is significant.

1.3.3 Future projections

In order to project the future climate variability with a global model simulation, inputs levels from different variables must be considered. For example, the future level of solar output, volcanic eruptions and natural aerosols is chosen to be constant. Then, a scenario for the future GHGs concentrations (same present levels, slowly accelerated, reduced after few decades, etc) is selected, which is continuously under discussion. Because of this uncertainty, climate models have been run with a wide variety of scenarios for the future concentrations of CO_2. In this sense, future climate models projections indicate that the increased warming rate of the globally averaged surface temperature is proportional to the faster rise in GHGs (see Figure 1.8c). The rate of temperature increase varies across climate models by the sensitivity of various factors (equilibrium climate, aerosols, heat uptake, etc). Other experiments of the future climate can include an accelerated increase of anthropogenic forcing (e.g., doubling or quadrupling the CO_2 concentrations in comparison to present day state), and then kept constant.

1.3.4 Limitations in the climate models

How trustworthy are climate models? In this regard, CGCMs have shown complications to reproduce local processes or ocean-atmosphere interactions. Many biases in CGCMs originate from both the atmospheric and oceanic components. The spatial

horizontal resolution is typically coarse (∼100 km), as well as the vertical component (∼30-60 levels), meaning that important processes must be parameterized because they cannot be resolved. In addition, discrepancies could be due to factors such as spatial and temporal variations in the quality of observations, natural multi-decadal variability, climate model parameter uncertainty, etc. Even with a standard set of metrics (some of which are more intelligible than others) it is difficult to establish whether one model is more skillful than another (see Figure 1.9b, Flato et al., 2013).

One of the most meaningful quantities that requires much attention to be correctly

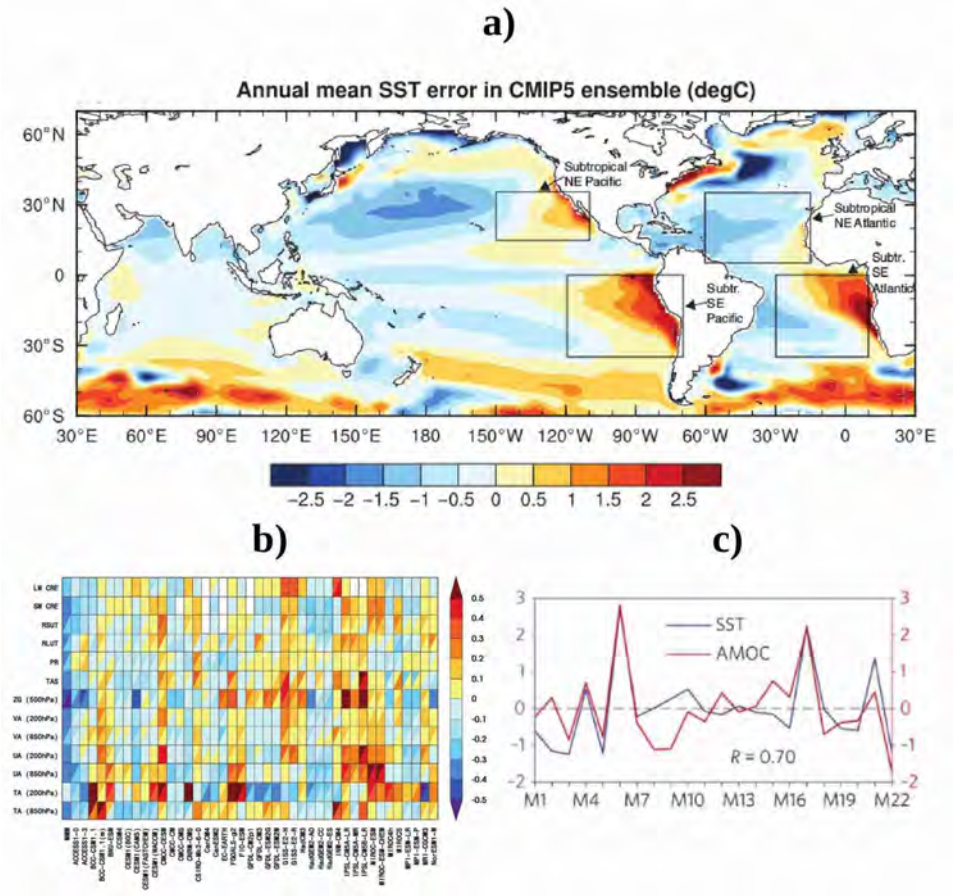

Figure 1.9: *a) Annual mean SST bias of the CMIP5 ensemble relative to the optimally interpolated SST (OISST) data set. After Richter, 2015. b) Relative error measures of CMIP5 model performance, based on the global seasonal-cycle climatology (1980–2005) computed from the historical experiments. Rows and columns represent individual variables and models, respectively. The error measure is a space–time root-mean-square error (RMSE), which, treating each variable separately, is portrayed as a relative error by normalizing the result by the median error of all model results. For example, a value of 0.20 indicates that a model's RMSE is 20% larger than the median CMIP5 error for that variable, whereas a value of –0.20 means the error is 20% smaller than the median error. After Flato et al., 2013. c) Expansion coefficients of SST bias and the Atlantic Meridional Overtuning Circulation (AMOC) for the first inter-model SVD mode (accounting for 45% of total variance). After C. Wang et al., 2014*

reproduced is the SST mean state (Figure 1.9a). In particular, the highest SST warm bias occurs in the Eastern Boundary Upwelling Systems (EBUS) and can exceed 5°C (e.g., Richter, 2015; C. Wang et al., 2014). Different causes have been proposed to understand it: i) bad representation of the stratocumulus deck (misrepresentation of the surface shortwave radiation), ii) unrealistic representation of mesoscale eddy activity (due to their low spatial resolution), iii) underestimation of the alongshore winds (Ekman dynamics), among others. Additionally, the misrepresentation of oceanic-atmospheric teleconnections can impact the regional biases found in the EBUS (e.g., thermohaline circulation, see Figure 1.9c, C. Wang et al., 2014). Thus, it is necessary to obtain a better representation of both regional processes and global teleconnections to improve the climate model performance. In particular, mixing processes in ocean models are especially crucial to reproduce the equatorial undercurrent systems and the surface mixed layer, which are both important for SST predictions. More importantly, the ocean has a small Rossby radius of deformation, which is hardly resolved by the current generation CGCMs beyond the equatorial band. It has been shown that a high resolution of 1/10° ($\sim$10 km) is necessary to resolve the eddy effects detected from satellite observations (e.g., F. O. Bryan et al., 2007).

1.4 Eastern Boundary Upwelling Systems

Eastern Boundary Upwelling Systems (EBUS) are among the most productive marine ecosystems of the world oceans, with the major coastal upwelling zones supporting around 20% of the global take of marine fish over an area of less than 1% of the global ocean (Chavez and Messié, 2009). The high levels of productivity in the EBUS result from the wind-driven circulation by large-scale atmospheric pressure systems. Through the Ekman dynamics, the alongshore equatorward winds force surface waters offshore, thereby pumping nutrient-rich deeper waters into the illuminated surface layers in the coastal zone (i.e., "upwelling"), where photosynthesis is favored (see Figure 1.10a). The four main EBUS correspond to: California, Canary/Iberian, Benguela and Humboldt (Peru-Chile). They are narrow regions of the coastal ocean that extend latitudinally over several thousands of kilometers and longitudinally to beyond the continental shelves whose widths range from 10 to 200 km. They are located in the eastern part of the oceans and on each side of the Equator from 10°-20° in latitude. The coastal geometries are quite similar in appearance, where relatively straight coasts are oriented approximately in a north–south direction, including capes and bays. The long-term mean oceanic circulation in EBUS is marked by broad, shallow, and slow surface flows which transport cool and relatively low-salinity waters

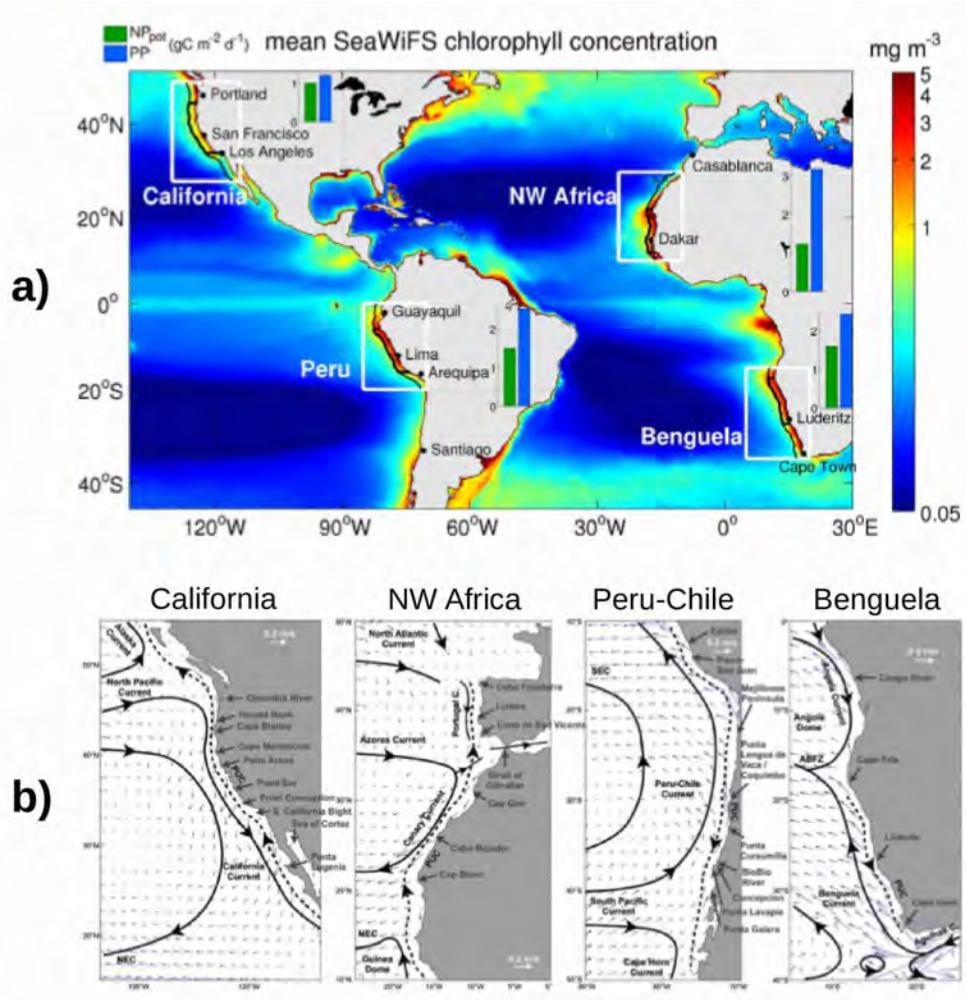

Figure 1.10: *The four main EBUS in the world Oceans. Colors are the mean SeaWiFS chlorophyll concentration (in mg/m3). White boxes delimit the four EBUS, the black lines are the 150 km offshore limit. The inserts show the mean potential new production derived from nitrate supply (in green) and the mean primary production (in blue). After Messié and Chavez, (2015). b) Schematics of the current systems in each of the EBUS, overlain on the long-term mean surface currents of the OFES general circulation model. After Strub et al., (2013)*

equatorward through the mid-latitudes, forming the eastern branches of the anticyclonic subtropical gyres (e.g., Strub et al., 2013). In addition, these regions share common characteristics, such as coastal upwelling favorable winds, equatorward surface currents, poleward undercurrents, alongshore instabilities, coastal trapped waves, or mesoscale eddies (see Figure 1.10b).

Over these regions, mesoscale ocean activity (referred to here as "eddies") and coastal upwelling are both resulting from the intensity of upwelling velocities and from the vertical structure of oceanic properties. On one hand, Ekman transport can produce upwelling through flow divergence in the coastal area due to the coastal boundary and in the offshore area due to wind curl. On the other hand, eddies play a key

role in the transport of water masses properties, from heat content to dissolved oxygen, into the open ocean across different spatial and temporal scales (Chaigneau et al., 2009; Chaigneau and Pizarro, 2005; Colas et al., 2012; Rossi et al., 2009; Stramma et al., 2013). These eddies affect the primary productivity and biogeochemistry of the ocean and, consequently, are potentially important for the climate of the planet (Chelton et al., 2011; C. Dong et al., 2014; McGillicuddy et al., 2007). In addition to surface mesoscale eddies, which have been rather well documented from satellite data (e.g., Chaigneau et al., 2009; Chaigneau and Pizarro, 2005; Chelton et al., 2011), EBUS show a distinctive class of subsurface or "intrathermocline" eddies that are much less known. For instance, these eddies are commonly anticyclonic and have a diameter close to the Rossby radius and a core with a thickness of approximately 500 m (Combes et al., 2015; Hormazabal et al., 2013; Pegliasco et al., 2015).

1.4.1 Future projections in EBUS

The CGCMs that are being used to estimate future changes in regional climate are particularly poor at simulating the present-day conditions in the EBUS (see Figure 1.9a). In particular, the warm SST bias is of order 5°C in these regions, which implies errors in the processes involved in upwelling, vertical mixing and horizontal advection. Still, the mechanisms supporting upwelling in EBUS originate from large-scale atmospheric-oceanographic coupling, therefore the amplitude and timing of upwelling-favorable winds are sensitive to climate variability and therefore global warming. It has been predicted that the increase of GHG concentration will impact atmospheric pressure gradients systems changing spatial wind distribution and hence an impact on coastal and offshore upwelling in the EBUS (Bakun et al., 2015; Rykaczewski et al., 2015; Sydeman et al., 2014; D. Wang et al., 2015). In this sense, the Hadley Cells are predicted to expand poleward in both hemispheres, and observational evidence indicates this has already begun to occur (J. Lu et al., 2007). These changes of the Hadley Cells suggest that the regional EBUS might expand poleward in both hemispheres. However, it is yet unclear. In addition to these dynamical changes in the Hadley Cells, local thermodynamic arguments suggest that regional upwelling winds in the EBUS may increase due to increased land-sea temperature gradient (e.g., Bakun, 1990; Bakun et al., 2015).

Under global warming conditions, continental temperatures will rise faster during the local heating seasons than will temperatures in the nearby ocean, thereby steepening the cross-shore pressure gradients that drive upwelling-favorable winds (see Figure 1.11a). Nevertheless, this hypothesis is still debated (Belmadani et al.,

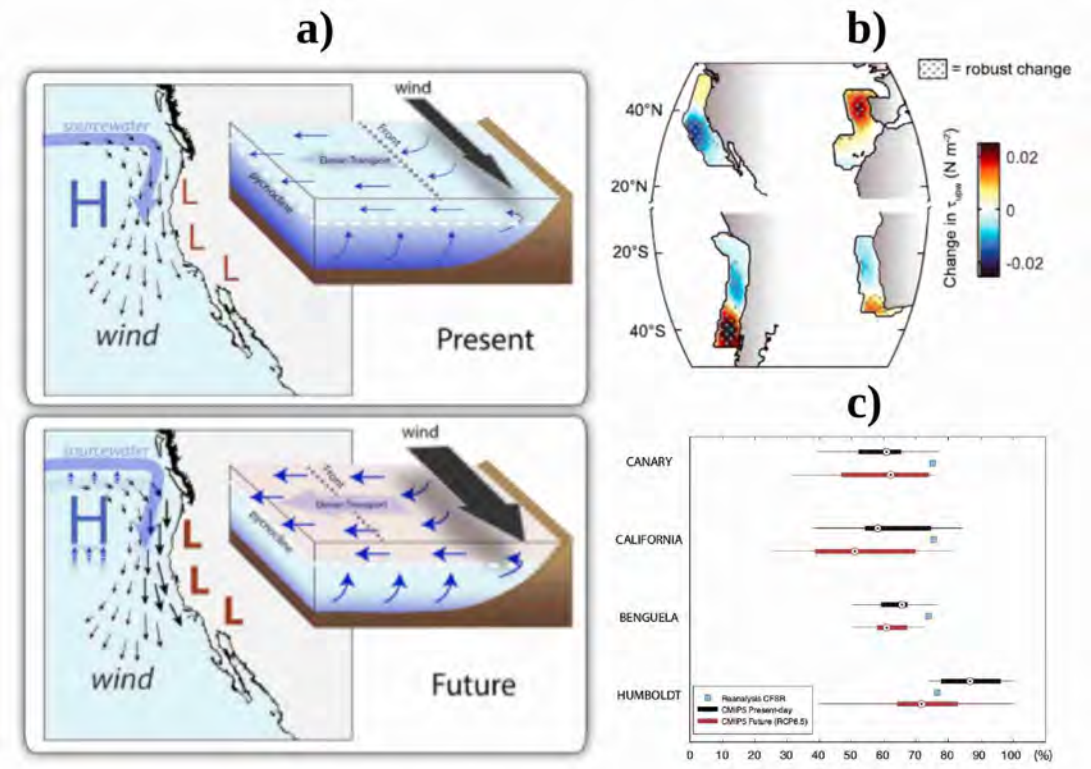

Figure 1.11: *a) Conceptual diagram of the present and future state of coastal upwelling zones, with the California Current as an example. After Bakun et al., 2015. b) Ensemble mean of the change between the two periods (2071–2100 mean minus 1861–1890 mean) of the meridional wind stress component relevant to the upwelling intensification. Stippling indicates the areas of robust change across models. After Rykaczewski et al., 2015. c) Relationship between migratory anticyclones and intense upwelling winds. Probability that a wind stress greater than the 75th percentile occurs together with a migratory anticyclone, for reanalysis CFSR and models for historical period (1970–1990) and projections under the RCP8.5 scenario (2080–2100). Circle indicates median, boxes the range 25th and 75th percentiles, and lines extend to the most extreme data points of the 16 models. After Aguirre et al., 2019.*

2014). Rykaczewski et al., 2015 suggested that only summertime winds near poleward boundaries of climatological upwelling zones are projected to intensify, while winds near equatorward boundaries are projected to weaken (see Figure 1.11b). Recently, Aguirre et al., 2019 proposed that future changes in upwelling-favorable wind events in EBUS could be linked to extratropical synoptic-scale migratory anticyclones (see Figure 1.11c). Notwithstanding, any change in coastal winds under global warming conditions will impact directly the mesoscale ocean activity and coastal upwelling in EBUS.

1.4.2 Impact of the mesoscale eddies on the ocean circulation

In EBUS, both the mean ocean circulation and eddy flow are not as energetic as in the western boundary currents. Mesoscale eddies in the global ocean are coherent rotating vortices of water with radial scales ranging from 25–250 km and lifetimes >16 weeks (Chaigneau et al., 2009; Chelton et al., 2011). Eddies play a significant role in the mixing and transport of heat, salt, and biogeochemical tracers across the global oceans. Moreover, eddies have been shown to influence near-surface winds, clouds, and rainfall within their vicinity (Chelton et al., 2004; Frenger et al., 2013) as well as marine ecosystems (Gaube et al., 2013). Thus, understanding global ocean eddy dynamics and their role in influencing various oceanographic, atmospheric, and biological phenomena is an important scientific concern. In the four EBUS, eddies share common characteristic (see Figure 1.12): i) they are mainly generated along the coast, ii) predominant westward propagation, iii) increase of their velocities toward the equator from 1-3 cm/s to 5-10 cm/s, iv) they have a radii of 70–160 km, and v) they are frequently observed along the coastal transition zones, dominated by cyclonic or anticyclonic eddies. Mesoscale eddies in EBUS reveal ubiquitous turbulent activity suggestive of baroclinic instability from the coastal current system, which has been confirmed through numerical modeling (Capet et al., 2008; Colas et al., 2013, 2012; Marchesiello et al., 2003).

The influence of baroclinic instability and its associated turbulent structures in EBUS are generally considered as modest, in comparison to western boundary currents systems or the Antarctic Circumpolar Current. However, kinetic energy of the eddies is much larger than that of the mean circulation, where the contribution from mesoscale eddies to the total transport can be comparable to that from large-scale horizontal wind and thermohaline-driven circulation (Z. Zhang et al., 2014). Thus, properties of eddy fluxes can potentially have substantial effects on the climate system. Generally, the water masses in EBUS are rich in carbon and nutrients affecting both primary biological production and export fluxes, which impact the distribution of chemical properties and biogeochemistry. In this sense, Figure 1.13 shows a schematic diagram of how mesoscale eddies impact the oceanic circulation and modify their biogeochemical properties in EBUS.

Gruber et al., 2011 showed that intense eddy activity is suppressing biological production and export, due to eddy-induced transport of nutrients from the coastal region to offshore (Figure 1.13a). In addition, Colas et al., 2013 suggested that eddy fluxes can balance the mean offshore air-sea heating and coastal upwelling, maintaining the equilibrium climate gradients (Figure 1.13b). One of the mechanisms generating vertical nutrient fluxes in eddy interiors is eddy-induced Ekman pumping that arises from

the interaction between eddy surface currents and winds, to generate upwelling in the interiors of anticyclones and downwelling in the interiors of cyclones. Thus, eddy-induced circulation cells within the mixed layer correspond to a shoreward flow above and offshore flow below, which creates a restratification effect. Accordingly, eddies are crucial to the movement and interaction of heat, momentum, trace chemicals, and biologically active oxygen and nutrients. Indeed, eddies and circulation determine the global and regional distributions of life in the sea, which is immediately visible in satellite images of the color of the ocean surface (see Figure 1.10a). It is further hypothesized that climate change will alter the characteristics and statistics of oceanic eddies with probably profound effects on the dynamics and functions of these systems. Moreover, ecosystems and fisheries are already under strong pressure from climate change globally, with projections pointing to an overall oceanic warming, acidification, deoxygenation, and reduced primary productivity (e.g., Beaugrand et al., 2019; Bopp et al., 2013; Breitburg et al., 2018). In particular, the response of the Peru-Chile Upwelling System

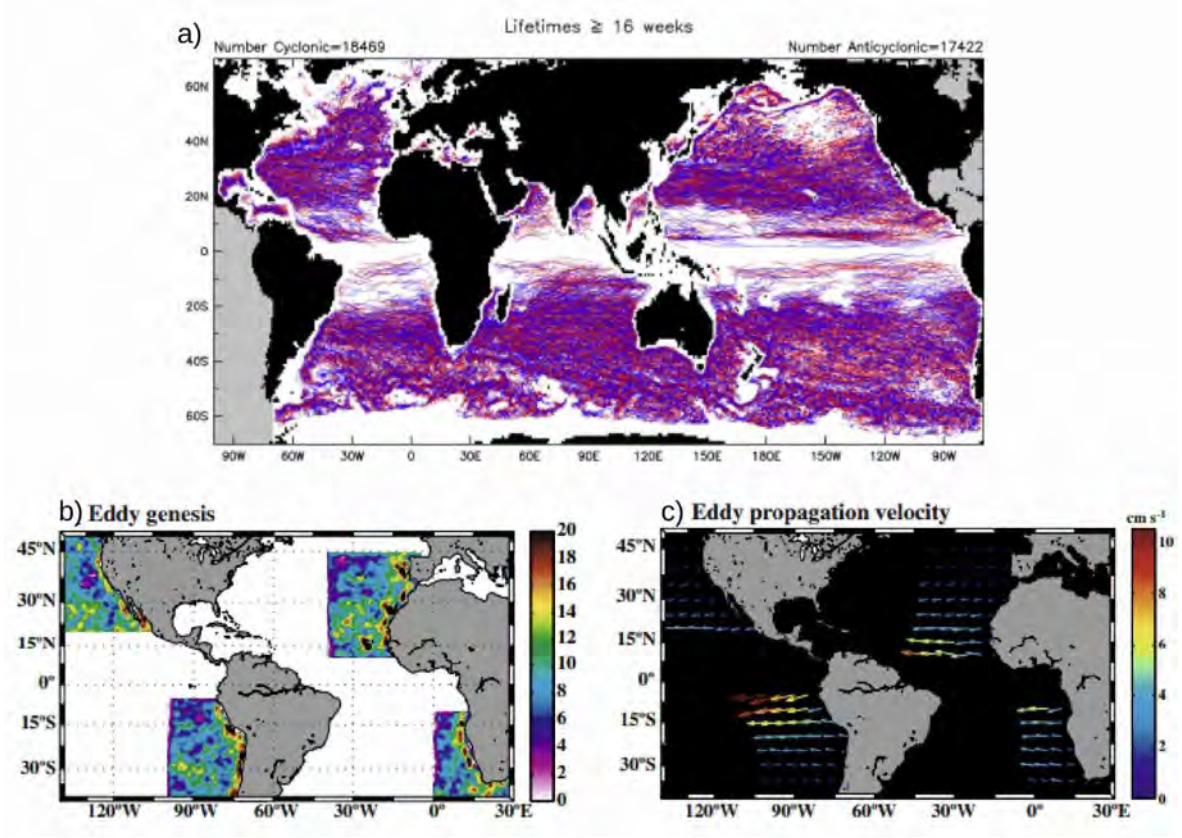

Figure 1.12: *a) The trajectories of cyclonic (blue lines) and anticyclonic (red lines) eddies over the 16-year period October 1992–December 2008 for lifetimes >16 weeks. After Chelton et al., 2011. b-c) Long-lived eddy genesis and propagation: b) Number of newly generated eddies, and c) propagation velocity vectors of both cyclonic and anticyclonic eddies. After Chaigneau et al., (2009).*

(PCUS) to global warming has been investigated in recent decade through downscaling studies (e.g., Belmadani et al., 2014; Echevin et al., 2012; Goubanova et al., 2011; Oerder et al., 2015). The understanding of the impact of climate change on the PCUS is motivated by two main reasons: i) the PCUS is one of the most productive EBUS (Chavez et al., 2008) being crucial to figure out whether upwelled waters could become less nutrient-rich and thereby reduce nearshore primary productivity, and ii) the PCUC has a rather tight connection to the equatorial Pacific and the globally strongest mode of interannual variability ENSO, which propagates via atmospheric and oceanic pathways into the PCUS and provokes specific physical and ecological responses.

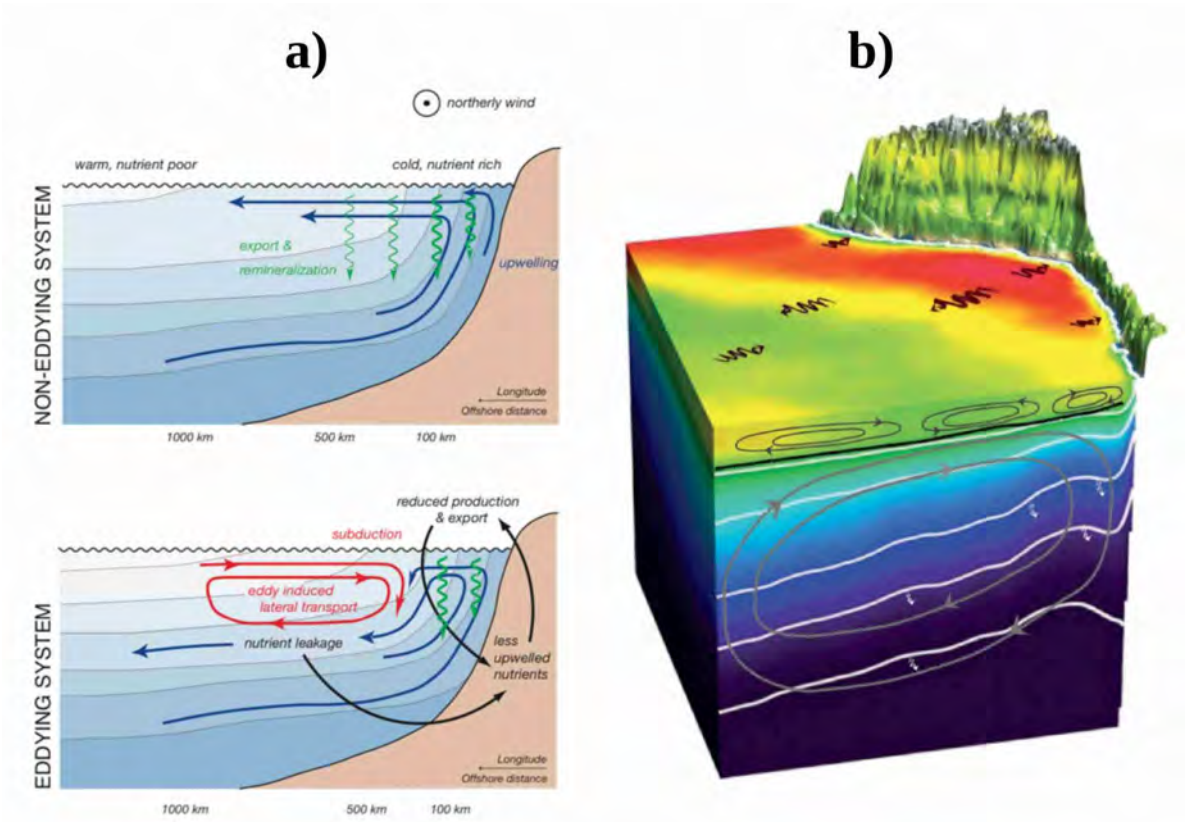

Figure 1.13: *a) Conceptual diagram of the impact of mesoscale eddies on coastal circulation, nitrogen transport, and organic matter production and export. The thick lines indicate total nitrogen transports and the thin lines depict circulation pattern. Shown in blue are the Ekman-driven transports and circulations. The red arrows show the eddy-driven transports and (bolus) velocities. Contour lines denote potential density and green arrows the vertical export of organic matter. After Gruber et al., (2011). b) 3-D schematic representation of the eddy effects in EBUS. After Colas et al., (2013).*

1.5 Scientific objectives

In this thesis, we take advantage of observations and numerical simulations to focus on two objectives: i) disentangle the mechanisms involved in the future SST pattern in the EBUS of the Southern Hemisphere using global climate models under warming conditions induced by GHGs, and ii) elucidate the relationship between the ENSO diversity and the turbulent flow in the Peru-Chile Upwelling System, one of the most productive marine ecosystems in the world, considering satellite data and two high-resolution oceanic models from regional to global scales. In this context, we can summarize the objectives as follows:

- To document the role of ocean dynamics and natural modes of variability in modulating the future SST pattern under anthropogenic forcing.
- To assess the contribution of the ocean advection components in the future SST mean-state, especially associated to both surface Ekman and geostrophic currents.
- To investigate the relationship between the ENSO diversity and the mesoscale activity in the South East Pacific throughout ocean-atmosphere teleconnections.
- To evaluate the ability of a long-term eddy-resolving CGCM simulation in reproducing the mesoscale activity in the South East Pacific and highlight some future projections under a global warmer climate.

The manuscript is organized as follows: In the second chapter, we provide a detailed description of the different data sets used from the available observations and reanalysis and global climate models. We also describe the methods to diagnose the mechanisms associated to the climate change SST patterns and the source of eddy kinetic energy. Chapter 3 deals with the mechanisms that describe the future pattern of sea surface temperature using climate models for projections at the end of the twenty-first century and considering the highest emission scenario (RCP8 .5). We highlight the importance of the dynamic response of the ocean and the natural variability of the climate system to modulate the average state of sea surface temperature under climate change. In Chapter 4 we demonstrate, using satellite data and high-resolution models of the region, that the natural variability of the tropical Pacific drives mesoscale activity along the Peru-Chile coast. The last chapter is dedicated to the conclusions and perspectives of this work.

Introduction générale (français)

Les Systèmes d'Upwelling de Bord Est (EBUS[1]) présentent un intérêt particulier car ils relient les bassins océaniques tropicaux aux latitudes moyennes par la circulation de renversement océanique-atmosphérique. Ces régions partagent des caractéristiques communes: des vents parallèles à la côte soufflant vers l'équateur favorables aux remontées d'eau côtières (phénomène appelé en anglais "upwelling"), des courants sous-jacents dirigés vers les pôles, des instabilités baroclines, des tourbillons ou des ondes piégées à la côte. Les EBUS abritent de riches écosystèmes océaniques et des pêcheries très productives, qui soutiennent environ 20% de la capture mondiale de poissons sur une superficie de moins de 1% de l'océan mondial. Ces régions correspondent aussi aux zones de subsidence de masses d'air sec associées à la circulation atmosphérique tropicale-subtropicale des cellules d'Hadley et de Walker. L'augmentation de la concentration de gaz à effet de serre (GHG[2]) a un impact sur les systèmes de gradients de pression atmosphérique qui modifient la distribution spatiale du vent et, par conséquent, modifient les remontées d'eau côtières et du large dans les EBUS. Ainsi comprendre comment le réchauffement climatique modifie la circulation océanique et son impact sur le pattern de la température de surface de la mer (SST[3]), de même que sur les propriétés biogéochimiques des eaux upwellées, reste un défi scientifique.

Au cours des dernières décennies, de nombreuses études ont prédit un réchauffement de la SST plus fort en régions équatoriales qu'aux latitudes moyennes de l'Hémisphère Sud, ce qui est maintenant reconnu comme une réponse robuste au réchauffement climatique dans les projections climatiques pour la fin du 21ème siècle. De plus, cette réponse équatoriale renforcée par rapport aux régions subtropicales est cohérente dans les trois océans de l'Hémisphère Sud. Ce gradient méridien de la SST est fortement prononcé dans l'océan Pacifique Sud-Est. Plusieurs études ont tenté d'expliquer cette réponse au forçage des GHG, principalement par le mécanisme de rétroaction "cloud-radiation-SST", de changements de pompage d'Ekman par la réponse du vent ou d'un refroidissement thermique latent accru par l'intensification des vents. Cependant, de grandes incertitudes dans les projections des modèles climatiques demeurent pour déterminer quels sont les mécanismes impliqués dans le pattern futur de SST et s'inscrivent dans les erreurs systématiques dues à l'inévitable propagation inter-modèles de la sensibilité climatique. Ces erreurs sont généralement associées à une mauvaise représentation des processus physiques, qui peut être amplifiée parmi les

[1] De l'anglais *Eastern Boundary Upwelling Systems*.
[2] De l'anglais *GreenHouse Gases*.
[3] De l'anglais *Sea Surface Temperature*.

composantes du climat, en particulier sous les tropiques, par une gamme de rétroactions nuageuses ou par les biais existants sur l'état moyen. En outre, l'incertitude sur le changement climatique à travers la variabilité interne, qui résulte de processus dynamiques non-linéaires intrinsèques à l'atmosphère, peut conduire à plusieurs hypothèses concernant les mécanismes couplés océan-atmosphère pouvant expliquer la réponse de la SST au forçage des GHG. Parce que les trois bassins tropicaux sont connectés via la circulation atmosphérique, tout changement dans l'amplitude de la tendance de la SST à travers l'océan tropical conduit à un gradient de SST inter-bassins qui entraîne des changements dans les circulations atmosphériques et océaniques aux échelles de temps interannuelle à décennale. En conséquence, il existe encore une grande incertitude dans les mécanismes à l'origine du pattern de changement climatique de la SST dans les régions tropicales et il est encore difficile de déconvoluer le rôle relatif des modes climatiques de la variabilité naturelle et/ou du forçage anthropique dans la conduite de ce changement.

De plus, les tourbillons à méso-échelle ont tendance à jouer un rôle important dans les propriétés des masses d'eau transportées au sein des EBUS, du contenu en chaleur à la concentration en oxygène dissous par exemple, où la contribution du transport due aux tourbillons peut être comparable à celle due au vent à grande échelle et à la circulation thermohaline. Leur plus forte influence océanique se manifeste principalement dans le Pacifique Sud-Est, une des régions d'upwelling les plus productives du monde, où l'activité méso-échelle est particulièrement intense par rapport aux autres EBUS de l'Hémisphère Sud. Dans cette région océanique, les tourbillons à méso-échelle ont été proposés pour modifier le bilan de chaleur, ce qui peut avoir des répercussions considérables sur le système climatique du Pacifique tropical, en particulier à l'échelle de temps El Niño, qui est le phénomène climatique dominant dans le Pacifique tropical, impactant la circulation atmosphérique globale et la circulation tropicale océanique.

Dans cette thèse, nous utilisons des observations et des simulations numériques pour nous concentrer sur deux objectifs scientifiques: i) identifier les mécanismes impliqués dans le pattern futur de la SST dans les EBUS de l'Hémisphère Sud à l'aide de simulations de modèles climatiques sous des scénarios de réchauffement induit par les GHG, et ii) élucider la relation entre la diversité du phénomène El Niño et le flux turbulent dans le système d'upwelling Pérou-Chili, l'un des écosystèmes marins les plus productifs au monde, à l'aide d'une part d'une modélisation océanique régionale et d'autre part d'une modélisation océanique mondiale à haute résolution. Dans le premier chapitre d'introduction nous résumons l'état des connaissances de l'impact du changement climatique sur l'océan. Nous décrivons aussi les contributions de la

variabilité naturelle et interne du système climatique et le rôle de l'activité de méso-échelle dans le système d'upwelling du Pérou-Chili. Ce chapitre fournit aussi le cadre général dans lequel s'inscrivent les questions abordées au cours de ce travail de thèse. Dans le deuxième chapitre, nous fournissons une description détaillée des différentes données utilisées, observations et réanalyses disponibles, et des modèles globaux climatiques. Nous décrivons aussi les bilans utilisés pour décrire les mécanismes associés au changement de la température de surface de la mer et l'énergie cinétique des tourbillons. Le chapitre 3 porte sur les mécanismes qui décrivent le pattern futur de la température de surface de la mer à l'aide de sorties de modèles climatiques pour les projections à la fin du 21ème siècle sous un scénario d'émission le plus élevé (RCP8.5). Nous mettons en évidence l'importance de la réponse dynamique de l'océan et de la variabilité naturelle du système climatique pour moduler l'état moyen de la température de surface de la mer sous le changement climatique. Dans le chapitre 4 nous démontrons à l'aide de données satellitaires et de modèles à haute résolution de la région que la variabilité naturelle du Pacifique tropical module l'activité à méso-échelle le long de la côte du Pérou-Chili. Le dernier chapitre présentera les conclusions et les perspectives de ce travail.

Chapter 2

Data sets and Methodology

In the present chapter we introduce the methodological framework used in this thesis. The first part corresponds to a complete description of the different datasets, from observations (satellite or in-situ) to reanalysis products used to evaluate the efficiency and skill of the numerical models simulations analyzed in terms of mean state and variability of the climate system, principally focused over the Pacific Ocean (in Chapter 4). The second part accounts for a concise description of the numerical models simulations used, from regional to global coupled models. The third part consists in a description of the analysis performed, which corresponds to: i) a heat budget over the mixed layer to disentangle the processes acting on the SST patterns in the EBUS of the South Hemisphere under climate change conditions (Chapter 3), ii) an EKE balance to describe the mechanisms associated to the low-frequency modulation of the eddy generation terms in the Peru-Chile Upwelling System (Chapter 4), and iii) statistical diagnostics. The last part includes specifications of the natural modes of variability.

2.1 Observations and Reanalysis products

2.1.1 Satellite altimeter data

We use sea surface height from the GEKCO (Geostrophic and Ekman Current Observatory) (Sudre et al., 2013) product to estimate the surface geostrophic EKE. This data set is based on altimeter data from DUACS (Data Unification and Altimeter Combination System) of AVISO (Archiving, Validation and Interpretation of Satellite Oceanographic data). Data are globally gridded from 1993 to present as daily values with a spatial resolution of $1/4°$ (~ 25 km).

2.1.2 Sea Surface Temperature

We used different data sets of SST over the last six decades. The use of different data sets is motivated by the need to evaluate the sensitivity of our results to the data

sets considering known differences in particular in the South Eastern Pacific where in situ data density is less. In particular the extrapolation procedure can generate artifacts where sampling is weak (Kent et al., 2017). 1) HadSST3 (Hadley Centre SST version 3) (J. Kennedy et al., 2011; J. J. Kennedy et al., 2011) provides monthly uninterpolated SST anomalies in 5°x5° grid box for 1850-present. The anomalies are relative to a 30-year climatology spanning 1961-1990. HadSST3 is based on in-situ measurements of SST from ships and buoys. 2) Kaplan extended v2 (Kaplan et al., 1998) is stored on a 5°x5° grid and consists in monthly anomalies from 1856-present. Anomalies are based on the 1951-1980 time period. Kaplan data uses optimal estimation in the space of 80 empirical orthogonal functions (EOFs) in order to interpolate ship observations of the U.K. Met Office database. 3) ICOADS (International Comprehensive Ocean-Atmosphere Data Set) offers surface marine data with gridded monthly products for 1°X1° boxes spanning 1960-present. Data sources range from early non-instrumental ship observations to more recent measurements from automatic measurement systems including moored buoys and surface drifters. 4) ERSST.v5 (Extended Reconstructed Sea Surface Temperature version 5) (B. Huang et al., 2017) derived from the International Comprehensive Ocean–Atmosphere Dataset (ICOADS) and distributed in monthly timestep from 1854 to the present, with a spatial resolution of 2°x2° grid. Major revisions for ERSST.v5 include: i) reducing spatial filtering in training the reconstruction functions Empirical Orthogonal Teleconnections, ii) using latest ICOADS Release 3.0 over 1854-2015, iii) using Argo profiling floats temperature above 5 meter depth that has not been used in previous version ERSST and other SST analysis, iv) using the latest UK Met Office HadISST2 ice concentration over 1870-2015, and v) revising ship SST bias correction relative to nighttime marine air temperature (NMAT) to the one relative to buoy SST observations.

2.1.3 Winds

Three global winds products (10-m surface winds and wind stress) with diverse spatial resolution were used. i) SCOW (Scatterometer Climatology Ocean Winds) (Risien and Chelton, 2008) estimated from climatological 10-year record (1999-2009) of wind measurements by the NASA QuikSCAT scatterometer with a spatial resolution of 0.25° ($\sim$ 25 km). ii) ERA-5 (Hersbach et al., 2020) is the latest climate reanalysis produced by ECMWF (European Center for Medium-Range Weather Forecasts), which replaces ERA-Interim, spanning the period from 1979 onward with a horizontal resolution of 0.3° ($\sim$ 31 km). iii) NCEP-NCAR (National Center for Environmental Prediction – National Center for Atmospheric Research) (Kalnay et al., 1996) reanalysis project of

global atmospheric fields from 1948 to the present with a spatial resolution of 2.5° (∼ 250 km).

2.1.4 Oceanic currents

Vertical section of the in-situ alongshore currents off Chile (30°S) is obtained from the COSMOS station, which is located at 71°47'W-30°21'S (∼ 50 km offshore). These currents measurements were collected by three Anderaa RCM7 current meters and an upward looking ADCP (Workhorse Sentinel 300 kHz) moored at ∼ 120 m depth. The time period with high resolution ADCP data covers the 2002-2008 years. This mooring is part of an observational system maintained by the Center for Oceanographic Research in the Eastern South Pacific (COPAS), University of Concepción, Chile, and is the only available long timeseries of subsurface current along the west coast of South America.

Two reanalysis products are used to evaluate the equatorial Pacific current system (zonal currents at 88°W) reproduced by the numerical models: SODA (Simple Ocean Data Assimilation, version 2.1.6) and ORAS5 (Ocean Reanalysis System, version 5). SODA 2.1.6 uses a general circulation ocean model based on the Parallel Ocean Program numerics (R. Smith et al., 1992), with an average 0.25° x 0.4° latitude-longitude horizontal resolution and with 40 vertical levels with 10 m spacing near the surface, covering the 1958-2008 period. ORAS5 (Zuo et al., 2019) is a new global eddy-permitting ocean-sea ice ensemble reanalysis system, including 5 ensemble members generated by perturbations in forcing, observations and initial conditions. However, for this study we only used the control member that is unperturbed. The ocean resolution is 0.25° (∼ 25 km), with 75 vertical levels and a near-surface resolution of 1 m, covering from 1979 onwards as monthly values.

2.1.5 Subsurface temperature

We use climatology subsurface temperature from CARS-2009[1]. (CSIRO Atlas of Regional Seas). The dataset is derived from a quality-controlled archive of all available historical surface and subsurface oceanic measurements. CARS-2009 covers the full global oceans on a 0.5° resolution (∼ 50 km) over 79 vertical levels, with increased resolution near the surface.

[1]http://www.marine.csiro.au/∼dunn/cars2009/

2.2 Numerical models of the climate system

2.2.1 CMIP5 models

The fifth phase of the Coupled Model Intercomparison Project (CMIP5) consists in a set of coordinated state-of-the-art climate simulations that focus on understanding past and future climate changes. The ongoing CMIP5 activities are performed by a broad international climate research community, where more than 20 modeling groups carry out the simulations using more than 50 models. We focused in the long-term experiments built for projected climate change to the end of the century and beyond. The CMIP5 experiments also include runs for studying unforced variability or climate change over the historical period (1920-2005). The spatial resolution of CMIP5 coupled models varies for the atmosphere (ocean) component from 0.5° to 4° (0.2° to 2°). The long-term experiments of climate change projections adopted four scenarios of greenhouse gases emission increases with specified concentrations, referred to as "representative concentration pathways" (RCP), by an escalating radiative forcing (in W/m^2) to understand the possible range of alternative future climates and the uncertainty associated with them. Because the implications of climate change not only depend on the response of the Earth system to radiative forcing, these scenarios have been also based on how humankind will respond to future population growth, technological development, economies, lifestyle and policy (Moss et al., 2010). The four scenarios consist in an increase of the radiative forcing throughout the twenty-first century before reaching a maximum level selected at the end of the century. The labels for the radiative forcing increases correspond to: a high emission scenario of +8.5 W/m^2 (RCP8.5) with $\sim$ 1370 p.p.m. of CO_2 concentration, two intermediate scenarios of +6.0 W/m^2 and +4.5 W/m^2 (RCP6 and RCP4.5, respectively), with 850 and 650 p.p.m. of CO_2 concentration, respectively, and a low peak-and-decay scenario of +2.6 W/m^2 (RCP2.6), with $\sim$ 490 p.p.m. CO_2 concentration, in which radiative forcing reaches a maximum near the middle of the twenty-first century before decreasing. We analyzed the surface temperature, sea level, precipitation and wind stress components (in Chapter 3) from 27 models (see Table 2.1) based on the highest emission scenario (RCP8.5).

N°	Model Name	Institution	Country
1	ACCESS1.3	Commonwealth Scientific and Industrial Research Organisation & Bureau of Meteorology	Australia
2	CanESM2	Canadian Centre for Climate Modelling and Analysis	Canada
3	CMCC-CESM	Centro Euro-Mediterraneo per i Cambiamenti Climatici	Italy
4	CMCC-CM	Centro Euro-Mediterraneo per i Cambiamenti Climatici	Italy
5	CMCC-CMS	Centro Euro-Mediterraneo per i Cambiamenti Climatici	Italy
6	CNRM-CM5	Centre National de Recherches Meteorologiques & Centre Europeen de Recherches et de Formation Avancee en Calcul Scientifique	France
7	CSIRO Mk3.6.0	Commonwealth Scientific and Industrial Research Organisation & Queensland Climate Change Centre of Excellence	Australia
8	FGOALS-s2	Institute of Atmospheric Physics & Chinese Academy of Sciences	China
9	GFDL-CM3	NOAA - Geophysical Fluid Dynamics Laboratory	USA
10	GFDL-ESM2G	NOAA - Geophysical Fluid Dynamics Laboratory	USA
11	GFDL-ESM2M	NOAA - Geophysical Fluid Dynamics Laboratory	USA
12	GISS-E2-R-CC	NASA - Goddard Institute for Space Studies	USA
13	GISS-E2-R	NASA - Goddard Institute for Space Studies	USA
14	HadGEM2-CC	Met Office Hadley Centre	UK
15	HadGEM2-ES	Met Office Hadley Centre	UK
16	inmcm4	Institute for Numerical Mathematics	Russia
17	IPSL-CM5A-LR	Institut Pierre Simon Laplace	France
18	IPSL-CM5A-MR	Institut Pierre Simon Laplace	France
19	IPSL-CM5B-LR	Institut Pierre Simon Laplace	France
20	MIROC5	Atmosphere and Ocean Research Institute, National Institute for Environmental Studies & Japan Agency for Marine-Earth Science and Technology	Japan
21	MIROC-ESM-CHEM	Atmosphere and Ocean Research Institute, National Institute for Environmental Studies & Japan Agency for Marine-Earth Science and Technology	Japan
22	MIROC-ESM	Atmosphere and Ocean Research Institute, National Institute for Environmental Studies & Japan Agency for Marine-Earth Science and Technology	Japan
23	MPI-ESM-LR	Max Planck Institute for Meteorology	Germany
24	MPI-ESM-MR	Max Planck Institute for Meteorology	Germany
25	MRI-CGCM3	Meteorological Research Institute	Japan
26	MRI-ESM1	Meteorological Research Institute	Japan
27	NorESM1-M	Norwegian Climate Centre	Norway

Table 2.1: *List of CMIP5 climate models, including each modeling group and country. The variables used for all the climate models were the surface temperature, sea surface height, precipitation and wind stress components. CMIP5 outputs can be obtained at https://esgf-node.llnl.gov/projects/esgf-llnl/.*

2.2.2 CESM-LENS

The Community Earth System Model - Large Ensemble (CESM-LENS) project, developed by the National Center for Atmospheric Research (NCAR), is a broad set of simulations to understand the relevance of the internal variability of the climate system (Kay et al., 2015). These simulations are based on the Community Earth System Model version 1 (CESM1, Hurrell et al., 2013), which involves four models of the climate system: i) the Community Atmosphere Model version 5 (CAM5), ii) the Parallel Ocean Program version 2 (POP2), iii) the Community Land Model version 4 (CLM4),

and iv) the Los Alamos Sea Ice Model (CICE). All the components are fully coupled with approximately 1° horizontal resolution using the Coupler version 7 (CPL7, Figure 2.1). In addition to land carbon cycle calculations, the CESM-LENS simulations also include diagnostic biogeochemistry calculations for the ocean ecosystem and the atmospheric carbon dioxide cycle (D. M. Lawrence et al., 2012; Lindsay et al., 2014; Long et al., 2013; Moore et al., 2013). The CESM-LENS project provides multiple realizations of the climate trajectories over the 1920-2100 period, using the same model and external forcing, where the members were perturbed by small differences in round-off level of the air temperature initial condition (order of 10^{-14} K). This led to each ensemble member to have its own unique climate trajectory, and the ensemble spread arises from internal climate variability alone. The latter is the principal advantage in comparison with the CMIP5 ensemble members, where it is difficult to make a diagnostic of the internal climate variability due to differences in model physics, numerics and parametrizations, which results in significant differences in dynamics, as evidenced for example by the strength of the cloud-radiation feedback (Ying and P. Huang, 2016a) or the ocean dynamical effect (Ying and P. Huang, 2016b).

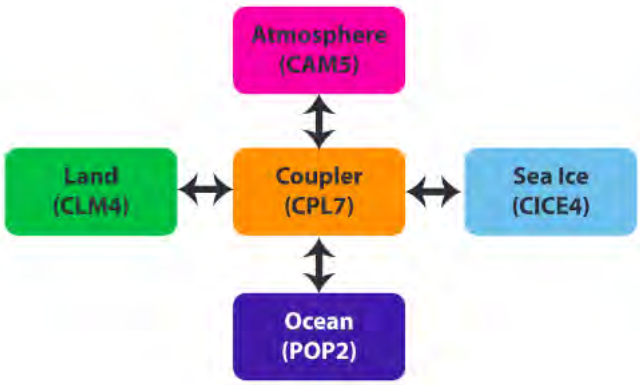

Figure 2.1: *CESM component models and coupling (Hurrell et al., 2013). All components were run at $\sim 1°$ horizontal resolution. After Kay et al., 2015.*

The CESM-LENS simulations consist in a multi-century 1850 control simulation with constant preindustrial forcing, and 40 ensemble members integrating the Historical and RCP8.5 runs. After a quasi-equilibrium of the 1850 control run, the first member was integrated forward from 1850 to 2100 (Figure 2.2). The other members were all started on 1st January 1920 by round-off level differences in their initial air temperature fields. All members of the CESM-LENS project follow the CMIP5 design protocol (Taylor et al., 2012) to have the specified external forcing for Historical simulations from 1920 to 2005 and RCP8.5 forcing from 2006 to 2100. The CESM-LENS outputs are publicly available vie the Earth System Grid (www.earthsystemgrid.org).

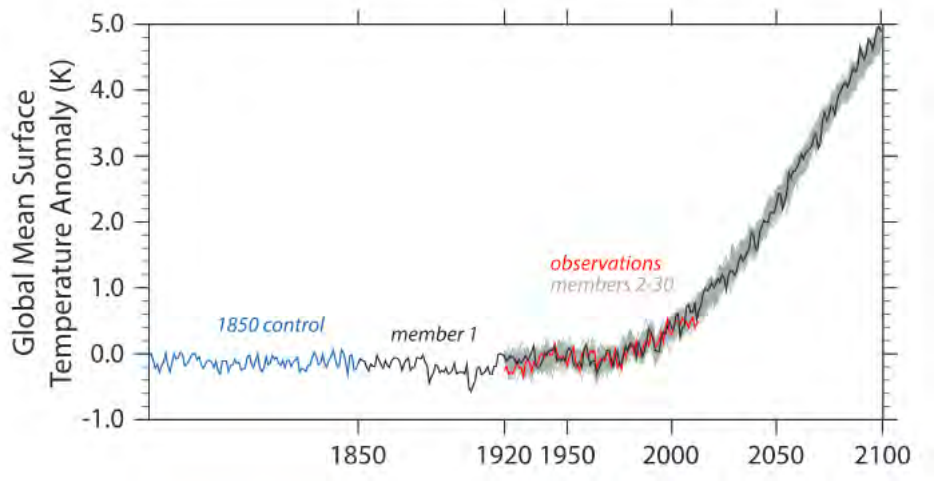

Figure 2.2: *Global surface temperature anomaly (1961-1990 base period) for the 1850 control run, individual ensemble members, and observations (HadCRUT4; Morice et al. 2012). After Kay et al., 2015).*

Furthermore, the CESM-LENS has been shown to be particularly skillful in accounting for the ENSO variability, specially the ENSO diversity (e.g., Cai et al., 2020; Carréric et al., 2019; Dewitte and Takahashi, 2017) considering the complexity ocean-atmosphere feedbacks involved into the different types of ENSO events.

2.2.3 High resolution global coupled model

We use fully global coupled simulations from the ultra-high-resolution CESM version 1.2.2 (UHR-CESM) to analyze the mesoscale activity in the PCUS (in Chapter 4). The atmosphere component is the CAM5 with 0.25° resolution ($\sim$ 25 km) and 30 vertical levels. The ocean component is the POP2 with 0.1° resolution ($\sim$ 10 km), decreasing from 11 km at the equator to 2.5 km at high latitudes, and 62 vertical levels. These resolutions are sufficient to resolve key mesoscale processes, both in the atmosphere and ocean (Small et al., 2014). The land model is the Community Land Model version 4 (CLM4) and the sea-ice component is the Community Ice Code version 4 (CICE4). The UHR-CESM simulations consist in three experiments with different levels of fixed greenhouse gas conditions: i) Present-day (PD) simulation with a CO_2 concentration of 367 p.p.m., ii) doubling the CO_2 concentration ($2xCO_2$, 734 p.p.m.), and iii) quadrupling the CO_2 concentration ($4xCO_2$, 1468 p.p.m.). All other greenhouse gases and aerosol concentrations have been kept at PD levels. In addition, the prognostic carbon-nitrogen cycle component was turned off. The century-long PD simulation was initialized from a quasi-equilibrated climate state (Small et al., 2014) and was then integrated for another 140 years. The $2xCO_2$ and $4xCO_2$ forcing experiments were branched off

from year 71 of the PD experiment and integrated for 100 years each (Figure 2.3). All the analysis of the three experiments was performed considering the last 120 years for the PD simulation, and the last 80 years for both $2xCO_2$ and $4xCO_2$ experiments. The UHR-CESM simulations were conducted by the IBS Center for Climate Physics climate data server of South Korea (https://climatedata.ibs.re.kr/) and are available upon request[2].

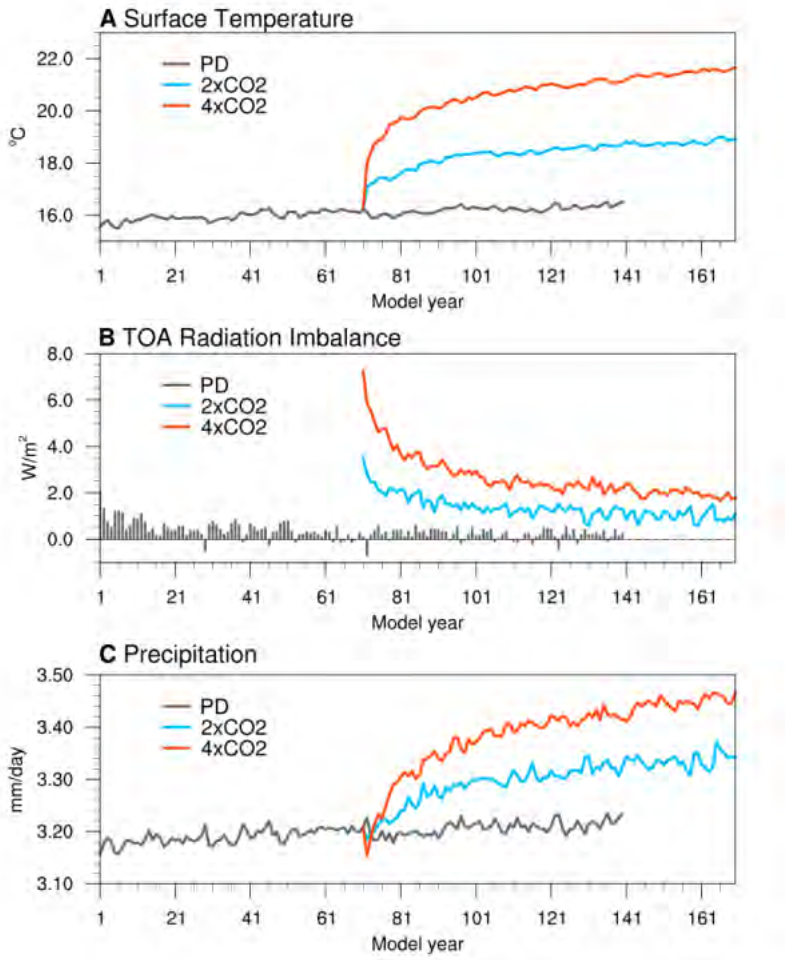

Figure 2.3: *Time series of the century-long global annual mean climate response to CO_2 concentration. a) Surface air temperature (in C), b) net radiation imbalance at top of the atmosphere (TOA) (positive downward, in W/m^2), and c) precipitation (in mm/day). Gray colors denote quantities for 140 years of the PD simulation, and blue and red lines indicate 100 years of $2xCO_2$ and $4xCO_2$ experiments started from year 71 of PD, respectively. After Chu et al., 2020.*

[2]https://ibsclimate.org/research/ultra-high-resolution-climate-simulation-project/

2.2.4 The regional oceanic modeling system (ROMS)

We use the long-term regional simulation from Dewitte et al., 2012 (Figure 2.4) to analyze the mesoscale activity in the Peru-Chile Upwelling System (Chapter 4). The simulation consists in a 1/12° resolution at the equator ($\sim$ 8 km) which was used to detect the SST changes along the Peruvian coast (Dewitte et al., 2012), the seasonal variability of the OMZ off Peru (Vergara et al., 2016), the equatorial Rossby waves contribution to the Peru-Chile Upwelling System (Vergara et al., 2017), and the interannual variability of the OMZ off central Chile (Pizarro-Koch et al., 2019). In addition, we conducted an experiment to determine the sensitivity of the Peru-Chile Upwelling system to the equatorial current system. The experiment consists in using the same model setting from Dewitte et al., 2012, but modifying the atmospheric forcing such that it remain steady (corresponding to year 2005) during the whole period. More details are given in Chapter 4.

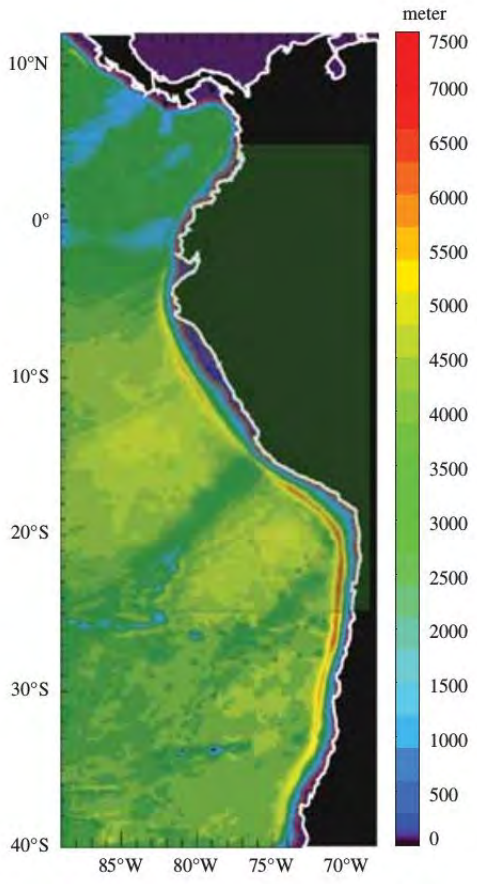

Figure 2.4: *Model domain and bathymetry (in meters) of the ROMS simulation used in Chapter 4. After Dewitte et al., 2012.*

2.3 Methods and diagnostics

2.3.1 Heat budget decomposition

In order to identified the mechanisms involved in the SST changes under greenhouse warming, we integrated the ocean temperature equation from the bottom of the mixed layer depth (H) to the surface:

$$\underbrace{\frac{1}{H}\int_{-H}^{0}\left(\frac{\partial T}{\partial t}\right)dz}_{Q_{ten}} = \underbrace{\frac{Q_{net}}{\rho_o C_p H}}_{Q_{net}} - \underbrace{\frac{1}{H}\int_{-H}^{0}\left(\vec{V}\cdot\nabla T\right)dz}_{Q_{adv}} + \underbrace{Residual}_{Q_{res}} \tag{2.1}$$

where the first term is the temperature tendency, the second term is the net surface heat flux into the ocean (positive downward), the third term is the ocean heat transport effect (three-dimensional advection) and the last term is the residual, which represents the ocean heat transport by subgrid-scale processes, i.e. vertical diffusivity and lateral mixing (e.g., DiNezio et al., 2009). Constant values correspond to sea water density (ρ_o = 1026 kg/m^3), specific heat at constant pressure (C_p = 3996 J/kgK). A steady ($\partial H/\partial t$ = 0) homogeneous ocean mixed layer depth (H = 50 m) is considered here, implying that vertical entrainment is also part of the residual term. The use of different layers for the ocean mixed layer (e.g. 30 or 80 m) weakly impact the results, although some differences in amplitude of the residual can be observed in some regions. The residual is in general larger when H is close to the mean observed mixed-layer. The conclusions are not altered because the residual remain much weaker than the advection and flux terms in most regions of interest. In order to understand the role of the long-term change of a particular variable onto a particular process (e.g. advection, latent heat), we consider the following decomposition:

$$X = \overline{X} + X_{lt}\cdot t \tag{2.2}$$

where X is the total random variable, $\overline{X}$ is the mean value over the 1980-2005 period (Historical simulations), X_{lt} is the linear trend of X over the 2006-2100 period (RCP8.5 simulations), and t is the time step over the 2006-2100 period (monthly values). This is equivalent to assuming that a particular variable in the future climate can be approximated by its linear fit to the long-term trend and that decadal variability is thus weak (i.e., $X' \approx X_{lt}$, where the prime stands for the future climate):

$$Q'_{ten} = Q'_{net} + Q'_{adv} + Q'_{res} \tag{2.3}$$

Since we focus on climate conditions at the end of the twenty-first century (2100), this is considered a relatively reasonable approximation. See Figure 2.5 for more details.

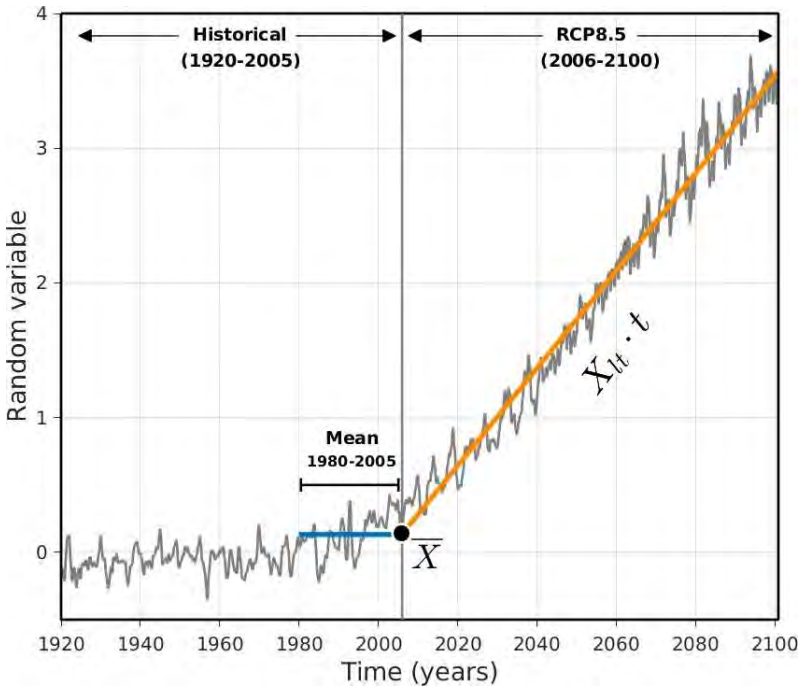

Figure 2.5: *Representation of the decomposition scheme from equation 2.2. The gray time series is a random variable (X) from 1920 to 2100. Blue line represents the mean value ($\overline{X}$, black circle) over the 1980-2005 period (Historical simulations) and yellow line corresponds to the linear trend (X_{lt}) over the 2006-2100 period (RCP8.5 forcing).*

Shortwave radiation decomposition

The net surface heat flux (Q_{net}) could be decomposed into:

$$Q_{net} = Q_{SW} + Q_{LW} + Q_{LH} + Q_{SH} - Q_{pen} \tag{2.4}$$

where Q_{SW}, Q_{LW}, Q_{SH}, Q_{LH} and Q_{pen} are the net shortwave radiation, net longwave radiation, sensible heat flux, latent heat flux and the shortwave radiation transmitted through the bottom of the mixed layer depth, respectively. Q_{pen} is calculated following Pacanowski and Griffies, 1999:

$$Q_{pen} = Q_{SW}(0.58e^{\frac{-H}{0.35}} + 0.42e^{\frac{-H}{23}}) \tag{2.5}$$

Considering equation 2.4 and the ocean mixed layer fixed at 50 m depth, the equation 2.5 could be written as:

$$Q_{net} = Q_{SW} + Q_{LW} + Q_{LH} + Q_{SH} - Q_{SW}(0.58e^{\frac{-H}{0.35}} + 0.42e^{\frac{-H}{23}}$$

$$Q_{net} = Q_{SW}(1 - 0.58e^{\frac{-50}{0.35}} - 0.42e^{\frac{-50}{23}}) + Q_{LW} + Q_{LH} + Q_{SH}$$

$$Q_{net} = 0.95 \cdot Q_{SW} + Q_{LW} + Q_{LH} + Q_{SH}$$

$$Q_{net} = Q_{SWp} + Q_{LW} + Q_{LH} + Q_{SH} \tag{2.6}$$

where Q_{SWp} represents the changes of the shortwave radiation including the part that penetrates into the ocean, corresponding to a 95% of the total shortwave radiation value.

Surface latent heat flux decomposition

Surface latent heat flux (Q_{LH}) is calculated by the bulk formula (Fairall et al., 1996:

$$Q_{LH} = \rho_a L_v C_E W(q_s - q_a) = \rho_a L_v C_E W[q_s(SST) - RH \cdot q_s(SST + \Delta T)] \tag{2.7}$$

where ρ_a is the surface air density, L_v is the latent heat of evaporation, C_E is the transfer coefficient, W is the surface wind speed at 10 m, q_s is the saturation specific humidity, RH is the surface relative humidity, and ΔT is the stability ($\Delta T = T_a \breve{} SST$), where T_a is the air surface temperature and SST is the sea surface temperature. The Clausius–Clapeyron equation is:

$$\frac{dln(e_s)}{dT} = \frac{L_v}{R_v T^2}$$

where e_s is the saturation vapor pressure, and R_v is the gas constant for moist air. Integrating this equation, one arrives at an analytic expression for e_s and the saturation specific humidity (q_s) can be expressed by:

$$q_s(SST) = q_o e^{\alpha SST}$$

where q_0 is a constant and $\alpha = L_v/(R_v T^2) \approx 0.06K^{-1}$. Thus, we can get:

$$q_s(SST + \Delta T) = q_s(SST)e^{\alpha \Delta T} \tag{2.8}$$

Substituting equation 2.8 into 2.7, we obtain:

$$Q_{LH} = \rho_a L_v C_E W(1 - RHe^{\alpha \Delta T})q_s(SST) \tag{2.9}$$

Thereby, variations in Q_{LH} are caused by changes in ocean forcing (through SST) and changes in atmospheric forcing including wind speed (W), relative humidity (RH) and

stability (ΔT). To estimate the contributions of the individual terms, we can linearize the equation 2.9 into several components following previous studies (e.g. Jia and Wu, 2013; Xie et al., 2010):

$$Q_{LH} = Q_{LH}(SST, W, RH, \Delta T)$$

$$dQ_{LH} = \underbrace{\left(\frac{\partial Q_{LH}}{\partial SST}\right) dSST}_{(1)} + \underbrace{\left(\frac{\partial Q_{LH}}{\partial W}\right) dW}_{(2)} + \underbrace{\left(\frac{\partial Q_{LH}}{\partial RH}\right) dRH}_{(3)} + \underbrace{\left(\frac{\partial Q_{LH}}{\partial \Delta T}\right) d\Delta T}_{(4)} \quad (2.10)$$

Developing the first term from equation 2.10:

$$\left(\frac{\partial Q_{LH}}{\partial SST}\right) dSST = \rho_a L_v C_E W (1 - RHe^{\alpha \Delta T}) \frac{\partial q_s(SST)}{\partial SST} dSST$$

and considering the Clausius–Clapeyron equation:

$$q_s(SST) = q_o e^{\alpha SST} = \frac{\partial q_s(SST)}{\partial SST} = \frac{\partial q_o e^{\alpha SST}}{\partial SST} = \frac{\partial \alpha SST}{\partial SST} \cdot q_o e^{\alpha SST} = \alpha q_o e^{\alpha SST} = \alpha q_s(SST)$$

$$\left(\frac{\partial Q_{LH}}{\partial SST}\right) dSST = \alpha \left[\rho_a L_v C_E W (1 - RHe^{\alpha \Delta T}) q_s(SST)\right] dSST = \alpha Q_{LH} dSST$$

which represents the ocean forcing by Newtonian cooling through evaporation. Considering the second term from equation 2.10:

$$\left(\frac{\partial Q_{LH}}{\partial W}\right) dW = \rho_a L_v C_E \frac{\partial W}{\partial W} (1 - RHe^{\alpha \Delta T}) q_s(SST) dW$$

$$\left(\frac{\partial Q_{LH}}{\partial W}\right) dW = \rho_a L_v C_E (1 - RHe^{\alpha \Delta T}) q_s(SST) dW = \frac{1}{W} Q_{LH} dW$$

which is the atmosphere forcing because of changes in wind speed, commonly known as the wind–evaporation–SST (WES) feedback (Xie and S. G. H. Philander, 1994). Third and fourth terms from equation 2.10 (i.e., relative humidity and stability) will be estimated as a residual term (Q_{LHr}):

$$Q_{LH} = Q_{LHo} + Q_{LHw} + Q_{LHr}$$

where Q_{LHo} and Q_{LHw} are the latent heat changes by oceanic and atmospheric forcing, respectively. The residual term is:

$$Q_{LHr} = Q_{LH} - Q_{LHo} - Q_{LHw}$$

Finally, the surface latent heat flux changes is decomposed as:

$$Q'_{LH} = \alpha \overline{Q}_{LH} SST' + \frac{\overline{Q}_{LH}}{\overline{W}} W' + Q'_{LHr} \tag{2.11}$$

where the overbar denotes the mean time over the 1980-2005 period (Historical simulations) and the prime corresponds to the linear trend over the 2006-2100 period (RCP8.5 simulations). See Figure 2.5 for details.

Accessing SST trend through assuming quasi-equilibrium

Now we can decompose the terms of equation 2.3 and assuming that the change (i.e., the linear trend) of the tendency temperature (Q'_{ten}) is equal to zero (e.g., Xie et al., 2010). This assumption is equivalent to considering that upper ocean processes are in a quasi-equilibrium with the slow GHG forcing, which is questionable. Nevertheless such an approximation is convenient since it allows accessing explicitly the tendency in SST through the latent heat formulation, as follows:

$$Q'_{ten} = Q'_{net} + Q'_{adv} + Q'_{res}$$

$$0 = Q'_{SWp} + Q'_{LW} + Q'_{SH} + Q'_{LH} + Q'_{adv} + Q'_{res}$$

$$0 = Q'_{SWp} + Q'_{LW} + Q'_{SH} + \alpha \overline{Q}_{LH} SST' + \frac{\overline{Q}_{LH}}{\overline{W}} W' + Q'_{LHr} + Q'_{adv} + Q'_{res}$$

$$SST' = \frac{-Q'_{SWp} - Q'_{LW} - Q'_{SH} - Q'_{LHw} - Q'_{LHr} - Q'_{adv} - Q'_{res}}{\alpha \overline{Q}_{LH}} \tag{2.12}$$

Note here that Q'_{adv} is the long-term tendency of the total advection, which include linear and non-linear advections (next section). The latter can be estimated following the decomposition proposed in section 2.3.1., but there is not necessarily a consistency between the two approaches due to different assumptions.

In order to illustrate the relevance of equation 2.12, we present in Figure 2.6 the actual SST trend in the RCP8.5 simulations from the CESM-LENS and the result of the calculation of the SST trend based on equation 2.12, considering $Q'_{adv} = 0$, and $Q'_{res} = 0$. The contribution of both atmospheric forcing and ocean advection trend patterns can explain to a great extent the minimum SST warming rate projected to the end of the twenty-first century over the Southeast oceans of the South Hemisphere.

However, in both equatorial Pacific and Atlantic regions there is an excessive warming which must be compensated by mixing processes (i.e., residual term). Apparently, mixing processes will be crucial to modulate the SST warming rate in the Indian ocean, especially over the equatorial region. More details are given in Chapter 3.

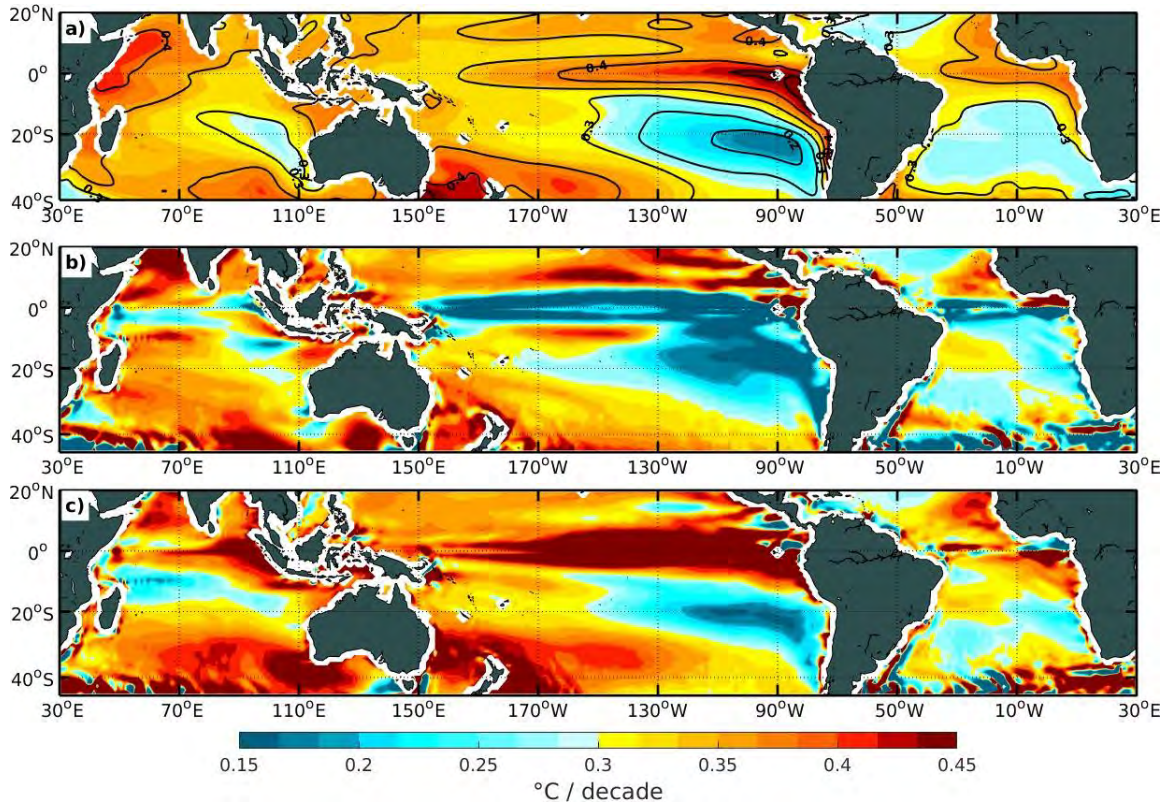

Figure 2.6: *Long-term SST trend pattern (shading) under greenhouse warming (RCP8.5 forcing) over the 2006-2100 period from CESM-LENS 40 mean-ensemble. a) SST from equation 2.12 (shading) and directly from CESM-LENS (black contours), b) SST from equation 2.12, with $Q'_{adv} = 0$, and c) SST from equation 2.12, with $Q'_{res} = 0$.*

Ekman and geostrophic ocean currents decomposition

The long-term trend of the three-dimensional ocean advection is decomposed as follows:

$$Q'_{adv} = -\left[\underbrace{\frac{1}{H}\int_{-H}^{0}\left(\vec{V}'\cdot\nabla\overline{T}\right)dz}_{(i)} + \underbrace{\frac{1}{H}\int_{-H}^{0}\left(\vec{\overline{V}}\cdot\nabla T'\right)dz}_{(ii)} + \underbrace{\frac{1}{H}\int_{-H}^{0}\left(\vec{V}'\cdot\nabla T'\right)dz}_{(iii)}\right] \quad (2.13)$$

where the overbars correspond to the mean variables over the 1980-2005 period, and the prime refers to the long-term trend over the 2006-2100 period. The right-hand

side of equation 2.13 represents the linear trend of the ocean advection decomposition due to: i) mean temperature by anomalous currents, ii) temperature anomalies by mean currents, and iii) non-linear processes. Furthermore, we split the total horizontal surface currents ($\vec{V_h}$) that is primarily composed by the sum of wind driven Ekman currents ($\vec{V_e}$) and pressure gradient driven geostrophic currents ($\vec{V_g}$).

$$\vec{V_h}' = \vec{V_e}' + \vec{V_g}' \tag{2.14}$$

To calculate the Ekman component of the ocean currents we used the Ekman regression model (Lagerloef et al., 1999; Meurs and Niiler, 1997), that represents the following linear steady momentum balance:

$$fh_e u_e + r_e v_e = \frac{\tau_y}{\rho_o} \tag{2.15}$$

$$r_e u_e - fh_e v_e = \frac{\tau_x}{\rho_o} \tag{2.16}$$

where u_e and v_e are the zonal and meridional Ekman currents components, respectively, $\tau_{(x,y)}$ is the wind stress field, ρ_o is the water density, f is the Coriolis parameter, h_e is the thickness of the Ekman layer and r_e is the linear drag coefficient that represents the vertical viscosity terms as a body force on the Ekman components. We consider a constant linear drag coefficient ($2.15x10^{-4}\ m/s$, Lagerloef et al., 1999). From equation 2.15 we can obtain the meridional Ekman component:

$$v_e = \frac{1}{r_e}\left(\frac{\tau_y}{\rho_o} - fh_e u_e\right)$$

replacing in equation 2.16, the zonal Ekman component could be written as follows:

$$\begin{aligned}
r_e u_e - fh_e\left[\frac{1}{r_e}\left(\frac{\tau_y}{\rho_o} - fh_e u_e\right)\right] &= \frac{\tau_x}{\rho_o} \\
r_e u_e - \frac{fh_e\tau_y}{r_e\rho_o} + \frac{f^2h_e^2 u_e}{r_e} &= \frac{\tau_x}{\rho_o} \\
u_e\left(r_e + \frac{f^2h_e^2}{r_e}\right) &= \frac{\tau_x}{\rho_o} + \frac{fh_e\tau_y}{r_e\rho_o} \\
u_e\left(\frac{r_e^2 + f^2h_e^2}{r_e}\right) &= \frac{1}{\rho_o}\left(\tau_x + \frac{fh_e\tau_y}{r_e}\right) \\
u_e &= \frac{1}{\rho_o}\left(\frac{r_e}{r_e^2 + f^2h_e^2}\right)\left(\tau_x + \frac{fh_e\tau_y}{r_e}\right) \\
u_e &= \frac{1}{\rho_o(r_e^2 + f^2h_e^2)}\left(r_e\tau_x + fh_e\tau_y\right)
\end{aligned} \tag{2.17}$$

Applying the same method to the meridional Ekman current, we obtain:

$$v_e = \frac{1}{\rho_o(r_e^2 + f^2 h_e^2)}\left(r_e \tau_y - f h_e \tau_x\right) \tag{2.18}$$

Finally, the geostrophic balance assumes that momentum advection and frictional forces are small. Outside the equatorial band (where the Coriolis force vanishes), geostrophic velocities are given by

$$u_g = -\frac{g}{f}\frac{\partial h}{\partial y} \tag{2.19}$$

$$v_g = \frac{g}{f}\frac{\partial h}{\partial x} \tag{2.20}$$

where y and x are the latitude and longitude positions, f is the Coriolis parameter, g is the gravitational acceleration (9.8196 m/s^2), and h is the elevation of the sea surface height referenced by the geoid. Figure 2.7 shows the magnitude of the total surface ocean current, and their decomposition of Ekman and geostrophic currents, from CESM-LENS 40 mean-ensemble over the 1980-2005 period. Outside the equatorial band the sum of both Ekman and geostrophic currents are in good agreement with the total value.

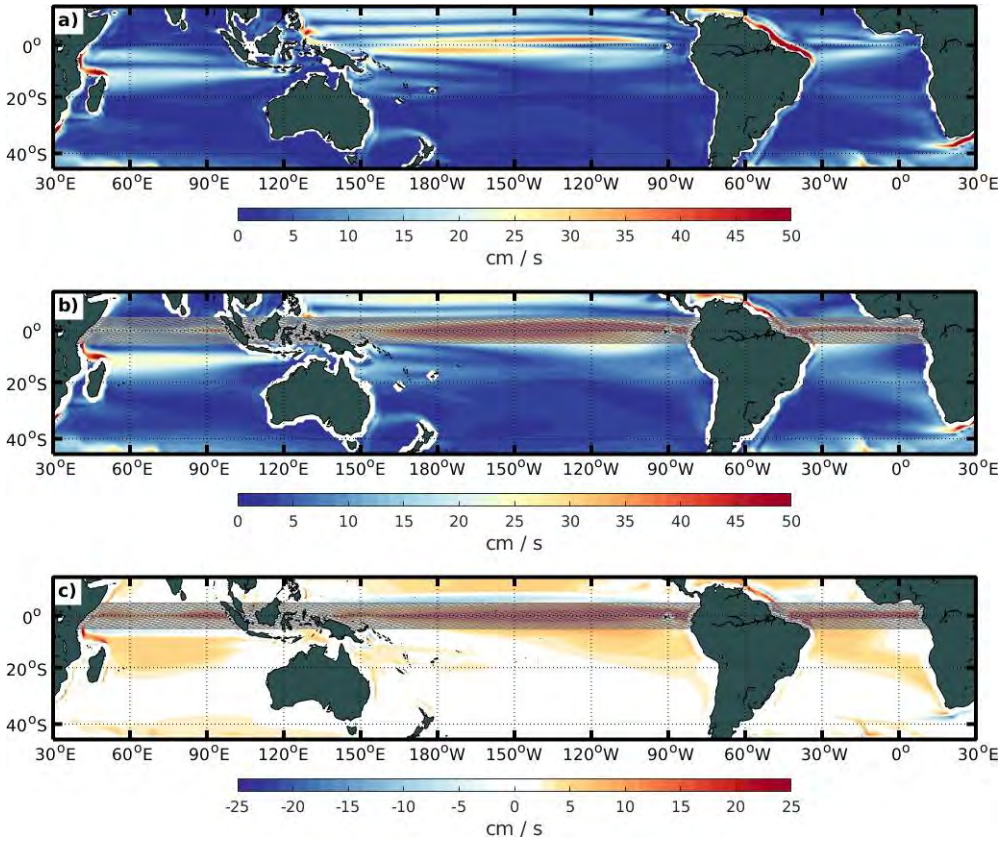

Figure 2.7: *Magnitude of the horizontal surface ocean currents from CESM-LENS 40 mean-ensemble over the 1980-2005 period. a) Total currents directly from the model, b) summatory of Ekman and Geostrophic components, and c) difference between b) minus a). The equatorial band (2°S-2°N) is masked in gray color because the Geostrophic approximation is not reliable.*

2.3.2 EKE budget over the Peru-Chile Upwelling System

The generation of mesoscale eddies by large-scale current instabilities in the PCUS has been documented on the last decades through numerical modeling (e.g., Belmadani et al., 2012; Colas et al., 2012; Leth and Middleton, 2004; Leth and Shaffer, 2001). The main processes are baroclinic and barotropic instabilities, which are associated with large-scale vertical and horizontal velocity shear, respectively. These instabilities obtain their energy from different sources: the barotropic instability from the kinetic energy of the mean flow, and the baroclinic instability from the potential energy of the mean flow. An effective method to identify which mechanism is at play on the generation of mesoscale eddies in a realistic turbulent flow is to pinpoint the energy source for the perturbations, i.e. the eddy part. To quantify their source of energy, we can calculate the eddy kinetic energy:

$$EKE = \frac{1}{2}\left(u'^2 + v'^2\right)$$

where the prime denotes fluctuations relative to the time average (the eddying motions) of the horizontal currents. The kinetic energy budget is calculated from the Naver-Stokes equations under the hydrostatic and Boussineq approximations, as follows:

$$\frac{\partial u}{\partial t} + \vec{V} \cdot \nabla u - fv = -\frac{1}{\rho_o}\frac{\partial P}{\partial x} + \Psi_u + \Omega_u \tag{2.21}$$

$$\frac{\partial v}{\partial t} + \vec{V} \cdot \nabla v + fu = -\frac{1}{\rho_o}\frac{\partial P}{\partial y} + \Psi_v + \Omega_v \tag{2.22}$$

$$\nabla \cdot \vec{V} = 0 \tag{2.23}$$

$$\frac{\partial P}{\partial z} = -\rho g \tag{2.24}$$

$$\tag{2.25}$$

where $\vec{V} = (u, v, w)$ represents the full velocity vector, P is the pressure, ρ is the density with reference value ρ_o (1025 kg/m^3), f is the Coriolis parameter, g is the gravitational acceleration (9.8196 m/s^2), $\vec{\Psi}_h = (\Psi_u, \Psi_v)$ is the vertical mixing, $\vec{\Omega}_h = (\Omega_u, \Omega_v)$ is the horizontal diffusion, and ∇ is the three-dimensional gradient operator. Then, to obtain the mesoscale energy equations, the variables are decomposed into its mean and eddy components and substituted into equations (2.21-2.25). Note that we are not considering the terms that are strictly produced by mean flow. Therefore:

$$\frac{\partial u'}{\partial t} + \vec{V'} \cdot \nabla \overline{u} + \vec{\overline{V}} \cdot \nabla u' + \vec{V'} \cdot \nabla u' - fv' = -\frac{1}{\rho_o}\frac{\partial P'}{\partial x} + \Psi'_u + \Omega'_u \tag{2.26}$$

$$\frac{\partial v'}{\partial t} + \vec{V'} \cdot \nabla \overline{v} + \vec{\overline{V}} \cdot \nabla v' + \vec{V'} \cdot \nabla v' + fu' = -\frac{1}{\rho_o}\frac{\partial P'}{\partial y} + \Psi'_v + \Omega'_v \tag{2.27}$$

$$\nabla \cdot \vec{V'} = 0 \tag{2.28}$$

$$\frac{\partial P'}{\partial t} = -\rho' g \tag{2.29}$$

$$\tag{2.30}$$

Multiplying the equations (2.26) and (2.27) by the eddy component u' and v', respectively, and summing them, we obtain the EKE budget as follows:

$$\underbrace{\left[\frac{\partial u'}{\partial t} + \frac{\partial v'}{\partial t}\right]}_{(i)} = -\underbrace{\left[u'\vec{V'} \cdot \nabla \overline{u} + v'\vec{V'} \cdot \nabla \overline{v} + u'\vec{\overline{V}} \cdot \nabla u' + v'\vec{\overline{V}} \cdot \nabla v' + u'\vec{V'} \cdot \nabla u' + v'\vec{V'} \cdot \nabla v'\right]}_{(ii)}$$

$$\underbrace{-\frac{1}{\rho_o}\left(u'\frac{\partial P'}{\partial x}+v'\frac{\partial P'}{\partial y}\right)}_{(iii)}+\underbrace{\vec{V_h'}\cdot\vec{\Psi}_h'}_{(iv)}+\underbrace{\vec{V_h'}\cdot\vec{\Omega}_h'}_{(v)}$$

where $\vec{V_h'}=(u',v')$ corresponds to the horizontal velocity. Now, from (i) and considering that: $x\frac{\partial x}{\partial t}=\frac{1}{2}\frac{\partial x^2}{\partial t}$ we can obtain the EKE tendency.

$$\implies u'\frac{\partial u'}{\partial t}+v'\frac{\partial v'}{\partial t}=\frac{1}{2}\frac{\partial u'^2}{\partial t}+\frac{1}{2}\frac{\partial v'^2}{\partial t}=\frac{1}{2}\frac{\partial}{\partial t}(u'^2+v'^2)=\frac{\partial}{\partial t}EKE$$

Based on equations 2.28 and 2.29, we can decompose the term (iii) as follows:

$$\frac{1}{\rho_o}\left(u'\frac{\partial P'}{\partial x}+v'\frac{\partial P'}{\partial y}\right)=\frac{1}{\rho_o}\left(u'\frac{\partial P'}{\partial x}+v'\frac{\partial P'}{\partial y}+w'\frac{\partial P'}{\partial z}+w'\rho' g\right)=\frac{1}{\rho_o}\vec{V'}\cdot\nabla P'+\frac{g}{\rho_o}w'\rho'$$

which represents that the contribution of the pressure gradient term (left side hand) can be separate into the divergence of an energy flux at the boundaries of the domain volume (first term, right side hand) and convertion between potential and kinetic energy (second term, right side hand). Now, considering (iv) the energy disipation by vertical mixing can be further divided into surface forcing and oceanic mixing components, we have:

$$\vec{V_h'}\vec{\Psi}_h'=\vec{V_h'}\left[\frac{\partial}{\partial z}\left(\mu\frac{\vec{V_h}}{\partial z}\right)'\Big|_{ocean}\right]+\vec{V_h'}\left[\frac{\partial}{\partial z}\left(\mu\frac{\vec{V_h}}{\partial z}\right)'\Big|_{surface}\right]$$

where μ is the vertical mixing coefficient. In ocean models, the air-sea interaction terms are involved via the sea surface boundary conditions ($z=0$) and can be parameterized as (e.g., R. Smith et al., 2010)

$$\mu\frac{\partial\vec{V_h}}{\partial z}=\frac{\vec{\tau_h}}{\rho_o}$$

$$\implies \vec{V_h'}\vec{\Psi}_h'=\vec{V_h'}\left[\frac{\partial}{\partial z}\left(\mu\frac{\vec{V_h}}{\partial z}\right)'\Big|_{ocean}\right]+\vec{V_{hs}'}\left(\frac{\vec{\tau_h'}}{\rho_o}\right)=\vec{\Psi}_{hfb}'+\vec{\Psi}_{hw}'$$

where $\vec{V_{hs}'}$ and $\vec{\tau_h'}$ represents the eddy parts of the surface horizontal ocean currents and wind stress, prespectively. Physically, $\vec{\Psi}_{hfb}'$ involves the oceanic friction and bottom drag processes, while $\vec{\Psi}_{hw}'$ denotes the wind power input.

Finally, we can rewritte the EKE budget:

$$\frac{\partial}{\partial t}EKE = -\underbrace{\left[u'\vec{V}'\cdot\nabla\overline{u} + v'\vec{V}'\cdot\nabla\overline{v}\right]}_{K_mK_e} - \underbrace{\frac{g}{\rho_o}w'\rho'}_{P_eK_e} + \underbrace{\vec{\Psi}'_{hw}}_{F_eK_e} + \vec{\Psi}'_{hfb} + \vec{V}'_h\vec{\Omega}'_h$$
$$\underbrace{-\frac{1}{\rho_o}\left(\vec{V}'\cdot\nabla P'\right) - \left[u'\vec{\overline{V}}\cdot\nabla u' + v'\vec{\overline{V}}\cdot\nabla v' + u'\vec{V}'\cdot\nabla u' + v'\vec{V}'\cdot\nabla v'\right]}_{\text{Boundary Transport}} \tag{2.31}$$

Thus, the mechanisms responsible for generation of transient eddies can be identified by looking at the source terms for the EKE from equation 2.31 (right hand side). K_mK_e corresponds to the conversion from mean kinetic energy to EKE (i.e., barotropic instability), which can be decomposed into horizontal and vertical Reynolds stress. P_eK_e is the conversion between eddy potential and EKE due to a vertical buoyancy flux (i.e., baroclinic instability). F_eK_e represents the transfer of energy from surface wind-forcing anomalies to EKE (i.e., wind work). The sum of both $\vec{\Psi}'_{hfb}$ and $\vec{V}'_h\vec{\Omega}'_h$ is associated to EKE dissipation. The last term correspond to the "Boundary Transport" of EKE, which is the sum of the divergence pressure fluctuations, advection of the mean flux or their perturbation.

Here, the contribution of major EKE generation processes at low-frequencies is evaluated from both regional (ROMS) and global (UHR-CESM) simulations (in Chapter 4). However, we focus on the energy conversion terms relevant to nearshore of the PCUS following previous studies (e.g., Belmadani et al., 2012; Colas et al., 2012; Marchesiello et al., 2003), which correspond to: wind work, barotropic instability, and baroclinic instability.

$$F_eK_e = \left\langle \frac{1}{H\rho_o}\left(u'\tau'_x + v'\tau'_y\right)\right\rangle \tag{2.32}$$

$$K_mK_e = \left\langle -\frac{1}{H}\int_H^0 \left(u'u'\frac{\partial\overline{u}}{\partial x} + u'v'\frac{\partial\overline{u}}{\partial y} + u'w'\frac{\partial\overline{u}}{\partial z} + v'u'\frac{\partial\overline{v}}{\partial x} + v'v'\frac{\partial\overline{v}}{\partial y} + v'w'\frac{\partial\overline{v}}{\partial z}\right)dz\right\rangle \tag{2.33}$$

$$P_eK_e = \left\langle -\frac{g}{H\rho_o}\int_H^0 \left(\rho'w'\right)dz\right\rangle \tag{2.34}$$

In this work, the prime stand for the anomalies relative to the mean climatology (overbar) calculated over the 1958-2008 period (120 years) from ROMS (UHR-CESM PD) simulation. Since we are interested here in the modulation of these terms at interannual timescales, the brackets stand for the mean over a 3-month running windows assuming that over such a time period eddy generation is modulated by mean state

change associated to interannual variability in the mean circulation. This also considers that the lifetimes of eddies in this region of the world is $\geq$ 35 days (Chaigneau et al., 2009). Thus, the 3-month running average of EKE is able to grasp interannual changes in mean EKE associated to transient eddy activity. In addition, we integrated $K_m K_e$ and $P_e K_e$ over the surface layer depth (H = 100 m), where the instabilities in the PCUS are confined (Belmadani et al., 2012; Colas et al., 2012) and can be directly comparable to $F_e K_e$.

2.3.3 Statistics analysis significance

The correlation (in Chapter 3) or linear trend (in Chapter 4) analysis were considered statistically significant at the 95% confidence level based on a two-tailed Student's t-test. In addition, linear trend from CMIP5 27 mean-models or CESM-LENS 40 mean-ensemble pattern was considered significant when more than 70% of the models/members have the same linear trend sign (e.g. Power et al., 2013).

2.4 Natural modes of variability

We used different indices to represent the natural modes of variability from the Earth system to represent their modulation and contribution to the SST trend pattern projection under a warmer climate (in Chapter 3). Here, we document those main natural modes of variability based on SST from observations over the three ocean basins of the South Hemisphere. Likewise, to quantify and understand their impact on the future SST changes, the same modes were calculated for the climate change projections from both CMIP5 and CESM-LENS models during the 2006-2100 period (in Chapter 3).

2.4.1 ENSO diversity

During the last decade it has been demonstrated that at least two types of El Niño events have occurred in the equatorial Pacific (Ashok et al., 2007; Kug et al., 2009; Yeh et al., 2009). Here, the two El Niño indices defined by Takahashi et al., 2011 are used, that are based on the principal components time series associated with the first two EOF modes of the monthly mean SST anomalies in the tropical Pacific (Figure 2.8). The SST data is from the ERSST.v5 product over the 1960–2019 period. The two uncorrelated indices are well suited for describing the so-called ENSO diversity (Capotondi et al., 2015) by accounting for the variability of Eastern Pacific El Niño (E-index) and Central Pacific El Niño and/or La Niña (C-index). The E and C indices depict for an SST

anomaly pattern that develops and persists in the eastern and central equatorial Pacific, respectively (Figure 2.8b-c).

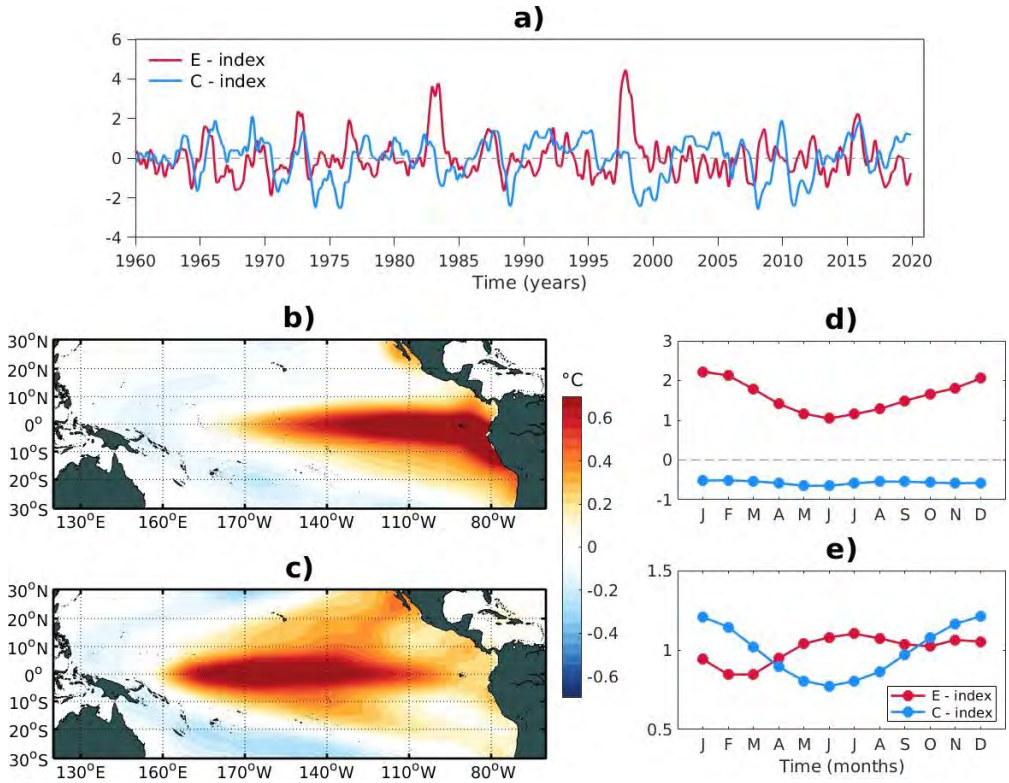

Figure 2.8: *ENSO diversity. a) Time series of the E and C modes, b) SST anomalies regression onto the E mode, c) SST anomalies regression onto the C mode, d) climatology skewness, and e) climatology standard deviation.*

Besides, both types of El Niño events differ in the intensity of the SST anomalies and in their seasonal evolution patterns (Figure 2.8d-e). During the EP El Niño events, the SST anomalies develop in the far Eastern Pacific during austral fall and extend westward over winter and spring. On the other hand, during the CP El Niño events, the SST anomalies extend from the eastern subtropics to the central equatorial Pacific during austral winter and spring. In addition, the skewness of E and C indices reflects the ENSO asymmetry. The positive (negative) skewness of the E (C) index suggests that this mode is associated to strong El Niño (La Niña) events in the Eastern (Central) Pacific.

2.4.2 South Pacific Meridional Mode

The methodology to calculate the SPMM follows the work of Chiang and Vimont, 2004. We derive the eigenvectors and eigenvalues of the cross-covariance matrix between 10-meter winds and SST anomalies with an SVD analysis. Taking into account

that in the tropical Pacific the interannual variability is controlled by ENSO, the Meridional Mode becomes dominant only when the ocean–atmosphere dynamical coupling (i.e., ENSO) is excluded in climate models (Chiang and Vimont, 2004; H. Zhang et al., 2014a). Previous studies removed the ENSO variability from original fields trough the Cold Tongue Index (i.e., SST anomalies averaged over the region 180°-90°W and 6°N-6°S) prior to the calculation of the Meridional Mode (e.g., Chiang and Vimont, 2004; Min et al., 2017; H. Zhang et al., 2014a).

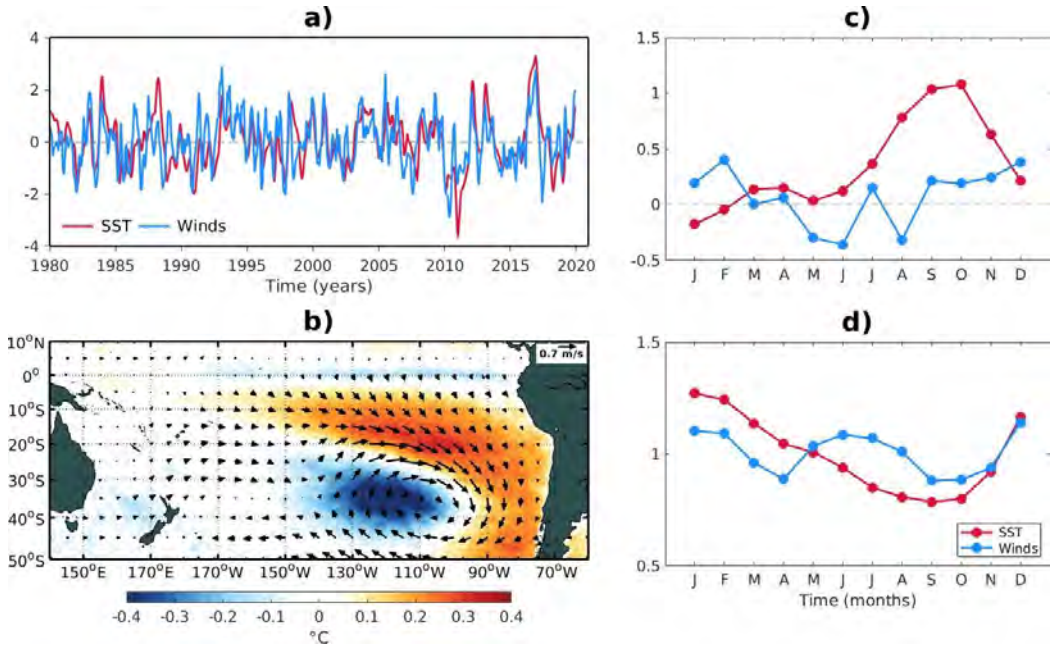

Figure 2.9: *South Pacific Meridional Mode estimated from ERA5 product over the 1980-2019 period. a) Time series associated to SST and 10-meter winds from the first SVD mode decomposition, b) linear regression coefficients between the SST (shading, in °C) and 10-meter winds (vectors, in m/s) anomalies onto the time series from a), respectively, c) climatology skewness, and d) climatology standard deviation. The observations correspond to ERA5 for both SST and 10-m winds. The anomalies were calculated removing the annual cycle and smoothed by 3-months running mean filter.*

However, it has been claimed that at least two indices should be considered in order to account for the different location of the peak SST anomalies during the ENSO events (e.g., Ren and Jin, 2013; Takahashi et al., 2011). Here, the contribution of both Eastern Pacific and Central Pacific modes from the ENSO diversity, i.e. both E and C indices, was removed through a bilinear regression from both monthly 10-m winds and SST fields prior to the SVD analysis. The monthly fields are from the ERA5 product over the 1980–2019 period. The spatial-temporal evolution of the SPMM is shown in Figure 2.9. The temporal evolution is represented by the first leading SVD mode associated to the 10-meter wind and SST fields (Figure 2.9a). In particular, these indices account for the exact share of the variability in SST (winds) that covaries with the winds (SST),

and it is thus not "contaminated" by noise (uncoupled variability). The correlation between both indices is 0.6 and explains about 55% of the total squared covariance.

2.4.3 Indian Ocean Dipole

The Indian Ocean Dipole (IOD), discovered at the end of the twentieth century (Saji et al., 1999; Webster et al., 1999), is a dominant interannual climate variability associated with large changes of the coupled ocean-atmosphere state over the eastern-western equatorial Indian ocean. The IOD is conventionally described as the Dipole Mode Index (DMI, Saji et al., 1999) and is calculated as the interannual SST anomalies difference between the equatorial western region (10°S-10°N and 50°E-70°W) minus the eastern equatorial region (10°S-0° and 90°E-110°E) (Figure 2.10). The mechanism corresponding to the IOD is described as follows: positive IOD events are initiated by the development of enhanced ocean upwelling along the Java and Sumatra coasts in the eastern Indian Ocean (Figure 2.10b). This generates cool SST anomalies in these regions, increasing the easterly winds and enhancing the ocean warming in the western equatorial Indian ocean, which is associated to an increase (decrease) in atmospheric convection over the western (eastern) region. The IOD activity is seasonally phase locked by the wind reversals associated with the Asian-Australian monsoons (Figure 2.10c-d). Positive events begin to develop around May-June as southeasterly trade winds form in the tropical eastern Indian ocean, and once established with a peak in September, ocean-atmosphere feedbacks are able to sustain and strengthen positive IOD anomalies until the reversal of the trade winds in October-November (Figure 2.10d) causes events to peak and then decay rapidly. The opposite occurs during negative phase of the IOD.

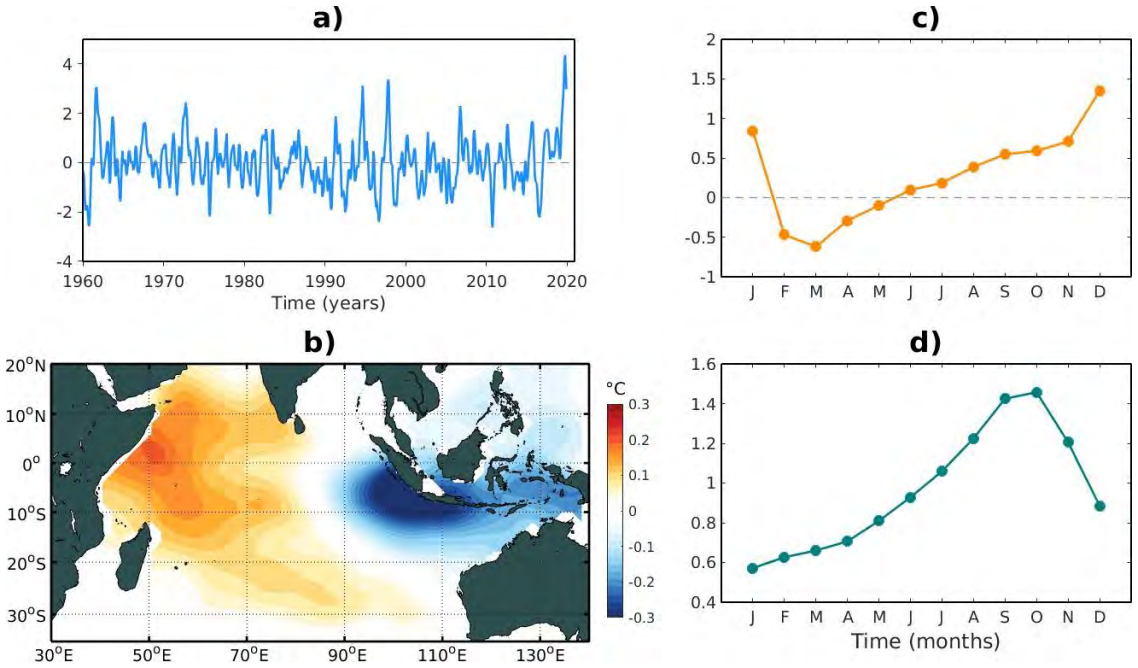

Figure 2.10: *Indian Ocean Dipole (IOD) or Dipole Mode Index (DMI) calculated from SST observations (ERSST.v5). a) Time series of the IOD mode, b) spatial pattern expressed as the SST anomalies regression onto the IOD mode, c) climatology skewness, and d) climatology standard deviation.*

2.4.4 Atlantic El Niño

This mode is defined by an index from the interannual SST anomalies averaged over 3°S-3°N and 20°W-0° region (Figure 2.11). The Atlantic El Niño consists in SST anomalies along the equatorial cold tongue region (Figure 2.11b) with the largest variability during austral winter (June–July–August; JJA, Figures 2.11c-d), when the thermocline is shallow and vertical mixing is at its maximum (Jouanno et al., 2011). The dynamics of the Atlantic El Niño are somewhat similar to those of a Pacific El Niño, which results from ocean-atmosphere interactions and equatorial wave dynamics through the Bjerknes feedback. In the positive phase of the Atlantic El Niño, warm SST anomalies in the eastern equatorial cold tongue region weaken the zonal pressure gradient which diminishes the east-to-west (trade) winds, driving an eastward propagating equatorial oceanic downwelling Kelvin wave that deepens the ocean thermocline in the eastern basin and thereby increases the oceanic heat content, reducing the entrainment of colder subsurface waters into the surface mixed layer in order to amplify the initial warm SST anomalies (Deppenmeier et al., 2016; Keenlyside and Latif, 2007; Ruiz-Barradas et al., 2000). The opposite happens during the negative phase of the Atlantic Niño events, i.e. the Atlantic La Niña.

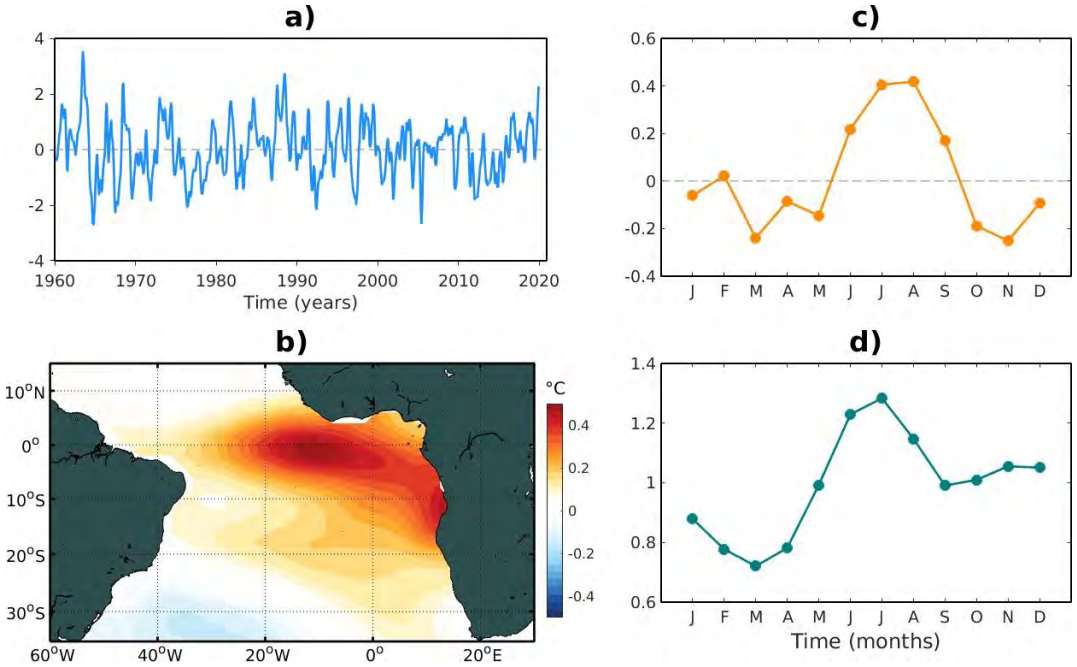

Figure 2.11: *Atlantic El Niño index, calculated as the interannual SST anomalies averaged over the 3°S-3°N and 20°W-0° region (black rectangle in b). a) Time series associated, b) spatial pattern, expressed as the linear regression coefficient (in °C) of the SST anomalies onto the Atlantic El Niño index, c) climatology skewness, and d) climatology standard deviation.*

Chapter 3

Processes driving climate-change SST pattern in EBUS

3.1 Overview and context

The EBUS are of particular interest because they connect the tropical ocean basins with the mid-latitudes through the oceanic-atmospheric overturning circulation. These regions share common characteristics: coastal upwelling favorable winds, poleward undercurrents, instabilities, eddies, coastal trapped waves, and so on (e.g., Strub et al., 2013). The EBUS contain very productive oceanic ecosystems and fisheries, supporting around 20% of the global take of marine fish over an area of less than 1% of the global ocean (Chavez and Messié, 2009). It is predicted that the increase of greenhouse gases (GHG) concentration will impact atmospheric pressure gradients systems changing spatial wind distribution and hence yield an impact on coastal and offshore upwelling in the EBUS (Rykaczewski et al., 2015; Sydeman et al., 2014; D. Wang et al., 2015). Thereby, understanding how the global warming will modify the oceanic circulation and their potential impact on the SST pattern as well as biogeochemical properties of upwelled waters over the ecosystems remains a scientific challenge (Bakun et al., 2015; García-Reyes et al., 2015; Strub et al., 2013). During the last decades many studies have predicted a stronger SST warming in the equatorial region relative to the mid-latitudes of the South Hemisphere, which is now recognized as a robust response pattern to global warming in global climate models (DiNezio et al., 2009; Leloup and Clement, 2009; Z. Liu et al., 2005; J. Lu and Zhao, 2012; Luo et al., 2015; Meehl et al., 2007; Timmermann et al., 2010; Vecchi and Soden, 2007; Xie et al., 2010; L. Zhang and T. Li, 2014; Zhu and Z. Liu, 2009). This SST pattern is illustrated in Figure 3.1, which displays the SST linear trend from observations (1960-2019) and climate models projections (2020-2100). The observations evidence that during the last sixty decades the tropics have been warming faster than the subtropics (Table 3.1 and Figure 3.1a), principally in the Pacific and Atlantic ocean of the South Hemisphere, while in the Indian

ocean the SST warming occurs over the whole basin at a constant rate of approximately 0.1°C per decade (e.g., Dhame et al., 2020; Du and Xie, 2008). This structure resembles a pan-tropical dipole-like pattern (e.g., X. Li et al., 2016) with large warming over the Indo-western Pacific and small part of the tropical Atlantic versus a cooling in the central Pacific, which is commonly recognized as the "global warming hiatus" to describe the slowdown or pause in the increase of global mean surface temperature since the end of the twentieth century (D. Hartmann et al., 2013). The mechanisms to explain this global warming hiatus remain unclear, varying from an increased subsurface ocean heat uptake (above 300m) linked to surface cooling in the tropical Pacific by strengthening trade winds, leading La a Niña-like pattern, that increases the wind-driven subduction (England et al., 2014; Kosaka and Xie, 2013; Meehl et al., 2011), changes in atmospheric water vapour (Solomon et al., 2010) and aerosols (Solomon et al., 2011), to natural factors, such as declining solar insolation, internal variability or radiative forcing (Kaufmann et al., 2011). Nevertheless, taking into account that we are considering long-term SST changes (1960-2020 period), instead the last 20 years where the global warming hiatus started, the SST warming rate in the eastern tropical Pacific (Atlantic) is around 47% (30%) faster than the subtropical region (Table 3.1). This robust pattern, corresponding to a minimum warming observed in the subtropics (or relative cooling in comparison to the global averaged warming), has been previously detected in the Pacific Ocean (Falvey and R. D. Garreaud, 2009). In addition, climate projections to the end of the twenty-first century from full-physics climate models suggest that this enhanced equatorial response (Z. Liu et al., 2005) warming relative to the subtropics will be consistent in the three EBUS of the South Hemisphere (Figure 3.1b). In the North Hemisphere, by contrast, the strong SST warming is due to the difference in land-sea distribution (Z. Liu et al., 2005) or weaker southeasterly trade wind relative to the South Hemisphere (Rykaczewski et al., 2015; Xie et al., 2010). The most pronounced SST meridional gradient is located in the Southeast Pacific ocean (Z. Liu et al., 2005; Xie et al., 2010), that exhibit a minimum warming rate in the subtropics of $\sim$0.2 °C per decade while is twice as large in the equatorial region (Figure 3.1b-c). Several studies have been trying to explain this SST pattern response to the GHG forcing, principally in terms of the cloud-radiation-SST feedback (Z. Liu et al., 2005), Ekman pumping changes by wind response (Timmermann et al., 2010), or increased latent heat cooling by winds intensification (e.g. J. Lu and Zhao, 2012; Xie et al., 2010).

Data sets	Equatorial Pacific	Subtropical Pacific	Equatorial Atlantic	Subtropical Atlantic	Equatorial Indian	Subtropical Indian
HadSST3	0.136	0.071	0.113	0.088	0.130	0.127
Kaplan	0.096	0.048	0.118	0.078	0.126	0.120
ICOADS	0.119	0.056	0.112	0.084	0.127	0.112
ERSST.v5	0.124	0.078	0.153	0.093	0.121	0.130

Table 3.1: *SST anomaly trend (in °C/decade) in the Southeast ocean of the South Hemisphere over the 1960-2019 period from different data sets. The oceanic regions averaged are: Equatorial Pacific (10°N-10°S; 120°W-80°W), Subtropical Pacific (10°S-40°S; 120°W-70°W), Equatorial Atlantic (10°N-10°S; 10°W-25°E), Subtropical Atlantic (10°S-30°S; 10°W-25°E), Equatorial Indian (10°N-10°S; 80°E-120°E) and Subtropical Indian (10°S-35°S; 80°E-120°E). All values are significant at the 95% confidence level based on a two-tailed Student's t-test.*

In spite of that, large uncertainties in climate model projections to determine what mechanisms are driven the future SST pattern remain in the systematic errors by the inevitable inter-model spread of the climate sensitivity. These errors are commonly associated to the misrepresentations of physical processes, which can be amplified among climate components especially in the tropics by a range of cloud-feedbacks (Dufresne and Bony, 2008; Sherwood et al., 2014), or to the existing biases on the mean state, including an overestimation of the SST in the eastern equatorial Atlantic (Richter and Xie, 2008b), an excessive equatorial Pacific cold tongue (G. Li and Xie, 2014), a double intertropical convergence zone (Lin, 2007), strengthening/weakening of the Atlantic Meridional Overturning Circulation (C. Wang et al., 2014), warmer SST in the EBUS (Richter, 2015), among others. In this perspective, the root mean square (RMS) of the SST trend pattern from CMIP5 27 multi-models (Figure 3.1c) indicates that in the western equatorial Pacific and central Atlantic regions, as well as in high latitudes, the dispersion among models projections is strong, reaching differential warming rate greater than 0.1°C per decade. Because the three tropical basins are connected via the atmospheric circulation (M. A. Alexander et al., 2002; Latif and Barnett, 1995) any change in the SST trend magnitude across the tropical ocean lead to an inter-basin SST gradient that drives changes in atmospheric and oceanic circulations from interannual to decadal timescales (Cai et al., 2019). In consequence, there is still a large uncertainty in the mechanisms driving climate change-SST patterns in the tropics and it has remained difficult to decipher the relative role of climate modes of the natural variability and/or the anthropogenic forcing in driving this climate change SST pattern . Thus, the underlying mechanism involved in the minimum warming rate associated to the

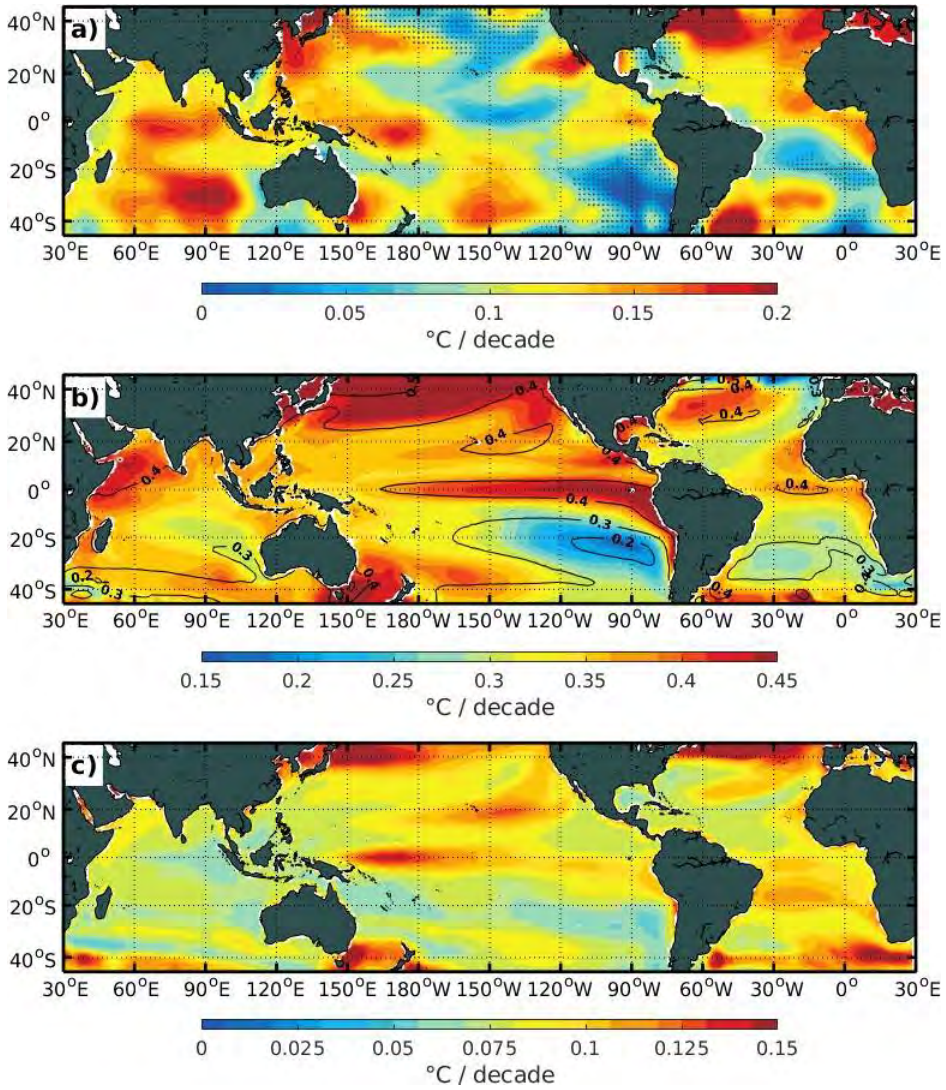

Figure 3.1: *Global maps of SST linear trend pattern (in °C/decade) from observations and climate models projections. a) Observations from ERSST.v5 over the 1960-2019 period, b) CESM-LENS 40 mean-ensemble (shading) and CMIP5 27 mean-models (contours) over the 2020-2100 period, and c) root mean square among the CMIP5 27 multi-models. Stippling in a) indicate that SST linear trend is non-significant at the 95% confidence level based on a two-tailed Student's t-test.*

subtropics, resulting in a differential warming rate in the EBUS between the coastal and the off-shore ocean, is yet to be elucidated.

On one hand, Z. Liu et al., 2005 suggested that the enhanced equatorial response warming in the Pacific Ocean is attributed to the changes in the ocean-atmosphere stability and the sea-air humidity gradient. In fact, these changes lead to a stronger latent heat loss and shortwave cooling in the subtropics due to the stronger mean trade wind and the increased low clouds, respectively, as well as a reduction of the entrainment cooling on the equator. On the other hand, Xie et al., 2010 proposed a physically based

methodology, integrating the ocean temperature equation over the mixed layer (see equation 2.1 in Chapter 2), assuming that both present-day and future climate states are in quasi-equilibrium. They suggest that the ocean transport effect (D_o), including ocean advection and vertical entrainment, balance the net surface flux (Q_{net}) to first order (i.e., $D_o = -Q_{net}$). The authors argue that the latent heat flux loss, through the wind-evaporation-SST (WES, Xie and S. G. H. Philander, 1994) feedback and mean evaporation distribution, is the main factor to generate the differential warming rate in both the Pacific and Atlantic oceans, meanwhile in the Indian ocean, it is the Bjerknes feedback that dominates (Cai et al., 2013; W. Liu et al., 2015; Luo et al., 2016; Xie et al., 2010). However, their approach has two main limitations: 1) it assumes that the ocean and atmosphere are in quasi-equilibrium state (i.e. $\partial T/\partial t \approx 0$ at longtime scales) although the timescales of adjustment to external forcing of the ocean and atmospheric dynamics can be significantly distinct and their can be an interaction between natural variability and forced variability at decadal timescales (Cai et al., 2020). In addition, this assumption is questionable in RCP8.5 scenario since external forcing has a steady increase and SST trend is significantly positive in most regions of the globe over the period of integration of the projections. 2) It does not provide an explicit calculation of the ocean advection and mixing terms, which can provide material for the interpretation of the redistribution of heat in the surface layer, and thus pinpoint key mechanisms at work for driving the climate change-SST pattern. Nonetheless, J. Lu and Zhao, 2012 supported the hypothesis proposed by Xie et al., 2010. The authors showed, through the overriding technique to isolate the effects of the feedbacks from wind-driven circulation and heat fluxes, that the WES-feedback is the leading mechanism to explain the tropical SST pattern formation under global warming. In a recent study, L. Zhang and T. Li, 2014 used a simple surface heat budget model to demonstrated that the future SST pattern, as showed in Figure 3.1, is determined by the present-day climate mean state and modulated by atmospheric wind, moisture, and temperature changes. Nevertheless, those mechanisms proposed to explain the SST pattern response to global warming follow the same diagnostic used by Xie et al., 2010 suggesting that the role of ocean dynamics is minor. Additionally, the uncertainty in the future climate change through the internal variability, which arises from non-linear dynamical processes intrinsic to the atmosphere, could lead to different coupled ocean-atmosphere mechanisms to explain the SST pattern response to GHG forcing (e.g., Dai et al., 2015; Deser et al., 2012; L. Dong and McPhaden, 2017; Meehl et al., 2013).

In this chapter, we build upon these former studies to disentangle the mechanisms involved in the SST pattern formation under global warming conditions in the EBUS of the South Hemisphere. We follow the methodology proposed by Xie et al., 2010

assuming quasi-equilibrium state in the future climate. However, conversely to their approach, we take a look here at the three-dimensional components of the ocean heat advection allowing to access an estimate of mixing/entrainment. Besides, the influence of the internal variability of the climate system is also examined based on the CESM-LENS simulations, described in Chapter 2, which is difficult to elucidate from the CMIP5 models. In addition, we also analyzed the horizontal contribution of the Ekman and Geostrophic currents by the ocean heat advection, which represents a novel contribution compared to previous comparable studies. In the first part of the present chapter, we contrasted the changes projected on the mean surface circulation between both CMIP5 and CESM-LENS climate models simulations, including the sensitivity among the climate models of the air-sea coupled response to climate change. The second part focuses on the mechanisms involved in the SST trend pattern through a heat budget analysis over the mixed layer from the CESM-LENS simulations. The last part of the chapter concludes with a synthesis of the results.

3.2 Changes in mean circulation

Natural and human-induced SST changes have large influences in the climate system in terms of amount, intensity or frequency on rainfall (droughts and floods), sea level, favorable upwelling winds, tropical cyclone development, monsoons circulation, storms tracks, and so on. During the last few decades, there have been numerous efforts to understand the mechanisms driving the future change of the climate system using numerical models. By contrasting multi-models datasets forced by different scenarios of GHG increased, a consistent tendency for future climate projections is expected (e.g., section 1.1.3), which elicits a consistent tendency for future climate projections. Still, internal parametrization in climate models produces a large ambiguity in future climate system response to greenhouse warming. In this section, we evaluate the trend patterns projections and their spread for the twenty-first century between CMIP5 multi-models and CESM-LENS simulations from different variables of the climate system.

3.2.1 Sea surface height

During the twentieth-century the global mean sea level has been rising around 1.2 cm per decade from 1900 to 1990, with a significant rate increase of 3 cm per decade since 1990 (J. Church et al., 2013; J. A. Church and N. J. White, 2011; Hay et al., 2015).

The main factors driven the current and future sea level change are the ocean thermal expansion, the mass loss of glaciers and ice sheets, and the land water storage (J. Church et al., 2013). Sea level rise has certainly tremendous consequences on societies and ecosystems, in particular for coastal areas that are expected to become more vulnerable to flooding and land loss (Nicholls and Cazenave, 2010). The dynamic sea surface height (SSH), or sea level relative to geoid, trend pattern from the CESM-LENS 40 mean-ensemble over the 2006-2100 period indicates that the sea level pattern is not spatially uniform (Figure 3.2b). The greatest SSH increase is projected over the western boundaries of the Indian and Pacific Ocean, as well as southward of 35°S. On the other hand, a significant reduction (relative to the global mean) in the SSH is detected over the Southeast Indian and Pacific Ocean, where the minimum SST warming rate is located. Only along the coasts of the Benguela Upwelling System an increase in the sea level is expected. Those patterns are robust from the CESM-LENS simulations, indicating that the anthropogenic forcing is important over these regions under a warmer climate. However, the SSH trend is slightly enhanced over the cold tongue of the Pacific Ocean and the equatorial Indo-Pacific region, which is non-significant. This could be related to the contribution of the internal climate variability induced by changes in large-scale wind patterns and buoyancy forcing (A. Hu and Deser, 2013). In this sense, natural climate variability can play a key role in determining the projected regional sea level rise, especially in the near term, while to the end of the century it is expected that anthropogenic forcing will dominate (Bilbao et al., 2015; A. Hu and S. C. Bates, 2018; Lyu et al., 2014). Furthermore, the mechanisms associated to local SSH trend could be ranged from changes in temperature-salinity, ocean currents circulation, water and ice redistribution between the land and ocean, or in atmospheric pressure. In addition, the RMS of the SSH trend pattern among the CMIP5 multi-models reveals a large spread, principally southward of 30°S and in the equatorial Pacific and Atlantic regions (Figure 3.2c). Note that the RMS from CMIP5 multi-models is greater than 2 cm per decade almost everywhere, while the dispersion from the CESM-LENS 40 ensemble only reaches 0.2 cm per decade in the western equatorial Pacific. This points out a likely diversity of mechanisms that drive the future SSH changes among the CMIP5 multi-models in a warmer climate.

3.2.2 Precipitation

Under GHG-induced warming the rainfall response may lead to increased surface aridity and more droughts in the mid-latitudes during the twenty-first century, with serious impacts on human adaptation to climate change. Future precipitation changes to anthropogenic forcing can be understood as a combination of thermodynamic and

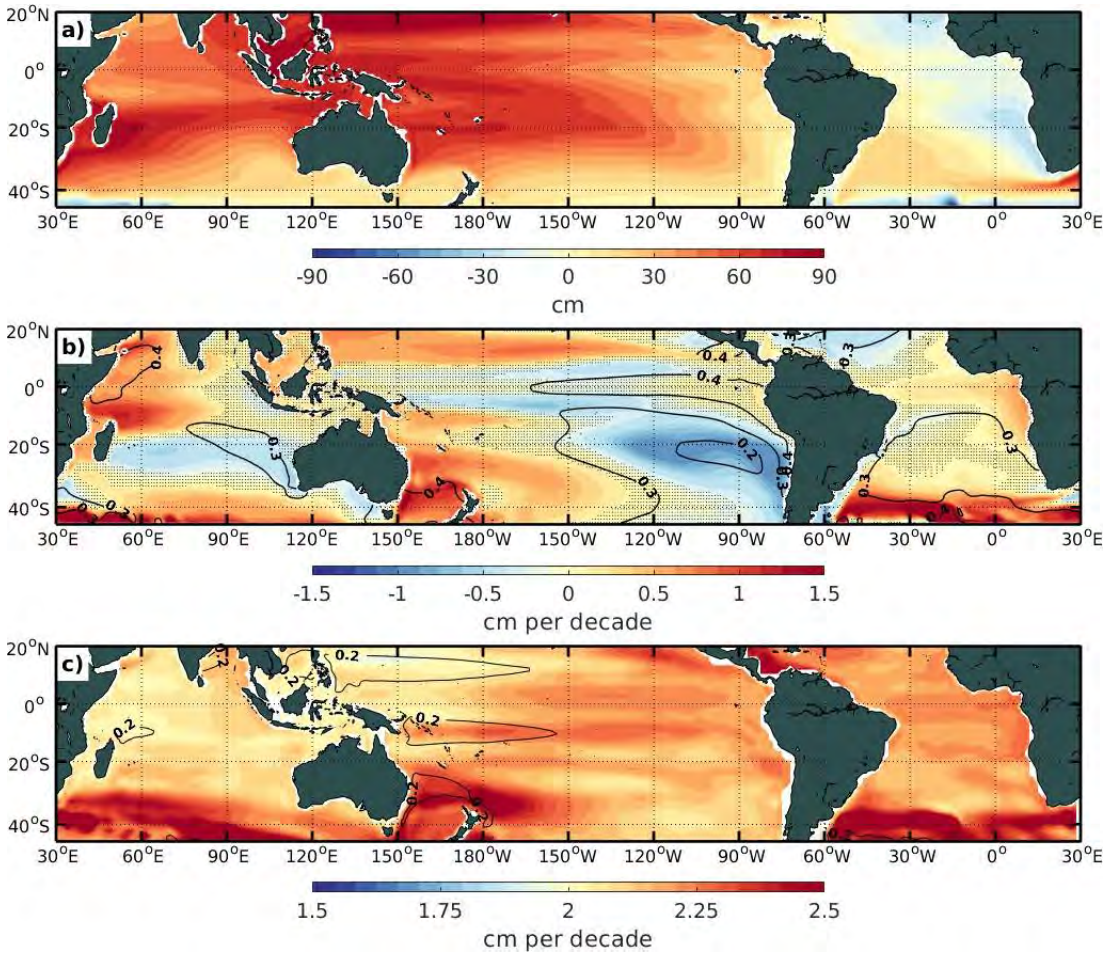

Figure 3.2: *Sea surface height variable from climate models CESM-LENS 40 mean-ensemble. a) Mean state (in cm) from CESM-LENS 40 mean-ensemble over the 1980-2005 period, b) linear trend pattern (in cm per decade) from CESM-LENS 40 mean-ensemble over the 2006-2100 period, and c) root mean square of the linear trend pattern (in cm per decade) from CMIP5 27 mean-members (shading) and CESM-LENS 40 mean-ensemble (black contour) over the 2006-2100 period. Black contour lines in b) correspond to the SST trend pattern formation from CESM-LENS 40 mean-ensemble over the 2006-2100 period. Stipplings in b) indicate where the linear trend is non-significant at 95% based on a two-tailed Student's t-test and more than 70% of the mean-ensemble have the same sign.*

dynamic responses (Seager et al., 2010). On one hand, the rich-get-richer hypothesis (Chou et al., 2009; Held and Soden, 2006), associated with thermodynamic increases in specific humidity and associated changes in moisture transport, would lead to wet regions becoming wetter and dry regions becoming drier. On the other hand, dynamical response of precipitation to the slowdown tropical circulation, SST variations and convective mass flux change could dominate the spatial pattern of precipitation under global warming projections (Chadwick et al., 2013; Ma et al., 2012; Xie et al., 2010). Figure 3.3b shows that the precipitation trend pattern over the 2006-2100 period from CESM-LENS 40 mean-ensemble will not be uniform despite the temperature warms

everywhere. For example, the equatorial Pacific is likely to experience the highest increase in mean precipitation as well as in mean SST. This enhanced SST warming in the equatorial Pacific anchors a band of rainfall increase where rainfall is currently low (Figure 3.3a). In others wet regions, as in the western equatorial Atlantic and Indian ocean, mean precipitation will also increase (Figure 3.3b).

On the other hand, in the subtropical dry regions, i.e. in the EBUS of the South Hemisphere (Figure 3.3a) where the minimum SST warming rate is located, mean precipitation will likely decrease (Figure 3.3b). Note that in the equatorial Indo-Pacific and eastern equatorial Atlantic ocean the precipitation trend pattern is non-significant and the internal variability could play a relevant role in the future precipitation changes. Thus, the spatial variations of the SST warming rate affect tropical rainfall by inducing anomalous circulation and modulating convective instability, following a warmer-get-wetter pattern (Ma and Xie, 2013; Xie et al., 2010), meaning that regions with the

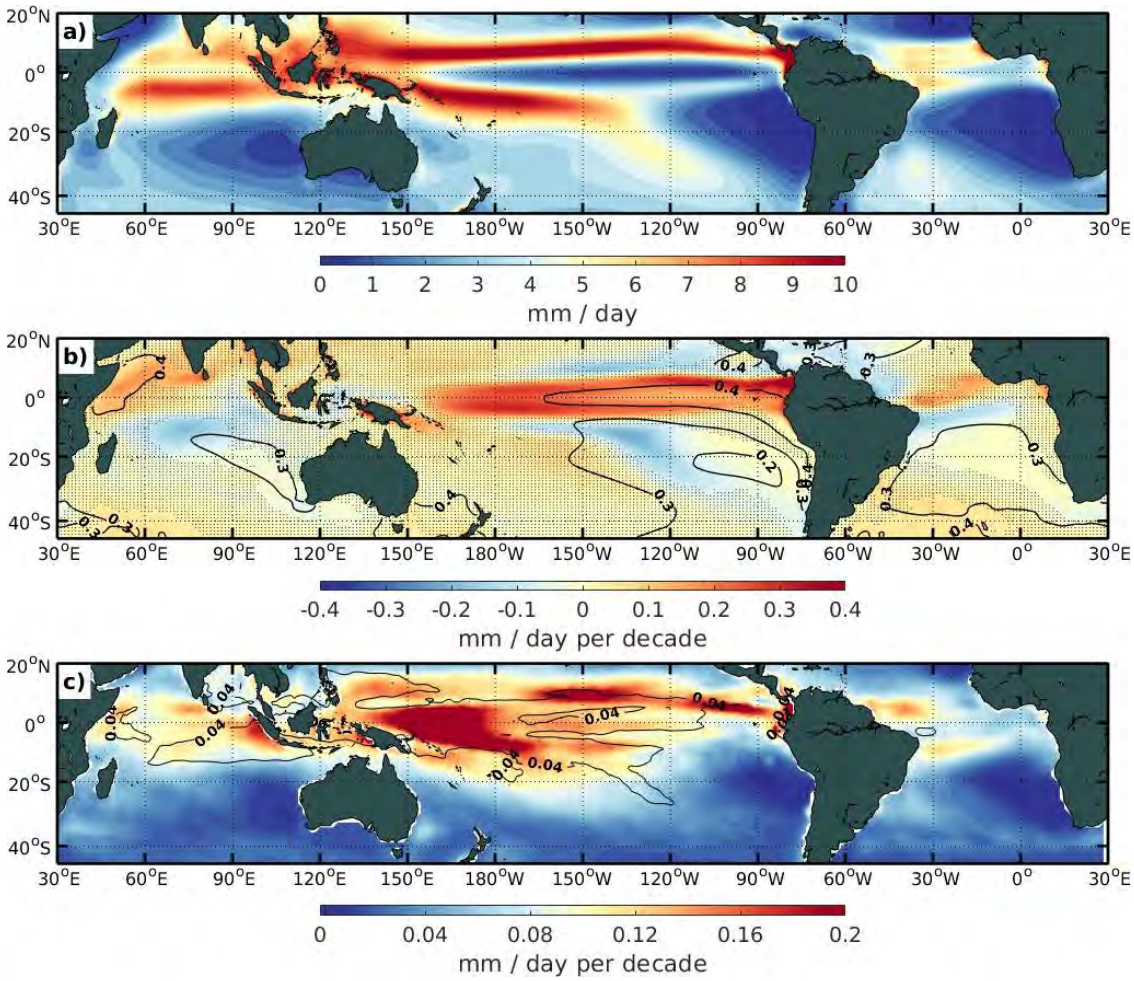

Figure 3.3: *Same as Figure 3.2, but for precipitation variable (in mm/day).*

greatest (lowest) SST warming would become wetter (drier). However, the precipitation trend pattern has an enormous CMIP5 inter-model dispersion with values around 0.2 mm/day per decade in the Indo-Pacific equatorial ocean (Figure 3.3c). The large spread among the climate models agrees with the position of the commonly double-ITCZ bias (Adam et al., 2018; Lin, 2007; X. Zhang et al., 2015), which is characterized by an excessive precipitation off equator and underestimated on the equator. The double-ITCZ bias is specially sensitive to SST by the strong SST-convection relationship over the tropical Pacific (Samanta et al., 2019), where several biases in ocean-atmosphere feedback affect this double-ITCZ over the equatorial Pacific (G. Li and Xie, 2014; Lin, 2007; Song and G. J. Zhang, 2016), such as an excessive Bjerknes feedback by excessive sensitivity of precipitation to SST, an overly SST-latent heat flux feedback by excessive sensitivity of surface air humidity to SST, or insufficient SST-shortwave flux feedback by insufficient sensitivity of cloud amount to precipitation. Thus, the poorly representation of those feedback in climate models generates a large uncertainty in what mechanisms are driving future precipitation change.

3.2.3 Winds

The atmospheric circulation is an essential element of the climate system, because trough their bridges they connect tropical and subtropical oceanic basins (i.e. Walker circulation and Hadley cells) modulating precipitation, moisture and energy transports, including tropical cyclone development and monsoons circulation. The weakening of tropical circulation is very robust among the twenty-first century global climate models simulations and occurs most in a longitudinal direction (Held and Soden, 2006; Vecchi and Soden, 2007). A weakening of the Walker circulation has already been observed (Vecchi et al., 2006). However, recent observational studies suggest that La Niña-like SST pattern on the Pacific ocean has been cooling the Earth via atmospheric teleconections in a resulting hiatus of the global warming during the last two decades (Kosaka and Xie, 2013). La Niña-like pattern is represented by positive (negative) SST anomalies in the central/western (eastern) Pacific, that reinforce the Bjerknes feedback and, in turn, enhance the Walker circulation through an intensification of the trade winds, which leads a positive feedback to the hiatus by increasing subsurface ocean heat uptake and equatorial upwelling (England et al., 2014). The strengthening of the atmospheric Walker circulation and slowdown warming over the early twenty-first century can be regarded as natural interdecadal variability (Meehl et al., 2016, 2014; Watanabe et al., 2014), internal climate variability (Dai et al., 2015), as well as to possible contributions from the Atlantic ocean basin (McGregor et al., 2014) or an externally forced response from small volcanic eruptions (Santer et al., 2014).

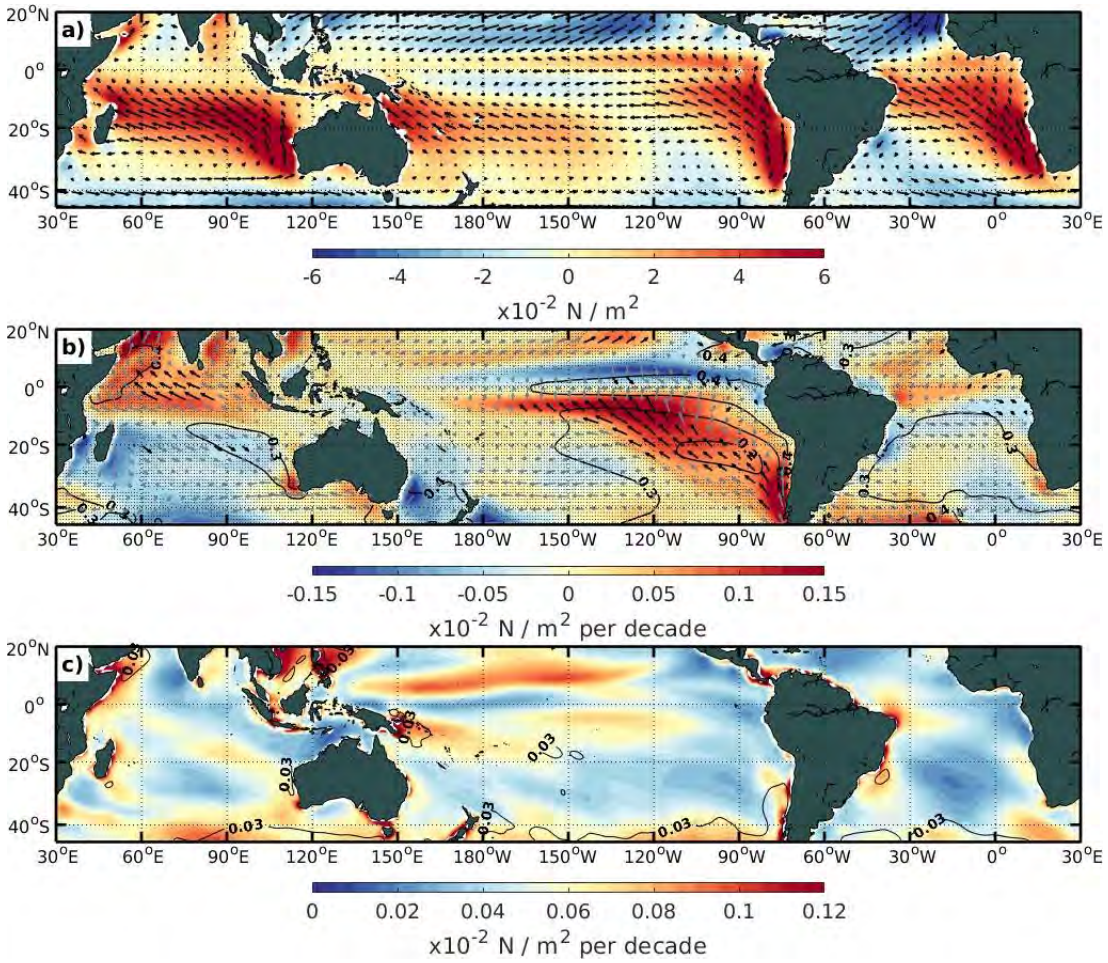

Figure 3.4: *Same as Figure 3.2, but for meridional wind stress (shading) variable (in N/m2). Vectors correspond to the magnitude and direction of the wind stress. Black (gray) vectors in b) indicate that the linear trend is significant (non-significant).*

Nevertheless, corrected SST observations (Karl et al., 2015) question the existence of the hiatus and its ability to influence the long-term trend. Figure 3.4b shows the wind stress trend pattern over the 2006-2100 period from CESM-LENS 40 mean-ensemble. In the eastern Pacific ocean the winds change are largely consistent with the SST warming patterns (Xie et al., 2010). The trade winds increase (decrease) in strength in the south-eastern (northeastern) subtropical Pacific, associated with collocated minimum (maximum) of SST warming. This is consistent with the WES feedback, in which stronger trade winds enhance evaporation, cooling SST, and in turn leading to stronger winds through strengthening the South Pacific anticyclone. On the other hand, over the most part of the Atlantic ocean basin the winds change are non-significant, suggesting a larger role of internal atmospheric variability. In the central equatorial Indian ocean a significant enhancement of the easterlies suggests that a positive Bjerknes feedback will dominate the future SST changes, reducing (increasing) the surface warming in

the eastern (western) region. The large dispersion among the CMIP5 multi-models for future projections of the winds changes is mostly concentrated in the western-central equatorial Pacific, the Chilean coasts (45°S-20°S) and the western equatorial Indian ocean (Figure 3.4c). There is a good agreement among the climate models to project a weakened easterlies in the eastern Pacific, an intensification of the trade winds in the southeastern equatorial Pacific and the enhancement of the easterlies in the equatorial Indian ocean.

3.2.4 Coupled processes in climate models

Since the low-level atmospheric circulation is coupled to SST in most regions of the tropics, the large spread of the linear trend patterns projected for the twenty-first century from different climate variables among the CMIP5 multi-models (Figures 3.2, 3.3 and 3.4) suggests that such a spread might be also present in other variables. In order to evaluate of the spread amongst models of the coupling between wind stress and SST trends, we performed a SVD analysis between SST and wind stress linear trend patterns amongst the models. Figure 3.5 shows the first SVD mode decomposition from CMIP5 27 multi-models and CESM-LENS 40 mean-ensemble. Note that the mean-ensemble linear trend pattern from both SST and wind stress (see Figures 3.1 and 3.4) was removed. In this sense, the expansion coefficients (Figure 3.5a) indicate the amplitude of the spatial pattern (Figure 3.5b) for each global model with respects to the mean-ensemble, and thus indicate regions where models differ the most in terms of the relationship between the wind stress and SST long-term trends. The percentage of co-variance explained for the first mode is high (88%) and the correlation between the expansion coefficients is large (r = 0.85). This indicates that the dispersion on future SST changes projected among the climate models is strongly coupled to changes in surface winds, and vice versa. The spatial pattern (Figure 3.5b) shows that some regions are very sensitive to coupled processes between SST and wind stress, such as the western Indian Ocean, equatorial Pacific Ocean, and the whole Atlantic Ocean basin. Besides, the expansion coefficients (Figure 3.5a) provide the magnitude of the coupled response (and its direction) relatively to the ensemble mean. In this sense, over those key areas the climate models projections have large discrepancies in terms of the magnitude of the linear trend pattern and even in their sign, which affects the co-variability between the SST and wind stress. In particular, it is interesting to remark that in the Pacific Ocean there is a robust connection between the projections in the western and eastern equatorial Pacific from both SST and wind stress, suggesting that differences in the eastern tropical Pacific between models could originate from their ability to simulate the SST trends over the warm pool region. Additionally, the value of the expansion

coefficient for the CESM-LENS are close to zero, indicating that the magnitude of the wind stress and SST trends in CESM does not deviate from that of the ensemble mean (and thus from the CMIP5 ensemble), which justifies to work with this model instead of the CMIP5 ensemble for our further analyses. Besides the practical motivation (i.e. working with a single model compared with working with a model ensemble), the relatively large number of members available for the CESM model allows for a more robust estimate of errors in the trends and of the role of natural variability.

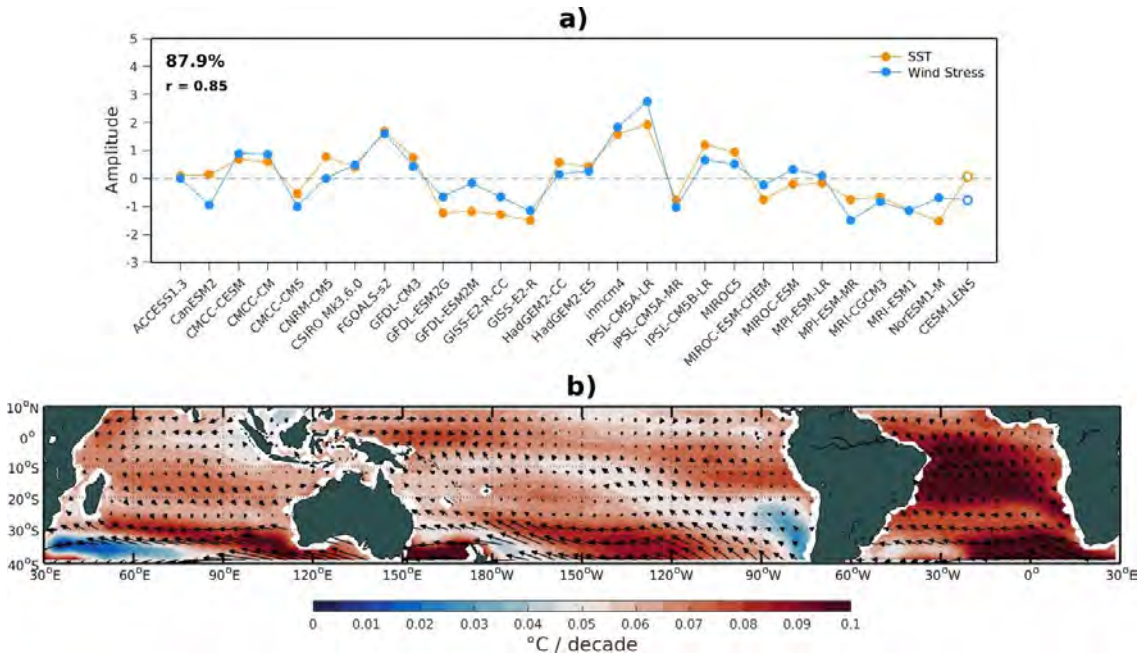

Figure 3.5: *First single value decomposition (SVD) mode from CMIP5 27 multi-models (see Table 2.1) and CESM-LENS 40 mean-ensemble between the trend patterns of SST (in °C per decade) and wind stress (in N/m2 per decade, upper panels), precipitation (in mm/day per decade, middle panels), and sea surface height (in cm per decade, lower panels). a) Spatial pattern of SST (shading), wind stress (vectors), precipitation (contours) and sea surface height (contours). b) Expansion coefficients (amplitude). The explained variance is indicated in b). The amplitude of the CESM-LENS corresponds to model number 28 (open white circles in b).*

3.3 Mixed-layer heat budget decomposition

To further understand the mechanisms driving the SST pattern formation under warmer climate, we performed a heat budget decomposition over the mixed-layer (described in Chapter 2) in the tropics and subtropics regions of the South Hemisphere (40°S-20°N), focusing on the CESM-LENS simulations. We showed in Chapter 2 that our formulation of the heat budget decomposition (equation 2.12) is able to explain a

large variance of the model SST trend in most regions (Figure 2.6), providing confidence in the interpretation of each terms estimated from the model. In the following we describe the contribution of each terms of the SST equation.

3.3.1 Mean evaporation, surface fluxes and ocean advection

The SST pattern formation has a strong dependency on surface evaporation that acts as a damping effect to balance the atmospheric fluxes and ocean advection, as shown in equation 2.12 (Chapter 2). The equatorial peak in SST warming could be understood in terms of the meridional variations in the Newtonian cooling coefficient (Figure 3.6a). The latter is proportional to the mean evaporation from latent heat flux, which is dominated by atmospheric forcing (e.g. wind speed). Thereby, the meridional distribution of the mean evaporation can be understood in terms of the weaker (stronger) winds and high (low) relative humidity in the tropics (subtropics) enabling less (more) evaporation, and as a consequence, an increased (reduced) SST warming . However, the location of the maximum relative cooling by evaporation is to the north of the minimum SST warming rate , principally in both the Pacific and Atlantic oceans (Figure 3.6b), which indicates the role of oceanic processes not fully balanced by thermal damping in driving the SST trends there. Nonetheless, in the three equatorial regions of the ocean basin, the weaker evaporation coincides with a maximum SST warming . Therefore, the equatorial warming could be interpreted as resulting from increased thermal damping equilibrating the oceanic response. In both the Pacific and Atlantic subtropical regions a strong cooling is observed, through the mean trade winds, which are situated around 10° northward of the minimum SST warming rate projected (Figure 3.6b). This discrepancy in the meridional SST pattern between the results of the simplified model and the full-physics model suggests that other terms than evaporation are involved in the SST pattern formation under anthropogenic forcing. In contrast, the Indian ocean shows a weaker meridional gradient in the SST warming rate, compared to Pacific and Atlantic oceans. The strong cooling by mean evaporation in the subtropics is located closer to the location of the minimum SST warming rate. In any case, mean evaporation controlling the SST warming rate is not the only mechanism at work to explain the future SST pattern formation. Moreover, the mechanism involved in the SST pattern response to climate change could be different among the three EBUS of the South Hemisphere.

Under the assumption of equilibrium under steady anthropogenic forcing, we are able to explain to a large extent the SST pattern in the tropical-to-subtropical regions of the South Hemisphere (see Figure 2.6). We can now have a look at each terms of the

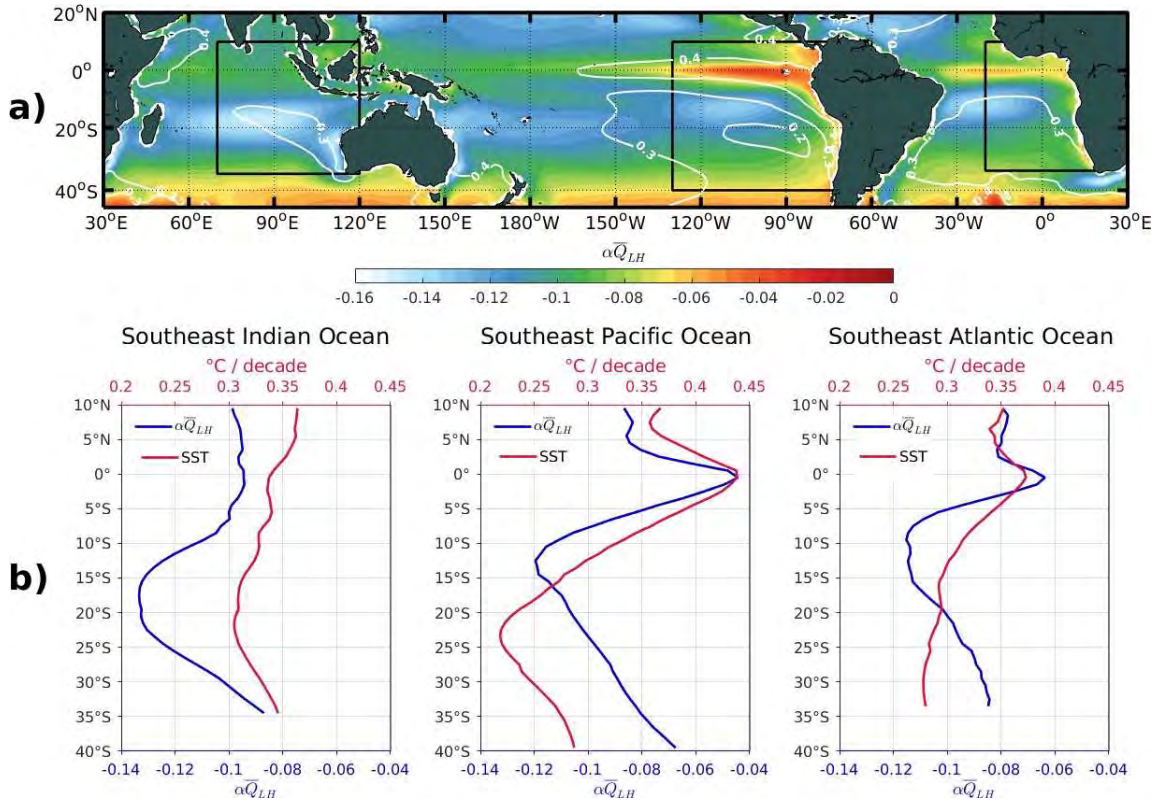

Figure 3.6: *CESM-LENS 40 mean-ensemble of the Newtonian cooling coefficient (alphaQLH) and SST trend projections (in °C/decade). a) Mean spatial distribution over the South Hemisphere for Newtonian cooling coefficient (shading) and SST trend pattern (white contours). b) Latitudinal distribution of the Newtonian cooling coefficient (blue line) and the SST trend pattern (red line) averaged over each Southeast ocean basin, indicated by black rectangles. The Newtonian cooling coefficient correspond to mean values over the 1980-2005 period from Historical simulations.*

heat budget in order to understand the processes at work. As a first step, we examine the contribution of atmospheric and oceanic processes separately (Figure 3.7). The surface atmospheric fluxes warm all the South Hemisphere with some regional difference among the basins (Figure 3.7a). In the western equatorial regions of the three basins and in both Southeast Pacific and Atlantic oceans, the atmospheric fluxes have less impact in the SST warming rate, even non-significant for the mean-ensemble. Such large-scale organization may be related to intrinsic variability from natural modes (e.g., ENSO, Indian Ocean Dipole, Atlantic El Niño) that imprint themselves upon the SST field. This suggests a significant role of internal variability over these regions, so that the SST trend pattern formation is not necessary linked to anthropogenic forcing. On the other hand, the ocean advection acts to warm the equatorial regions of the three basins, especially in the Pacific and Atlantic (Figure 3.7b). The decrease in equatorial SST zonal gradients in the future climate in the Atlantic and Pacific basins can be

interpreted in terms of the reduction in the Walker circulation that weakens the easterlies winds in both the Pacific and Atlantic oceans (Vecchi and Soden, 2007; Vecchi et al., 2006), which allows the displacement of warmer waters from western to eastern regions. In the EBUS of the South Hemisphere, particularly the Peru-Chile and Benguela Upwelling Systems, the ocean advection plays an important role to warm the coasts, extending thousand kilometers offshore and northward of 20°S where the minimum warming rate is located (0.2-0.3°C per decade). Notwithstanding, the residual term indicates that the SST warming by the ocean advection is compensated by vertical diffusivity and lateral mixing, largely in the central-eastern equatorial regions over the three basins and negligible far from the tropics (Figure 3.7c). In addition, it is interesting to note that in the equatorial Indian Ocean the mixing processes achieve to reproduce a SST dipole-like warming, which suggests a rectification of the IOD-like in the residual pattern.

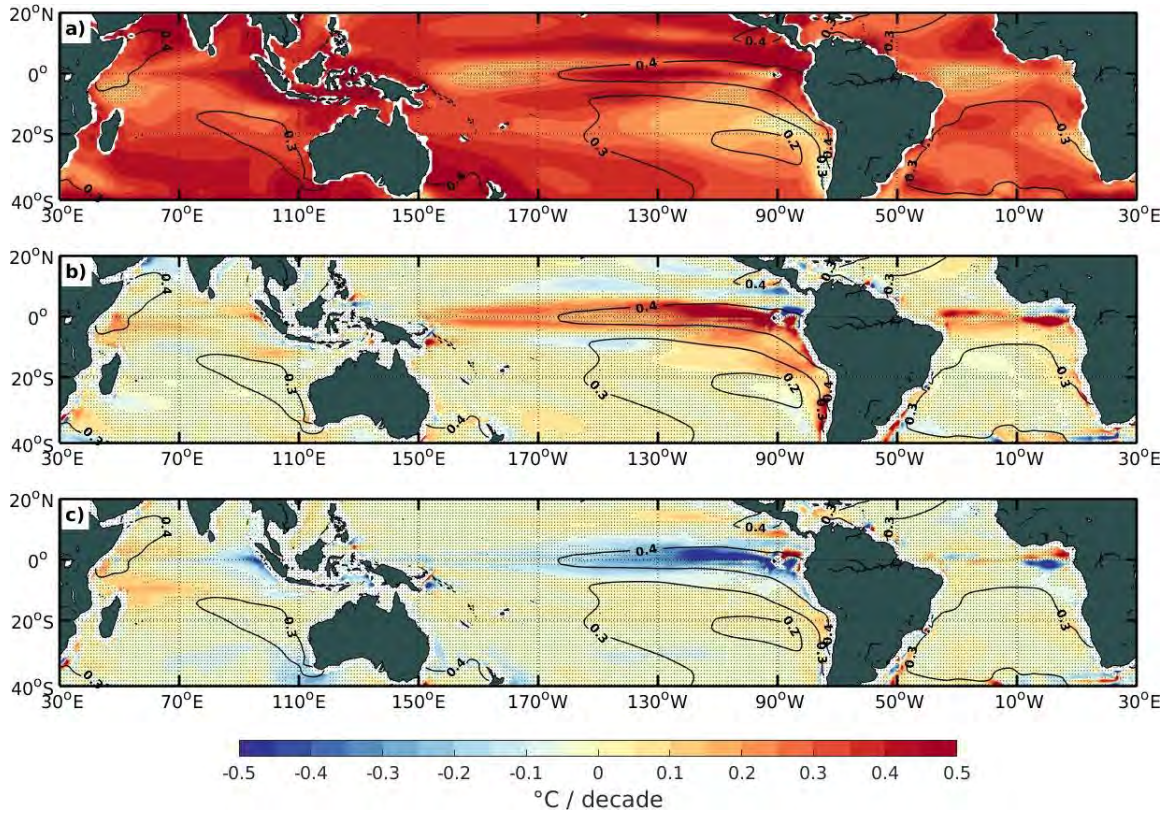

Figure 3.7: *CESM-LENS 40 mean-ensemble linear trend patterns (in °C/decade) of the principal terms involved in equation 2.9 (see Chapter 2) that contribute to the SST trend pattern formation over the 2006-2100 period. a) atmospheric forcing, b) ocean advection, and c) residual. Black contour lines correspond to the SST trend pattern formation from CESM-LENS 40 mean-ensemble. Stipplings indicate where the linear trend is non-significant at 95% based on a two-tailed Student's t-test and more than 70% of the mean-ensemble have the same sign.*

3.3.2 Disentangling the atmospheric forcing

The contribution to the SST trend of each atmospheric heat flux term from equation 2.12 is shown in Figure 3.8. The SST is warming everywhere by the net longwave radiation (Figure 3.8a). Meanwhile the SST increase, the water vapor content in the atmosphere raises and amplify the initial SST warming. This water vapor feedback is the major mechanism that controls the global warming induced by anthropogenic forcing (Held and Soden, 2000, 2006). On the other hand, in the regions where the net atmospheric forcing has less impact on the SST trend pattern, the net shortwave radiation plays a substantial role to reduce the SST warming (Figure 3.8b). In the western and central equatorial regions, chiefly in the Pacific Ocean, an increase in SST intensifies deep convection of the atmosphere and reduces solar radiation even more, damping the initial SST warming. In the subtropics, an increase in the stratocumulus clouds might reduce the solar radiation at the sea surface, diminishing the SST warming rate. The sensible heat tends to warm the three basins, but their contribution to the future SST changes is negligible with values weaker than for the others atmospheric terms by about an order of magnitude in absolute value (Figure 3.8c). Another important term to reduces the SST warming rate is the heat loss through wind changes (Figure 3.8d). The mechanism associated to the ocean-atmosphere coupling is the WES-feedback (Xie and S. G. H. Philander, 1994): considering a surface with warm (cold) water, the surface winds are weaken (strengthen) over that surface reducing (enhancing) the evaporation and inducing further warming (cooling). In these sense, the intensification of both trade winds in the mid-latitudes of the Pacific ocean and the Southeast Pacific Subtropical Anticyclone (see Figure 3.4b), through a southward expansion of the Hadley cell (J. Lu et al., 2007; Tao et al., 2016), enhance the heat loss in the south central tropical Pacific and slightly offshore the Chilean region, where the minimum SST warming rate is located (Figure 3.8d). On the contrary, across the eastern equatorial Pacific warmer waters weaken the trade winds, reducing the evaporation. In the Atlantic Ocean, the changes in heat flux due to the WES-feedback yields a warming tendency conversely to the Pacific Ocean. The wind intensification in the eastern equatorial region tends to reduce the SST warming by increasing the latent heat loss, while in the subtropics occur the opposite. However, the changes projected by winds over these regions are not-significant (Figure 3.4b). In the central equatorial Indian Ocean, the intensification of the trade winds (see Figure 3.4b) enhances the evaporation and could be indicative that the positive Bjerknes feedback is controlling the SST trend pattern (e.g., Xie et al., 2010). The last term associated to a warming tendency is due to change in latent heat flux induced by changes in surface relative humidity and stability (Figure 3.8e).

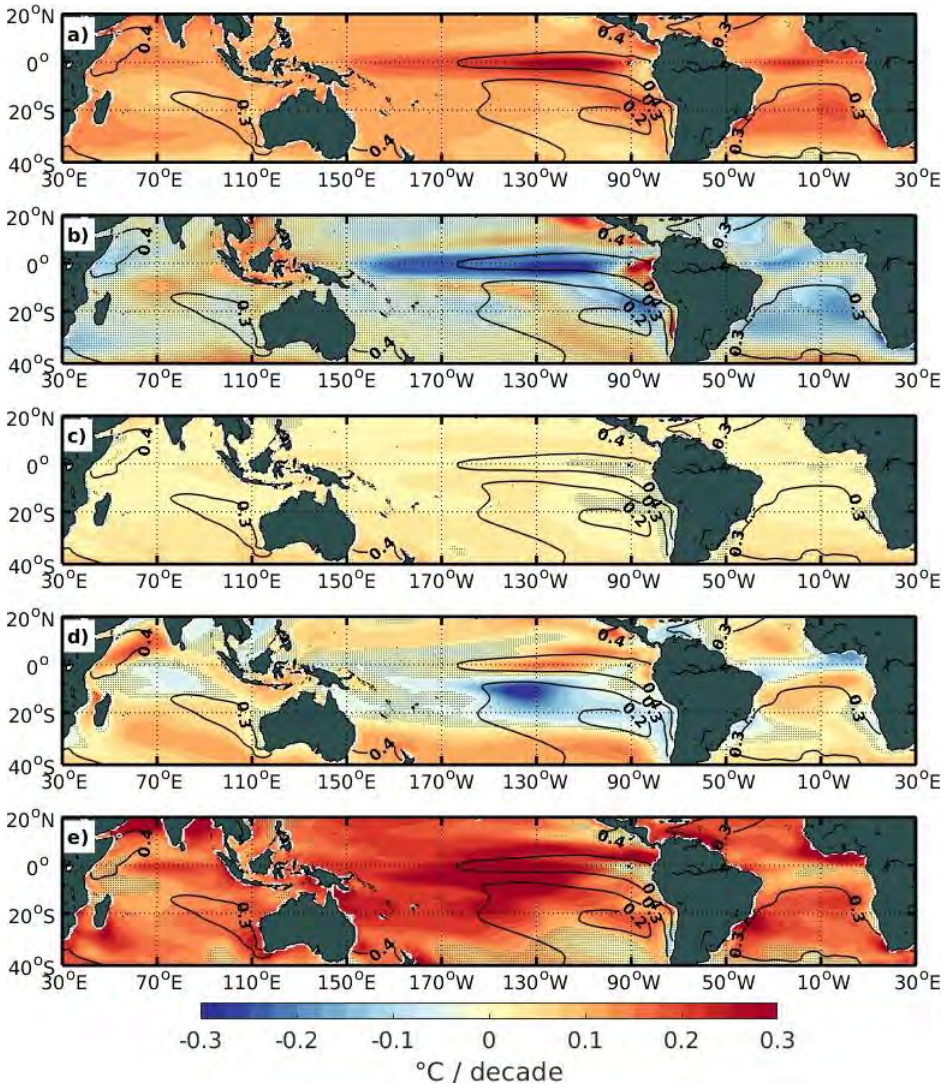

Figure 3.8: *CESM-LENS 40 mean-ensemble linear trend patterns (in °C/decade) of the atmospheric fluxes involved in equation 2.12 (see Chapter 2). a) Longwave radiation, b) shortwave radiation, c) sensible heat, d) latent heat by the WES-feedback, and e) latent heat by relative humidity and stability effects. Black contour lines correspond to the SST trend pattern from CESM-LENS 40 mean-ensemble. Stipplings indicate where the linear trend is non-significant at 95% based on a two-tailed Student's t-test and more than 70% of the mean-ensemble have the same sign.*

Changes in surface stability (i.e., the air temperature warms relative to the surface ocean) are projected to increase in a warmer climate modulating the atmospheric bridge from the tropics to mid-latitudes (Chou and Chen, 2010; J. Lu et al., 2008). Due to the high heat capacity of the ocean, warming response of the ocean to anthropogenic forcing is slower than that of the atmosphere, so that the enhanced surface stability helps to trap moisture near the surface and thus contributes to the increase in surface relative humidity (Richter and Xie, 2008a), reducing the evaporation and amplifying

the SST warming. The peak contribution of latent heat through changes in relative humidity and stability warming is located in the central Pacific and the subtropics regions, while non-significant local minima are found in the eastern coastal equatorial regions of both the Pacific and Atlantic oceans, and in the western equatorial Indian Ocean.

3.3.3 The role of ocean dynamics

The ocean advection has an essential role in the distribution of the surface ocean warming. The influence of each advection terms is presented in Figure 3.9. The zonal component is predominantly important (warming tendency) in the Pacific ocean rather than the others basins (Figure 3.9a) , with a warming rate peaking to 0.3°C per decade and which extends across the whole equatorial region and alongshore the Peru-Chile Upwelling System (PCUS), forming a EP El Nino-like pattern. Note, however, that the warming tendency cancels out along the coast of Chile from 18°S until 25°S, which corresponds to the location where zonal advection has a cooling effect. Along the coast of Peru and Chile, vertical advection has a minor contribution to the warming tendency. In the Atlantic ocean, southward of 20°S, the coastal region is warming, while along the equator a dipole structure in zonal advection is formed which warms the western coasts and cools the eastern side. In the Indian basin the zonal ocean advection helps to warm the equatorial band, but the values of this tendency term are non-significant in almost all the basin. On the other hand, the meridional component of the ocean advection contributes to the SST warming in the equatorial and Southeast oceans of both the Pacific and Atlantic basins (Figure 3.9b). The warming tendency associated to meridional advection in the Peru-Chile and Benguela Upwelling Systems reaches 0.3-0.4°C per decade, principally southward of 20°S. Northward of that latitude, the meridional advection extends the enhanced SST warming from the coast to the offshore ocean and towards the equator in both the Pacific and Atlantic oceans. Besides, the meridional current tends to warm the SST around 0° from eastern to central equatorial regions, which is noticeable northward (southward) of the equatorial Pacific (Atlantic) Ocean. In addition, near both the northeastern equatorial Pacific and Atlantic oceans the meridional ocean advection is reducing the SST warming. In the Indian ocean, the meridional currents are acting to warm the SST, but the values are weak. Eventually, the vertical component of the ocean advection is only significant near the eastern equatorial region of both Pacific and Atlantic oceans (Figure 3.9c). In the southern part of the equator (i.e., 5°S-0°) the vertical advection acts to warm the SST by deepening the thermocline tied to weaker winds over these regions, which could be associated with

the slowdown of the Walker circulation (e.g., Vecchi et al., 2006). In the western equatorial regions of the three basins, as well as over the whole Indian ocean, the effect of vertical advection is negligible. Note that in the three basins of the South Hemisphere the ocean advection is not contributing directly in the minimum SST warming pattern located close to the EBUS. Instead, the ocean advection induces a southward displacement of the minimum SST warming produced by the atmospheric forcing, associated to the WES-feedback and shortwave radiation (Figure 3.8), contributing to the formation of both a latitudinal and coastal-offshore gradients in the SST trend pattern, essentially in the Pacific and Atlantic oceans. Noteworthy, in the Southeast Pacific ocean both the zonal and meridional components of the ocean advection contribute to the SST trend pattern formation, while in the Southeast Atlantic ocean only the meridional ocean advection plays a main role.

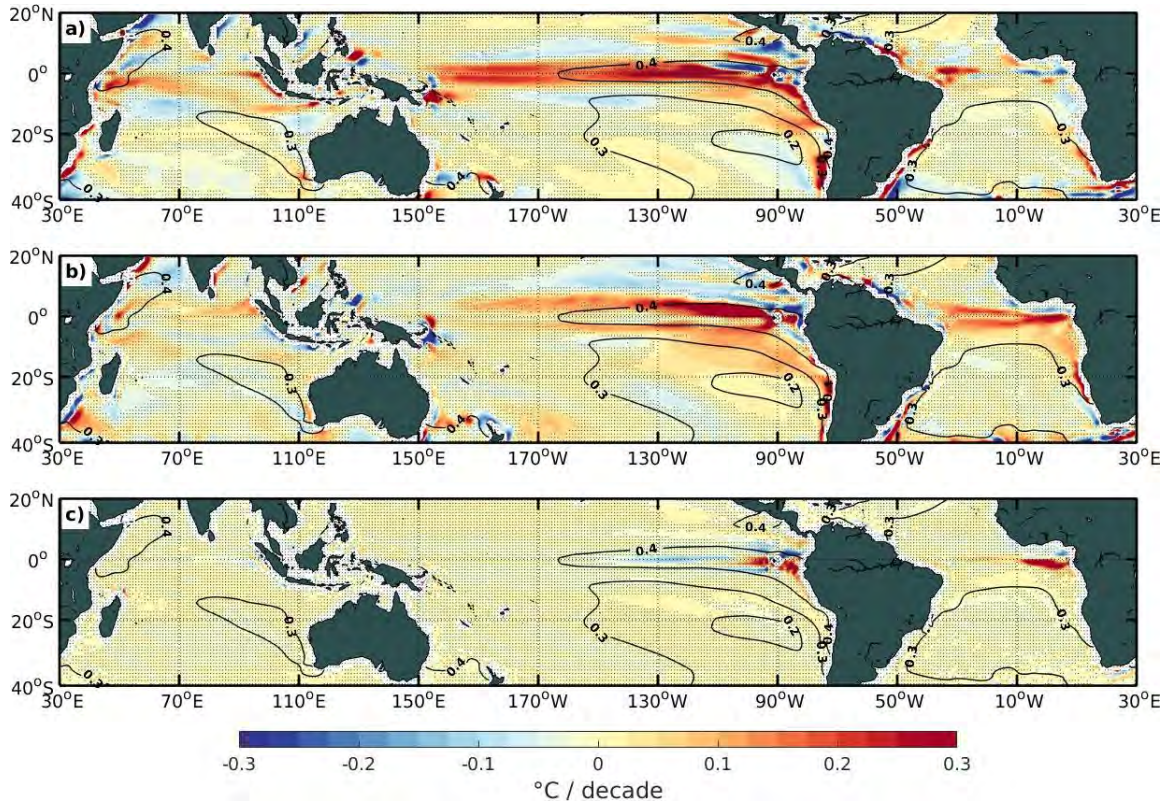

Figure 3.9: *CESM-LENS 40 mean-ensemble linear trend patterns (in °C/decade) of the ocean advection separated into the three-dimension components over the 2006-2100 period. a) Zonal, b) meridional, and c) vertical components. Black contour lines correspond to the SST trend pattern formation (in °C/decade) from CESM-LENS 40 mean-ensemble. Stipplings indicate where the linear trend is non-significant at 95% based on a two-tailed Student's t-test and more than 70% of the mean-ensemble have the same sign.*

3.3.4 Ekman and geostrophic currents

Previously, we have shown the importance of the ocean advection in warming the tropics and subtropics, principally in the EBUS of the South Hemisphere. In these regions, it has been hypothesized that the increased GHG concentrations will impact the cross-shore thermal and atmospheric pressure gradients between the ocean and continents, which in turn will intensify the coastal winds that cause upwelling (Bakun, 1990; Bakun et al., 2015). Recent observations have been supported this notion (Sydeman et al., 2014), while global model projections indicates an intensification of the upwelling-favorable winds only in the poleward portions of the EBUS (Rykaczewski et al., 2015; D. Wang et al., 2015). Besides changes in upwelling-favorable winds modulating SST trend along the coasts, change in the mean meridional SST gradients along the coasts of the EBUS could also produce a cross-shore geostrophic flow response (e.g., Marchesiello and Estrade, 2010). In order to examine this hypothesis, we separate the contribution of the surface geostrophic and Ekman currents to the changes in surface currents, and estimate through a Reynolds decomposition, their contribution to both zonal and meridional advection. Since vertical advection has a weak contribution to the future SST pattern formation in the EBUS (Figure 3.9c), we focused on the horizontal components of advection. The results indicate that, along the coast of Peru-Chile, the SST warming is induced by the horizontal ocean advection driven by both Ekman and Geostrophic currents (Figures 3.10a-b and 3.11a-b), although the Ekman contribution dominate. Along the coast of Peru, anomalous zonal advection by the geostrophic current of mean temperature contribute to the warming tendency, indicating that the SST warming pattern induces an on-shore geostrophic current that yield a positive zonal advection. On the other hand, the surface geostrophic flow will also increase the SST alongshore of the PCUS by an adjustment of anomalous currents (Figure 3.10d and 3.11d), while in the northern part of Chile (30°S-20°S) the zonal component of the surface geostrophic current will reduce the SST warming (Figure 3.10b). Interestingly, the non-linear horizontal advection tends to oppose to the warming tendency off Peru, although its contribution is weaker than the other terms. In the Southeast Atlantic ocean, major part of the SST warming is due to Geostrophic currents-induced meridional advection of temperature anomalies by mean currents, northward of 20°S (Figure 3.11b-d). Southward of 20°S, the warming is mostly associated with Ekman currents-induced zonal advection of temperature anomalies by mean currents (Figure 3.10a-e). Alike the PCUS, non-linear advection has almost not contribution to the warming SST pattern in the Benguela Upwelling System. Lastly, the Indian ocean is affected by changes in the ocean advection principally in the equatorial band (5°S-5°N), which is dominated by non-linear advection of both meridional Ekman and Geostrophic currents.

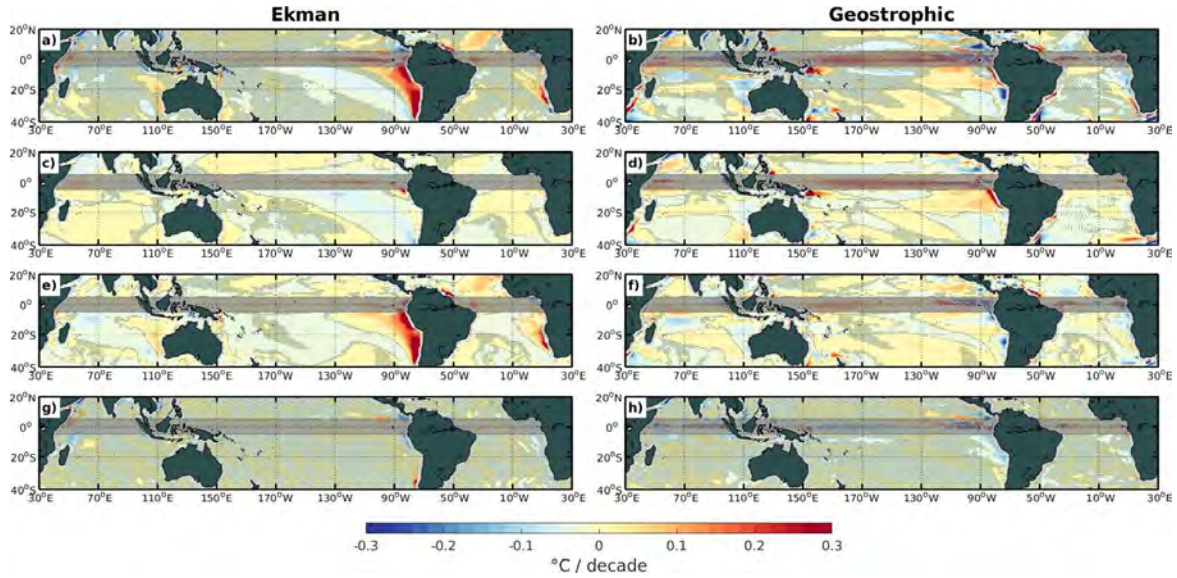

Figure 3.10: *CESM-LENS 40 mean-ensemble linear trend patterns (in °C/decade) of the zonal ocean advection component separated into Ekman and surface Geostrophic currents by a Reynolds decomposition (see section 2.3.5 in Chapter 2) over the 2006-2100 period. a-b) Total ocean advection, c-d) advection of mean temperature gradient by anomalous currents, e-f) advection of anomalous temperature gradient by the mean currents, and g-h) non-linear advection. The equatorial band (2°S-2°N) is masked in white color because the Geostrophic approximation is not reliable. Stipplings indicate where the linear trend is non-significant at 95% based on a two-tailed Student's t-test and more than 70% of the mean-ensemble have the same sign.*

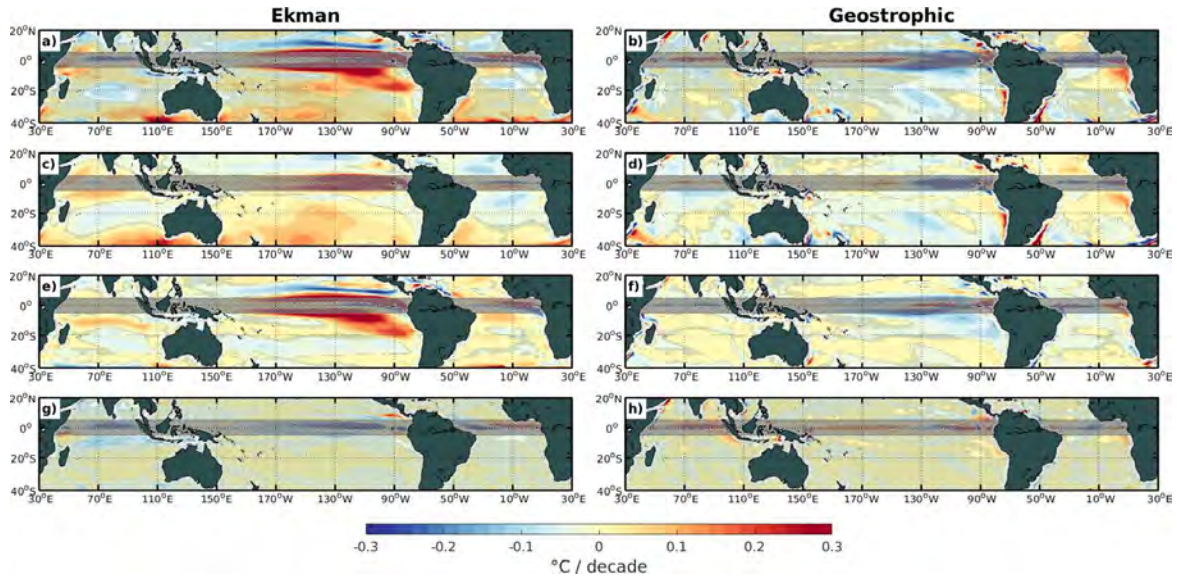

Figure 3.11: *Same as Figure 3.11, but for the meridional ocean advection component.*

3.4 Natural variability signature

Global climate projections have diverse source of uncertainties (Hawkins and Sutton, 2009) such as different parameterizations among models, persistent bias on the mean climate state or internal variability of the climate system. In particular, the internal variability comes from the natural variability of the climate system including intrinsic atmospheric, oceanic and coupled processes, which have usually a prominent signature on the climate change SST pattern in future projections, especially in the mid-to-high latitudes (Deser et al. 2012). Here, we attempt to interpret the climate change SST pattern in terms of its modulation by natural climate modes (see section 2.4 in Chapter 2), with a focus on the Southeast ocean basins. To quantify the natural variability signature (NVS) onto the future SST change, we diagnosed these natural modes in both CMIP5 and CESM-LENS models over the 2006-2100 period to contrast with the present climate from observations. Figure 3.12 represents the spatial patterns of the principals natural modes of variability from observations and climate models. Although previous studies indicate that natural climate modes can experience changes in amplitude and pattern under greenhouse warming (e.g., Cai et al., 2014ab, 2015, 2018), the overall pattern and center of action of these modes is maintained in the future climate, which allows for using these modes for interpreting the climate change SST pattern. See section 2.4 for more detailed description of these natural modes of variability.

Now that we have established the spatial patterns of the natural modes of variability projected to the end of the twenty-first century by the climate models, we want to elucidate the implications of those patterns to enhance or diminish the future SST changes. Since observations and climate models projections indicate an average SST warming over the South Hemisphere (Figure 3.1), we subtracted the mean SST trend value averaged over the whole region (45°S-20°N) in the observations and both the CMIP5 and CESM-LENS models (Figure 3.13). This means that positive (negative) trend values correspond to a relative warming (cooling) rate with respect to the mean SST trend over the whole region for both observations and climate models. Note that different methods to estimate the relative SST warming (e.g., removing only the equatorial band, the full-global pattern, normalized area, etc) achieve the same outcome (i.e., relative warming of the tropics to the subtropics) denoting a confidence in our results and interpretations. Despite the fact that the mean SST trends predicted by the models is about three times greater than the observations (i.e., they range from 0.12 to 0.32°C per decade in observations and models, respectively) the spatial patterns are quite similar between the observations and the climate models. The strong latitudinal

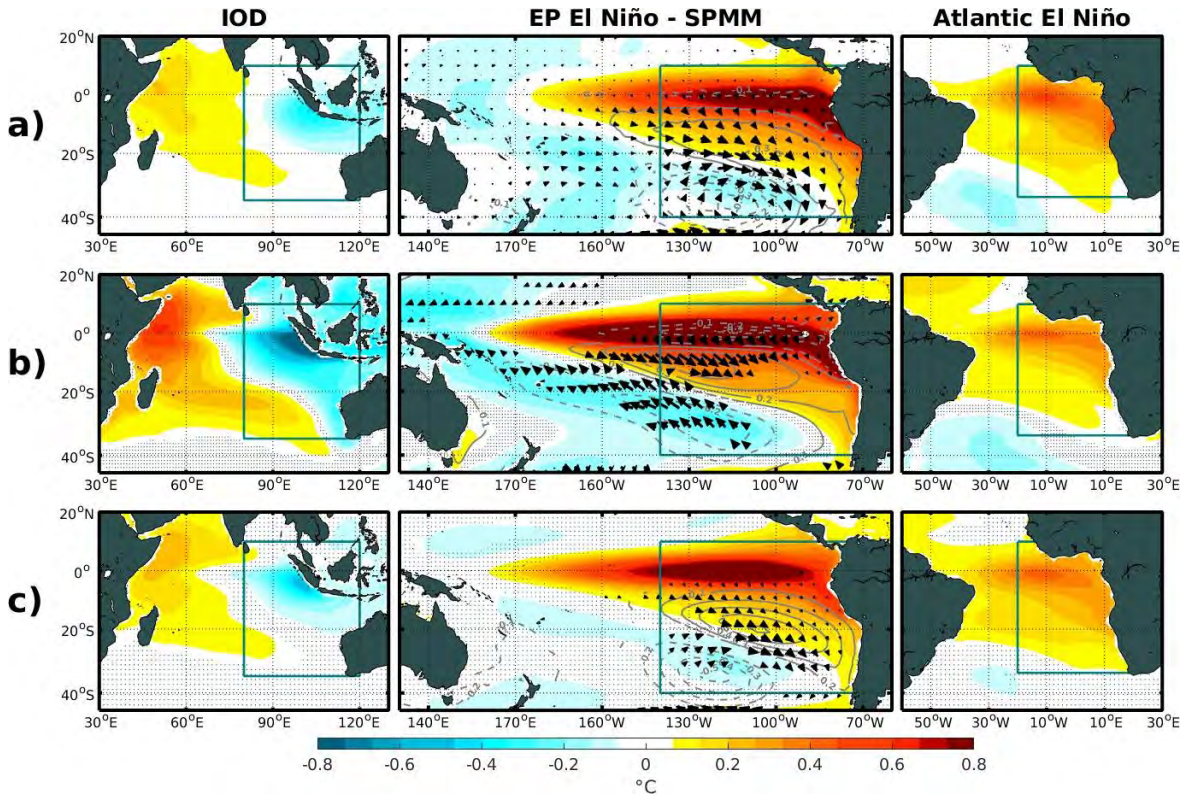

Figure 3.12: *Linear regression coefficients (in °C, shading) between the SST anomalies and the index of natural modes of variability from a) Observations, b) CESM-LENS 40 mean-ensemble, and c) CMIP5 27 mean-models. The observations correspond to ERSST.v5 (ERA5) for the IOD, EP El Niño and Atlantic El Niño (SPMM) over the 1960-2019 (1980-2019) period. See section 2.3.9 in Chapter 2. The linear regression coefficients for both CESM-LENS and CMIP5 models were calculated over the 2006-2100 period. The SST anomalies were calculated removing the annual cycle over the corresponding period for observations and climate models. Gray contours indicate the positive (continues lines) and negative (dashed lines) phases of the SPMM. Black vectors correspond to the significant linear regression coefficients between the surface wind components and the SPMM. Green rectangles represent the different Southeast ocean basins. Stipplings indicate where the linear regression is non-significant at 95% based on a two-tailed Student's t-test.*

gradient distribution of the SST changes between the tropics and subtropics is noticeable, with an evident minimum warming rate, or relative cooling, over the Southeast Pacific and Atlantic oceans in both observations and climate models. However, over the Indian ocean basin both observations and climate models differ in terms of the warming pattern: a warming over the central basin is observed in the present day conditions, while a dipole-like pattern (i.e., larger warming in the western equatorial than in the eastern equatorial region and subtropics) is projected by the climate models.

At this point, we project the SST trend pattern onto the selected climate modes over a selected domain corresponding to the Southeast ocean basins where the minimum warming rate, or relative cooling, is located (see green rectangles in Figure 3.12).

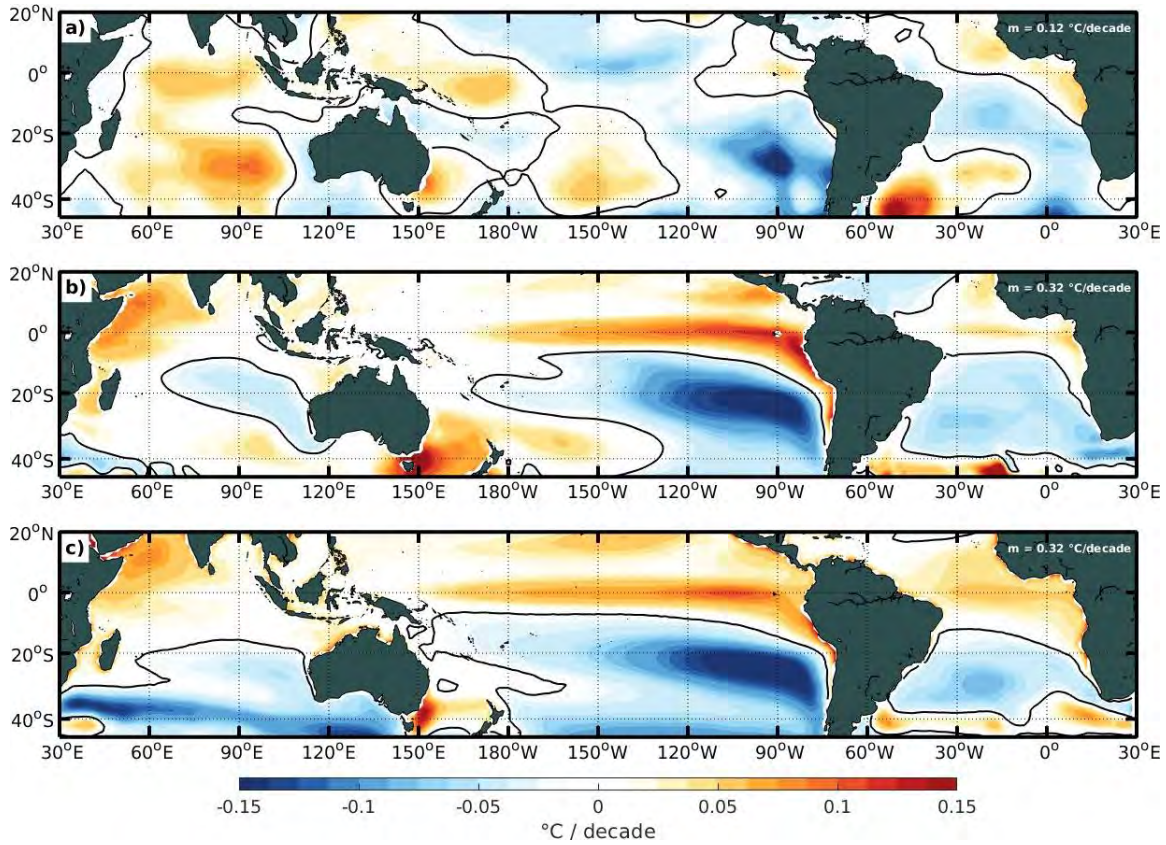

Figure 3.13: *Relative long-term SST trend pattern (in °C per decade, shading) from a) observations (ERSST.v5), b) CESM-LENS 40 mean-ensemble simulations, and c) CMIP5 27 mean-models. The relative SST trend is calculated removing the mean SST trend over the whole domain. Observations (CESM-LENS and CMIP5) correspond to the 1960-2019 (2006-2100) period. Black contours indicate the mean SST trend (in °C per decade) over the whole domain, indicated in each panel.*

The domains are: Southeast Pacific (10°N-40°S; 140°W-70°W), Southeast Atlantic (35°S-10°N; 20°W-20°E), and Southeast Indian (80°E-120°E; 35°S-10°N) oceans. Thus, the natural variability signature (NVS) onto the future SST change was estimated as follows:

$$NVS(y) = \frac{1}{N_x} \int_{longitude(n)}^{longitude(i)} \Big[RM_{(x,y)} \cdot RLT_{(x,y)} \Big] dx \tag{3.1}$$

where RM represents the regression maps between SST anomalies onto the natural modes of variability (Figure 3.12) and RLT corresponds to the relative long-term SST trend pattern (Figure 3.13). N_x stand for the longitudinal area of each Southeast ocean basin. The RM was normalized by their spatial standard deviation before the integration. The equation 3.1 will provide a synthetic view of the natural variability signature onto the SST trend pattern formation under a warmer climate as a function of latitude. Note that the interpretation of this analysis is focused on the latitudinal gradient of the

future SST changes and not on the cross-shore gradient. Figure 3.14 shows the contribution of the natural modes of variability associated to the relative long-term SST trend pattern formation from both observations and climate models (through the equation 3.1).

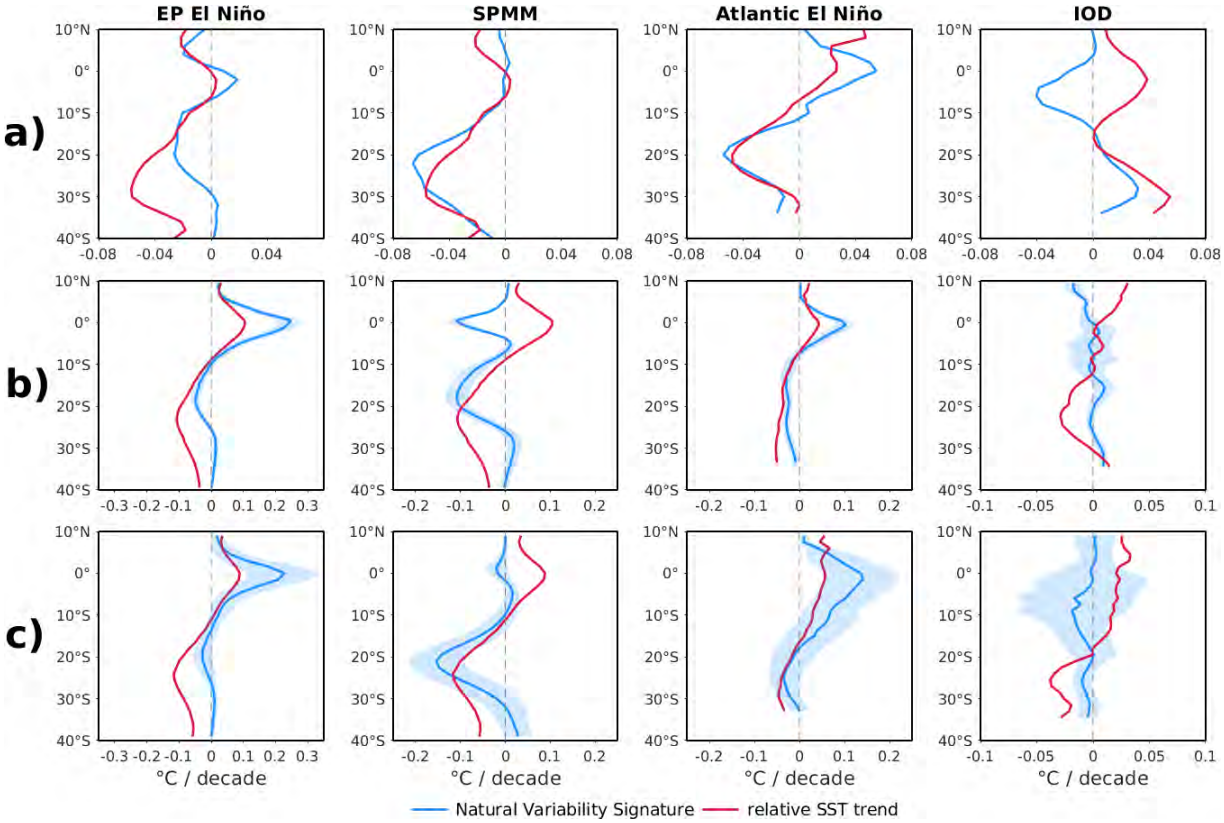

Figure 3.14: *Natural variability signature (NVS, blue line) of the principal natural modes of variability onto the relative SST trend pattern averaged over the Southeast ocean basins from a) Observations, b) CESM-LENS 40 mean-ensemble, and c) CMIP5 27 mean-models. The red line represents the relative long-term SST trend pattern (see Figure 3.12). Shadows in b-c) correspond to the standard deviation of the NVS among the climate models.*

These results inform on where along the coast natural variability is more susceptible to modulate the climate change SST pattern and influence the meridional SST gradient imposed by global warming. Where the amplitude of $NVS(y)$ is as large as that of RLT, this means that natural modes of variability can either amplify or damp the climate change SST pattern. On the eastern Pacific, the relative equatorial warming is allied with the EP El Niño mode while in the off-equatorial regions, where the relative cooling is positioned, the SPMM has a substantial contribution to reduce or enhance the SST warming rate. The Atlantic El Niño clearly modulates the latitudinal SST warming rate over the whole Southeast Atlantic ocean. It is striking that $NVS(y)$ correlates strongly to $RLT(y)$ over the latitudinal range [0°-35°S] for the observations and to a lesser extend for the CESM-LENS in the Atlantic and Pacific oceans. This

indicates that both the Atlantic El Niño and the SPMM modes strongly modulate the climate change SST pattern in these EBUS. This is distinct than in the Indian Ocean where $NVS(y)$ has a meridional dipole structure (with a node at 15°S). As a result, when the IOD amplifies the climate change SST pattern in the equatorial region (north of 15°S), it tends to reduce its magnitude in the mid-latitudes (south of 15°S). On the other hand, regarding the influence of the EP El Nino mode on RLT, it is mostly north of 20°S, consistent with the fact that RLT has a El Nino-like pattern in the eastern tropical Pacific. This influence tends to be overestimated in the models in the near equatorial region.

3.5 Synthesis

Our results suggest that different mechanisms are acting to explain the strong warming in the tropics relative to the subtropics in the Southeast oceans of the South Hemisphere. The dependence of the SST on the mean evaporation is one of the dominant processes that controls the long-term SST trend pattern (Figure 3.6). Knutson and Manabe, 1995 argued that the reduction in the zonal tropical SST gradient in the Pacific ocean under GHG forcing is due by the evaporative damping effect. Although our results indicate that the mean evaporation is able to reproduce the future SST changes in the equatorial region (Figure 3.6), this pattern is not related with the minimum SST warming rate projected by climate models in the subtropics (Figure 3.1). This meridional SST distribution has been explained by three processes: shortwave radiation, ocean mixing and change in the latent heat flux by surface winds (Leloup and Clement, 2009; Z. Liu et al., 2005; J. Lu and Zhao, 2012; Xie et al., 2010; L. Zhang and T. Li, 2014). Despite the indubitable relevance of the atmospheric forcing driving the SST trend pattern formation under warmer climate, our analysis indicates that both the oceanic dynamical response and the natural modes of variability play a fundamental role to reproduce the future SST changes in the Southeast ocean basins of the South Hemisphere. A synthesis of the processes involved to explain the long-term SST trend pattern response to anthropogenic forcing is shown in Figure 3.15. The principal terms involved to increase/decrease the SST warming rate, through the heat budget decomposition from equation 2.12 (see Chapter 2), are latitudinal averaged over the Southeast oceans of the South Hemisphere (see green rectangles in Figure 3.12).

While future SST changes has been commonly explained through the dependence on the mean evaporation, our results suggest that the latitudinal distribution of the SST warming rate is part of a delicate balance between tendency terms associated to

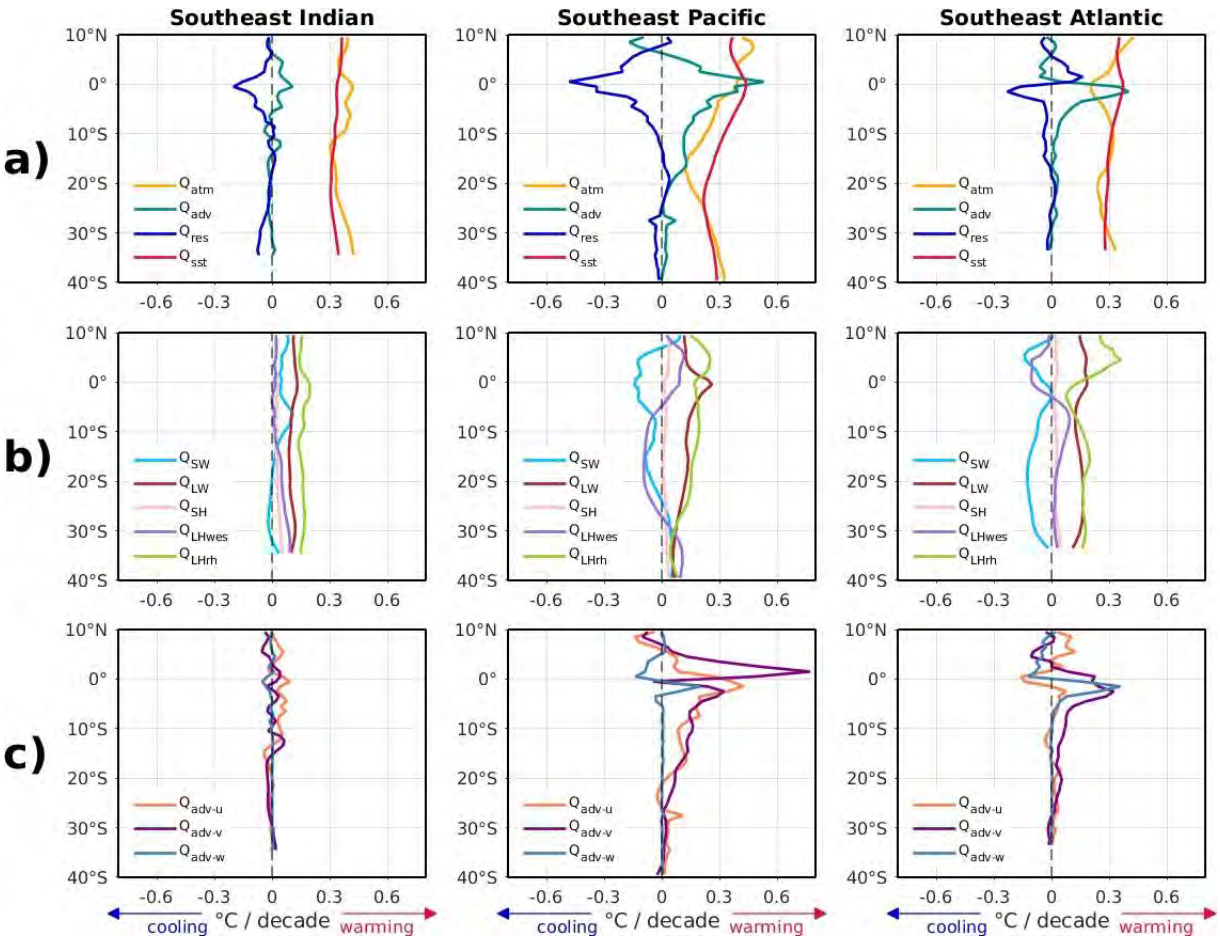

Figure 3.15: *CESM-LENS 40 mean-ensemble linear trend patterns (in °C/decade) of the principal terms involved in equation 2.12 (see Chapter 2) over the 2006-2100 period and latitudinal averaged over the Southeast oceans of the South Hemisphere. a) Atmospheric forcing (Q_{atm}), total ocean advection (Q_{adv}), residual (Q_{res}), and sea surface temperature (Q_{sst}). b) Atmospheric forcing decomposed into: shortwave radiation (Q_{SW}), longwave radiation (Q_{LW}), sensible heat (Q_{SH}), latent heat by WES feedback (Q_{LHwes}) and latent heat by relative humidity and stability effects (Q_{LHrh}). c) Ocean advection decomposed into: zonal (Q_{adv-u}), meridional (Q_{adv-v}) and vertical (Q_{adv-w}) components. All terms are divided by the Newtonian cooling coefficient. The averaged area corresponding to the Southeast ocean is indicated in Figure 3.12 by green rectangles.*

oceanic and atmospheric processes. Thus, the mechanisms for the tropical and subtropical circulation response to GHG forcing involves atmospheric internal dynamics and ocean–atmosphere coupled processes (Figure 3.15a). The continuous increase in GHG concentrations, such as CO2 through the anthropogenic forcing, will intensify everywhere the global surface temperature by reducing the amount of outgoing longwave radiation to space, increasing the relatively humidity and static stability (Figure 3.15b). Thus, energy accumulates in the climate system and the planet warms. This will enhance the water vapor feedback (Held and Soden, 2000, 2006) as well as the

static stability of troposphere through moist adiabatic adjustment (Knutson and Manabe, 1995), heating (cooling) over the climatological descending (ascending) zones, and reduces the mean state descending (ascending) motion (Ma et al., 2012). These global-mean patterns change have large-scale impacts on the tropical troposphere circulation, where the meridional Hadley circulation acts with the Walker circulation to regulate atmospheric temperature, humidity, cloudiness, and rainfall in the tropics and subtropics trough atmospheric bridge and oceanic tunnels (Z. Liu and M. Alexander, 2007). In this sense, it has been demonstrated from observations and climate models projections that the SST increase will modify the sea level pressure, reducing the western-eastern pressure gradient in equatorial regions, especially in the Pacific and Atlantic regions, weakening the easterlies and thus slowndown the Walker circulation (DiNezio et al., 2013; Tokinaga et al., 2012; Vecchi and Soden, 2007; Vecchi et al., 2006). The weakening of the large-scale tropical circulation leads to a reduced transport of water vapor from the boundary layer to the free atmosphere (Held and Soden, 2006), thereby affecting the global water cycle. However, recent studies argued that the strength-weaken of the tropical circulation seem to follow to a large part the pre-existing dominant mode of internal variability (Bayr et al., 2014; Deser et al., 2012). In spite of that, the increasing SST will enhance the evaporative surface cooling (greater in the western than eastern equatorial regions), which leads a reduction in the zonal SST gradient, weakened the easterlies winds (Knutson and Manabe, 1995). This implies an eastward displacement of the atmospheric deep convection to central equatorial in both Pacific and Atlantic oceans. In this sense, the negative cloud-radiation-SST feedback is acting as a thermostat and regulates the maximum SST warming (Ramanathan and W. Collins, 1991), which is illustrated by our results through a negative trend in the shortwave radiation (Figures 3.8b and 3.15b). Moreover, observations reveal a widening of the tropical belt during recent decades (J. Lu et al., 2009; Seidel and Randel, 2007; Staten et al., 2018) which is projected to continue under anthropogenic forcing (Seidel et al., 2008). Notwithstanding, the poleward expansion of the tropics entails a shift of the Hadley cell, jet streams, subtropical dry zones, extratropical storm tracks and density of migratory anticyclones (Aguirre et al., 2019; Archer and Caldeira, 2008; Bender et al., 2012; Y. Hu and Fu, 2007; J. Lu et al., 2007; Tao et al., 2016). As a consequence of this expansion, an increase in the subtropical gyre is expected, including the enhance of upwelling-favorable wind over the poleward portions in the EBUS (Rykaczewski et al., 2015; D. Wang et al., 2015). This is partially supported by our results, showing an increase of the trade and coastal winds in the Pacific ocean (Figure 3.4b), but it is not clear for the Atlantic or Indian ocean, where the internal atmospheric variability seems to be important. In this framework, the wind intensification is acting to reduce

the SST warming through the heat loss by the WES-feedback in the subtropical Pacific ocean, while in the Atlantic ocean occurs the opposite (Figures 3.8d and 3.15b). Furthermore, over the Peruvian coast (northward of 20°S) our results shown a reduction in meridional winds magnitude, suggesting a future intensification of the stratification and deepening the thermocline by limiting the ocean mixing (e.g., G. Li et al., 2020), which in consequence weakens the upwelling zone. Thus, the SST warming over the Peru-Chile coasts will be driven by an adjustment of the horizontal ocean advection (Figure 3.15c) principally by Ekman currents-induced zonal advection of temperature anomalies by mean currents (Figure 3.10a-e). On the other hand, in the Atlantic ocean our results shown that the ocean advection by meridional currents is redistributing the SST warming over the subtropics regions, while in the equatorial region is a combination of both vertical and meridional advection (Figure 3.15c). In the Indian ocean, the mean evaporation and the positive Bjerknes feedback intensification will dominate substantially the future SST changes (Figures 3.6b and 3.15). The eastward displacement of the western equatorial Pacific atmospheric deep convection leads an increase in the easterlies with faster (slower) warming in the western (eastern) equatorial region and relative cooling in the eastern equatorial region, mainly through the ocean mixing and shallow thermocline (Cai et al., 2013; W. Liu et al., 2015; Luo et al., 2016; Xie et al., 2010; Zheng et al., 2013). A surface cooling off Sumatra–Java suppresses convection, cloud cover and precipitation, leading a positive trend in the shortwave radiation into the ocean (Figures 3.8b and 3.15b). Nevertheless, we have also showed that the future SST changes could be strongly modulated by the spatial patterns of the natural modes of variability (Figure 3.14). Overall, our results suggest that the ocean dynamical response to anthropogenic forcing under a warmer climate is crucial to understand the SST trend pattern formation, with an enhanced equatorial warming versus a minimum warming rate in the subtropics. Indeed, our results evoke the important role of the natural modes of variability regulating the future SST changes through atmospherics and oceanic teleconnections.

Chapter 4

Low-frequency Modulation of the Turbulent Flow in the Peru-Chile Upwelling System: The Tropical Oceanic Teleconnection

4.1 Introduction

Regional climate is driven by a combination of both local physical processes and the non-local responses to large-scale phenomena or dominant modes of climate variability. Those local and remote drivers can in particular modulate SST or oceanic heat content at regional scale, which thereby impacts regional climate through air-sea interactions. Difficulties in investigating regional climate therefore relates to the need to decipher processes acting as external forcing to the regional system, to those triggered locally by remote influences. This is a specially challenging issue in EBUS, where the turbulent flow participates to the natural variability of the oceanic circulation. In particular, since the mean circulation in EBUS is relatively much weaker than in western boundary current systems, mesoscale activity represents a salient feature of the oceanic circulation (Chaigneau et al., 2009) that can modulate significantly the mean circulation (e.g. Belmadani et al., 2017). Eddy activity in EBUS has been shown to be fueled by the instabilities of the coastal current systems (Capet et al., 2008; Colas et al., 2013, 2012; Marchesiello et al., 2003) which are themselves connected to basin scale modes of variability through oceanic teleconnection. Therefore, eddy activity in EBUS represents a conduit by which the oceanic teleconnection from remote regions could modulate the regional climate. This topic is notably relevant for addressing the issue of the impact of climate change in EBUS, because current-generation climate models used for climate prediction are not eddy-resolving, not even eddy-permitting in the mid-latitudes and beyond. As an illustration, the Figure 4.1 represents the mean EKE over the South

Hemisphere from both satellite altimeter data and a member of the CESM-LENS. Despite the strong mesoscale activity in the western boundary current system, the global coupled model is not able to reproduce, in general terms, the mean EKE south of 10°S. This points out an interesting challenge in terms of understanding the impact of the climate change on the oceanic circulation.

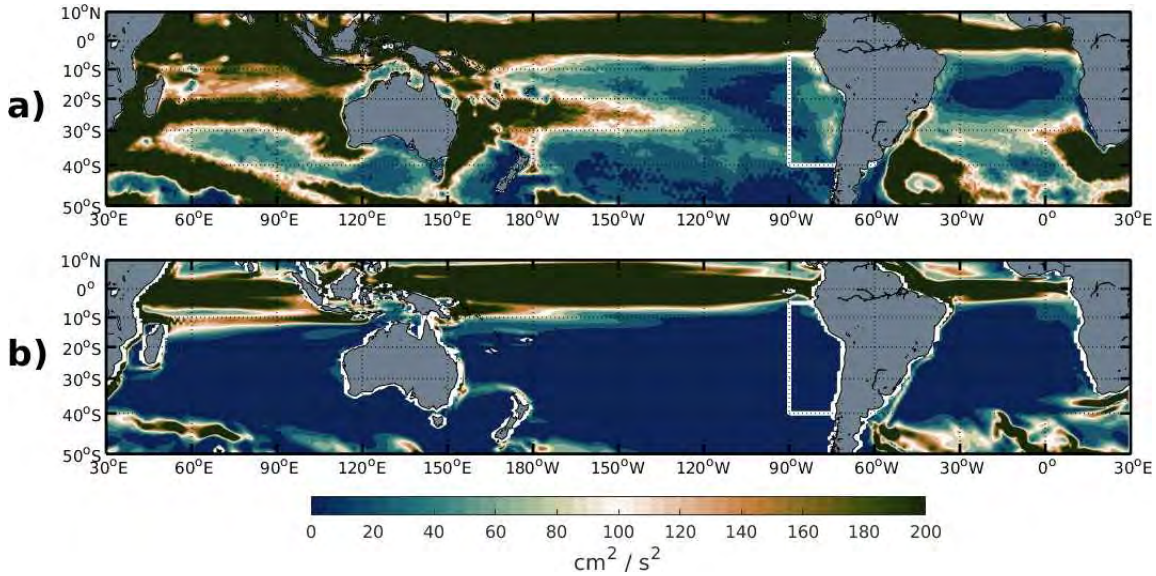

Figure 4.1: *Mean Eddy Kinetic Energy (EKE, in cm^2/s^2) from a) satellite altimeter observations (1993-2018 period), and b) CESM-LENS 40 mean-ensemble (1980-2005 period). The white rectangle corresponds to the Peru-Chile Upwelling System.*

The mesoscale eddies in EBUS can transport mass properties from the coastal region to the open ocean, such as heat content, oxygen, etc (Gruber et al., 2011). Through their connection to the equatorial current system, that usually feed the coastal circulation in EBUS, they can also carry these properties from remote regions and modify the oceanic conditions alongshore in EBUS. Given the fact that CGCMs cannot simulate realistically eddy activity in EBUS due to their low-resolution, it limits somehow confidence in their projections and also calls for better understanding how the tropical climate modes can modulate the turbulent flux in the EBUS. This is the main objective of this chapter that focuses on the Peru-Chile Upwelling System (PCUS) owing to its ideal setting. In particular, eddy activity is present along a large portion of the South American coast (see Figure 4.1a) and the PCUS is under the direct influence of the ENSO, the most important natural climate mode. Dewitte et al., 2012 showed in particular that the PCUC is modulated by ENSO, which in turn has the potential to modulate the stability of the current system and trigger eddy formation along the coast. Here our objective is to investigate such issue from a variety of data sets and

document the mechanisms associated to the oceanic teleconnection. We used in specific altimeter data, that now spans almost 30 years and sampled two strong El Niño events (1997/98 and 2015/16). Our approach is also based on the experimentation with a regional oceanic model in a forced mode and the analysis of a new resource to the community consisting in long-term (>100 years) simulations of a ultra-high resolution general circulation model.

In this chapter, we thus analyzed the low-frequency modulation of the turbulent flux in the PCUS and its connection with the equatorial Pacific current system through both observations and high-resolution modeling. The first part consists in documenting the drivers of the interannual-to-decadal variability of the mesoscale activity and their connection with the ENSO diversity during the last decades from satellite altimeter data and comparing with regional model simulations with different boundary conditions. In the second part, we take advantage of a ultra high-resolution ocean-atmosphere coupled model long-term simulation to gain confidence in the statistics and explore further the mechanisms of the modulation of mesoscale activity in the Peru upwelling system by ENSO. The last section correspond to a synthesis, followed by a discussion on expected future changes of eddy activity in the PCUS, based on the analysis of sensitivity experiments with the high-resolution climate model to CO_2 forcings.

4.2 Interannual-to-decadal variability of mesoscale eddies

ENSO is the dominant climatic phenomenon in the tropical Pacific, impacting the global atmospheric circulation and the oceanic tropical circulation. Its strongest oceanic influence is manifested in the Southeast Pacific, where the mesoscale activity is particularly intense in comparison to the other EBUS of the South Hemisphere (Figure 4.1a). In this region, mesoscale eddies have been proposed to modify the heat budget (Colas et al., 2012) that can have considerable repercussions in the tropical Pacific climate system, specially at ENSO timescales (Toniazzo, 2010). In this section, we documented the low-frequency variability of the EKE in the PCUS through satellite altimeter data and long-term regional oceanic modeling simulations. We showed that the mesoscale activity off Peru and Chile is to a large extent driven by ENSO diversity, which yields a variability in eddy activity at both interannual and decadal timescales. In particular, the interannual EKE variability is mostly associated to strong Eastern Pacific (EP) El Niño events, where the mesoscale activity tends to increase along the Peruvian coast up to northern Chile and decreases off central Chile, while it is hardly changed during Central Pacific (CP) El Niño and La Niña events. On the other hand, at decadal timescales

we observed that strong EP El Niño events can trigger decadal changes in EKE, which is not linked to the low-frequency natural mode of variability, such as the Interdecadal Pacific Oscillation. In addition, our findings reveal that such a EKE-ENSO relationship arises from the oceanic equatorial teleconnection since a model experiment for which climatological atmospheric forcing is used yields comparable results than the control run experiment. However, the magnitude of the EKE changes during strong EP El Niño events is not proportional to their strength, resulting in a non-linearity of the EKE-ENSO relationship. The complete description of our results is found below in the form of an article published in "Scientific Reports" in October 2020. Note that the "Supplementary Information" is included in Appendix A.

Citation: Conejero, C., Dewitte, B., Garçon, V., Sudre, J., and Montes, I. (2020). ENSO diversity driving low-frequency change in mesoscale activity off Peru and Chile. Scientific Reports, 10, 17902. https://doi.org/10.1038/s41598-020-74762-x

www.nature.com/scientificreports

scientific reports

Check for updates

OPEN

ENSO diversity driving low-frequency change in mesoscale activity off Peru and Chile

Carlos Conejero[1]✉, Boris Dewitte[1,2,3,4], Véronique Garçon[1], Joël Sudre[1] & Ivonne Montes[5]

Transient mesoscale oceanic eddies in Eastern Boundary Upwelling Systems are thought to strongly affect key regional scale processes such as ocean heat transport, coastal upwelling and productivity. Understanding how these can be modulated at low-frequency is thus critical to infer their role in the climate system. Here we use 26 years of satellite altimeter data and regional oceanic modeling to investigate the modulation of eddy kinetic energy (EKE) off Peru and Chile by ENSO, the main mode of natural variability in the tropical Pacific. We show that EKE tends to increase during strong Eastern Pacific (EP) El Niño events along the Peruvian coast up to northern Chile and decreases off central Chile, while it is hardly changed during Central Pacific El Niño and La Niña events. However the magnitude of the EKE changes during strong EP El Niño events is not proportional to their strength, with in particular the 1972/1973 El Niño event standing out as an extreme event in terms of EKE increase off Peru reaching an amplitude three times as large as that during the 1997/1998 El Niño event, and the 2015/2016 El Niño having instead a weak impact on EKE. This produces decadal changes in EKE, with a similar pattern than that of strong EP El Niño events, resulting in a significant negative (positive) long-term trend off Peru (central Chile).

In Eastern Boundary Upwelling Systems (EBUS), where the mean circulation is relatively weak, mesoscale eddies tend to play an important role in transporting water masses properties, from heat content to dissolved oxygen[1–4]. It has been shown that the predominant direction of propagation of mesoscale eddies is westward[5] and the total transport contribution can be comparable to that from large-scale wind and thermohaline driven circulation[6]. They can in particular rectify the mean circulation forming quasi-zonal jets or striations[7,8], which appears conspicuous in eastern boundary current systems owing to the relatively weak mean circulation[9–11]. In the Southeast Pacific, eddy activity is also suspected to have a significant contribution to the heat budget[3] with potential feedback to the tropical Pacific climate system considering the sensitivity of large scale winds to sea surface temperature (SST) in the far Eastern Pacific, in particular at El Niño-Southern Oscillation (ENSO) timescale[12,13]. The inability of low-resolution global climate models to account realistically for the eddy heat flux has been invoked as one of the reasons why these models have a persistent warm bias in EBUS[3,14]. Eddy-induced circulation was also shown to be essential for shaping the mean structure and seasonal variability in the oxygen minimum zones (OMZs) for the Southeast Pacific[15,16] and Northeast Pacific[17], with also probably important feedbacks to the climate system through their role on the biological pump. Understanding how eddy activity is modulated at climatic timescales is thus important for improving our knowledge of the circulation in EBUS and their role in the climate system, and particularly in the Southeast Pacific that is sensitive to tropical Pacific variability[18,19] and that hosts one of the largest OMZs in the world[20].

Eddies in the EBUS are generated by the instability of the coastal current system[21,22], principally by the Peru–Chile Undercurrent (PCUC) in the Southeast Pacific[22]. There, climatologically forced regional oceanic models were shown to reproduce reasonably well the observed eddy activity as measured by mean eddy kinetic energy (EKE)[3], indicating that it is dominantly associated with transient propagating eddies impacting the circulation at intraseasonal timescales of variability although eddies themselves can live longer than a few months[23,24]. This is consistent with a modeling study showing a relatively weak sensitivity of eddy activity to intraseasonal equatorial forcing[25] despite the efficient oceanic teleconnection at such a timescale[26]. This is because equatorially forced intraseasonal fluctuations in coastal currents act as a high-frequency white noise to the instability process,

[1]Laboratoire d'Etudes en Géophysique et Océanographie Spatiales (LEGOS), Toulouse, France. [2]Centro de Estudios Avanzados en Zonas Áridas (CEAZA), Coquimbo, Chile. [3]Departamento de Biología, Facultad de Ciencias del Mar, Universidad Católica del Norte, Coquimbo, Chile. [4]Millennium Nucleus for Ecology and Sustainable Management of Oceanic Islands (ESMOI), Coquimbo, Chile. [5]Instituto Geofísico del Perú (IGP), Lima, Peru. ✉email: carlos.conejero@legos.obs-mip.fr

and not as a background change over which instability characteristics (i.e. growth rate and frequency) can vary. At interannual frequency however, there are some evidences that mean EKE could be modulated by the equatorial variability. Chaigneau et al.[23] show that eddy activity (and the number of generated eddies) has significant interannual variations off the coast of Peru and Chile, although they do not correlate to the NINO3.4 index, i.e. SST anomalies averaged in the region (150°E–150°W; 5°S–5°N), the most commonly used index to measure ENSO strength. Conversely, the modeling study by Combes et al.[27] found that the generation of subsurface anticyclonic eddies off central Chile is significantly correlated with the ENSO equatorial signal, which is associated with an increase of the PCUC transport. On the other hand, the modeling study of Dewitte et al.[28], focused on the Peru region, suggested that eddy activity may be influenced by the ENSO amplitude modulation associated with the low-frequency changes in the frequency of occurrence of the two types of El Niño, that is the Eastern Pacific (EP) El Niño with maximum SST anomalies in the eastern equatorial Pacific, and the Central Pacific (CP) or Modoki El Niño with maximum SST anomalies concentrated in the central equatorial Pacific[29–32]. Besides their few numbers, the different methodological approaches and regional focus of these studies call for further investigation of the relationship between eddy activity and climate variability in this region. Here our objective is to revisit the relationship between ENSO, the dominant climate mode in the tropical Pacific, and mean EKE along the coast of Peru and Chile, taking into account the so-called ENSO diversity that broadly refers to the existence of at least two classes of El Niño events, with distinct dynamics[33] and oceanic teleconnection in the Southeast Pacific[28,34]. We take advantage of 26 years of satellite altimeter data (1993–2018) that has now sampled two strong El Niño events (1997/1998 and 2015/2016), which allows addressing the impact of extreme events and that spans almost three decades, providing also insights on decadal variability. Through high-resolution regional oceanic modeling (ROMS), we are able to expand the time period of investigation over five decades (1958–2008)[28] and address the modulation of ENSO diversity, which is an expression of the modulation in ENSO amplitude (i.e. moderate vs strong El Niño events) and patterns (CP vs EP) at decadal timescales. Regional model simulations, which include a Control Run (CR) and a sensitivity experiment to boundary forcing (Kelvin), are also used for investigating processes at work and forcing mechanisms.

Results

EKE-ENSO relationship during satellite data era. The instantaneous EKE-ENSO relationship is diagnosed from the bilinear regression of interannual EKE variability from satellite altimeter data onto two independent ENSO indices (E and C, see "Methods" section) during the 1993–2018 period. Figure 1 shows the spatial patterns of the lag-regression coefficients indicating where the maximum variation in EKE is located during either EP El Niño events (E index) and CP El Niño or La Niña events (C index). The results indicate that the region of Peru is where the regression coefficient onto the E index is the largest (see box 1 in Fig. 1a), which also corresponds to the peak in explained variance (more than 30%). Off central Chile the change in EKE due to EP El Niño is much weaker and opposite than that over the Peru region (see box 3 in Fig. 1a). 6 months prior to the peak of EP El Niño events, the mesoscale activity increases (decreases) off Peru (central Chile). As EP El Niño events develop, mesoscale activity amplifies offshore and decreases near the coast of Peru. Off central Chile, the weak reduction of EKE persists during the EP El Niño cycle. On the other hand, during CP El Niño events (Fig. 1b), mesoscale activity only increases off the Peruvian coast northward of 14°S. Southward of the Pisco region, around 15°S (see box 2 in Fig. 1b), the mesoscale activity is markedly decreased, with significantly negative values of the regression coefficient. Off central Chile, the relationship between CP El Niño and EKE is weak although a significantly positive value of the regression coefficient can be found between 25°S and 30°S in the offshore region. In order to evaluate the phase relationship between ENSO and EKE, the lagged correlation between EKE, in the region where the regression coefficient is the largest (i.e. off northern Peru, cf. box 1 in Fig. 1a), and the ENSO indices is estimated (Fig. 1c). The latter indicates that EKE is ahead of the ENSO peak by 2 months ($r = 0.86$) during EP El Niño events. Since the C index accounts for both CP and La Niña events, and that La Niña event tends to follow strong EP El Niño event, EKE reduction appears ahead of the C index by almost two years. If the correlation is performed for the 2001–2018 period, when no La Niña events were preceded by a strong El Niño event, we find that EKE increases during CP El Niño events, although the correlation is not significant at the 95% level based on a student *t* test. On the other hand, the instantaneous conditional correlation between EKE and the C index when C is negative (i.e. during La Niña events) reaches − 0.6 southward of the Pisco region (box 2), which is significant at the 95% level based on a student *t* test (see Table S1). The latter indicated that EKE decreases (increases) during CP El Niño (La Niña) events. These results reveal that EKE is modulated by EP El Niño events more than by CP El Niño or La Niña events. It is interesting to highlight that the strong 1997/1998 El Niño event is the most extreme EP event in the last 30 years, which differs in amplitude with the recently strong 2015/2016 El Niño event (Fig. S1) marked by record-breaking warm anomaly in the central Pacific. The pattern of Fig. 1a tends thus to be representative of EKE changes during the 1997/1998 El Niño events. On the other hand, the spatial pattern of EKE during the 2015/2016 El Niño event resembles that during the 2002/2003 El Niño event (Fig. S1) which is of CP type.

Interannual EKE variability dominated by EP El Niño events. In this section, model results are analyzed. We provide in the supplementary information the material for the assessment of the realism of the simulation used here to extend the observational analysis and investigate processes at work. Overall, our results indicate that despite a tendency of the model to overestimate mean EKE[16,28,34], the EKE pattern and the EKE–ENSO relationship are rather realistic (see Table S2 and Figs. S2, S3). As a further evaluation of the model skill in accounting for EKE changes at interannual timescales, we present the results of the EOF decomposition for both observations and model simulations (CR and Kelvin, see Methods section) in Fig. 2. The first EOF mode pattern explains comparable percentage of variance (40% for CR and 30% for both Kelvin and altimetric observations)

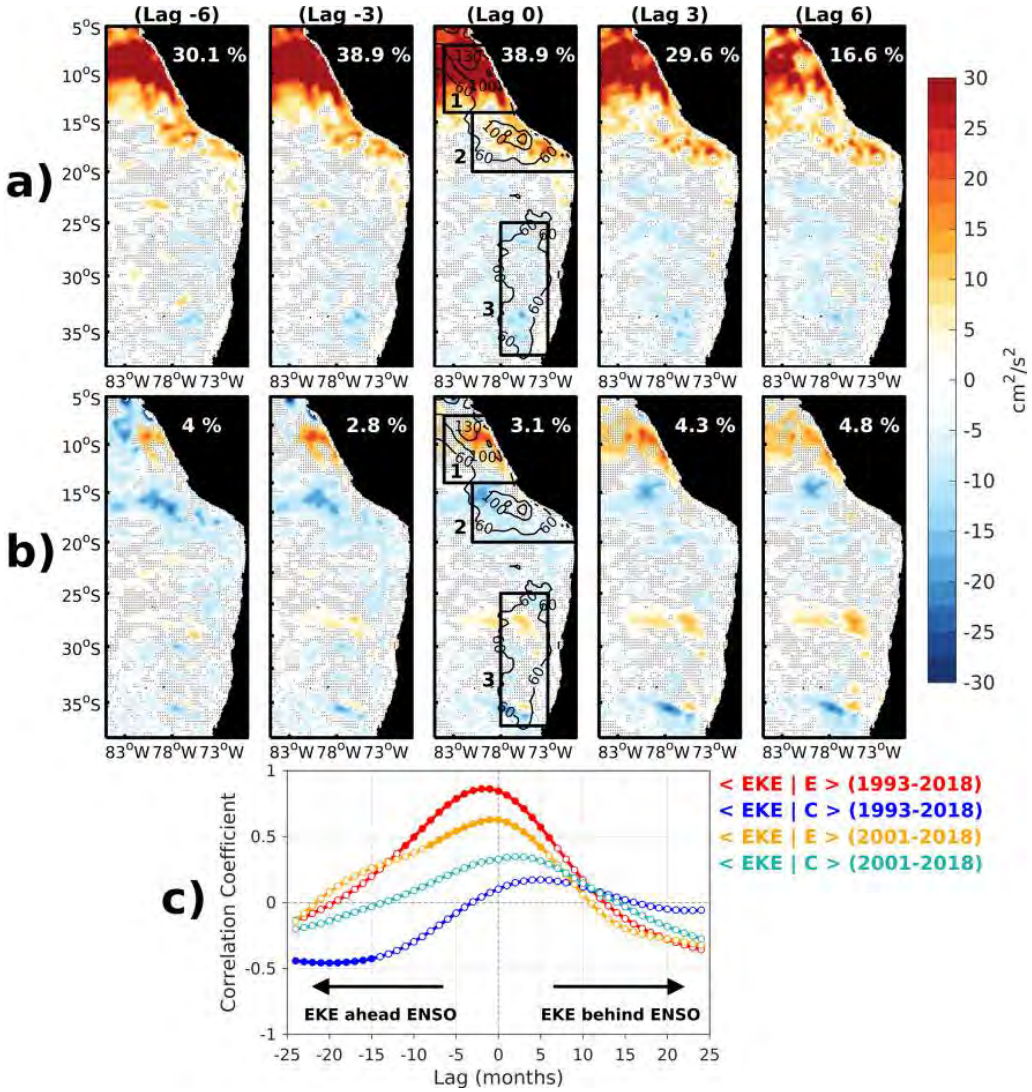

Figure 1. Regression coefficients between interannual EKE variability and the (**a**, upper panels) E index and the (**b**, middle panels) the C index for altimetric observations over the 1993–2018 period at different time lags [negative (positive) lag indicates that EKE is ahead (behind) the ENSO indices in all panels]. The boxes in the panels for lag zero correspond to the regions [northern Peru (box 1), southern Peru (box 2) and offshore central Chile (box 3)] where EKE is averaged for statistics provided in Table S1 (Supplementary Material). The percentage of explained variance averaged over the box 1 is indicated in each panel. Black contour lines (60, 100 and 130 cm^2/s^2) in the map for lag zero correspond to the mean EKE values over the whole period. Stippling indicates that regression coefficients are non-significant at the 95% confidence level based on the Student's *t* test. (**c**) Lagged-correlation between EKE averaged over the box 1 and the ENSO indices, considering different time periods. Full (white) circles indicate that correlation is significant (non-significant) at the 95% confidence level based on the Student's *t* test. Lag is in month in all panels.

and resembles the projection of EKE onto the EP mode (spatial correlation > 0.8), with EKE increasing off Peru and decreasing off central Chile. The principal components (PCs-1) account to a large extent for EP El Niño events (maximum correlation = 0.55 at lag = 2 months, PC-1 ahead the E index) for both observations and model simulations. Note that similar results were found considering EKE estimated from intraseasonal anomalous currents (see "Methods" section) indicating that these variations do arise from change in eddy activity rather than changes in large scale circulation. A striking feature of the PCs-1 from the model simulations is that the amplitude of the changes is not linearly related to the amplitude of the EP El Niño events accounted for by the E index. In particular, there is a significant change in EKE during the 1972/73 El Niño (almost three times as large than during the 1997/98 El Niño) although this event was not considered as extreme event compared to the three strong events over the period of interest[35] (i.e. 1982/1983, 1997/1998, 2015/2016). Noteworthy a similar feature

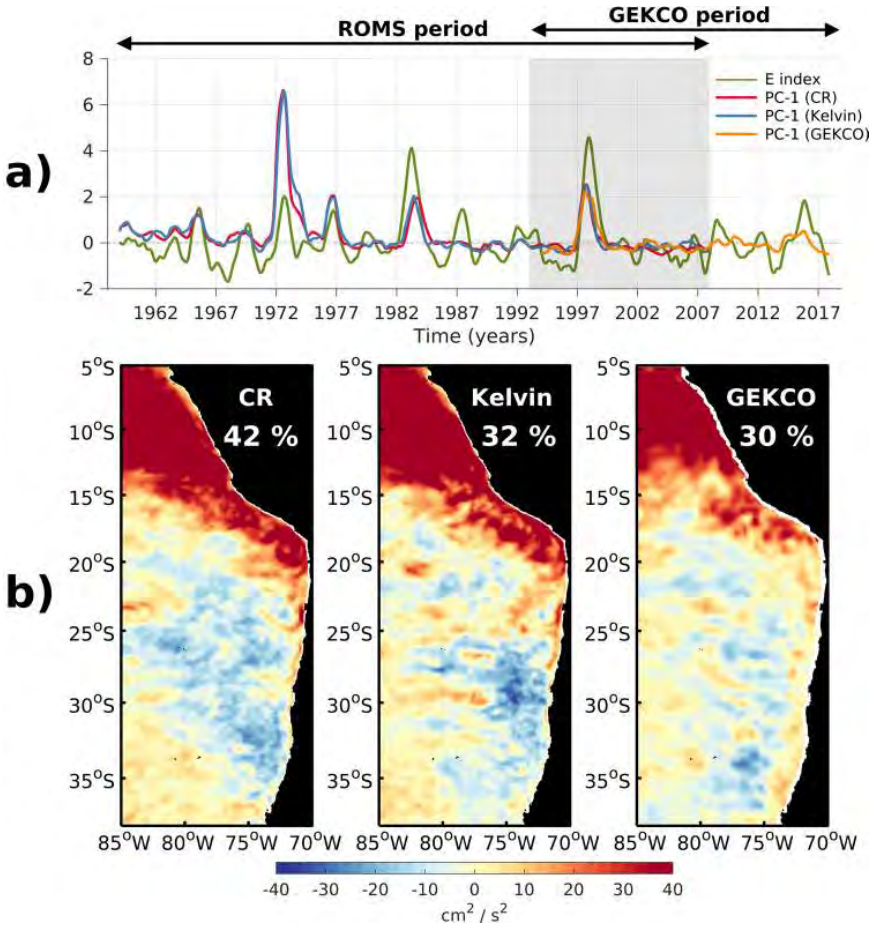

Figure 2. First EOF mode of interannual EKE variability for the model simulations (CR and Kelvin) and the altimetric observations: (**a**) Principal components (PCs) and (**b**) spatial patterns. In (**b**) from left to right, the CR, Kelvin, and altimetric observations. The EOF decomposition of performed over 1958–2008, while satellite data covers 1993–2018 period. EKE anomalies were calculated by removing the seasonal cycle computed over the same period (i.e. 1993–2008) for both satellite data and model simulations, and the pattern for observations was scaled so that CR and observation have an equal standard deviation of PC-1 for during the common period (1993–2008). Explained variance is provided in the maps. Shading in (a) indicates the common period for both observations and model simulations. The green thick line is the E index.

is found for the Kelvin simulation, which indicates that this originates from the equatorial oceanic forcing and could be related to specific ocean boundary conditions affecting the stability of the coastal current during the 1972/1973 El Niño (see below).

Decadal EKE variability. The long-term simulation offers the opportunity to document the decadal EKE variability, and supports the interpretation of the one evidenced from observations which only span 26 years. The dominant mode of decadal EKE variability for both altimetric observations and model simulations are comparable (Fig. 3). The striking feature is that the decadal mode resembles a lot the one for interannual variability in Fig. 2b (spatial correlation = 0.92). It has also a comparable amplitude, with a larger explained variance, which suggests that decadal change in EKE is probably more detectable than interannual changes, despite the fact that the amplitude of decadal SST variability is less than interannual SST variability in the Eastern tropical Pacific. The PC-1 in both CR and Kelvin simulations is associated with a long-term negative trend, which is significant at the 95% level based on a student t-test. Note that current data have been linearly detrended prior to calculating EKE (see "Methods" section) so that such a trend has to emerge from long-term changes in mean EKE. There is a tendency to have an out of phase relationship between PC-1 and the Interdecadal Pacific Oscillation (IPO) ($r = -0.52$). Although this is eroded after the climate regime shifts in 1975/76 with a tendency for a quarter-of-a-period phase shift, that is during negative IPO phases, the mesoscale eddy activity reached a maximum (minimum) in the Peru (Chile) region. The amplitude modulation is such that there is a negative

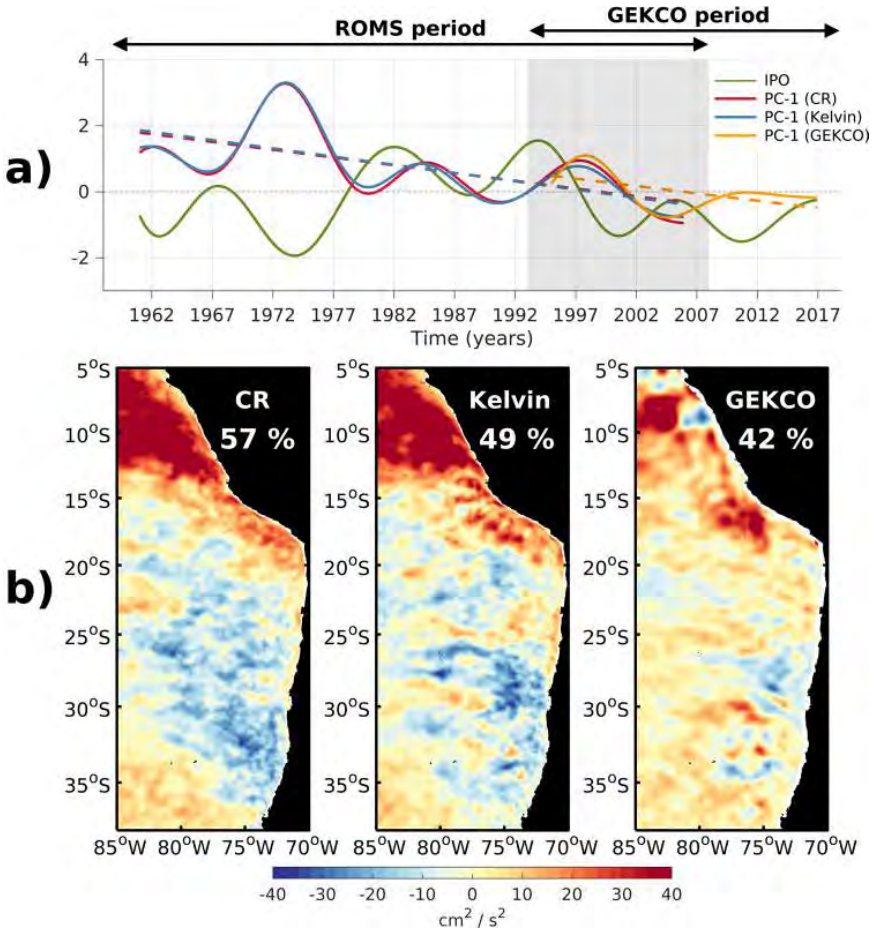

Figure 3. Same as Fig. 2 but for decadal variability. (**a**) Principal components (PCs), and (**b**) spatial patterns. The green line in (**a**) corresponds to the IPO tripole index.

trend that results in enhanced (reduced) eddy activity offshore Chile (Peru) in the last decades. Such a tendency is also suggested from observations, which results however from the large amplitude modulation (positive) of EKE during the 1997/1998 El Niño event. The similar results from both CR and Kelvin simulations suggest that the decadal modulation of eddy activity is forced at the oceanic boundaries and may result from the ENSO amplitude modulation or diversity owing to the similar patterns of the modes for interannual and decadal variability. The amplitude in decadal modulation of EKE is somewhat weaker than for interannual timescales over the domain but is as large off Peru. The analysis of the model simulations supports the interpretation of the decadal variability in the observations resulting from a physical process and not from a statistical artifact (due to the shortness of the record). The simulations suggest in particular that the negative trend in PC-1 is influenced by the large amplitude in EKE during the 1972/1973 El Niño event (see also Fig. 2a).

The 1972/73 El Niño event. While the 1972/1973 El Niño event can be considered as a strong event since it has a comparable value of the NINO3.4 index than other strong El Niño events (e.g. 1982/1983, 1997/1998 or 2015/2016) that have been recorded in the last five decades, it did not have an Eastern Pacific warming as high as in the 1982/1983 and 1997/1998 El Niño events, with an E value less than half of those years (Fig. 2a, see also Fig. S1). Still it produces the largest changes in EKE off Peru in the model simulations, which questions the extent to which this does not result from a model artifact. We thus provide here some material to support the fact that the large EKE anomalies produced during the 1972/1973 El Niño event do not result either from an unrealistic CR simulation of the circulation along the coast during this event, or from rectification processes within the model domain associated with turbulent dynamics, particularly near the western boundary of the regional model. The evaluation of the model variability was made by using sea level data from tide gauges and in-situ SST observations from HadISST3 data set (Fig. 4, see "Methods" section). The results indicate that the model is realistic and accounts for the magnitude and evolution of the 1972/1973 El Niño event along the coast of Peru

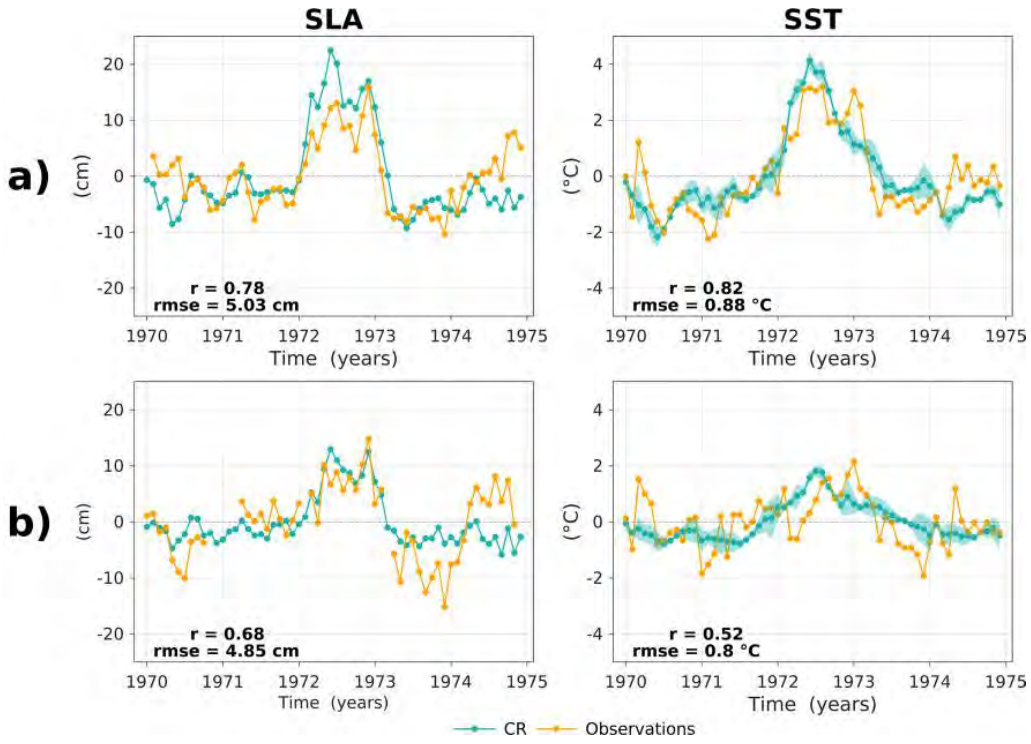

Figure 4. Evolution of sea level (SLA, left panels) and sea surface temperature (SST, right panels) anomalies from observations and the CR simulation over the 1970–1974 period at (**a**) Caldera (12°S) in Peru, and at (**b**) Antofagasta (23°S) in Chile. The correlation (r) and root mean square error (rmse) are indicated in each panel. The seasonal cycle over the period 1970–1974 was removed for both observation and model. The light shading in the curves for model SST anomalies represents the dispersion amongst the 6 values corresponding to the 5-day mean average within a month of the model outputs (i.e. ± the standard deviation amongst these 6 values).

and Chile. Further, the analysis of SODA and the CR simulation nearby the western boundary in the equatorial band indicates that the model propagates realistically the boundary condition variability into the model domain. The EOF analysis over the domain (z = [0:400 m], y = [5°S–5°N]) of zonal current anomalies from interannual to decadal variability of both SODA and CR simulation at 88°W (Fig. S4) indicates in particular a very good agreement between both the regional model solution and SODA, with the correlation of the dominant PCs reaching 0.95 and the rms difference between the spatial patterns smaller than 6 cm/s.

Whether or not the SODA data accounts realistically for the subsurface circulation in the eastern equatorial Pacific during the 1972/1973 El Niño event would need further investigation, which is difficult to address owing to the paucity of data during that period. Noteworthy similar amplitude and pattern of the zonal current anomalies in 1972/1973 were obtained from the ORA-S4 reanalysis[36] (not shown). With such limitation in mind, from our results, we can support the fact that the 1972/1973 El Niño event was associated with a large increase in EKE off Peru, suggesting a non-linear relationship between the El Niño strength as measured by SST indices and the magnitude of eddy activity changes off Peru and northern Chile (see Figs. 1c, S3). Considering the strong oceanic equatorial teleconnection at interannual timescales, essentially through the PCUC[37,38], such a non-linear response has to originate from details in the fluctuations of the equatorial current systems in the eastern equatorial region impacting the stability of the coastal current systems (see "Discussion").

Mechanisms associated with low-frequency EKE variability. As a support to the physical interpretation of the above results, the main terms of the EKE budget (see "Methods" section) were analyzed in a similar manner than for EKE. We present a section as a function of distance from the coast to offshore and latitude of the mean values of the tendency terms (Fig. 5a) in order to emphasize regional differences in their relative contributions. Figure 5a indicates that wind work (F_eK_e, Eq. 1) has a weak contribution to the eddy generation off Peru and central Chile, in contrast with the barotropic (K_mK_e, Eq. 2) or baroclinic (P_eK_e, Eq. 3) instabilities that contribute the most to EKE change in the Southeast Pacific[25], which is consistent with both CR and Kelvin simulations exhibiting very similar results at least off Peru and northern Chile. Maximum mean values of K_mK_e and P_eK_e are confined in the first 100–150 km offshore and decay westward, with two contrasted regions where their relative contribution varies meridionally: the Peru region (between 17°S–7°S) and central Chile (37°S–25°S). In the Peru region, the P_eK_e appears to be the dominant EKE generation term whereas in central Chile the three energy conversion terms have a comparable contribution. To document their low-frequency variations, an EOF analysis is performed separately over these two regions, which provides coastal profiles as dominant mode pat-

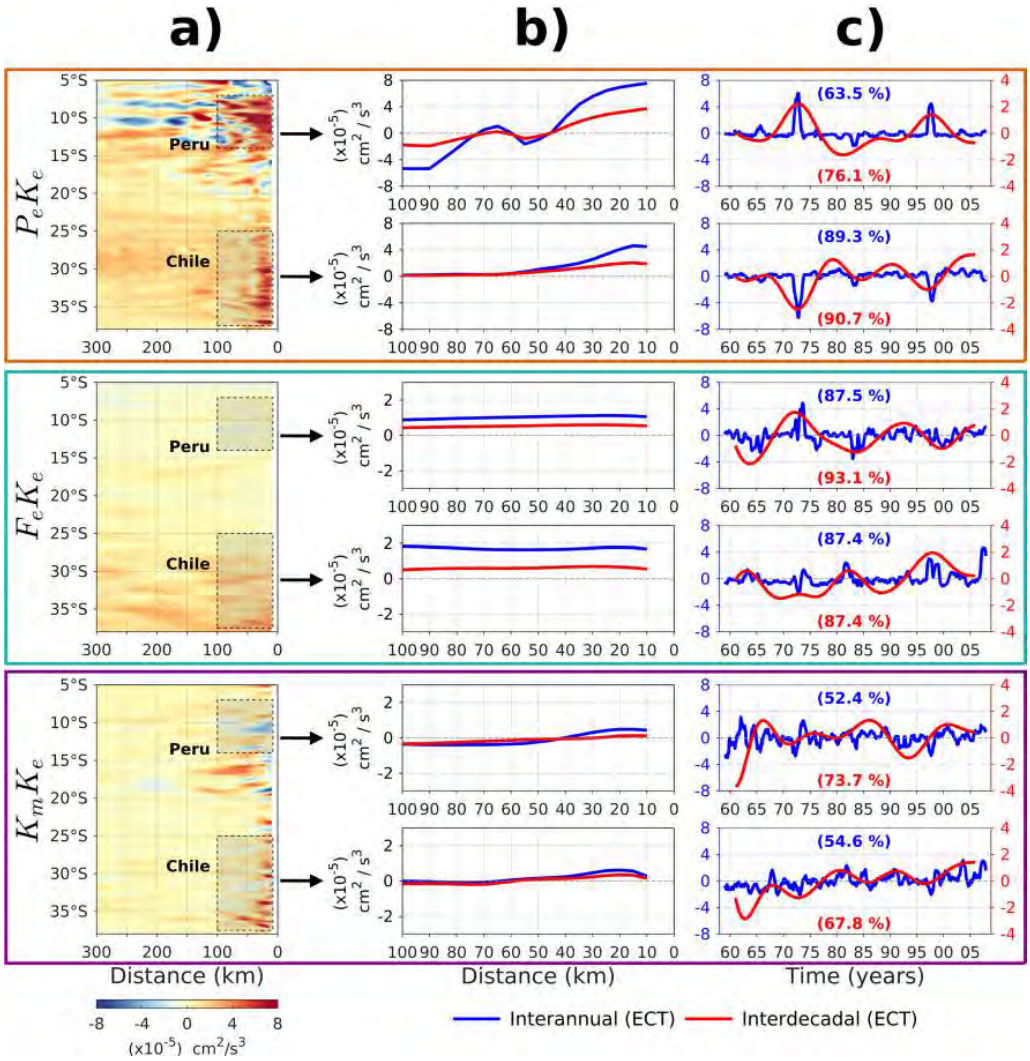

Figure 5. Energy conversion terms: baroclinic instability (P_eK_e, Eq. 3, upper panels), wind work (F_eK_e, Eq. 1, middle panels), and barotropic instability (K_mK_e, Eq. 2, lower panels) from the CR simulation over the 1958–2008 period. (**a**) Offshore distance-latitude diagram of mean values over the whole period. The coastline is considered from the 100 m isopleth, which corresponds to the vertical integration of K_mK_e and P_eK_e. (**b**) First EOF mode profiles of the energy conversion terms average over the Peru and Chile regions (see rectangles in light shading in (**a**) for the latitudinal range of the considered regions) for interannual (blue curve) and decadal (red curve) timescales. (**c**) Associated principal components. Explained variance is provided in (**c**). Note the different scales in (**b**) for P_eK_e (−8 to 8) and F_eK_e/K_mK_e (−3 to 3).

terns for both interannual and decadal timescales (Fig. 5b,c). In terms of spatial pattern and time-evolution, it is clear that EKE variations are controlled to a large extent by P_eK_e at both timescales, that exhibit the largest amplitude near the coast in both the Peru and Chile regions, meanwhile F_eK_e and K_mK_e have a much weaker amplitude (Fig. 5b). Baroclinic instabilities are generated in the first 50 km offshore, with the largest amplitude variability at interannual timescales. Note that during strong EP El Niño events the EKE increases over the Peru region, while it decreases in the central Chile. In some cases (e.g. 1972/1973 or 1997/1998), the changes are such that they impact the decadal variability and long-term tendency in EKE. This is evidenced from the results of the EOF analysis of EKE from both altimetric observations and model simulations (Figs. 2, 3) which show that both the 1972/1973 and 1997/1998 El Niño events yield a long-term negative (positive) tendency in EKE off Peru (Chile). Moreover, the analysis of the lagged-correlation between the PCs-1 of eddy conversions terms and the PC-1 of EKE at interannual to decadal variability, shows that the maximum positive/negative correlations ($|r|>0.5$) are associated with the baroclinic instability process (Fig. S5). Thus, P_eK_e fluctuations appear as the main driver of EKE changes at interannual to decadal variability in the Southeast Pacific.

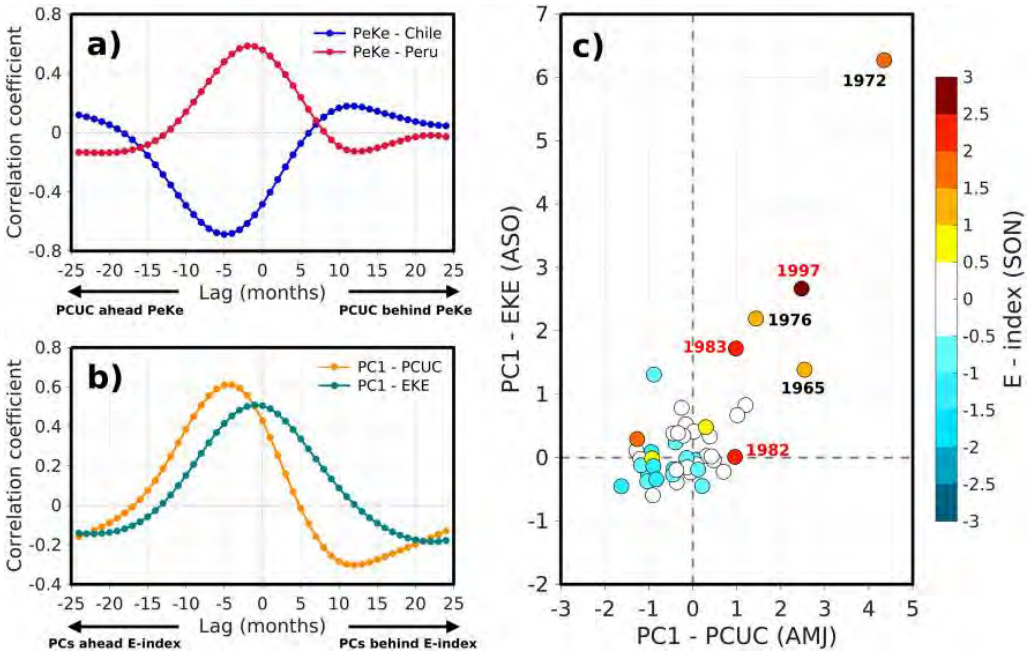

Figure 6. (**a**) Lagged-correlation between PCs of the PCUC transport (cf. Fig. S6a) and baroclinic instability (P_eK_e, cf. Fig. 5c) for the Peru (red) and Chile (blue) regions at interannual timescale. (**b**) Lagged-correlation between the E-index and PCs of the PCUC transport and EKE (cf. Fig. 2a). Lag is in months in both (**a**–**b**) panels. (**c**) Scatterplot of PC1 for the PCUC transport (AMJ: April–May–June) against PC1 for EKE (ASO: August–September–October). The selection of the 3-month period for averaging the PCs is based on (**b**) taking the lag that maximizes the correlation with a reference season in SON (September–October–November) that corresponds to the peak climatological variance for the E-index. Colour dots indicate the magnitude of the E index (color bar). The EP El Niño years are indicated near the dots. See text for the method to derive the PCUC transport.

Non-linearity of the EKE–ENSO relationship. Since baroclinic instability is generally associated with changes in the vertical shear of the coastal system currents in EBUS[21,22], it is worth documenting the PCUC transport along the coast that acts as a source of vorticity and can produce P_eK_e changes during EP El Niño event (Fig. 6). We find that the PCUC variability (as inferred from the PC-1 timeseries of the PCUC core along the coast, Fig. S6) is highly correlated (anti-correlated) with the PC1-P_eK_e over the Peruvian (Chilean) region, with PC1-PCUC ahead PC1-P_eK_e by ~ 3–5 months (maximum correlation larger than 0.5) (Fig. 6a). The phase shift relationship between PCUC transport and P_eK_e can be interpreted as resulting from the increase in PCUC during the recharge process of ENSO that peaks around 5–6 months prior to the culmination of El Niño[38] (Fig. 6b). The dominant EOF pattern for the PCUC along the coast (Fig. S6) indicates that the PCUC increases everywhere during the development of ENSO, with however significant latitudinal variability. In particular, two regions of maximum poleward PCUC transport at ~ 14°S and ~ 19°S coincide with the local maximum in EKE changes (Fig. 2), meanwhile in central Chile the PCUC transport is reduced. Note that the PCs-1 of PCUC transport and zonal currents around the equator at 88°W (see Figs. S4, S6) are highly correlated ($r > 0.70$ which is significant at the 95% level based on a student t-test) at both interannual and decadal timescales and that the rms difference of the two timeseries is weak (~ 70% of the mean rms), indicating that the PCUC transport changes are linearly associated with the changes in the equatorial circulation from the Equatorial Undercurrent (EUC) transport. The relationship between EKE changes and the E index is however highly non-linear (Fig. 6c). In particular, the 1972/73 El Niño event experiences a change in the amplitude of the PC1-EKE and PC1-PCUC that is 363.8% and 443.9% (235.4% and 175.9%) larger than that of the 1982/83 (1997/98) El Niño event, respectively, despite much weaker value of the E index (Fig. 6c). Besides, the regression coefficient between both the E index and the PC-1 for EKE is very sensitive to whether or not we exclude one of the three strong EP El Niño events from the analysis. Variations in the regression coefficient reach 60% of the mean values.

Discussion

In this paper, we documented the modulation of mesoscale activity in the Southeast Pacific at ENSO timescales through observations and long-term numerical simulations. The satellite altimeter data have now sampled two strong El Niño events, which allows getting insight into the relationship between ENSO and eddy activity. Here we address this issue aided by a previous modeling work dedicated to producing a realistic regional long-term simulation of the Southeast Pacific[28], overcoming in particular limitations in atmospheric forcing products[39,40].

The study also takes into account the ENSO diversity[33] that refers to the existence of two types of El Niño events with distinct spatial pattern and amplitude[31]. It is shown that the interannual EKE variability is mostly associated with strong EP El Niño events. The latter yields an enhanced (reduced) mesoscale activity off Peru and northern Chile (central Chile). On the other hand, during CP El Niño (La Niña) events, the mesoscale activity is hardly changed, with a weak increase (decrease) off Peru and a reduction (increase) southward of the Pisco region (15°S). While model results are consistent with our findings from altimetry, they also indicate that the EKE-ENSO relationship arises mostly from the oceanic teleconnections since the model simulation with steady atmospheric forcing (Kelvin) yields comparable results. This is consistent with ENSO-related equatorial Kelvin wave propagating along the coast modulating coastal current stability and stratification. In particular, this oceanic teleconnection is distinct for EP and CP El Niño events, which explains why CP El Niño events are not influential in EKE. First the oceanic teleconnection during CP El Niño event is much less energetic than during EP El Niño which is reflected into the magnitude of SST anomalies along the coast of Peru[28]. This is due to the fact that the energy of the equatorial Kelvin waves during CP El Niño is less than during EP El Niño and they cannot propagate far into the eastern equatorial Pacific, because they encounter a density front near 120°W along the equator associated with the sloping thermocline and dissipate there[41]. Second, the energy of equatorial Kelvin waves during CP El Niño events peaks in the intraseasonal frequency band (i.e., periods between 30 and 90 days) so that they are trapped along the coast, conversely to equatorial Kelvin waves at interannual timescales that radiate as extra-tropical Rossby waves once they reach the South-American coast[26]. This trapping makes that they are much less influential on the baroclinic instability process[25]. This interpretation is confirmed by the results of the EKE budget that indicates that the baroclinic instabilities are modulated at interannual to decadal timescales. The results also suggest a significant non-linearity in the relationship between the amplitude of ENSO (as measured by SST anomalies) and the EKE changes. For example, the model suggests that the 1972/1973 El Niño yielded the strongest EKE change off Peru, while the altimeter observations indicate that EKE was weakly impacted during the strong 2015/2016 El Niño, although these two events have a comparable amplitude in terms of the E index (Fig. S1a) and had a comparable seasonal evolution[35]. Large EKE changes during the 1972/1973 and 1997/1998 El Niño events also appear to rectify on the decadal variability (Fig. 5c), yielding a negative (positive) long-term tendency in EKE off Peru (central Chile). This points out to the likely importance of details in the dynamics of El Niño events in modulating the eddy flux off the coast of Peru. In particular, the 2015/2016 El Niño event with a comparable value of the NINO3.4 index at its peak phase than previous strong events, which was favored by the build-up of heat content[42] back to the beginning of 2014, has been classified as a strong EP El Niño event. However it was not as strong in the far Eastern Pacific due to air-sea feedbacks off Peru that damped its growth in the far Eastern Pacific[35] and its dynamics shared characteristics of that of a CP El Niño event[43]. This may explain its weak impact on EKE and its similarity with CP El Niño event in terms of its impact in EKE off Peru. Another interesting case occurs with the 2017 coastal El Niño event that has recently drawn the interest of the community[44,45]. This event yielded heavy rainfall along the coast of Northern Peru comparable to that of the 1997/1998 El Niño event[46]. This event was characterized by a localized strong warming off the coast of Peru while the central equatorial Pacific experiences near-normal (slightly cooler) conditions. Interestingly, it also was associated to a relatively weak negative EKE anomaly off Peru (see Figs. 2, S7). Model results suggest that this event was triggered by a relatively weak amplitude downwelling oceanic equatorial Kelvin wave combined to anomalous northerly coastal winds[45]. The latter may have resulted from the local atmospheric response to the developing warm coastal SST anomalies, when the climatological southward branch of the intertropical convergence zone starts to develop, i.e. from February-March[45,47,48]. On the other hand, the 1972/1973 El Niño event is associated with a record EKE increase off Peru despite its similarity with the 2015/2016 El Niño event in terms of its magnitude in the far Eastern Pacific[35]. This extreme event in EKE (i.e. 1972/1973) yields a long-term negative trend in EKE off Peru. Similarly, the observational record evidences a significant decreasing trend in EKE due to the large positive anomaly during the 1997/1998 El Niño event. This indicates that strong EP events have the ability to produce decadal changes in EKE not necessarily related to natural mode of decadal variability in the Southeast Pacific like the IPO. We find a weak correlation between the IPO index and the PC-1 timeseries associated with decadal variability in EKE (see Fig. 3a). While the model experiment was not specifically designed to investigate decadal variability, which could explain the relatively weak correlation, our result suggests that decadal variability in EKE could arise from the rectified effect of strong EP El Niño in EKE. The results suggest in particular that strong EP El Niño events that take place every decade or so, can produce energetic "spikes" in the eddy flow through the baroclinic instability that have a residual on the long-term mean (Fig. 5c, top panel), yielding the decadal change in EKE. In other words, EP El Niño events energize EKE decadal variance acting as a red noise process[49]. The reasons why there is a diversity in the response of EKE to strong EP El Niño events would deserve further investigation. At this stage we can speculate that the impact of strong EP El Niño on EKE changes along the coast of South America depends on mean state conditions along the coast of Peru and Chile. In particular, the 1972/1973 El Niño event took place prior to the 1976/1977 climate shift when the mean state was relatively cooler, which may have preconditioned the coastal current system towards being unstable and thus more sensitive to ENSO-induced fluctuations of the PCUC. Although decadal variability in the model simulations maybe biased due to limitations in the atmospheric forcing[39] that may underestimate in particular the contribution of IPO-induced winds, we find that in both experiments that the baroclinic instability was also reduced from before and after the 1976/1977 climate shifts (i.e. P_eK_e over 1958–1975 is 45.8% (86.2%) larger than over 1978–2008 over the Peru domain in CR (Kelvin) simulation), which is consistent with this hypothesis. We also note that in the regional simulations, the PCUC transport changes during the 1972/1973 El Niño are twice as large as during the 1997/1998 El Niño event (Fig. 6c), which could also explain the large EKE change during that event. This large PCUC transport is associated with a large EUC anomaly at 88°W in the boundary oceanic conditions (Fig. S6) and is ahead the peak of the 1972/1973 El Niño by ~ 2 months. This indicates that the 1972/1973 El Niño event was associated with a significant recharge process, comparable to that of the 1997/1998

El Niño event (Fig. S8), although the processes that yielded the increase in heat content were certainly different[50]. This strong recharge may thus explain the large PCUC anomalies during this particular event observed in the simulations. During the recharge process of ENSO (i.e. 9 to 6 months prior to the ENSO peak), the zonal pressure gradient across the equator is enhanced, which is associated to an overall increase in the equatorial trade winds[51]. This tends to increase the EUC transport which variability is correlated to the PCUC anomaly at seasonal and interannual timescales[37]. However the EUC is not directly connected to the PCUC. Montes et al.[52] show that in fact the PCUC is predominantly fed by two narrow eastward subsurface currents (also known as Tsuchiya jets) at ~ 3–4°S (primary) and 7–8°S (secondary), which dynamics are highly non-linear[53]. The recharge process also involved non-linear processes[54] and can be influenced by atmospheric high-frequency noise[55] so that the relationship between both the ENSO recharge and the EUC, and between the EUC and the PCUC may deviate from linearity.

While we have focused here on surface EKE taking advantage of altimeter data, model studies[27,56] and *in-situ* observations[24,57] suggest that subsurface eddies or "Intrathermocline Eddies" (ITEs), also called Puddies[58], exist in the Southeast Pacific which tend to be anticyclonic. These eddies have a weaker surface signature and are thus not well observed by altimetry, although they represent a significant source of natural variability in the euphotic layer. They are also thought to be connected to the variability of the PCUC[56], which suggests that their activity could be also modulated by strong EP El Niño events. In particular we find that in the model, EKE off central Chile increases at 200 m during strong EP El Niño (Fig. S9) while it decreases at the surface, suggesting that ITEs are favored during strong El Niño conditions, a result consistent with Combes et al.[27]. This has clear implications for the understanding of the natural variability of the OMZ in the Southeast Pacific since these subsurface eddies, with their core closer to the oxycline, can transport offshore water masses properties and thus modulate the OMZ. Such a process of ENSO-induced variability of the OMZ would deserve further study from the same experimental set up used here[16], which is planned for future work.

Methods

Sea level and sea surface temperature data. We use sea surface height from the GEKCO[59] (Geostrophic and EKman Current Observatory) product to estimate the surface geostrophic EKE. This data set is based on altimetric data from DUACS (Data Unification and Altimeter Combination System) of AVISO (Archiving, Validation and Interpretation of Satellite Oceanographic data). Data are globally gridded from 1993 to present as daily values with a spatial resolution of 1/4°. We also use sea level anomaly (SLA) data and SST anomalies to validate the model simulation over the period prior to the satellite era. SLA data from tide gauge was provided by the UHSLC (University of Hawaii Sea Level Center), while SST data was obtained from HadSST3[60,61] (Hadley Centre Global Sea Surface Temperature version 3), which provides monthly uninterpolated SST anomalies in 5° × 5° grid box for 1850-present. The anomalies are relative to a 30-year climatology spanning 1961–1990. HadSST3 is based on *in-situ* measurements of SST from ships and buoys.

Model simulations. A long-term simulation with the ROMS[62] (Regional Ocean Modelling System) model is used over the 1958–2008 period developed in Dewitte et al.[28]. This model configuration, which is used as a Control Run (CR) simulation, has a horizontal resolution of 1/12° at the equator, covering the domain extending from 12°N to 40°S, and from the coast to 88°W. 5-daily mean oceanic outputs from SODA (Simple Ocean Data Assimilation, version 2.1.6) provide the open boundary conditions (OBC) for temperature, salinity, horizontal velocity and sea level. To force the regional model at the air/sea interface, wind speed and wind stress from the downscaled product[39] were used, which was shown to provide realistic forcing from atmospheric reanalysis that generally do not resolve properly near-shore winds[63]. Atmospheric fluxes were derived from the bulk formula using the air temperature from COADS[64] (Comprehensive Ocean–Atmosphere Data Set) 1° monthly climatology. The reader is invited to refer to Dewitte et al.[28], Vergara et al.[16,34], Pizarro-Koth et al.[65], and to supplementary information for more details on the model description, skill and validation. To evaluate the impact of equatorial forcing onto EKE variability, a sensitivity experiment to atmospheric forcing was performed. This experiment, called Kelvin, consists in using the same oceanic boundary conditions than CR simulation but using a wind forcing corresponding to the 2005 year repeated each year. This 2005 year is selected as a "normal" year in terms of surface atmospheric circulation in the SEP despite the development of a CP El Niño event in 2004. This Kelvin simulation allows assessing the role of the equatorial oceanic forcing on the EKE modulation off the Peru–Chile coasts.

El Niño and decadal variability indices. The two El Niño indices defined by Takahashi et al.[31] are used, that are based in the principal components time series associated with the first two EOF modes of the monthly mean SST anomalies in the tropical Pacific (see Fig. S1a). The SST data are from the ERSST.v3b[66] (Extended Reconstructed Sea Surface Temperature) product of NOAA (National Oceanic and Atmospheric Administration) over the 1958–2018 period. The two uncorrelated indices are well suited for describing the so-called ENSO diversity[33] by accounting for the variability of Eastern Pacific El Niño (E-index) and Central Pacific El Niño and/or La Niña (C-index). In addition, the Tripole Index for the Interdecadal Pacific Oscillation (IPO) was obtained from NOAA/ERSST.v3b over the same period (see Fig. S1a). The index is based on the difference between the SST anomalies averaged over the central equatorial Pacific and the average of the SST anomalies in the Northwest and Southwest Pacific[67]. Note that both ENSO and IPO indices obtained from observations are very close to those obtained from SODA reanalysis (correlation is above 0.9 for all indices), which was used as an OBC in the regional model.

Quantifying variability in eddy activity. Most of the existing literature on mesoscale activity in the Southeast Pacific has used geometric methods to count the number of mesoscale structure either directly from dynamic height data or estimate of vorticity[5,23,68]. While these studies provide key information on eddy activity, methodological[69] and observational[70] limitations remain. Here, for simplicity and to avoid comparing different methodological approaches, mesoscale activity is measured from the estimate of EKE (estimated as $EKE = (u'_g{}^2 + v'_g{}^2)/2$), which represents a physically-based metrics that obeys a tracer equation and thus can be objectively interpreted from theory. The EKE was obtained from 5-days detrended surface geostrophic currents anomalies (u'_g, v'_g), which are derived from sea surface height. Interannual anomalies were computed from 5-days mean outputs removing the monthly climatology interpolated at 5-days temporal resolution. Then, mean EKE over 3-months running windows followed by a monthly average is estimated, providing series of monthly "mean EKE", which we refer as just EKE. The seasonal cycle from monthly EKE was further removed to derive EKE anomalies. Intraseasonal anomalies in the velocity field were also considered to derive EKE anomalies to filter out the contribution of changes in the circulation at interannual timescale. The intraseasonal anomalies consist of the departure from the monthly mean following previous studies[71,72]. In either case, a 1-year running mean filter is further applied on the resulting anomalies to filter out remaining high-frequency variations associated with the low-frequency modulation of the seasonal cycle. The obtained interannual EKE field is then analyzed through regressing on indices and/or EOF decomposition. For addressing decadal EKE variability, a butterworth filter (order 5 with a 10 years cut-off period) is used.

EKE budget. The contribution of each EKE generation process is evaluated from the regional model based on the tracer equation for EKE. We focus here on the energy conversion terms relevant to nearshore following previous studies[21,25]: wind work (F_eK_e, Eq. 1), barotropic instability (K_mK_e, Eq. 2) and baroclinic instability (P_eK_e, Eq. 3). F_eK_e represents the transfer of energy from surface wind-forcing anomalies to EKE, K_mK_e corresponds to the barotropic conversion of mean kinetic energy (K_m) into EKE, and P_eK_e corresponds to the baroclinic conversion of eddy potential energy (P_e) into EKE. From the horizontal equation of motion, one can derive the expressions:

$$F_eK_e = \langle \frac{1}{H\rho_0}\left(u'\tau_x{}' + v'\tau_y{}'\right)\rangle \tag{1}$$

$$K_mK_e = \langle \frac{-1}{H}\int_H^0 \left(u'u'\frac{\partial \overline{u}}{\partial x} + u'v'\frac{\partial \overline{u}}{\partial y} + u'w'\frac{\partial \overline{u}}{\partial z} + v'u'\frac{\partial \overline{v}}{\partial x} + v'v'\frac{\partial \overline{v}}{\partial y} + v'w'\frac{\partial \overline{v}}{\partial z}\right)dz\rangle \tag{2}$$

$$P_eK_e = \langle \frac{-g}{H\rho_0}\int_H^0 \left(\rho'w'\right)dz\rangle \tag{3}$$

where wind stress (τ_x,τ_y), velocity field (u,v,w) and density (ρ) variables with prime stand for the anomalies relative to the mean climatology (overbar) calculated over the 1958–2008 period. Since we are interested here in the modulation of these terms at interannual timescales, the brackets stand for the mean over a 3-month running windows to capture transient eddy effect on EKE rate of change. For methodological consistency, anomalies were then calculated in a similar manner than EKE. The constant variables are the gravitational acceleration ($g = 9.8196$ m/s^2) and the reference water density ($\rho_0 = 1025$ g/L). K_mK_e and P_eK_e were integrated over the surface layer depth ($H = 100$ m), where the instabilities in the Southeast Pacific are confined[3,25] and can be directly comparable to wind work.

Peru–Chile undercurrent (PCUC) transport. The integrated poleward transport of the PCUC was calculated considering the average of along-shore southward current over the area coinciding with the mean position of the PCUC, as inferred from cross-shelf sections along the coasts (see Fig. S10). We considered a rectangular box approximating the vertical extension of the PCUC ranging from 60 to 400 m depth, and its cross-shelf extension, spanning from the coast to ~ 100 km. Furthermore, current speeds smaller than 2 cm/s were not considered in the poleward transport calculation. The use of slightly different boxes size did not change the variability of the transport.

Received: 3 January 2020; Accepted: 5 October 2020
Published online: 21 October 2020

References

1. Rossi, V. *et al.* Surface mixing and biological activity in the four Eastern Boundary Upwelling Systems. arXiv Prepr. arXiv0909.0115 (2009).
2. Gruber, N. *et al.* Eddy-induced reduction of biological production in eastern boundary upwelling systems. *Nat. Geosci.* **4**, 787–792 (2011).
3. Colas, F., McWilliams, J. C., Capet, X. & Kurian, J. Heat balance and eddies in the Peru–Chile current system. *Clim. Dyn.* **39**, 509–529 (2012).
4. Stramma, L., Bange, H. W., Czeschel, R., Lorenzo, A. & Frank, M. On the role of mesoscale eddies for the biological productivity and biogeochemistry in the eastern tropical Pacific Ocean off Peru. *Biogeosciences (BG)* **10**, 7293–7306 (2013).

5. Chelton, D. B., Schlax, M. G. & Samelson, R. M. Global observations of nonlinear mesoscale eddies. *Prog. Oceanogr.* **91**, 167–216 (2011).
6. Zhang, Z., Wang, W. & Qiu, B. Oceanic mass transport by mesoscale eddies. *Science (80-.)* **345**, 322–324 (2014).
7. Schlax, M. G. & Chelton, D. B. The influence of mesoscale eddies on the detection of quasi-zonal jets in the ocean. *Geophys. Res. Lett.* **35**, 1–5 (2008).
8. Buckingham, C. E. & Cornillon, P. C. The contribution of eddies to striations in absolute dynamic topography. *J. Geophys. Res. Ocean.* **118**, 448–461 (2013).
9. Maximenko, N. A., Melnichenko, O. V, Niiler, P. P. & Sasaki, H. Stationary mesoscale jet-like features in the ocean. *Geophys. Res. Lett.***35**, L08603 (2008).
10. Wang, J., Spall, M. A., Flierl, G. R. & Malanotte-Rizzoli, P. Nonlinear radiating instability of a barotropic eastern boundary current. *J. Phys. Oceanogr.* **43**, 1439–1452 (2013).
11. Belmadani, A. *et al.* Striations and preferred eddy tracks triggered by topographic steering of the background flow in the eastern South Pacific. *J. Geophys. Res. Ocean.* **122**, 2847–2870 (2017).
12. Toniazzo, T. Climate variability in the south-eastern tropical Pacific and its relation with ENSO: A GCM study. *Clim. Dyn.* **34**, 1093–1114 (2010).
13. Takahashi, K. & Dewitte, B. Strong and moderate nonlinear El Niño regimes. *Clim. Dyn.* **46**, 1627–1645 (2016).
14. Richter, I. Climate model biases in the eastern tropical oceans: Causes, impacts and ways forward. *Wiley Interdiscip. Rev. Clim. Chang.* **6**, 345–358 (2015).
15. Montes, I. *et al.* High-resolution modeling of the Eastern Tropical Pacific oxygen minimum zone: Sensitivity to the tropical oceanic circulation. *J. Geophys. Res. Ocean.* **119**, 5515–5532 (2014).
16. Vergara, O. *et al.* Seasonal variability of the oxygen minimum zone off Peru in a high-resolution regional coupled model. *Biogeosciences* **13**, 4389–4410 (2016).
17. Margolskee, A., Frenzel, H., Emerson, S. & Deutsch, C. Ventilation pathways for the North Pacific Oxygen Deficient Zone.*Glob. Biogeochem. Cycles* **33**, 875–890 (2019).
18. Sprintall, J., Cravatte, S., Dewitte, B., Du, Y. & Sen Gupta, A. Oceanic Teleconnections. in El Niño in a Changing Climate (eds. McPhaden, M. J., Santoso, A. & Cai, W.) Ch. 15 (Wiley, Hoboken, New Jersey, 2020).
19. Pizarro, O. & Montecinos, A. Interdecadal variability of the thermocline along the west coast of South America (2004). https://doi.org/10.1029/2004GL020998.
20. Paulmier, A. & Ruiz-Pino, D. Oxygen minimum zones (OMZs) in the modern ocean. *Prog. Oceanogr.* **80**, 113–128 (2009).
21. Marchesiello, P., McWilliams, J. C. & Shchepetkin, A. Equilibrium structure and dynamics of the California Current System. *J. Phys. Oceanogr.* **33**, 753–783 (2003).
22. Capet, X., Colas, F., McWilliams, J. C., Penven, P. & Marchesiello, P. Eddies in eastern boundary subtropical upwelling systems. *Ocean Model. Eddying Regime Geophys. Monogr. Ser* **177**, 131–147 (2008).
23. Chaigneau, A., Eldin, G. & Dewitte, B. Eddy activity in the four major upwelling systems from satellite altimetry (1992–2007). *Prog. Oceanogr.* **83**, 117–123 (2009).
24. Cornejo D'Ottone, M. *et al.* Biogeochemical characteristics of a long-lived anticyclonic eddy in the eastern South Pacific Ocean. *Biogeosciences (BG)* **13**, 2971–2979 (2016).
25. Belmadani, A., Echevin, V., Dewitte, B. & Colas, F. Equatorially forced intraseasonal propagations along the Peru–Chile coast and their relation with the nearshore eddy activity in 1992–2000: A modeling study. *J. Geophys. Res. Ocean.***117**, C04025 (2012).
26. Clarke, A. J. & Shi, C. Critical frequencies at ocean boundaries. *J. Geophys. Res. Ocean.* **96**, 10731–10738 (1991).
27. Combes, V., Hormazabal, S. & Di Lorenzo, E. Interannual variability of the subsurface eddy field in the Southeast Pacific. *J. Geophys. Res. Ocean.* **120**, 4907–4924 (2015).
28. Dewitte, B. *et al.* Change in El Niño flavours over 1958–2008: Implications for the long-term trend of the upwelling off Peru. *Deep Sea Res. Part II Top. Stud. Oceanogr.* **77**, 143–156 (2012).
29. Ashok, K., Behera, S. K., Rao, S. A., Weng, H. & Yamagata, T. El Niño Modoki and its possible teleconnection. *J. Geophys. Res. Ocean.***112**, C11007 (2007).
30. Kug, J.-S., Jin, F.-F. & An, S.-I. Two types of El Niño events: Cold tongue El Niño and warm pool El Niño. *J. Clim.* **22**, 1499–1515 (2009).
31. Takahashi, K., Montecinos, A., Goubanova, K. & Dewitte, B. ENSO regimes: Reinterpreting the canonical and Modoki El Niño. *Geophys. Res. Lett.***38**, L10704 (2011).
32. Wang, D., Qin, Y., Xiao, X., Zhang, Z. & Wu, X. E. Niño and El Niño Modoki variability based on a new ocean reanalysis. *Ocean Dyn.* **62**, 1311–1322 (2012).
33. Capotondi, A. *et al.* Understanding ENSO diversity. *Bull. Am. Meteorol. Soc.* **96**, 921–938 (2015).
34. Vergara, O., Dewitte, B., Ramos, M. & Pizarro, O. Vertical energy flux at E NSO time scales in the subthermocline of the Southeastern Pacific. *J. Geophys. Res. Ocean.* **122**, 6011–6038 (2017).
35. Dewitte, B. & Takahashi, K. Diversity of moderate El Niño events evolution: role of air–sea interactions in the eastern tropical Pacific. *Clim. Dyn.* **52**, 7455–7476 (2019).
36. Balmaseda, M. A., Mogensen, K. & Weaver, A. T. Evaluation of the ECMWF ocean reanalysis system ORAS4. *Q. J. R. Meteorol. Soc.* **139**, 1132–1161 (2013).
37. Pizarro, O., Shaffer, G., Dewitte, B. & Ramos, M. Dynamics of seasonal and interannual variability of the Peru–Chile Undercurrent. *Geophys. Res. Lett.* **29**, 21–22 (2002).
38. Pizarro, O., Clarke, A. J. & El Van Gorder, S. Niño sea level and currents along the South American coast: Comparison of observations with theory. *J. Phys. Oceanogr.* **31**, 1891–1903 (2001).
39. Goubanova, K. *et al.* Statistical downscaling of sea-surface wind over the Peru–Chile upwelling region: Diagnosing the impact of climate change from the IPSL-CM4 model. *Clim. Dyn.* **36**, 1365–1378 (2011).
40. Astudillo, O. *et al.* Surface winds off Peru–Chile: Observing closer to the coast from radar altimetry. *Remote Sens. Environ.* **191**, 179–196 (2017).
41. Mosquera-Vásquez, K., Dewitte, B. & Illig, S. The Central Pacific El Niño intraseasonal Kelvin wave. *J. Geophys. Res. Ocean.* **119**, 6605–6621 (2014).
42. Levine, A. F. Z. & McPhaden, M. J. How the July 2014 easterly wind burst gave the 2015–2016 El Niño a head start. *Geophys. Res. Lett.* **43**, 6503–6510 (2016).
43. Paek, H., Yu, J. Y. & Qian, C. Why were the 2015/2016 and 1997/1998 extreme El Niños different?. *Geophys. Res. Lett.* **44**, 1848–1856 (2017).
44. Garreaud, R. D. A plausible atmospheric trigger for the 2017 coastal El Niño. *Int. J. Climatol.* **38**, e1296–e1302 (2018).
45. Peng, Q., Xie, S. P., Wang, D., Zheng, X. T. & Zhang, H. Coupled ocean-atmosphere dynamics of the 2017 extreme coastal El Niño. *Nat. Commun.* **10**, 1–10 (2019).
46. Takahashi, K. *et al.*The 2017 coastal El Niño [in "State of the Climate in 2017"]. *Bull. Am. Meteorol. Soc.***99**, Si–S310 (2018).
47. Takahashi, K. & Martínez, A. G. The very strong coastal El Niño in 1925 in the far-eastern Pacific. *Clim. Dyn.* **52**, 7389–7415 (2019).
48. Xie, S. P. *et al.* Eastern pacific ITCZ dipole and ENSO diversity. *J. Clim.* **31**, 4449–4462 (2018).
49. Frankignoul, C. & Hasselmann, K. Stochastic climate models, Part II Application to sea-surface temperature anomalies and thermocline variability. *Tellus* **29**, 289–305 (1977).

50. Hong, L. & Jin, F. A southern hemisphere booster of super El Niño. *Geophys. Res. Lett.* **41**, 2142–2149 (2014).
51. Ren, H. L. & Jin, F. F. Recharge oscillator mechanisms in two types of ENSO. *J. Clim.* **26**, 6506–6523 (2013).
52. Montes, I., Colas, F., Capet, X. & Schneider, W. On the pathways of the equatorial subsurface currents in the eastern equatorial Pacific and their contributions to the Peru–Chile Undercurrent. *J. Geophys. Res. Ocean.* **115**, 1–16 (2010).
53. Furue, R., McCreary, J. P., Yu, Z. & Wang, D. Dynamics of the southern Tsuchiya jet. *J. Phys. Oceanogr.* **37**, 531–553 (2007).
54. Lengaigne, M. *et al.* Mechanisms controlling warm water volume interannual variations in the equatorial Pacific: Diabatic versus adiabatic processes. *Clim. Dyn.* **38**, 1031–1046 (2012).
55. McGregor, S., Timmermann, A., Jin, F. F. & Kessler, W. S. Charging El Niño with off-equatorial westerly wind events. *Clim. Dyn.* **47**, 1111–1125 (2016).
56. Contreras, M., Pizarro, O., Dewitte, B., Sepulveda, H. H. & Renault, L. Subsurface mesoscale eddy generation in the ocean off central Chile. *J. Geophys. Res. Ocean* **124**, 5700–5722 (2019).
57. Hormazabal, S. *et al.* Intrathermocline eddies in the coastal transition zone off central Chile (31–41 S). *J. Geophys. Res. Ocean.* **118**, 4811–4821 (2013).
58. Frenger, I. *et al.* Biogeochemical role of subsurface coherent eddies in the ocean: Tracer cannonballs, hypoxic storms, and microbial stewpots?. *Glob. Biogeochem. Cycles* **32**, 226–249 (2018).
59. Sudre, J., Maes, C. & Garçon, V. On the global estimates of geostrophic and Ekman surface currents. *Limnol. Oceanogr. Fluids Environ.* **3**, 1–20 (2013).
60. Kennedy, J. J., Rayner, N. A., Smith, R. O., Parker, D. E. & Saunby, M. Reassessing biases and other uncertainties in sea surface temperature observations measured in situ since 1850: 2. Biases and homogenization. *J. Geophys. Res. Atmos.***116**, D14104 (2011).
61. Kennedy, J. J., Rayner, N. A., Smith, R. O., Parker, D. E. & Saunby, M. Reassessing biases and other uncertainties in sea surface temperature observations measured in situ since 1850: 1. Measurement and sampling uncertainties. *J. Geophys. Res. Atmos.***116**, D14103 (2011).
62. Shchepetkin, A. F. & McWilliams, J. C. The regional oceanic modeling system (ROMS): A split-explicit, free-surface, topography-following-coordinate oceanic model. *Ocean Model.* **9**, 347–404 (2005).
63. Cambon, G. *et al.* Assessing the impact of downscaled winds on a regional ocean model simulation of the Humboldt system. *Ocean Model.* **65**, 11–24 (2013).
64. Da Silva, A. M. Atlas of surface marine data 1994, 1: algorithms and procedures. *NOAA Atlas NESDIS* **6**, 83 (1994).
65. Pizarro-Koch, M. *et al.* Seasonal variability of the southern tip of the Oxygen Minimum Zone in the eastern South Pacific (30°-38° S): A modeling study. *J. Geophys. Res. Ocean.* **124**, 8574–8604 (2019).
66. Smith, T. M., Reynolds, R. W., Peterson, T. C. & Lawrimore, J. Improvements to NOAA's historical merged land-ocean surface temperature analysis (1880–2006). https://doi.org/10.1175/2007JCLI2100.1.
67. Henley, B. J. *et al.* A tripole index for the interdecadal Pacific oscillation. *Clim. Dyn.* **45**, 3077–3090 (2015).
68. Pegliasco, C., Chaigneau, A. & Morrow, R. Main eddy vertical structures observed in the four major Eastern Boundary Upwelling Systems. *J. Geophys. Res. Ocean.* **120**, 6008–6033 (2015).
69. Souza, J., de Boyer Montégut, C. & Le Traon, P. Y. Comparison between three implementations of automatic identification algorithms for the quantification and characterization of mesoscale eddies in the South Atlantic Ocean. *Ocean Sci.* **7**, 317 (2011).
70. Amores, A., Jordà, G., Arsouze, T. & Le Sommer, J. Up to what extent can we characterize ocean eddies using present-day gridded altimetric products?. *J. Geophys. Res. Ocean.* **123**, 7220–7236 (2018).
71. Lin, J.W.-B., Neelin, J. D. & Zeng, N. Maintenance of tropical intraseasonal variability: Impact of evaporation–wind feedback and midlatitude storms. *J. Atmos. Sci.* **57**, 2793–2823 (2000).
72. Dewitte, B. *et al.* Modes of covariability between sea surface temperature and wind stress intraseasonal anomalies along the coast of Peru from satellite observations (2000–2008). *J. Geophys. Res. Ocean.***116**, C04028 (2011).

Acknowledgements
Carlos Conejero was supported by a doctoral scholarship from the National Chilean Research and Technology Council (CONICYT) through the program Becas Chile (scholarship N°72170554). B.D. and I.M. acknowledge supports Fondecyt (project N°1190276). This work was granted access to the HPC resources of CALMIP supercomputing center under the allocations 2018-1044 and 2019-1044.

Author contributions
C.C. and B.D. conceived the study and wrote the initial manuscript in collaboration with V.G. C.C. performed the analyses and generated the final figures. J.S. provided the satellite altimeter data. J.S. and I.M. participated in discussion of the results and commented on the manuscript.

Competing interests
The authors declare no competing interests.

Additional information
Supplementary information is available for this paper at https://doi.org/10.1038/s41598-020-74762-x.

Correspondence and requests for materials should be addressed to C.C.

Reprints and permissions information is available at www.nature.com/reprints.

Publisher's note Springer Nature remains neutral with regard to jurisdictional claims in published maps and institutional affiliations.

4.3 ENSO-induced modulation of mesoscale eddies

In the previous section we pointed out that low-frequency variability of the mesoscale activity over the PCUS is mostly driven by strong EP El Niño events, while during CP El Niño or La Niña events it is barely modified. We take advantage of satellite altimeter data and regional oceanic model simulations to show that during strong EP El Niño events, the mesoscale activity increases along the Peruvian coast and northern Chile by baroclinic instabilities, decreasing off central Chile. However, the sole strong EP El Niño event detected during the satellite era (i.e., 1993-present) is the 1997/98 El Niño event, while the 2015/16 El Niño event reaches only about half of the magnitude of the 1997/98 El Niño in terms of its loading on the EP El Niño mode, and had a relatively strong fitting on the CP El Niño mode. In consideration of the few strong EP El Niño events to characterize the mechanisms associated with mesoscale activity changes along the Peruvian coast, we extended out the study period (1958-2008) through the regional model simulation that allows documenting two additional strong El Niño events (1972/73 and 1982/83). In spite of that, the handful number of events is still insufficient to have a robust statistic of the EKE-ENSO relationship. Presently, and thankfully to the effort of the IBS center of climate physics, the long-term UHR-CESM PD (Present Day) simulation (section 2.2.3 for details on the model simulation) allows us the possibility to gain confidence in the statistics established from observations and the regional model simulation. The fully coupled UHR-CESM model is particularly skillfull in simulating the mean state of mesoscale activity in the Southeast Pacific, principally in the Peru region (Figure 4.2a). The strong EKE values (>100 cm^2/s^2) alongshore Peru are in good agreement with those derived from satellite altimeter data. The standard deviation of EKE anomalies, where anomalies are computed as departures from the long-term monthly seasonal cycle, exhibits large variability along the Peruvian coast (Figure 4.2b), consistent with observations. Two areas can be distinguished: the northern Peru (10°S-5°S) and southern Peru (18°S-13°S), which are noted by white rectangles in Figure 4.2b. These two regions of high EKE variability are strongly modulated by ENSO diversity at interannual timescales (Conejero et al., 2020). In this context, we will focus in this section on the mesoscale activity changes over the Peru region, which is more sensitive to fluctuations from the equatorial current system than the Chile region. The motivation for focusing on the Peru region and not including in our analysis the Chile region is related to the fact that the model has a mean state bias in stratification off Central Chile that renders coastal current much more stable reducing the sensitivity of mesoscale activity to fluctuations in current originating from the equatorial region.

Despite such a bias, there is a general good qualitative agreement between model

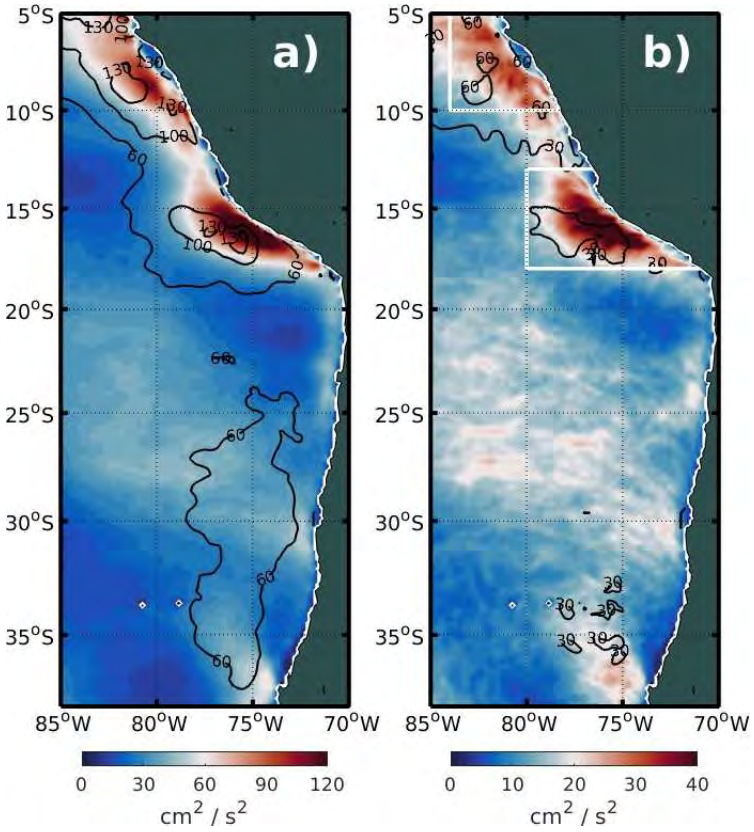

Figure 4.2: *Eddy Kinetic Energy (EKE, in cm^2/s^2) from UHR-CESM PD simulation (shading) and satellite altimeter data (contours). a) Mean state. b) Standard deviation of the interannual anomalies. The white rectangles indicate the northern and southern Peru regions.*

and observations (Reanalysis) in terms of the climatological state. The complete description of the UHR-CESM model skill is presented in Appendix B. Briefly, we recall here some important remarks: i) The climatological SST conditions are highly improved in the EBUS, especially in the Pacific ocean. The warm bias is considerably reduced in the PCUS, but SST is still overestimated along the Peruvian coast by around 1-2°C (Figure B.1). The eastern equatorial thermocline remains deeper and the warm pool in the western equatorial Pacific is slightly warmer (Figures B.2-3). ii) The coastal winds and Ekman pumping are better estimated in terms of spatial distribution and magnitude (Figure B.4). The negative wind stress curl values, associated with upwelling alongshore of the Peru-Chile coasts, are improved in comparison with the coarse-resolution version of the model and other products with lower spatial resolution. iii) The equatorial Pacific current system and the coastal currents of the Peru-Chile Upwelling System are well represented (Figures B.5-6). In particular, the Peru-Chile Undercurrent (PCUC) along the American continent coasts agrees well with observations (Figure B.5), principally at 30°S (Chile) with respect to their core magnitude (∼12-15 cm/s at 100-150 m depth) and vertical extension (∼50-400 m depth) although surface

currents are underestimated in the model (Figure B.5c). iv) The increased spatial resolution in the oceanic component allows to reproduce correctly the mesoscale activity, especially in the Peru region (Figure B.7). However, the maximum mesoscale activity offshore Chile is still weak. v) The ENSO diversity is well reproduced through the EP and CP modes (Figures B.8-10) which is an important aspect for the low-frequency modulation of the mesoscale activity in the Peru-Chile Upwelling System.

4.3.1 Relationship between the equatorial current system and EKE off Peru

In section 4.2 we showed that the interannual EKE variability is mostly driven by ENSO-driven changes in baroclinic instabilities of the PCUC through the oceanic equatorial teleconnection. The 120-year UHR-CESM PD simulation offers the opportunity to test the robustness of such a mechanism of EKE modulation with a larger sample of strong EP El Niño events. In this sense, 12 strong EP El Niño events (E-index greater than 1.5 standard deviation) are simulated by the global model, in contrast with the 3 events simulated by the regional oceanic simulation (section 4.2) or the sole 1997/98 event from the satellite altimeter data (Figure 4.3).

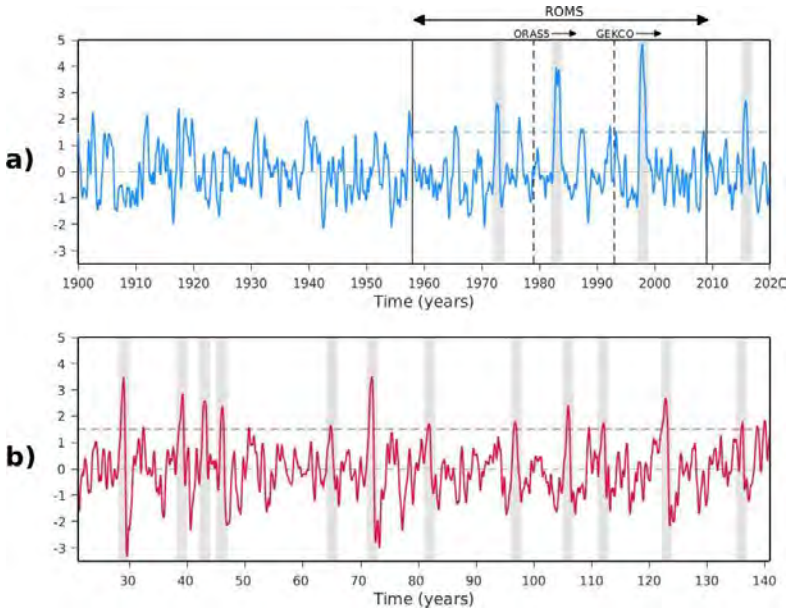

Figure 4.3: *Eastern Pacific El Niño mode (E-index) from a) ERSST.v5, and b) UHR-CESM PD simulations. Black dashed lines in a) indicate the start of the reanalysis ORAS5 (1979) and satellite altimeter GEKCO (1993) products, while the solid lines correspond to the ROMS oceanic simulation (1958-2008 period) used in section 4.3. Gray shadows correspond to strong Eastern Pacific El Niño events (i.e. E-index greater than 1.5).*

The monthly evolution of the interannual EKE anomalies, over the two regions of intense EKE variability off Peru (see white rectangles in Figure 4.2b) and the Equatorial Undercurrent (EUC) anomalies during strong EP El Niño events are shown in Figure 4.4 for both observations-reanalysis products and the UHR-CESM PD simulation. Note that the EUC is defined as the mean zonal equatorial current (2°S-2°N) over a rectangular box in the subsurface layer (40-150 m depth), which corresponds to the mean location of the core of the peak at 88°W (see Figure 4.5). During June-July months (austral winter) about 6 months before the peak of EP El Niño events in December (Figure 4.4a-b), the amplitude of the EUC anomalies is maximum (Figure 4.4c-d) in both observations-reanalysis products and UHR-CESM PD simulation. This corresponds to an enhancement of the eastward subsurface equatorial current at 88°W, which is opposite to what is observed for the EUC in the central equatorial Pacific during El Niño (Izumo, 2005; X. Yu and McPhaden, 1999). This can be interpreted as resulting the shallower and stronger thermocline in the eastern Pacific than in western Pacific favoring the contribution of the higher-order vertical mode Kelvin waves (Dewitte et al., 1999) or from fluctuations in mass transport of the tropical shallow meridional overturning cells (STCs, Izumo, 2005; P. Lu et al., 1998).

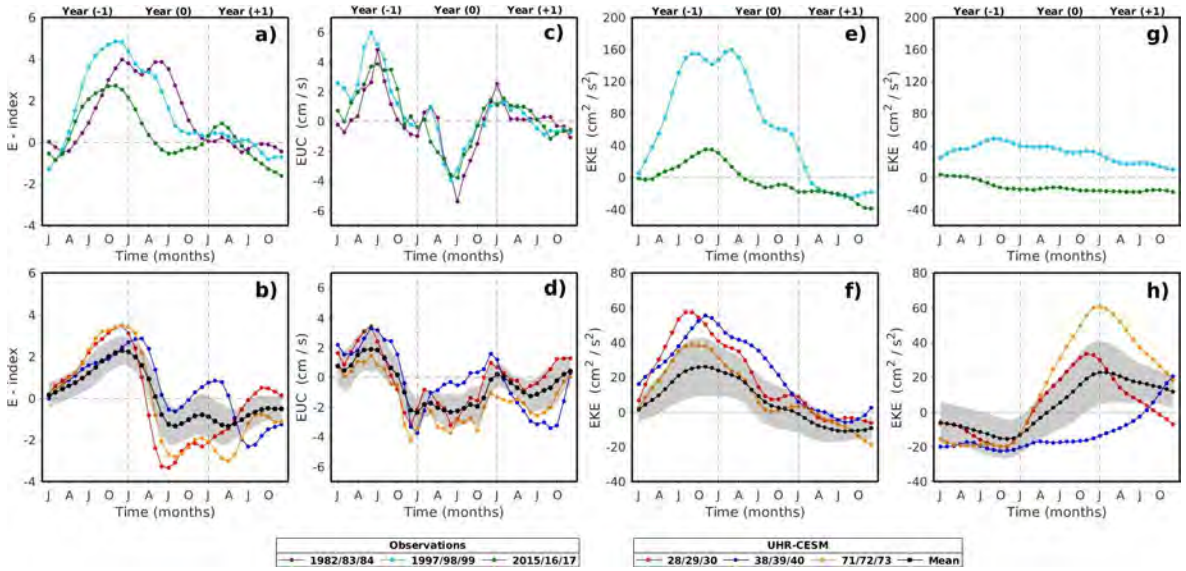

Figure 4.4: *Monthly evolution during strong Eastern Pacific El Niño events from observations (upper panels) and UHR-CESM PD simulation (lower panels) of interannual anomalies of a-b) E-index, c-d) Equatorial Undercurrent (EUC), e-f) Eddy Kinetic Energy (EKE) over the northern Peru, and g-h) EKE over the southern Peru. The strong EP El Niño events selected from observations (UHR-CESM) are 3 (12). The mean of 12 EP El Niño events from UHR-CESM is in black dots and the gray shadow corresponds to the standard deviation among the 12 events. The observation dataset corresponds to ERSST.v5 for E-index, ORAS5 for EUC, and GEKCO for EKE. The EKE anomalies were averaged off northern Peru (12°S-7°S and 83°W-coast). See Figure 4.2 for northern and southern Peru regions.*

During the strengthening of the EUC, the EKE anomalies in the northern part off Peru (Figure 4.4e-f) start to increase, reaching the maximum amplitude between September and November. In contrast, the EKE anomalies in the off southern Peru (Figure 4.4g-h) are less impacted before the EP El Niño event for observations. This is not the case for the UHR-CESM PD simulation that simulates negative EKE anomalies values off southern Peru during the peak of an EP El Niño event (Figure 4.4h). Note that this is quite similar to the EKE anomalies during the 2015/16 El Niño event from observations (Figure 4.4g). The EUC anomalies start to reverse sign at the peak of El Niño (December) in both observations and the model, while the mesoscale activity peaks at the same period. Nevertheless, after the El Niño peak, the UHR-CESM PD simulation shows a faster increase in mesoscale activity southern off Peru, with a maximum in January of Year (+1), i.e. one year after the peak of EP El Niño event. On the other hand, satellite altimeter data do not exhibit a maximum in mesoscale activity off southern Peru after the peak of neither 1997/98 or 2015/2016 El Niño event (Figure 4.4g). Overall there is a rather good agreement between the model and the observations, in particular in terms of the lagged relationship between the EKE and EUC peak anomalies off northern Peru (Figure 4.4). A main difference between the model and the observation is the faster decay of the EUC in the UHR-CESM PD simulation than in the reanalysis products at the peak of El Niño (Figure 4.4c-d). During the peak of EP El Niño events (austral summer), the EUC is anomalously weak (negative anomalies) in the model simulation, while in observations it is close to its mean state. In addition, the weakening of the EUC observed in the model simulation occurs 6 months after the peak of the EP El Niño events in observations (Figure 4.4c). Nevertheless, the monthly evolution of the EKE anomalies from the model simulation is overall in good agreement with the observations (Figure 4.4e-f), although their amplitude tends to be lower in comparison to the strong 1997/98 EP El Niño event ($\sim$140 cm^2/s^2) and more comparable to the 2015/16 El Niño event ($\sim$ 40 cm^2/s^2). In that regard, through both observations and model simulation, our results indicate that the maximum interannual EKE anomalies northern off Peru is achieved after the strengthening of the EUC and before the peak of the EP El Niño events.

At this stage, we are interested in establishing the relationship between the EUC variability and the coastal currents of the PCUS, which are the main source of EKE generation processes through baroclinic instabilities (e.g., Marchesiello et al., 2003; Belmadani et al., 2012; Colas et al., 2012; Conejero et al., 2020). Figure 4.5 represents the first EOF mode of the interannual zonal equatorial currents anomalies at 88°W between surface and 250 m depth from both reanalysis products (ORAS5) and UHR-CESM PD simulation. The first principal component (PC1) in both ORAS5 and UHR-CESM PD

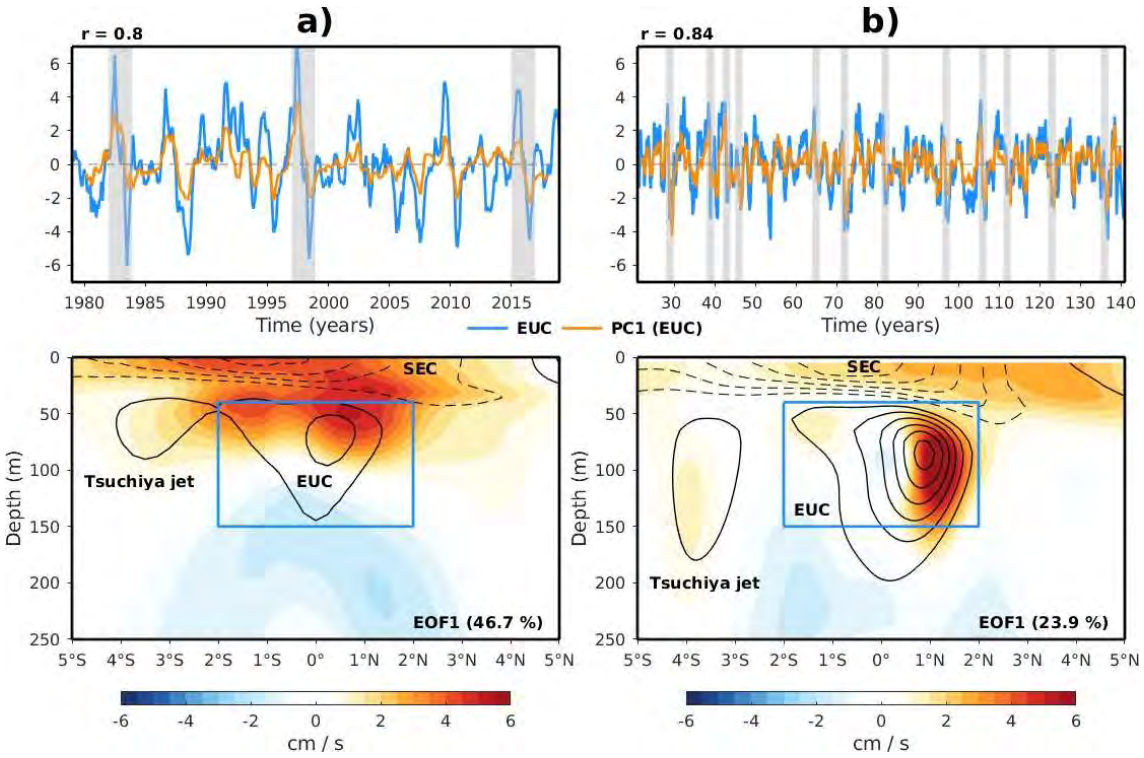

Figure 4.5: *First Empirical Orthogonal Function (EOF) mode of interannual zonal equatorial currents anomalies at 88°W and the Peru-Chile Undercurrent (PCUC) transport. a) zonal equatorial currents from ORAS5 reanalysis, b) zonal equatorial currents from UHR-CESM PD simulation. The EUC anomalies in a-b) panels is calculated by the average of the blue box in lower panels. The explained variance is provided in the EOF patterns in lower panels. The black solid (dotted) contour lines in a-b) panels correspond to mean eastward (westward) currents every 5 (-5) cm/s. The equatorial currents represented are: Equatorial Undercurrent (EUC), South Equatorial Current (SEC), and the Tsuchiya jet. Gray shadows correspond to strong Eastern Pacific El Niño events from ORAS5 reanalysis and UHR-CESM PD simulation.*

simulation is highly correlated with the interannual EUC anomalies (r > 0.8) (Figure 4.5, upper panels), indicating that the first EOF mode captures the EUC interannual fluctuations in both products. The mode pattern indicate that the first EOF model also accounts for the variability of both the Surface Equatorial Current (SEC) and the EUC over the first 150 m depth, as well as partially the Tsuchiya jet in the southern equatorial band. During positive (negative) phases of the PC1 the SEC is weakened (strengthened) while the EUC and the Tsuchiya jet are strengthened (weakened), as revealed by the sign of the mode pattern at the mean position of these currents (Figure 4.5, lower panels). As the EUC and Tsuchiya jets extend to the American coast, they start feeding the PCUC through a complex of pathways (Montes et al., 2010). The PCUC strength is estimated as the integrated alongshore poleward transport averaged over the mean position of the PCUC defined as a rectangular box approximating the vertical extension ranging from 60 to 400 m depth, and its cross-shelf extension spanning from the

coast to $\sim$ 100 km (see Methods in Conejero et al., 2020). We then diagnose its temporal and meridional variability through the first EOF mode of the interannual PCUC transport, all along the Peruvian coast (Figure 4.6).

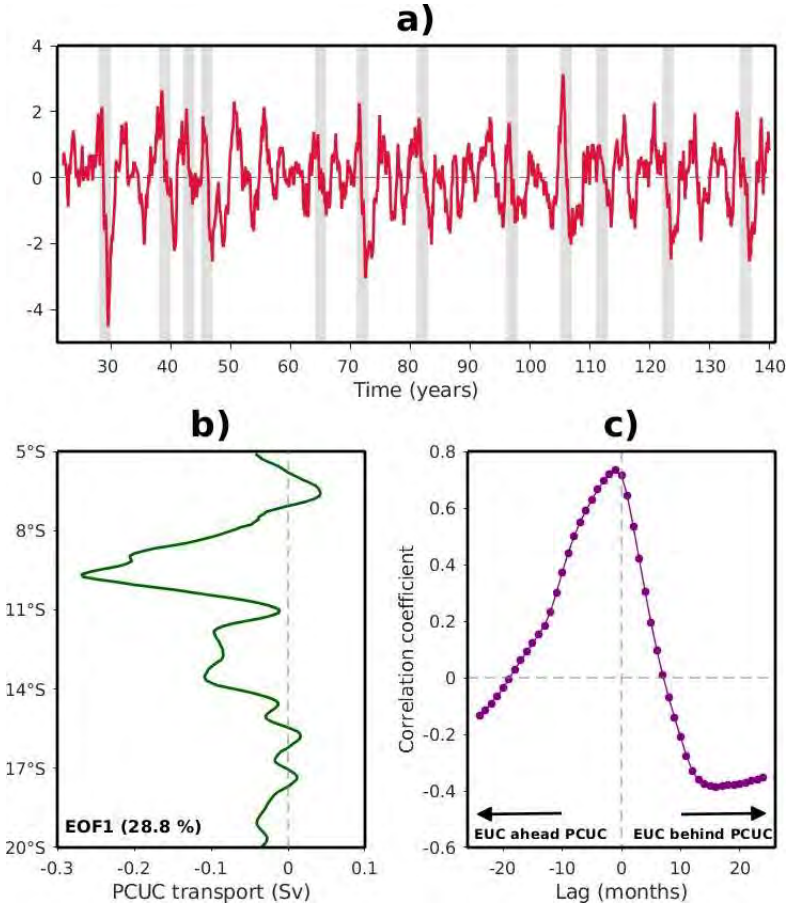

Figure 4.6: *Interannual variability of the Peru-Chile Undercurrent (PCUC) transport from UHR-CESM PD simulation. a) First Principal Component (PC1). b) First Empirical Orthogonal Function (EOF1) mode. c) Lagged-correlation between the PC1s of Equatorial Undercurrent (EUC, Figure 4.5b) and the PCUC transport.*

The explained variance of this mode reaches 29% and the maximum strength of the PCUC transport (i.e. minimum values of the first EOF mode) change occurs during the positive phases of the PC1 (Figure 4.6a) in the northern Peru, around 11°S-8°S (Figure 4.6b). The correlation of the PC1-EUC and the PC1-PCUC peaks at 0.8 when the EUC leads the PCUC transport by 1 month (Figure 4.6c). This relationship indicates that when the EUC increases prior to the peak of a strong EP El Niño event, the PCUC transport off Peru is also increased with a first maximum at $\sim$ 10°S and a second relative maximum around 14°S (see EOF1 pattern in Figure 4.6b). This strengthening in both EUC and PCUC transport during EP El Niño events will generate an increase in baroclinic instabilities alongshore, enhancing the mesoscale activity off Peru. These results indicate a strong connectivity between the equatorial Pacific current system and

the coastal currents of the American continent during EP El Niño event, which is a key process to understand how the turbulent flux is modulated by tropical modes of variability such as ENSO.

4.3.2 EKE tendency changes and their relationship with the equatorial current system

In this section we document the source terms of the EKE rate of change off Peru and investigate their relationship with equatorial variability. Due to the propagating nature of the eddies on the one hand, and of the coastal variability on the other hand, we use Complex Empirical Orthogonal Function (CEOF) analysis. We present in Figure 4.7 the spatial-temporal evolution of the EKE tendency changes ($\partial EKE/\partial t$) at interannual timescale from both satellite altimeter data and UHR-CESM PD simulation through the reconstruction of the first CEOF mode. The CEOF1 mode explains 33.2% and 18.4% for observations and UHR-CESM PD simulation, respectively. The maximum amplitude of EKE tendency changes take place during strong EP El Niño events.

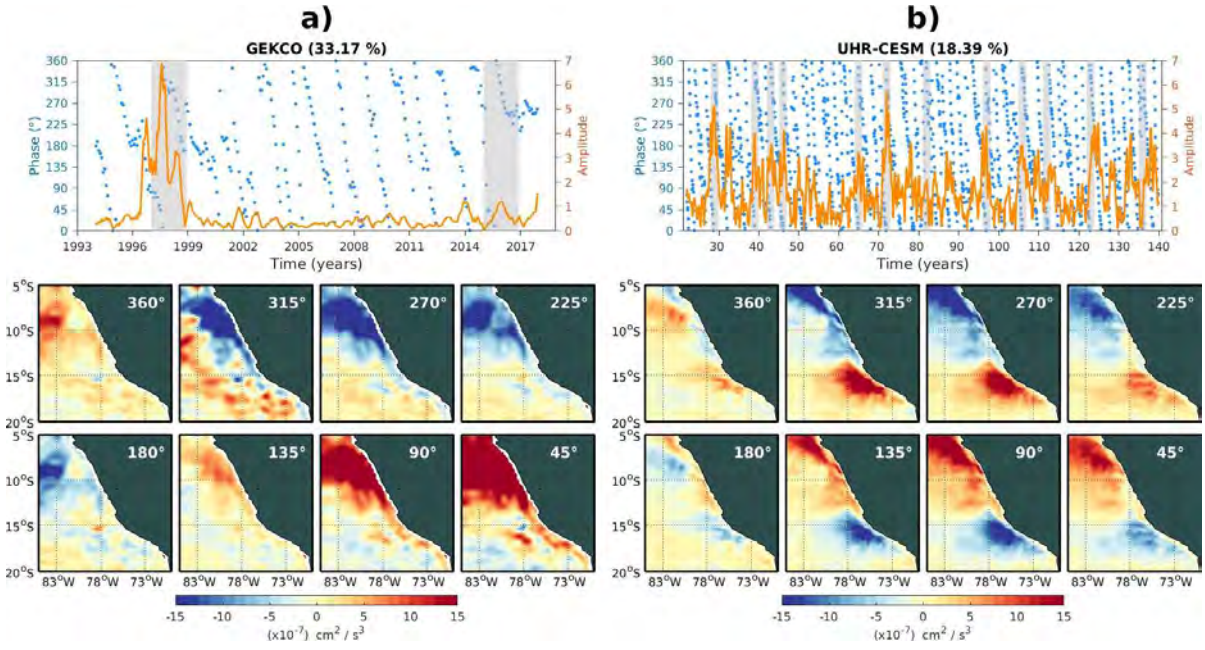

Figure 4.7: *Spatial-temporal sequence of the reconstructed interannual EKE tendency anomalies calculated from the first Complex Empirical Orthogonal Function (CEOF) mode for a) satellite altimetric data, and b) model simulation. The temporal sequence is expressed in terms of phase (in degrees, blue dots) and amplitude (standardized, orange line) in upper panels. The spatial sequence is represented by a composite analysis for each 45° during the whole period. Gray shadows correspond to strong Eastern Pacific El Niño events from altimetric data (2 events: 1997/98 and 2015/16) and UHR-CESM PD simulation (12 events). The explained variance is indicated in upper panels.*

To clarify this point, Figure 4.8 represents the composite evolution of the reconstructed CEOF1 phase and amplitude of the 12 strong EP El Niño events in the model contrasted against the equivalent quantities for the strong 1997/98 EP El Niño event from satellite altimeter data. The mesoscale activity changes off Peru begin around one year prior to the peak of EP El Niño events. In particular, during the strong 1997/98 El Niño event, the amplitude of EKE tendency starts to increase slightly in austral spring-summer of 1997, strengthening the EKE north of the Pisco region (∼15°S) during phases 135° to 45° of the CEOF1 (Figure 4.7).

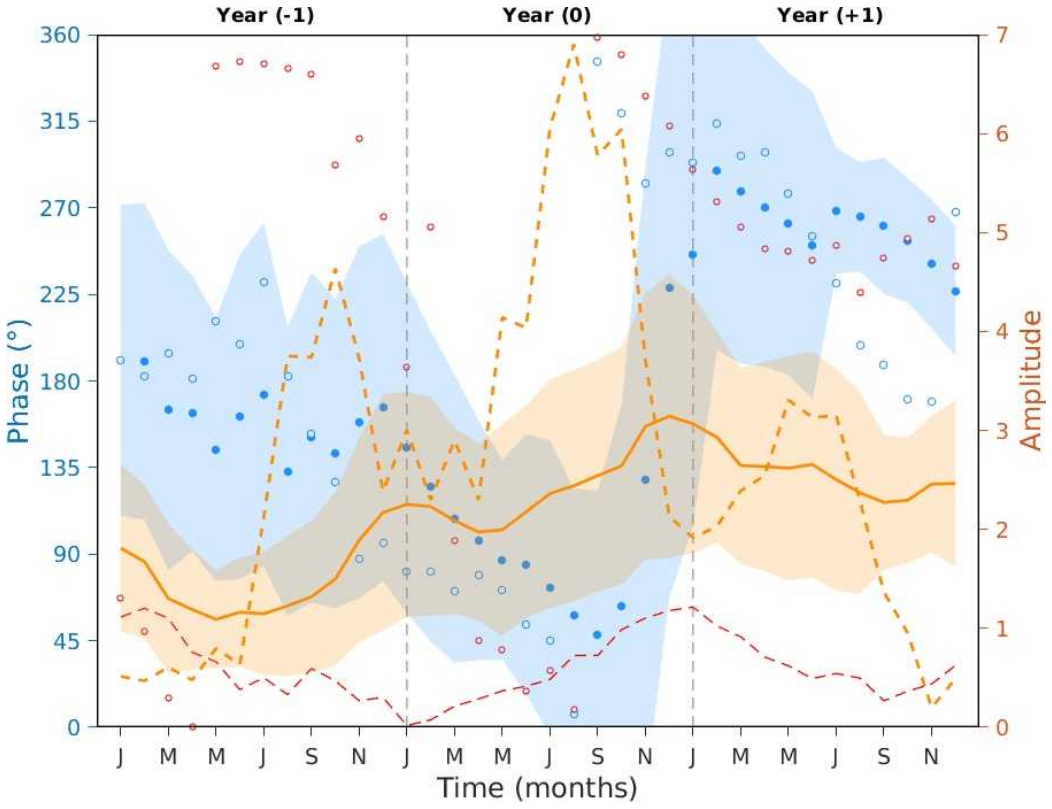

Figure 4.8: *Composite of temporal sequence of the reconstructed interannual EKE tendency anomalies during strong EP El Niño events (see Figure 4.7) for UHR-CESM PD simulation (solid orange line and filled blue dotes) and during 1996/97/98 (2014/15/16) El Niño event for observations in dashed orange (red) line and white dotes.*

During this period, an offshore propagation of the positive EKE rate of change anomalies is detected, reaching a maximum at phase 45° (austral autumn). After the 1997 austral winter season, anomalies of EKE rate of change start to decay (phase 360°, Figures 4.7 and 4.8). The weakened EKE tendency occurs alongshore off northern Peru (phase 315°). However, at this moment, a positive tendency is also observed off Peru and southward of Pisco region (15°S), which yields a alongshore dipole-like pattern. During the 1998 austral spring season, i.e. at the reversal to La Niña conditions, negative anomalies of EKE rate of change are still observed principally off northern Peru

(phase 180°). Noteworthy, the model exhibits comparable characteristics than the observation in terms of the spatial patterns and time evolution of the CEOF1 mode of the EKE rate change. The main difference is in the alongshore dipole-like pattern of the CEOF1 mode that is more pronounced in the UHR-CESM PD simulation than in the observations. This is associated in particular to a stronger loading of the CEOF1 mode pattern off central Peru (Chile) in the model than in the observation. Still, the overall good agreement between model and observations for this quantities is encouraging and bring confidence in the model simulation for investigating further the source and sink terms of the EKE rate of change. In particular, it calls for elucidating the mechanisms associated to the dipole-like pattern of the EKE rate of change.

4.3.3 EKE generation processes

To determine the mechanisms associated to the EKE tendency variability in the UHR-CESM PD simulation, we analyze the key eddy conversions terms (ECT) in the EKE budget (see section 2.3.2), considering their mean state and standard deviation from interannual anomalies (Figure 4.9).

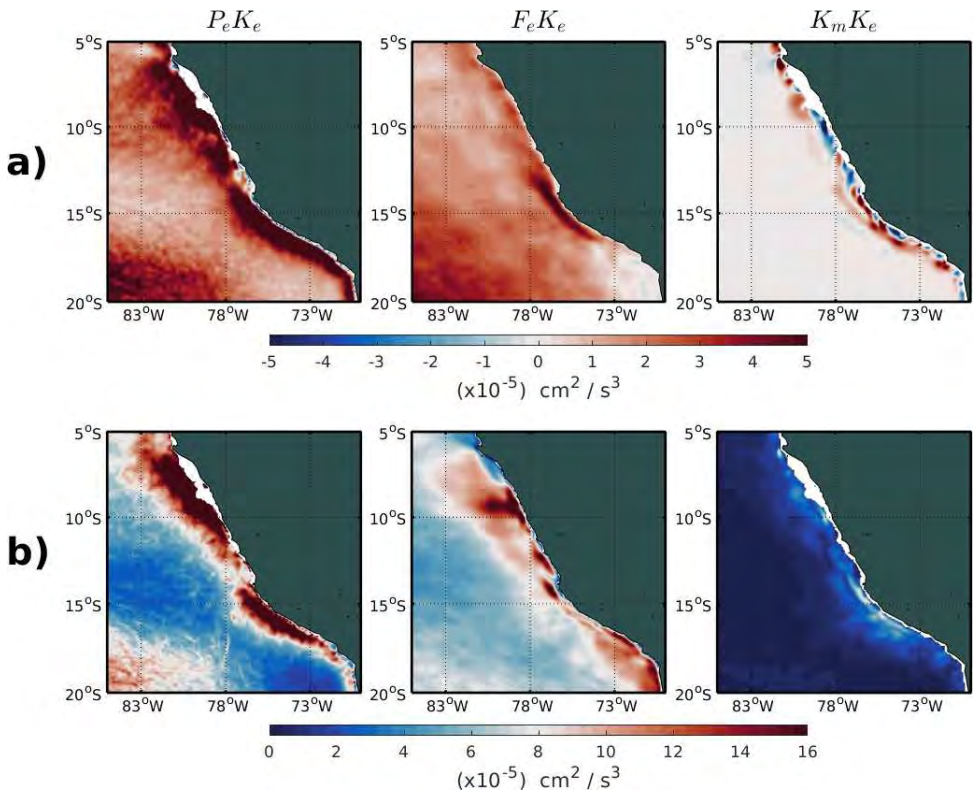

Figure 4.9: *Eddy conversions terms from UHR-CESM PD simulation: baroclinic instability (P_eK_e), wind work (F_eK_e), and barotropic instability (K_mK_e). a) Mean state. b) Standard deviation of the interannual anomalies.*

The mean state of the ECT indicates that the baroclinic instability (P_eK_e) and wind work (F_eK_e) are the main sources of mean mesoscale eddy generation along the Peruvian coast, while the barotropic instability (K_mK_e) is confined along the coast (first 100km) with a somewhat noisy spatial pattern (Figure 4.9a). A node of positive K_mK_e can still be observed nearby south of the Pisco region at 15°S. Among these three terms, only P_eK_e and F_eK_e exhibit significant interannual variations as evidenced by maps of the interannual standard deviation of the ECT (Figure 4.9b). K_mK_e standard deviation is in particular much weaker than the other two terms and this is not likely to contribute the modulation of mean EKE off Peru. As a means to documenting the evolution of the ECT, we present the reconstructed first CEOF mode at their interannual anomalies in Figures 4.10 (P_eK_e), 4.11 (F_eK_e) and 4.12 (K_mK_e).

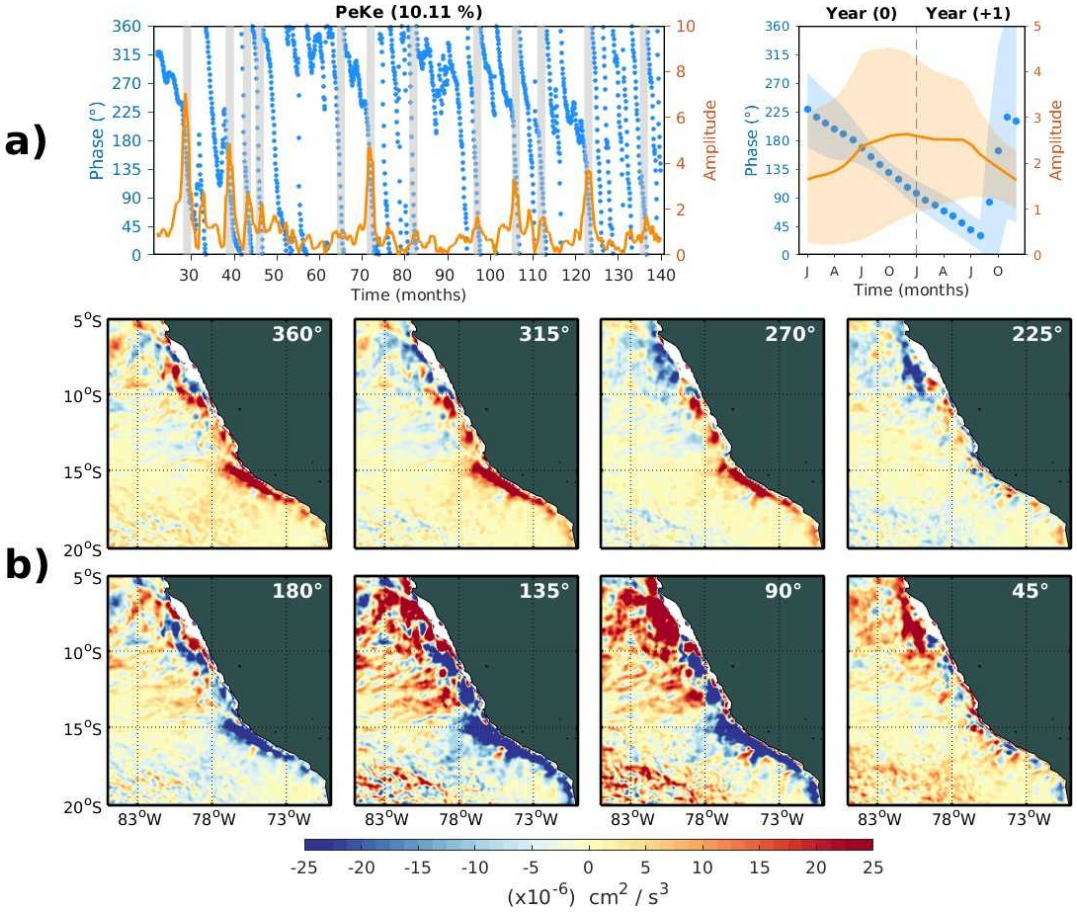

Figure 4.10: *Spatial-temporal sequence of the reconstructed interannual baroclinic instability (P_eK_e) anomalies calculated from the first Complex Empirical Orthogonal Function (CEOF) mode of UHR-CESM PD simulation. a) Left panels: temporal sequence expressed in terms of phase (in degrees, blue dots) and amplitude (standardized, orange line). Gray shadows correspond to 12 strong EP El Niño events. Right panels: composite of the temporal sequence during the 12 strong EP El Niño events. The blue and orange shadows indicate the standard deviation among the 12 events for the phase and amplitude, respectively. b) Spatial sequence represented by a composite analysis for each 45° during the whole period.*

The composite evolution (every 45°) of the spatial patterns from the CEOF1 mode shows that PeKe is available to reproduce the dipole-like pattern of EKE rate of change off Peru during strong EP EL Niño events (Figure 4.10b). In particular, intensified (reduced) P_eK_e take place in austral winter (associated to the phases 180°-135°) when an increase (reduction) of EKE rate of change is also observed (Figure 4.4 and 4.8) off northern (southern) Peru. Throughout the EP El Niño culminating phase, PeKe anomalies remain strong in the northern off Peru (phases 90°-45°) while in the southern off Peru the opposite occurs. After the EP El Niño peak, in the following austral winter, the amplitude of PeKe begins to decay, but positive anomalies take place in the southern off Peru (phases 360°-315°). This dipole-like pattern is clearly related to the interannual EKE rate of change off Peru, suggesting that PeKe is a main driver of EKE change during EP El Niño events. On the other hand, F_eK_e is also important to the generation of mesoscale activity, principally northward of the Pisco region at 15°S (Figure 4.11). The amplitude of F_eK_e anomalies is also increasing during the austral winter prior to EP El Niño peak (Figure 4.11a).

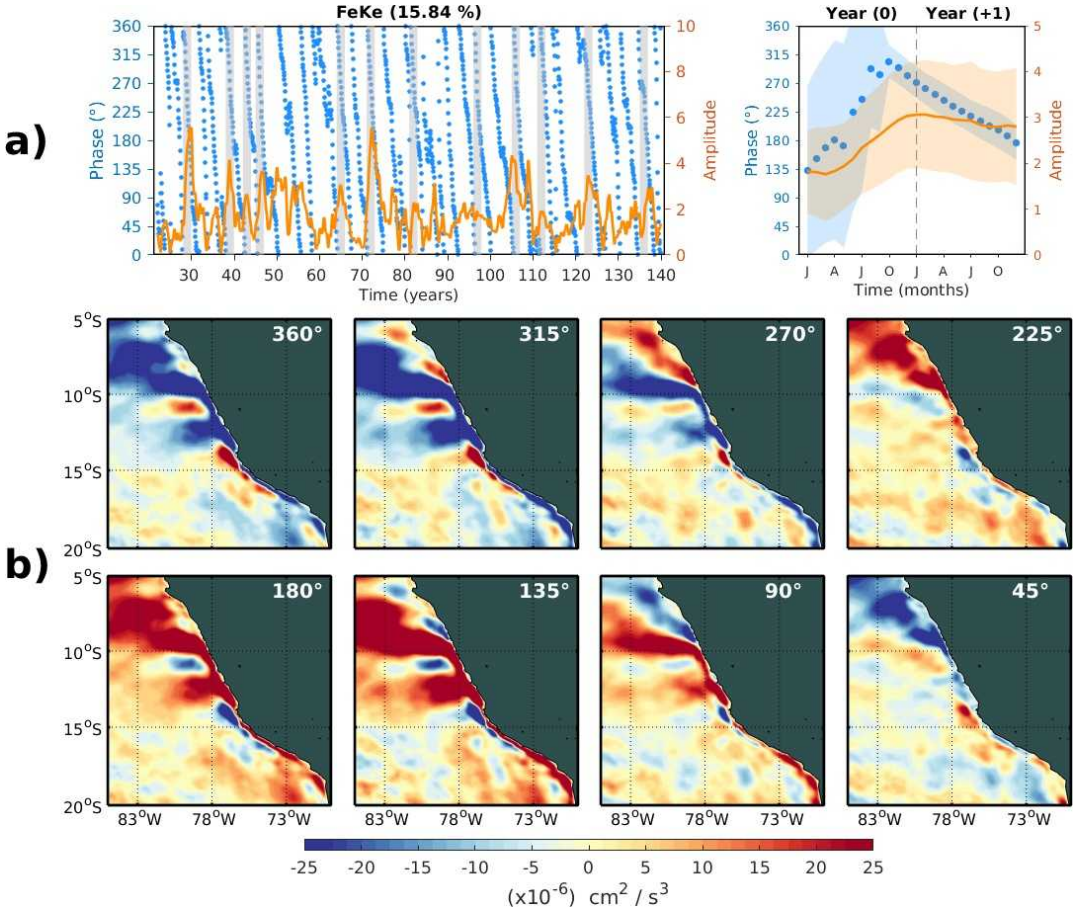

Figure 4.11: *Same as Figure 4.10, but for wind work (F_eK_e).*

However, positive anomalies located off northern Peru (phase 180°) start to diminish until the EP El Niño peak in austral summer (phase 360°). During the following austral winter, after the EP EL Niño peak, the wind work anomalies return positive. The spatial patterns exhibits a complex structure alternating between positive and negative anomalies in the northern off Peru (Figure 4.11b), but their offshore influence is unequivocally robust and persistent during EP El Niño events. Interestingly, F_eK_e anomalies during non-EP El Niño years with amplitude comparable to that during EP El Niño years can be observed (Figure 4.11a). The mechanisms yielding to F_eK_e fluctuations at interannual timescales may involve processes of air-sea interactions and atmospheric teleconnection, which would deserve further investigation. Finally, K_mK_e appears to be less important to modulate the mesoscale activity (Figure 4.12). The anomalies are weak and restricted to a narrow band along the Peruvian coast northward of 15°S, which cannot explained the offshore propagation of EKE rate of change off Peru (Figure 4.12b).

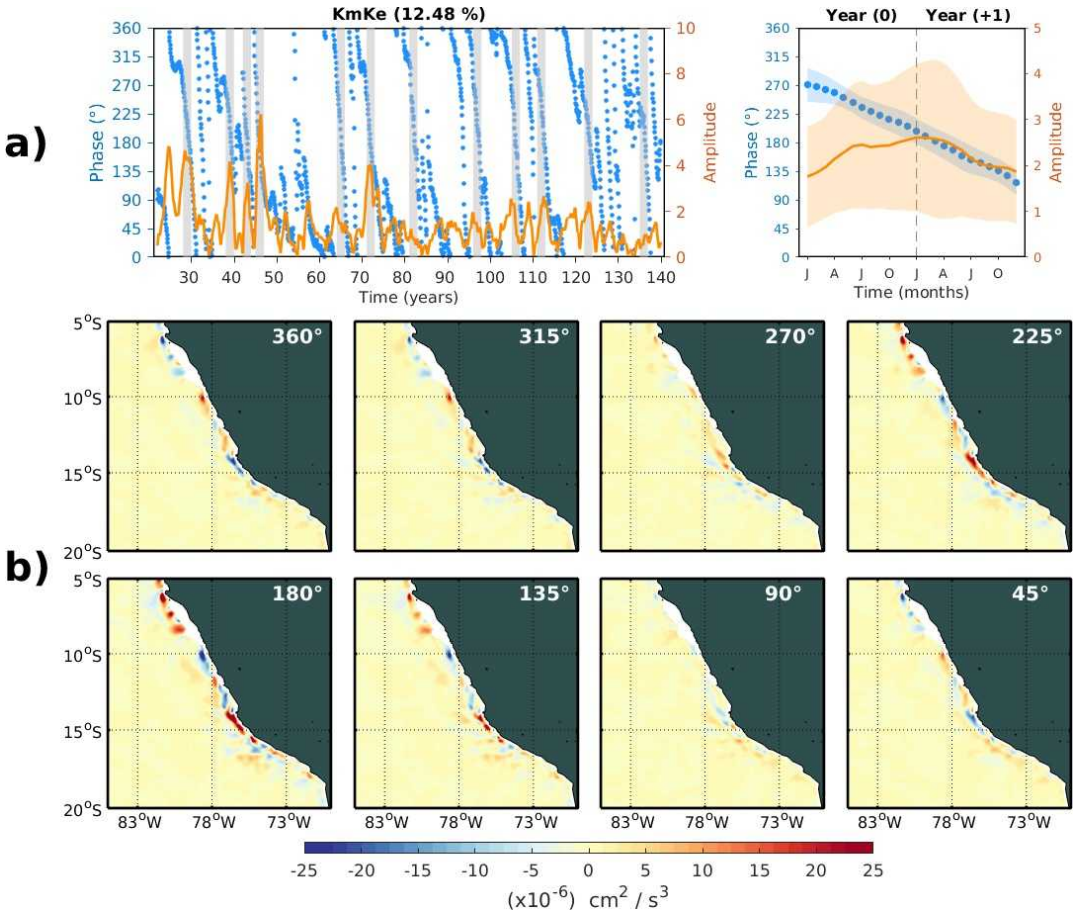

Figure 4.12: *Same as Figure 4.10, but for barotropic instability (K_mK_e).*

While the results of the CEOF analysis allows evidencing a statistically robust linear relationship between ETC changes and EP El Niño, they also reveals some non-linearity in this relationship associated with the fact that the amplitude of the ETC changes is not necessarily proportional to the strength of the EP El Niño events as measured by the E index. As an attempt to evaluate which terms is the most influential on the non-linear relationship between EKE changes and El Niño, the scatter plot showing monthly amplitude values of EKE tendency against ECT is presented in Figure 4.13. In addition, the season of strong mesoscale activity (i.e. August-September-October (ASO)) prior to EP El Niño peak (i.e. October-November-December (OND)) are marked by color dots, where the color indicates the magnitude of the E index (i.e. El Niño "strength"). The correlation between the EKE tendency and ECT, during ASO, is higher for P_eK_e (r = 0.65) and F_eK_e (r = 0.55), while it is weak for K_mK_e (r = 0.38). This confirms the dominant role of these two terms (P_eK_e, F_eK_e) in driving EKE changes. Noteworthy, there is a larger deviation from the linear fit during strong EP El Niño events for P_eK_e than for F_eK_e.

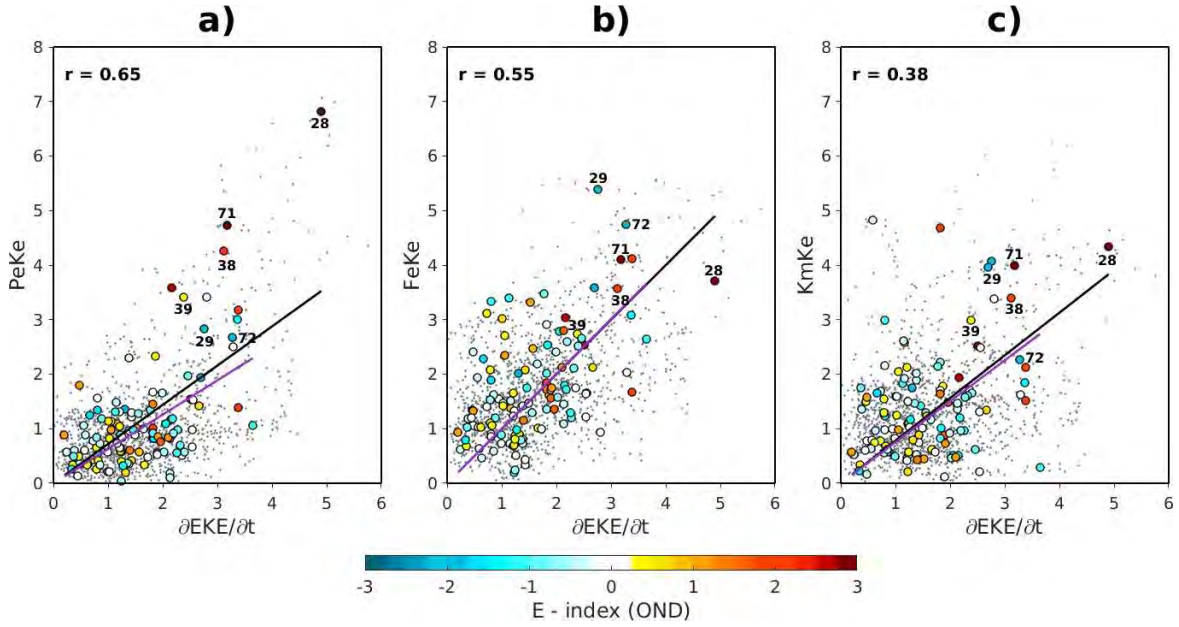

Figure 4.13: *Scatter plot of the monthly amplitude of interannual temporal reconstruction of the CEOF1 from UHR-CESM PD simulation between the EKE tendency (x-axis) and the eddy conversions terms (y-axis). a) Baroclinic instability (P_eK_e), b) wind work (F_eK_e), and c) barotropic instability (K_mK_e). Dots colors correspond to the August-September-October seasonal values of the EKE tendency terms and the eddy conversions terms, where the colors are associated to E-index values during October-November-December.*

In particular, the value of the slope of the P_eK_e-$\partial EKE/\partial t$ relationship is reduced by 13% when the three strongest EP El Niño events (i.e. 28/29, 38/39 and 71/72) are not considered in the calculation (compared to a change in 4% for FeKe, contrast black

and purple straight lines in Figure 4.13). In addition, PeKe tends to be ahead F_eK_e (compare figures 4.10a and 4.11a). This indicates that P_eK_e is the key term to fuel changes in mean EKE during EP El Niño events, which is consistent with the ENSO equatorial oceanic teleconnection driving the modulation of the instability processes along the coast of Peru. In order to support this latter statement, we present the Figure 4.14b that shows the relationship between the EKE tendency change off Peru and the EUC variability during strong EP El Niño events for both the satellite altimeter data and the UHR-CESM PD simulation.

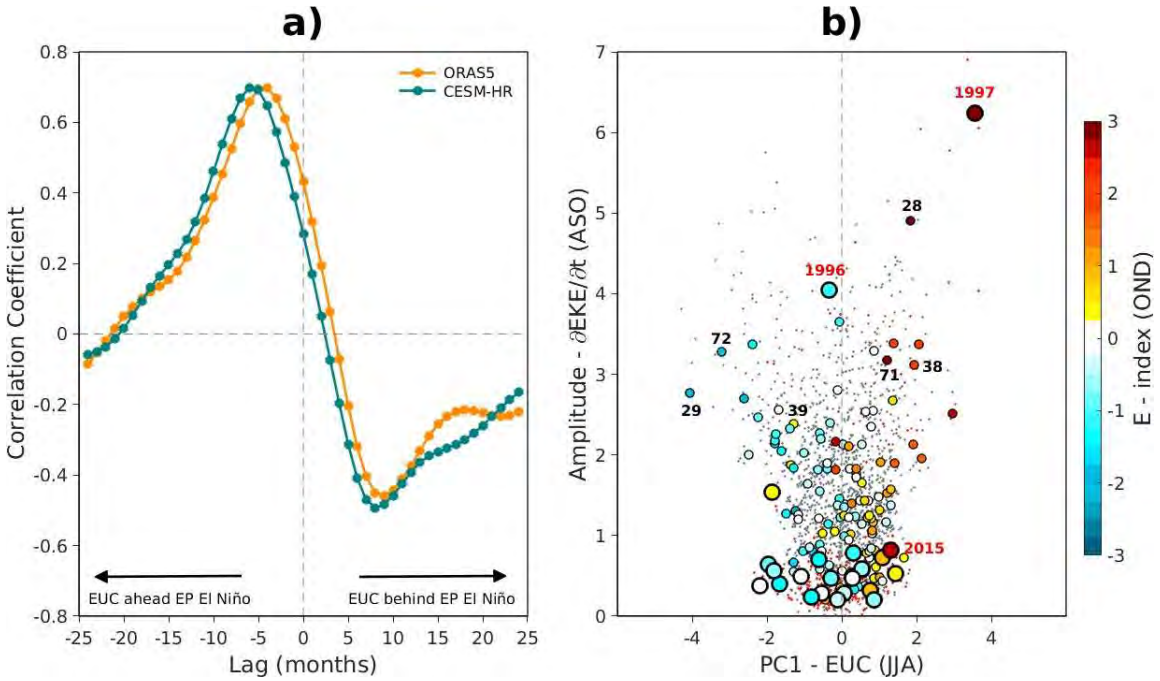

Figure 4.14: *a) Lag-correlation between the PC1 of the Equatorial Undercurrent (EUC, see Figure 4.5) and the EP El Niño events (E-index, see Figure 4.3) from ORAS5 reanalysis and UHR-CESM PD simulation. b) Scatter diagram between the interannual EKE tendency amplitude (see Figure 4.7), PC1-EUC and EP El Niño events during different seasons from observations (thick dotes) and UHR-CESM PD simulation (small dotes). The red and gray small dotes represent the monthly values from observations and UHR-CESM PD simulation, respectively. Some years of strong ENSO events are marked close to dotes in red and black for observations and UHR-CESM PD simulation, respectively.*

It was previously checked that the model simulate realistically simulate the phase-lagged relationship between the EUC anomalies at 88°W and the E index (Figure 4.14a). In particular the model simulates an enhancement of the EUC in the far eastern Pacific 6 months ahead the peak of EP El Niño events, which compares remarkably well with the observations. Regarding the EUC-$\partial EKE/\partial t$ relationship (Figure 4.14b), we thus observe a significant linear relationship consistently with the ENSO oceanic teleconnection along the coast modulating P_eK_e. However, the magnitude of EKE tendency

change is not proportional to the strength of the El Niño events, indicative of a non-linearity of the EKE-ENSO relationship similar to that suggested from observations and regional model simulations (see section 4.2).

4.4 Synthesis

Transient mesoscale eddies are salient features of the oceanic circulation thought to play a key role in the climate system. They are currently not realistically resolved in CGCMs participating to the CMIP to investigate the past, present and future climate state. In this chapter we took advantage of observations and numerical modeling, from regional to global scale, to document the turbulent flux at low-frequencies, which represents a source of mesoscale eddies to the open ocean via the non-linear dynamics of coastal upwelling in the Peru-Chile Upwelling System. In the first part, we demonstrated that the turbulent flux is modulated by ENSO diversity in both satellite altimeter data and regional oceanic modeling. In particular, the strong EP El Niño events largely impact the mesoscale eddy variability in the PCUS. This yields an enhanced (reduced) mesoscale activity off Peru and northern Chile (central Chile). In contrast, during CP El Niño (La Niña) events, the mesoscale activity is hardly changed, with a weak increase (decrease) off Peru and a reduction (increase) southward of the Pisco region (15°S). The dominant mechanism is through changes in baroclinic instability of the coastal currents along the American continent, principally by the PCUC, which arises from the ENSO oceanic teleconnections with the eastern equatorial Pacific current system. Nonetheless, the magnitude of the EP El Niño events is not proportional to the intensity of EKE changes. For example, the regional oceanic modeling results indicate that the 1972/73 El Niño event is standing out as an extreme event in terms of EKE increase off Peru reaching an amplitude three times as large as that during the 1997/98 El Niño event. This is confirmed by observations where the 2015/16 El Niño event, marked by record-breaking warm anomaly in the central Pacific, has a weak impact on mean EKE off Peru. In the second part, we take advantage of state-of-the-art fully coupled UHR-CESM long-term simulations, to gain confidence in our results. The UHR-CESM model is skillful in simulating realistically many aspects of the circulation along the coast of Peru. In particular, it simulates realistically the EKE mean and variability patterns, as well as the relationship between the EUC variability in the far eastern Pacific and the rate of change of EKE. It has also some skill in simulating ENSO diversity, which allows selecting 12 strong EP El Niño events and access robust statistics in terms of the relationship between EP El Niño and the terms of the EKE budget. The model results are consistent with that suggested from observations: During

strong EP El Niño events mesoscale activity off northern (southern) Peru is enhanced (reduced) prior to the peak of the event, resulting in a alongshore dipole-like in mean EKE changes that reverses sign over a ENSO cycle. This dipole-like pattern is driven by the ENSO-induced modulation of baroclinic instability along the coast, while wind work mostly contributes to the northern node of the dipole and is behind baroclinic instability. This dipole-like pattern is well defined in the model while more ubiquitous in observations, which may result from the too few numbers of El Niño events in the forced regional simulation or from model biases.

The existence of fluctuations of mesoscale activity driven by natural climate modes of variability questions the extent to which the turbulent flow can impact patterns of climate change in the Southeast Pacific, and vice versa. The connection of the PCUS with the eastern equatorial Pacific current system evidenced earlier implies that the mesoscale circulation along the coast of Peru and Chile could be sensitive to global warming through a variety of mechanisms. The UHR-CESM simulations are a powerful tool to elucidate and understand the relevance of the turbulent flow in the climate system. The mean EKE and its interannual standard deviation in the simulations where warmer climate conditions are imposed through CO_2 gas increase (i.e. $2xCO_2$ and $4xCO_2$), are contrasted with the PD simulation in Figure 4.15.

In the $2xCO_2$ experiment an increase of mesoscale activity is shown in the northern of Peru with values around 20 cm^2/s^2 over the mean EKE in PD conditions. In contrast, a significant reduction appears southward of the Pisco region (15°S) with values less than 40 cm^2/s^2 with respect to the mean EKE in PD conditions. Offshore Chile no large changes in mean EKE are simulated by the model, although these are significant relatively to the low mean EKE in PD conditions. Under $4xCO_2$ conditions the mesoscale activity changes are much important off Chile, in particular in the open ocean where it increases by $\sim$100% compared to the mean EKE values in PD conditions. In the northern of Peru the EKE values get greater than 40 cm^2/s^2 over the mean EKE in PD conditions, as well as in the offshore region. In the south of Peru, around the Pisco region, mean EKE still exhibits a strong reduction. Central and northern Chile (30°S-20°S) exhibit slightly reduced values of EKE, while offshore the mesoscale activity will increase as the climate warms. The interannual standard deviation of the EKE in PD simulation shows that the largest variability is located along the central Peru coast. Under both $2xCO_2$ and $4xCO_2$ warmer climate conditions, the interannual variability is expected to increase offshore Peru in the open ocean and northward of the Pisco region at 15°S, while in southern Peru it is strongly reduced. The Pisco region appears to be a key region for future EKE changes under warmer climate. Offshore central Chile the EKE variability increases drastically under $4xCO_2$ conditions. The results of these

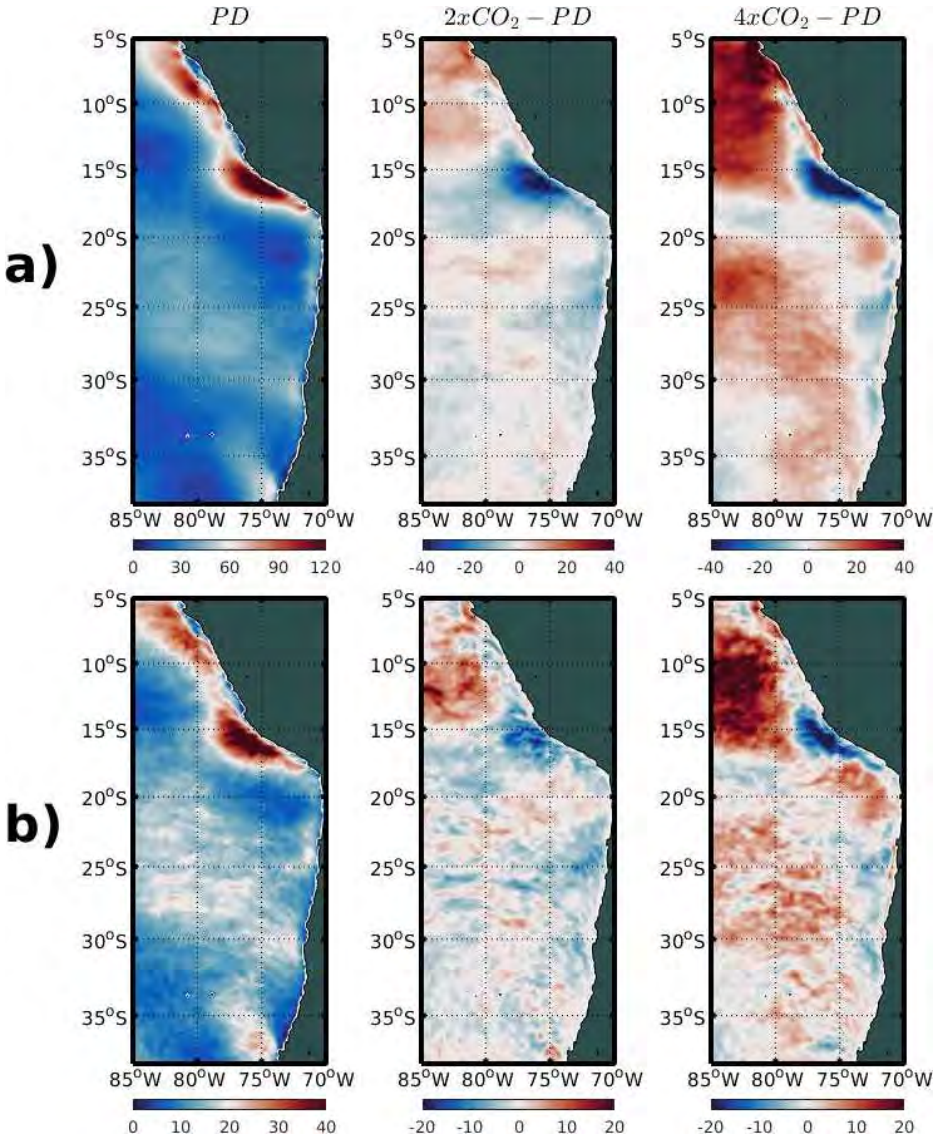

Figure 4.15: *Eddy Kinetic Energy (EKE, in cm^2/s^2) from UHR-CESM PD simulation (left panels) and the future climate response of $2xCO_2$ (middle panels) and $4xCO_2$ (right panels) simulations. a) Mean state. b) Standard deviation of the interannual anomalies. The future climate response is calculate as the difference between the future climate ($2xCO_2$ or $4xCO_2$) minus the PD simulation.*

sensitivity experiment indicate that changes in mean EKE in a warmer climate are of the same order of magnitude than that associated to ENSO, which suggests a likely role in the formation of the climate change SST pattern. It calls for investigating the change in SST and heat content associated to the modulation of mean EKE off Peru in particular. The modeling setup to tackle this issue is not straight-forward but it could be addressed from the experimentation with a regional ocean-atmosphere coupled model in which the instability process along the coast is externally controlled. This would deserve further investigation that is beyond the scope of this thesis.

Chapter 5

Conclusions and Perspectives

In this thesis we have investigated the processes involved in the SST pattern formation under a warmer climate in the EBUS of the South Hemisphere, including the influence of natural modes, internal climate variability and mesoscale activity. To this extent, we adopted a modeling approach based on state-of-the-art fully coupled CESM simulations: i) Large Ensemble (CESM-LENS) performed by NCAR, and ii) eddy-resolving ultra-high-resolution (UHR-CESM) performed at the IBS Center for Climate Physics (ICCP).

In the first part of the work, we have analyzed the CESM-LENS simulations to disentangle the oceanic and atmospheric processes involved in the future SST changes related to the mean climate change pattern in the EBUS of the South Hemisphere. We performed a mixed-layer heat budget for the 2006-2100 period for the highest greenhouse gases (GHG) emission scenario (RCP8.5), assuming a quasi-equilibrium between the radiative external forcing and the upper-ocean processes, in order to interpret the climate change pattern in these regions that have been predicted to warm less than the tropical regions by the models participating to the CMIP. While this robust SST pattern response has been commonly explained through the dependence of the SST on the mean evaporation, controlled by the mean climatological latent heat/precipitation pattern, our results indicate that the magnitude and latitudinal location of the minimum SST warming in the subtropics deviates significantly from that inferred from theory, revealing in particular a delicate balance between tendency terms associated to oceanic and atmospheric processes. From the atmospheric point of view, the continuous rise in GHG concentrations will increase everywhere the global surface temperature by reducing the amount of outgoing longwave radiation to space, increasing the relative humidity and static stability. At the same time, the SST warming will enhance the evaporative surface cooling (greater in the western than eastern equatorial regions) leading to a reduction in the zonal SST gradient, which in turn will weaken the easterlies. In this sense, our results indicate that the cooling trend associated to shortwave radiation could be understood as an eastward displacement of the atmospheric deep

convection to the central equatorial in both the Pacific and Atlantic oceans, by weaker winds. This implies a negative cloud-radiation-SST feedback acting as a thermostat that regulates the maximum SST warming in the equatorial band. On the other hand, near the coast of Peru and Chile, changes in shortwave radiation yields a warming tendency, which can be interpreted as resulting from a reduction in low-cloud cover. This participates to shape the meridional gradient of the climate change pattern (i.e. stronger warming trend on shoreward) in South tropical regions, particularly in the Pacific Ocean. Consistently with previous studies, changes in latent heat associated to changes in winds (i.e. WES feedback mechanism) also contribute to strengthen this meridional gradient, but it is not the dominant contributor south of $\sim$15°S. In summary our results indicate an important role of the cloud feedback in explaining the climate change SST pattern in the South Eastern Pacific and South East Atlantic. The future SST changes along the coast of Peru/Chile in the Pacific yields in particular a relative reduction in cooling due to radiation blocking, while in the open ocean a relative cooling tendency is associated to a combination of both reduced solar radiation forcing and enhanced evaporation cooling due to the WES feedback.

This balance in heat flux tendency terms indicate a strong coupling with ocean processes. An explicit heat budget decomposition reveals in particular that the stronger warming trend along the coast of Peru and Chile is associated to the warming tendency of horizontal (both zonal and meridional) advection. This makes the climate change SST patterns in the South East Pacific resembling an Eastern Pacific El Niño-like pattern, although the warm anomalies extend further south for the warming trend. The change in horizontal advection can be interpreted in terms of changes in winds (Ekman contribution), density (geostrophic compensation) and changes in meridional SST gradient advected by the mean current. Our results indicate that changes in advection due to changes in Ekman currents is weak. However the changes in cross-shore SST gradient along the coast are advected by the mean Ekman zonal (meridional) current yielding the largest contribution to the warming tendency due to advection near (offshore) the coast of Peru and Chile. Advection due to changes in zonal (meridional) geostrophic currents contribute to the relatively stronger warming along the coast of Peru (Chile). The analysis of the advection terms indicates that changes in surface winds along the coast of Peru/Chile are not the primarily cause of the formation of the climate change pattern since total advection is largely dominated by the contribution of advection of anomalous temperature by the mean currents. Changes in advection rather results from changes in density gradients that are advected either by changes in Ekman currents or geostrosphic currents. In this model, changes in vertical advection have also a negligible contribution to the warming trend, which could be due to

limitations of the model physics in particular regarding coastal upwelling dynamics. Overall this analysis reveals the complex of processes involved in the formation of the climate change pattern in the South East Pacific, which could explain the rather significant dispersion amongst the models participating to CMIP5 in accounting for the magnitude and patterns of the SST trend in the EBUS (see Figure 3.5)

We have also showed that the climate change SST pattern in the tropics and mid-latitudes of the South Hemisphere has a significant projection on the patterns of the natural modes of variability in the Pacific ocean (i.e. El Niño and the South Pacific Meridional Mode), the Atlantic ocean (Atlantic El Niño), and Indian ocean (Indian Ocean Dipole), suggesting that it can be strongly modulated by natural variability. In the Pacific, this has societal implications for Peru and Chile since the projected increase of occurrence of EP El Niño events could yield in the future in extreme near-shore SST conditions with detrimental impacts on the marine ecosystems on the one hand, but also in terms of extreme weather events. This questions the extent to which extreme convective rainfall events could take place along the usually dry coast of Chile, which could be also favored by the intrusion of atmospheric rivers originating from the branch of the South Pacific Convergence Zone. Similarly in the Indian ocean, our results support that the positive IOD-like pattern modulates the future SST changes only in the equatorial band, which has large implications for climate and weather extremes such as the 2019 Australian bushfires and African floods. This represents an emerging area of research which calls for better understanding the formation mechanisms of the climate change SST pattern at regional scale.

While natural oceanic variability can originate from climate modes, it can be also produced by processes not realistically accounted for in the current generation of the climate models. In particular, mesoscale eddies are salient features in EBUS which can modulate the mean circulation. We have investigated this issue based on the experimentation with a high-resolution regional model and altimeter data. Despite the shortness of the record from the satellite era (1993-to-present), our findings showed that the interannual EKE variability is modulated by strong Eastern Pacific (EP) El Niño events, where the mesoscale activity tends to increase along the Peruvian coast up to northern Chile and decreases off central Chile, while it is hardly changed during Central Pacific (CP) El Niño and La Niña events. The changes in EKE have the same order of magnitude that that of mean EKE. At decadal timescales, we also found that strong EP El Niño events can produce decadal changes in EKE, resulting in a significant negative (positive) long-term trend off Peru (central Chile), which is not linked to the low-frequency natural mode of variability (e.g. Interdecadal Pacific Oscillation).

Secondly, to elucidate which mechanisms are controlling the EKE-ENSO relationship in the PCUS, we conducted regional oceanic simulations with the ROMS model. Our findings confirm that the EKE variability arises from the oceanic teleconnections between the equatorial current system and the alongshore currents of the PCUS. In particular, we propose that equatorial Kelvin waves propagate along the American continent modulating the Peru-Chile Undercurrent at low-frequencies through baroclinic instabilities. However, the magnitude of the mesoscale activity changes during ENSO events is not proportional to their strength, resulting in a non-linear relationship. For example, the model simulation suggests that the 1972/1973 El Niño yielded the strongest EKE change off Peru, while the altimeter observations indicate that EKE was weakly impacted during the strong 2015/2016 El Niño, although these two events have a comparable amplitude in terms of the EL Niño index (EP mode).

In order to extend these results in a different modeling framework and address climate change, we have analyze a suite of simulations of the ultra-high-resolution version of the CESM (UHR-CESM) model to investigate the effect of the mesoscale activity on the CGCM, considering three experiments with differing CO_2 concentration: present day (367 p.p.m.), doubling (734 p.p.m.) and quadrupling (1468 p.p.m.). The current CGCMs are designed to perform century-to-multicentury simulations with a resolution around or greater than 1° (∼100 km), such as that employed in CMIP5 climate models. These models with relatively coarse resolutions can reproduce the major observed features of the large-scale circulations, including natural climate variability (e.g., ENSO, PDO, IOD, NAO, etc). However, they are unable to explicitly resolve small-scale features such as tropical cyclones, mesoscale storms, polar fronts or oceanic mesoscale motions associated with the Rossby radius length scale, like transient mesoscale eddy fluctuations and baroclinic boundary waves. In this thesis we showed that when the ocean model resolution is refined adequately to capture transient mesoscale motions (∼10 km), the simulations reproduce realistically fine scale details of the boundary currents, coastal upwelling zones and turbulent fluctuations. In particular, the UHR-CESM simulates realistically the EKE variability pattern in the PCUS, chiefly as a consequence of the well-defined PCUC along the American continent. This global fully-coupled model simulations support our previous results, showing that the magnitude and evolution of mesoscale activity during El Niño events is largely controlled by baroclinic instabilities from the PCUC, which in turn is strongly connected with the Equatorial Undercurrent (EUC) variability. Indeed, during the peak of strong EP El Niño events (i.e. austral spring-summer) the UHR-CESM evidences a tendency to enhance (reduce) the mesoscale activity northern (southern) off Peru. This pattern might be understood as a dipole-like emulating both an alongshore

and off-shore propagation of EKE anomalies during an ENSO cycle. Our results also suggest that the wind work is an important EKE generation process that could be modulating the EKE variability off Peru. Overall, our findings from satellite observations and both regional to global oceanic simulations suggest low-frequency ENSO-induced variability of mesoscale activity in the PCUS.

Finally, the UHR-CESM simulations indicate that with increasing CO_2 concentrations there will be an enhancement of the mesoscale activity off northern Peru and offshore central Chile, while southern of Peru around the Pisco region (18°S-14°S) an important reduction is projected. Although the generation mechanisms of the mean EKE under $2xCO_2$ and $4xCO_2$ experiments were not discussed, we can speculate that future wind changes along the coast of Peru and Chile potentially provide an energy flux into or out of the eddy field, especially around Pisco region, which might be modulated by the eddy wind work. Nevertheless, despite limitations associated to the experimental setup (in particular the abrupt change in CO_2 concentration), our results suggest that changes in mesoscale oceanic eddies in the near future could have the same order of magnitude that that of present-day mean EKE, which indicate that changes in mean circulation could take place through rectification process of the eddy flow on the mean. This has implications for the interpretation of long-term trend in the regional circulation in EBUS as simulated by current generation climate models (e.g. CMIP) since such process is not accounted for.

Overall, this thesis calls for a better understanding of the oceanic circulation response to climate change. The study of the future SST changes highlighted the complexity and interplay of the processes acting to modulate the pattern projected from CGCMs by the end of the twenty-first century. Considering the role of both coupled ocean-atmosphere dynamics and natural modes of variability is crucial to encompass the future of the climate system projected from CGCMs. Similarly, the incorporation of mesoscale processes in CGCMs (increasing the spatial resolution of the oceanic component) brings greater knowledge about the relevance of the turbulent flux in the PCUS, highlighting their key role to modulate climate variability under warmer conditions.

In this thesis, we have used a combination of datasets from observations and numerical simulations to understand both SST and EKE patterns on the climate system. As a matter of fact, several limitations of our study could be remarked. Despite large uncertainties in CGCMs projections (differing model parameterizations, internal variability of the climate system, or severe SST warm bias in the EBUS), in Chapter 3 we disentangle the mechanisms acting to drive the future SST changes projected to the end of the twenty-first century assuming a quasi-equilibrium of the upper-ocean processes. However, this assumption is questionable although the long oceanic time-scales in the

climate system imply that coupled simulations may require ∼1,000 years to reach a new equilibrium (e.g., Danabasoglu and P. R. Gent, 2009; Rugenstein et al., 2019). In this regard, Heede et al., 2020 have found, using idealized experiments from CESM, that different mechanisms are controlling the future SST changes in the tropical Pacific during the transient (lasting between 20-100 years) or equilibrium (emerging after 50-100 years) response. This highlights that it would be worth addressing properly diagnostics to improve our knowledge of the ongoing and future climate change. On the other hand, the low-resolution (∼100 km) of CGCMs does not allow to include mesoscale processes (∼10km) in the ocean component, which are very important in the EBUS because they can modulate the mixed-layer heat budget and mean circulation (upwelling). In this sense, the philosophy of the modeling research community has been to focus on developing fully-coupled simulations of the climate system considering a broad set of experiments, user-friendly with public access on modern computational platforms, properly documented, and carefully validated. Now, the research centers are improving these climate simulations by increasing the spatial resolution, principally in the ocean component to include meso-to submesoscale processes. In this direction, with the novel ultra-high resolution global climate simulations (UHR-CESM), we demonstrated the relevance of the natural climate variability in the EBUS, with ENSO-induced variability of the mesoscale activity in the PCUS. In addition, these state-of-the-art climate model experiments could enable us to characterize the effect of the thermal and current feedbacks, which are important to regulate the turbulent flux (Renault et al., 2016a,b), in the EBUS under warmer climate conditions. Even though we did not perform a heat balance considering the UHR-CESM simulations, this thesis proposes some directions for the future work to understand the impact of climate change on the oceanic circulation, where the mesoscale activity is called to play an important role.

Conclusions et Perspectives (français)

Dans cette thèse, nous avons étudié les processus impliqués dans la formation du patron de la SST sur le changement climatique dans l'EBUS de l'hémisphère sud, y compris l'influence des modes naturels, la variabilité du climat interne et l'activité méso-échelle.

Dans la première partie de ce travail, nous avons analysé les simulations du modèle CESM-LENS pour débrouiller les processus océaniques et atmosphériques impliqués pour le futur développement de la SST liés au patron de changement climatique moyen dans l'EBUS de l'hémisphère Sud. Malgré la pertinence indubitable du forçage atmosphérique à l'origine des futurs changements du système dans des conditions de réchauffement climatique, nous avons constaté que la réponse dynamique océanique et les modes naturels de variabilité jouent un rôle fondamental pour reproduire le taux de réchauffement minimal de la SST dans les latitudes moyennes de l'hémisphère Sud. Notre décomposition du bilan de chaleur révèle que l'advection océanique est le principal responsable de la formation du patron de réchauffement de type El Niño projeté dans les océans Pacifique et Atlantique, en particulier dans le Pacifique équatorial oriental et le long de la côte du Pérou et du Chili. Ce patron de tendance au réchauffement est le résultat d'un équilibre entre l'advection induite à la fois par le changement des courants d'Ekman horizontaux et la compensation géostrophique. D'un autre côté, nos résultats suggèrent que le taux de réchauffement minimal de la SST offshore est lié aux changements de vent, principalement dans l'océan Pacifique. Le mécanisme associé est la rétroaction WES (de l'anglais « wind-evaporation-SST »), où l'intensification des alizés aux latitudes moyennes de l'océan Pacifique et de l'anticyclone subtropical du Pacifique Sud-Est, par une expansion vers le sud de la cellule de Hadley, augmente la perte de chaleur dans le Pacifique tropical central sud et au offshore des côtes chiliennes. Pourtant, dans l'océan Atlantique, le taux minimum de réchauffement de la SST est principalement lié à une rétroaction cloud-radiation-SST négative. Au contraire, les mécanismes impliqués pour les futurs changements de la SST dans l'océan Indien diffèrent des océans Pacifique et Atlantique. Dans ce cas, nos résultats suggèrent qu'un réchauffement plus rapide dans la région équatoriale ouest qu'est entraîne un renforcement des vents d'est, ce qui à son tour intensifie la circulation de Walker et intensifie la phase positive de la rétroaction de Bjerknes. Alors, l'évaporation moyenne et le mélange océanique contrôlent le patron de tendance de la SST projeté dans l'océan Indien. En plus de cela, l'un des principaux résultats de cette thèse révèle que le futur patron de changements SST a une projection significative sur les patronnes des modes naturels de variabilité, ce qui suggère qu'il peut être compensé par la variabilité naturelle.

Dans la deuxième partie de cette thèse, nous nous sommes concentrés sur la téléconnexion océanique entre la diversité d'ENSO (de l'anglais « El Niño Southern Oscillation ») et le flux turbulent le long du système d'upwelling Pérou-Chili. Premièrement, nous avons utilisé les données altimétriques satellitaires pour documenter les implications de différents événements d'ENSO sur l'activité à méso-échelle (mesurée comme l'énergie cinétique moyenne des tourbillons, EKE, de l'anglais « eddy kinetic energy ») le long de la côte du Pérou et du Chili à des échelles de temps interannuelles à décennales. Nos résultats ont montré que la variabilité interannuelle de l'EKE est modulée par de forts événements El Niño du Pacifique Est (EP, de l'anglais « Eastern Pacific »), où l'activité à méso-échelle a une tendance à augmenter le long de la côte péruvienne jusqu'au nord du Chili et diminue au centre du Chili, alors qu'elle est à peine modifiée lors des événements La Niña et/ou El Niño du Pacifique central (CP, de l'anglais « Central Pacific »). À des échelles décennales, nous avons également constaté que de forts événements EP El Niño peuvent déclencher des changements décennaux de l'EKE, entraînant une tendance à long terme négative (positive) et significative le long du Pérou (centre du Chili), qui n'est pas liée au mode naturel de variabilité de basse fréquence (par exemple, l'Oscillation Interdécennale du Pacifique). De plus, nous avons effectué des simulations océaniques régionales avec le modèle ROMS pour confirmer que la variabilité de l'EKE provient des téléconnexions océaniques entre le système de courant équatorial et les courants littoraux du Pérou-Chili. En particulier, nous proposons que les ondes Kelvin équatoriales se propagent le long du continent américain en modulant le sous-courant Pérou-Chili (PCUC, de l'anglais « Peru-Chile Undercurrent ») aux basses fréquences par instabilités baroclines. Cependant, l'ampleur des changements d'activité à méso-échelle pendant les événements d'ENSO (El Niño ou La Niña) n'est pas proportionnelle à leur force, ce qui entraîne une forte relation de non-linéarité. Par exemple, la simulation du modèle ROMS suggère que El Niño de 1972/1973 a produit le plus fort changement de l'EKE le long de Pérou, alors que les observations altimétriques indiquent que l'EKE a été faiblement impacté pendant le fort El Niño de 2015/2016, bien que ces deux événements aient une amplitude comparable en termes de l'indice EL Niño. De plus, nous profitons d'une suite des simulations d'ultra-haute résolution du modèle CESM (UHR-CESM) pour étudier l'effet de l'activité méso-échelle dans un modèle global, en considérant trois expériences de concentration de CO2: état actuel (367 p.p.m.), doublement (2xCO2, 734 p.p.m.) et quadruplement (4xCO2, 1468 p.p.m.). Ces simulations de modèle global entièrement couplé étayent nos résultats précédents, montrant que l'ampleur et l'évolution de l'activité à méso-échelle pendant les événements fort de El Niño sont largement contrôlées par les

instabilités barocliniques du PCUC, qui à son tour sont fortement liées à la variabilité du sous-courant équatorial (EUC, de l'anglais « Equatorial Undercurrent »). Dans l'ensemble, nos résultats des observations satellitaires et des simulations océaniques régionales et globales suggèrent qu'à basses fréquences, la variabilité d'ENSO induite l'activité à méso-échelle dans le système d'upwelling Pérou-Chili. Enfin, les simulations du modèle UHR-CESM indiquent qu'en augmentant les concentrations de CO2, il y aura une augmentation de l'activité méso-échelle au nord du Pérou et au centre du Chili, pendant qu'au sud du Pérou, autour de la région de Pisco (18°S-14°S), une réduction importante est projeté. Étant donné que les mécanismes de génération de l'EKE sous les expériences 2xCO2 et 4xCO2 n'aient pas été discutés, nous pouvons supposer que les futurs changements de vent le long de la côte du Pérou et du Chili fournissent potentiellement un flux d'énergie dans ou hors du champ des tourbillons, en particulier autour de la région de Pisco. Néanmoins, nos résultats suggèrent que les tourbillons océaniques à méso-échelle ont le potentiel de rétroaction des processus océan-atmosphère régionaux aux interactions à grande échelle.

Appendix A

Conejero et al., (2020): Supplementary Information

Supplementary Information for:

ENSO diversity driving low-frequency change in mesoscale activity off Peru and Chile

Carlos Conejero[1*], Boris Dewitte[1,2,3,4], Véronique Garçon[1], Joël Sudre[1], and Ivonne Montes[5]

[1] Laboratoire d'Etudes en Géophysique et Océanographie Spatiales (LEGOS), Toulouse, France.

[2] Centro de Estudios Avanzados en Zonas Áridas (CEAZA), Coquimbo, Chile.

[3] Departamento de Biología, Facultad de Ciencias del Mar, Universidad Católica del Norte, Coquimbo, Chile.

[4] Millennium Nucleus for Ecology and Sustainable Management of Oceanic Islands (ESMOI), Coquimbo, Chile.

[5] Instituto Geofísico del Perú (IGP), Lima, Perú.

* Corresponding author e-mail: carlos.conejero@legos.obs-mip.fr

Table S1. Conditional correlation between interannual EKE variability from satellite altimeter data and ENSO indices over different phases (i.e. E and C indices either positive or negative) and time periods. The EKE was averaged over different regions in the Southeast Pacific (see boxes in the middle panels of Figure 1a). Bold numbers indicate that correlation is significant at the 95% confidence level based on the Student's t-test.

ENSO Phase	**< EKE | E > 1993-2018**	**< EKE | C > 1993-2018**	**< EKE | E > 2001-2018**	**< EKE | C > 2001-2018**
Box 1: Positive (E, C > 0)	**0.88**	0.04	**0.48**	**0.56**
Box 1: Negative (E, C < 0)	**0.49**	- 0.22	**0.56**	- 0.36
Box 2: Positive (E, C > 0)	**0.67**	- 0.31	- 0.18	- 0.21
Box 2: Negative (E, C < 0)	0.04	- **0.50**	0.03	- **0.60**
Box 3: Positive (E, C > 0)	- 0.25	- 0.05	- 0.04	- 0.08
Box 3: Negative (E, C < 0)	- 0.15	- 0.01	0.14	0.08

Table S2. Comparisons of the spatial patterns of the linear regression coefficients of the interannual EKE variability onto the E index (in cm^2/s^2) over the 1993-2008 period (see Figure S2 at lag zero) between satellite altimeter data and the model simulations (CR and Kelvin). SigmaF is the ratio RMS(model)/RMS(altimeter), where RMS is the Root Mean Square, and r is the correlation. RMS difference (diff) corresponds to RMS(altimeter – model).

Model simulation	**r**	**RMS (model)**	**RMS (diff)**	**SigmaF**
CR	0.75	21.31	13.9	1.41
Kelvin	0.77	21.45	14.2	1.42

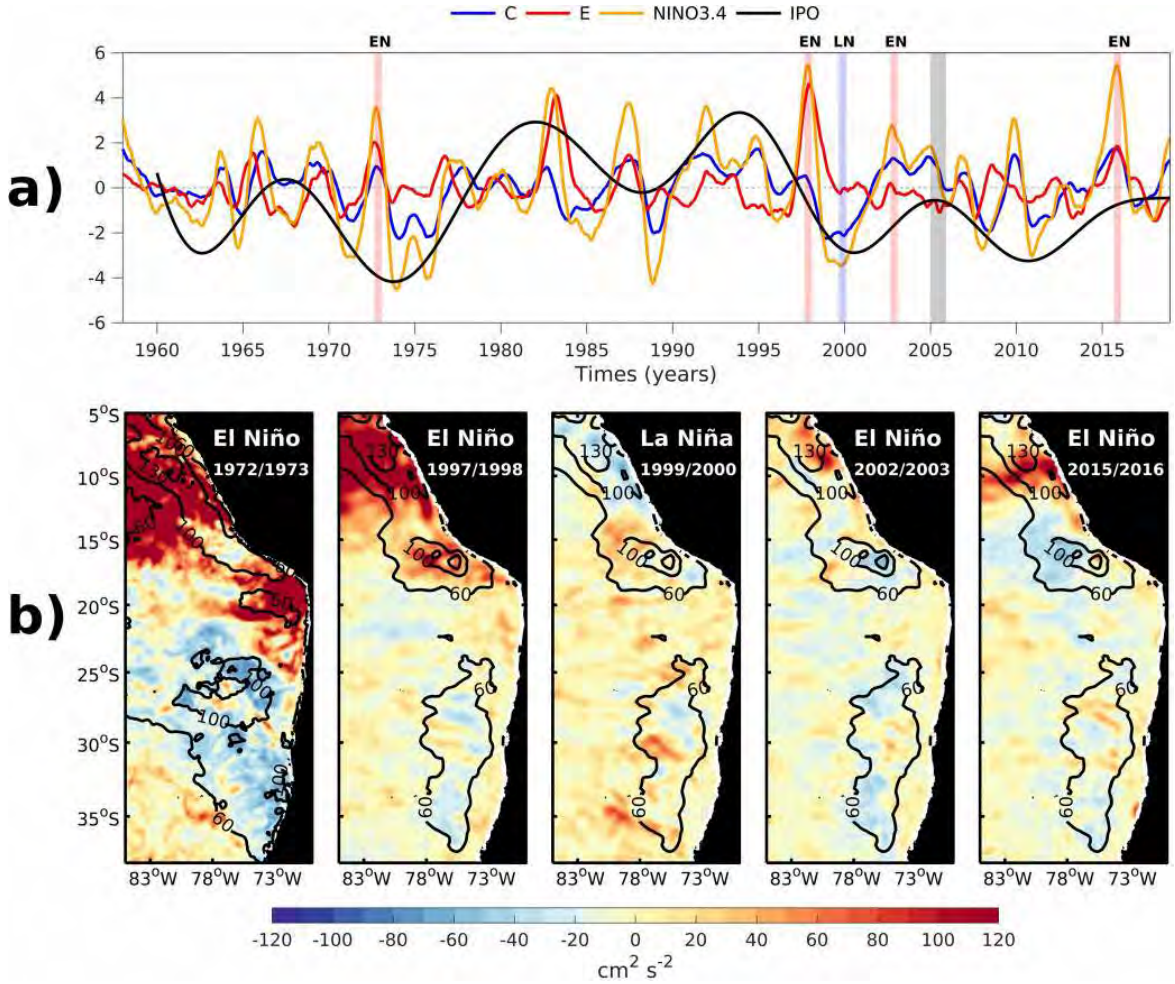

Figure S1. (a) Climate indices (ENSO and IPO) calculated from ERSST.v3b over the 1958-2018 period. (b) EKE anomalies during spring-summer (September to February) of different ENSO events. EKE anomalies during the 1972/1973 El Niño event were calculated from ROMS-CR simulation and during the others events were calculated from satellite altimeter GEKCO (see Methods in main text). Red and light blue shadow colors in (a) correspond to spring-summer period used to different El Niño (EN) and La Niña (LN) events. The gray shading in (a) indicates the 2005 year used as a repetitive atmospheric forcing for Kelvin simulation (see main text), showing that there were no marked anomalous climatic conditions during that particular year. The EKE anomalies were calculated removing the seasonal cycle over the 1993-2018 (1958-2008) period from GEKCO (ROMS). Black contour lines in the maps (60, 100 and 130 cm^2/s^2) correspond to the mean EKE values over the 1993-2018 (1958-2008) period from GEKCO (ROMS).

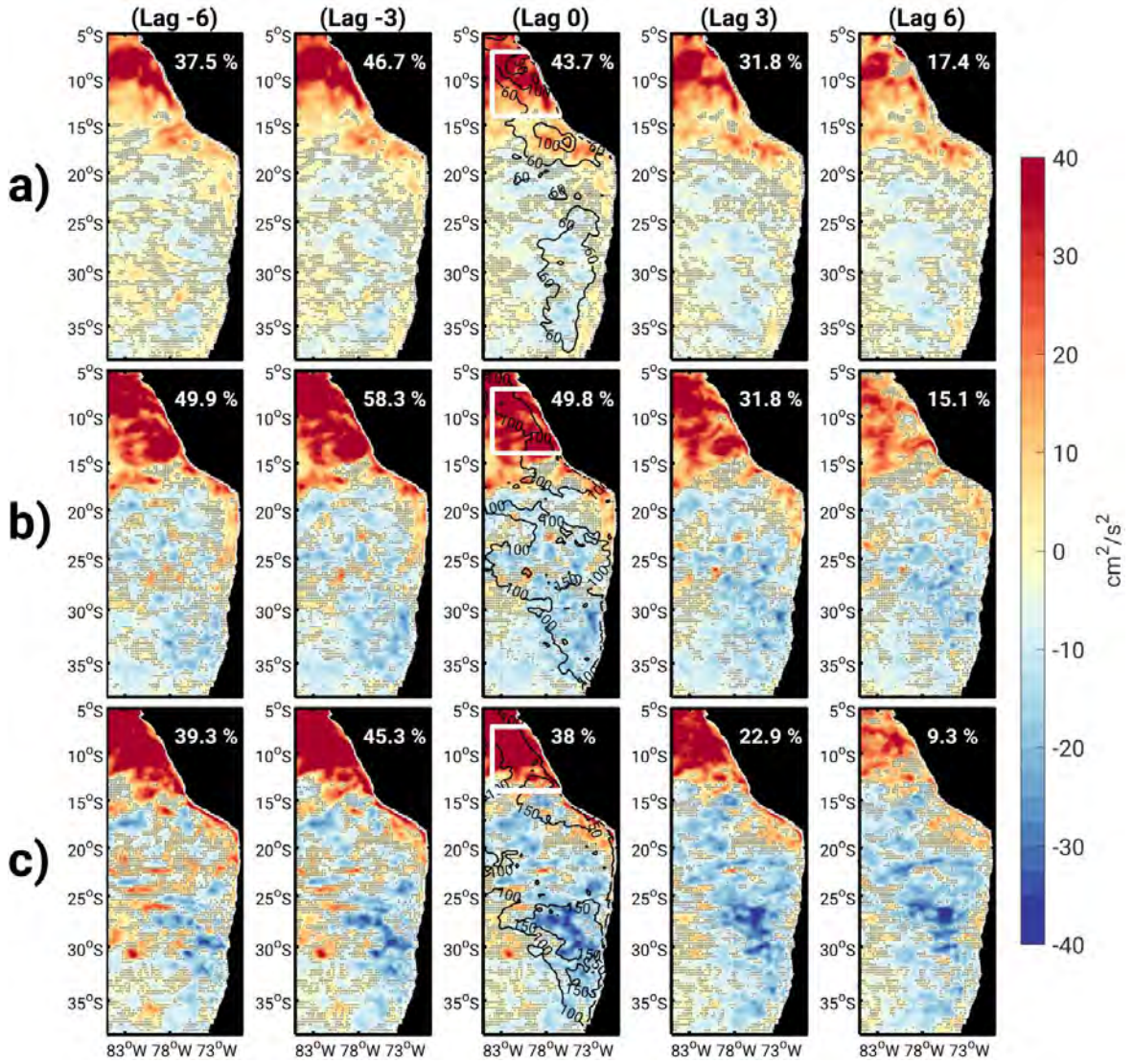

Figure S2. (a) Same as Figure 1a (see main manuscript) but for the analysis performed over the common period between model simulations and observations, i.e. 1993-2008, and (b, c) for the model simulations ((b) CR and (c) Kelvin). The percentage of explained variance averaged over the Peru region (see white box in the maps at lag zero) is indicated on each panel.

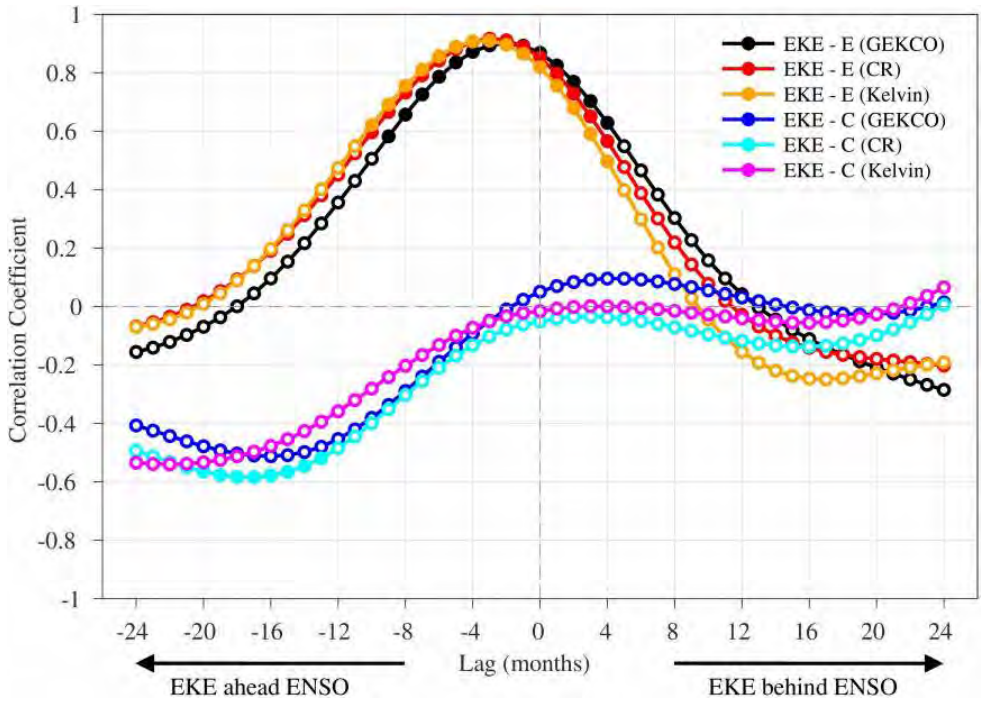

Figure S3. Lag-correlation between interannual EKE anomalies, averaged over the Peru region (14°S-7°S, 83°W-coast), and ENSO indices over the 1993-2008 period. The EKE anomalies were calculated from satellite altimeter data (GEKCO) and model simulations (CR and Kelvin). Full (white) circles indicate that correlation is significant (non-significant) at the 95% confidence level based on the Student's t-test.

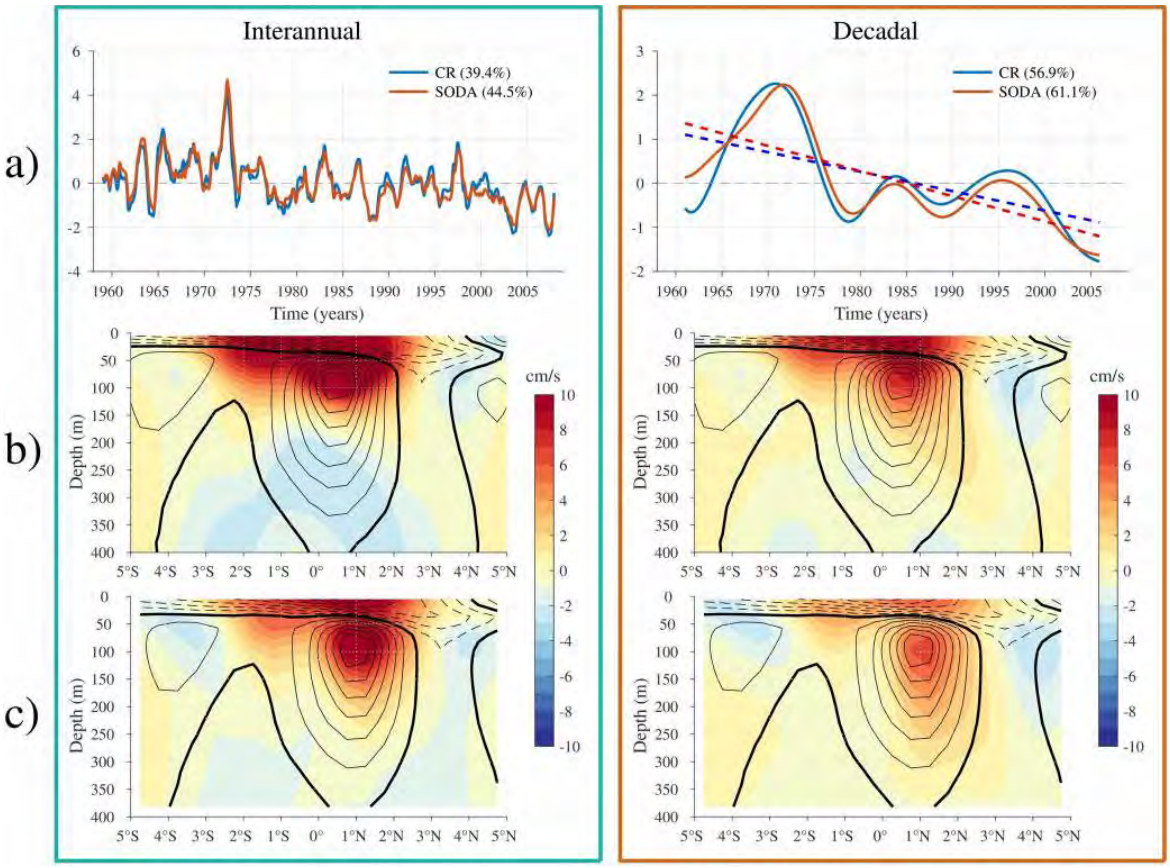

Figure S4. First EOF mode of the low-frequency variability (interannual to decadal) of the zonal currents anomalies at 88°W and over the domain (z=[0:400m], y=[5°S-5°N]) for the CR simulation and SODA, over the 1958-2008 period. a) Principal components, b,c) spatial pattern for b) SODA, and c) CR simulation. Explained variance is provided in a). Solid thick black line in b,c) corresponds to 0 cm/s, and thin (dotted) black lines correspond to positive (negative) eastward (westward) velocities every 2 cm/s. Note that the Equatorial Under Current (EUC) is centered around 0°-1°N and 100 m depth for both CR experiment and SODA. Linear long-term trends are plotted in a) for decadal variability (dashed lines), which are significant at the 95% level based on the Student's t-test.

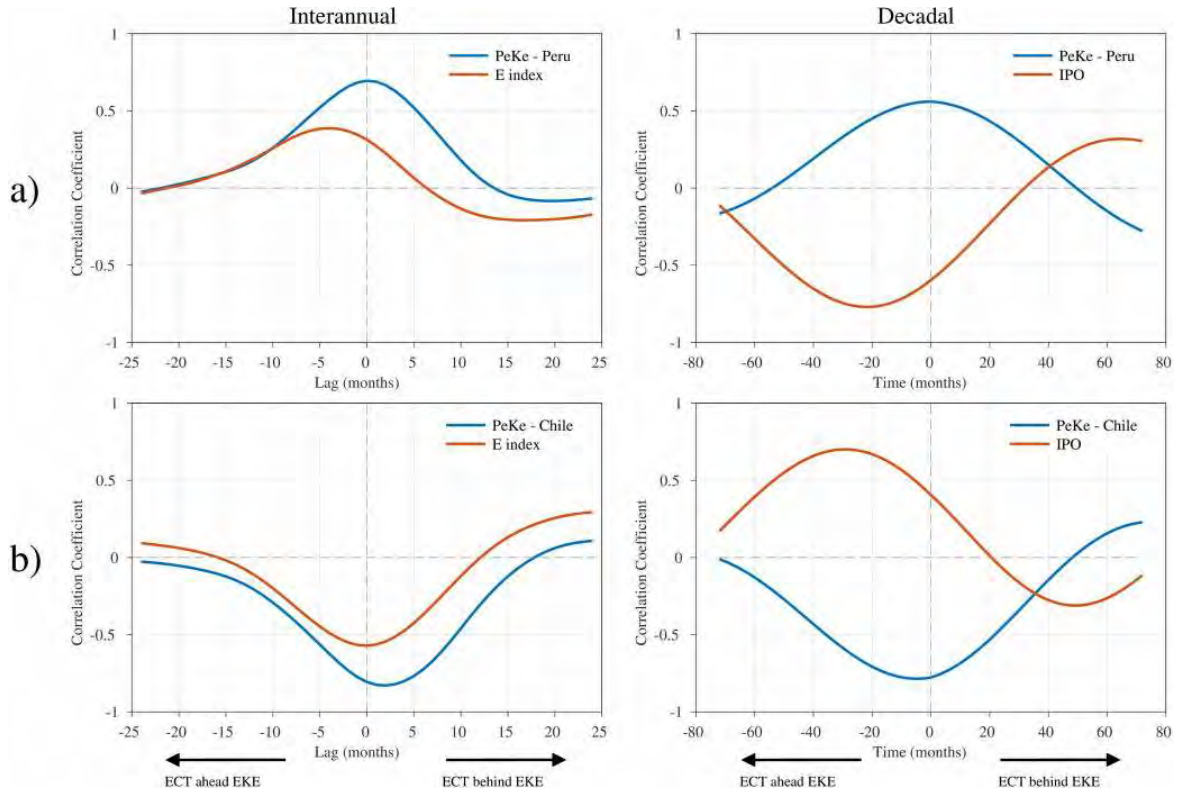

Figure S5. Lag correlation between the PCs-1 of the eddy conversion terms (ECT) and EKE from CR simulation at (left panels) interannual to (right panels) decadal timescales for the a) Peru and b) Chile regions. Note that the maximum/minimum correlations ($|r| > 0.5$) are associated with the baroclinic instability process.

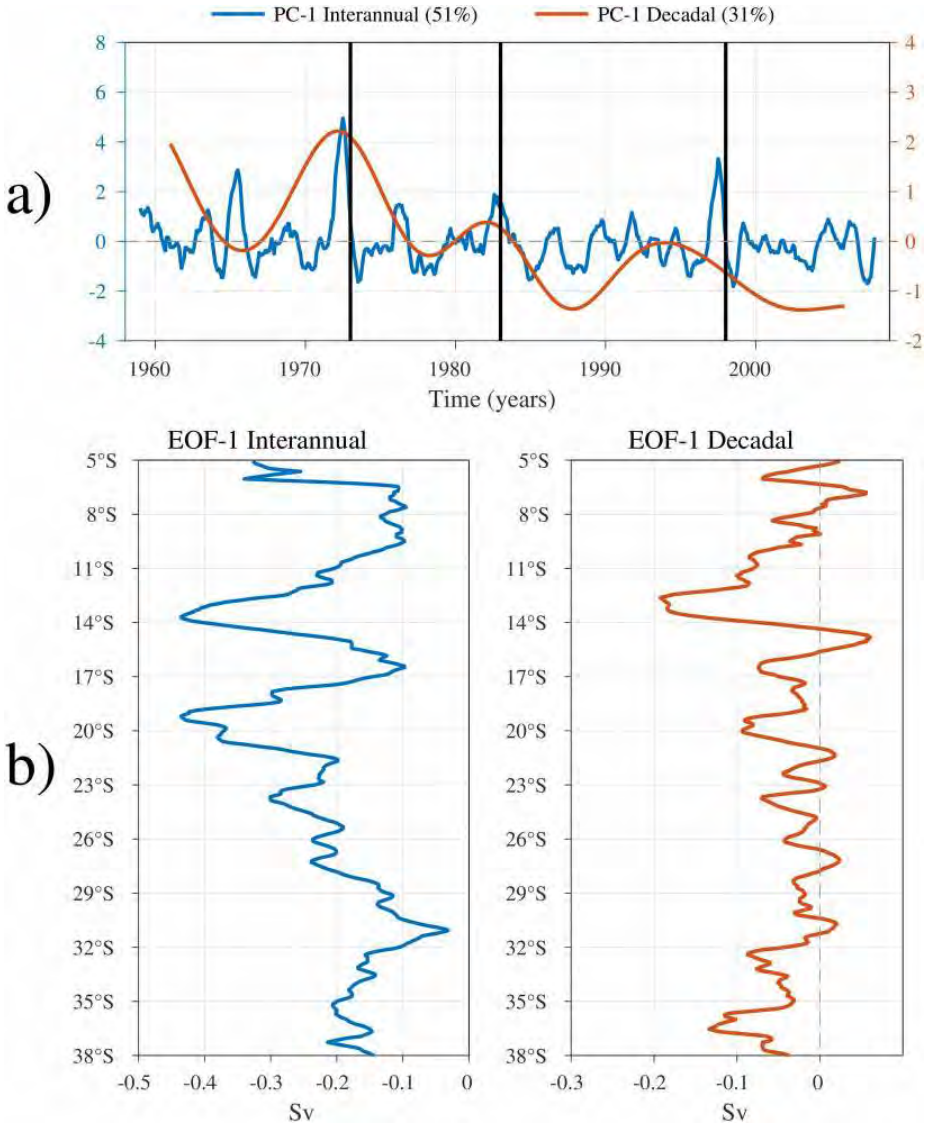

Figure S6. First EOF mode of the Peru-Chile Undercurrent transport (see Methods section) between 5°S and 38°S for interannual (blue) and decadal (red) timescales in the CR simulation over the 1958-2008 period. a) Principal components, b) spatial pattern. Explained variance is provided in a). Black lines in a) represent the peak of El Niño during 1972/73, 1982/83 and 1997/98 events, which corresponds to January of 1973, 1983 and 1998, respectively.

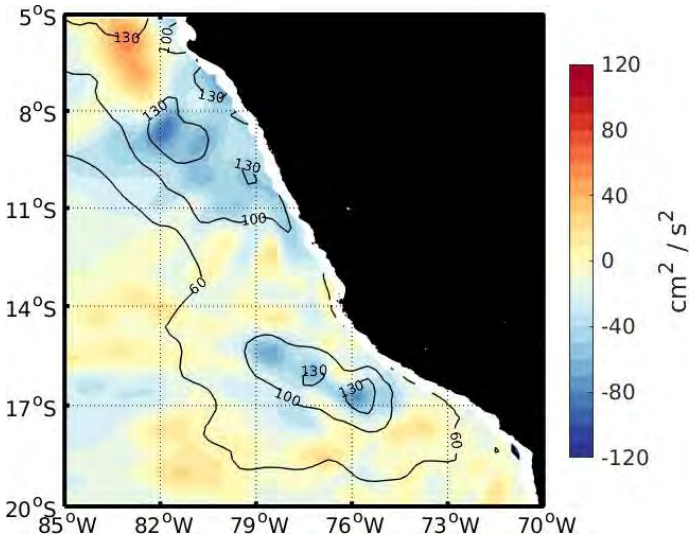

Figure S7. EKE anomalies averaged over the season February-March-April during the 2017 coastal El Niño event from observations (GEKCO). The EKE anomalies were calculated removing the seasonal cycle over the 1993-2018 period. Black contour lines (60, 100 and 130 cm^2/s^2) correspond to the mean EKE values over the 1993-2018 period.

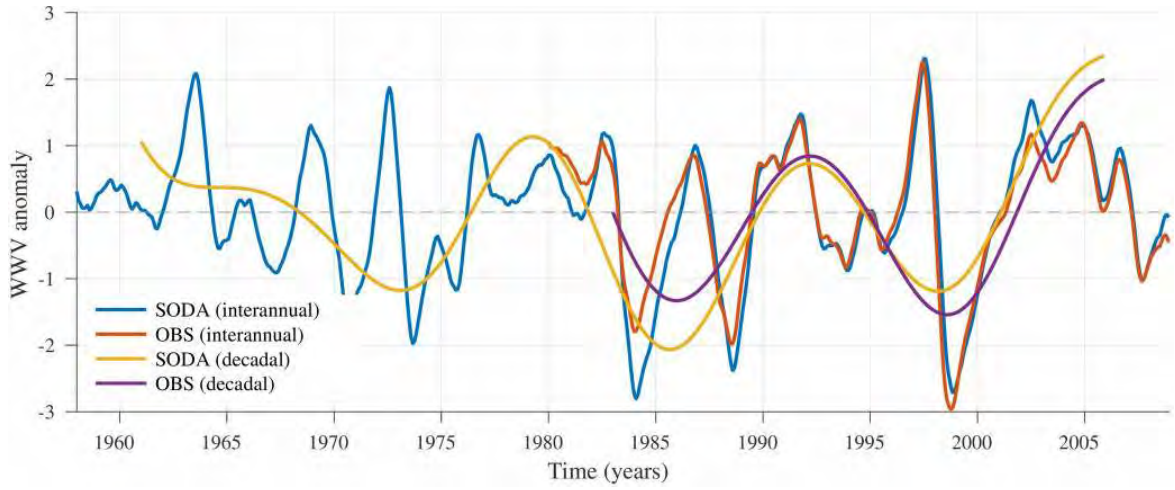

Figure S8. Low-frequency variability of the Warm Water Volume (WWV) from observations and the SODA Reanalysis. The WWV was calculated as the depth averaged temperature over the upper 300 m (T300) in oceanic regions of the equatorial Pacific between 5°N to 5°S, 120°E to 80°W . The WWV observations are from the ocean analyses of the Bureau National Operations Centre (BNOC) at the Australian Bureau of Meteorology, which are based on temperature profiles from TAO moorings, Argo floats and XBTs.

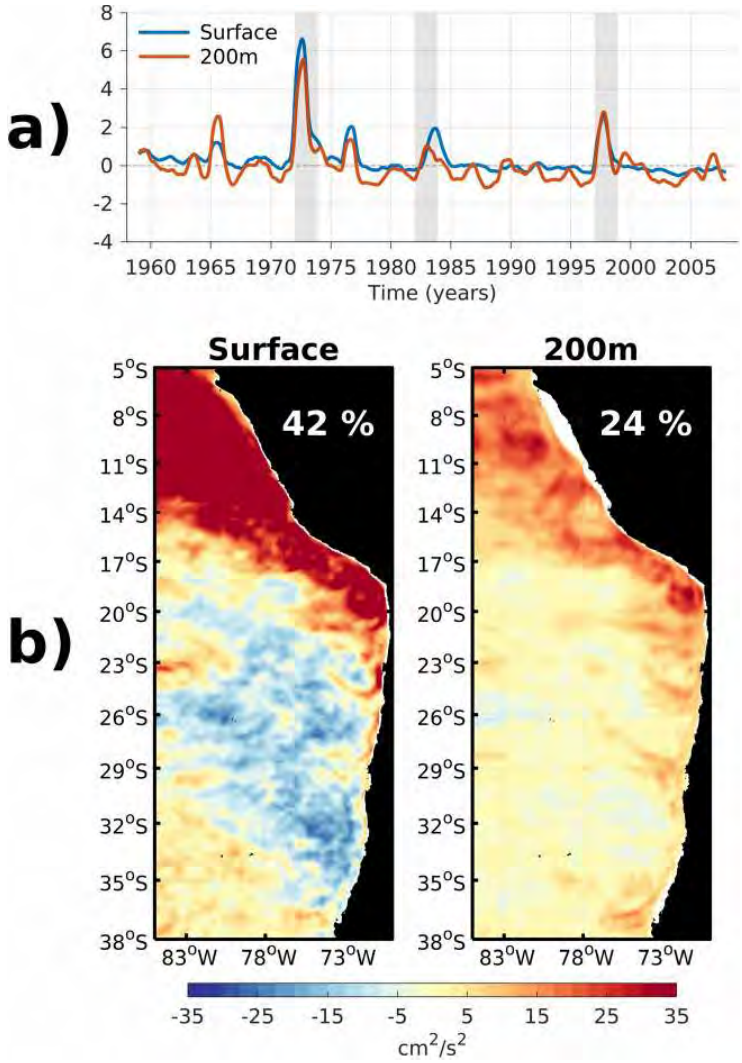

Figure S9. First EOF mode of interannual EKE variability in the Southeast Pacific at the surface and at 200m depth from the CR simulation over the 1958-2008 period. a) Principal components, and b) spatial patterns. Light gray shading in a) corresponds to the three strong EP El Niño events (1972/73, 1982/83 and 1997/98). Explained variance of the EOF modes is provided in the maps.

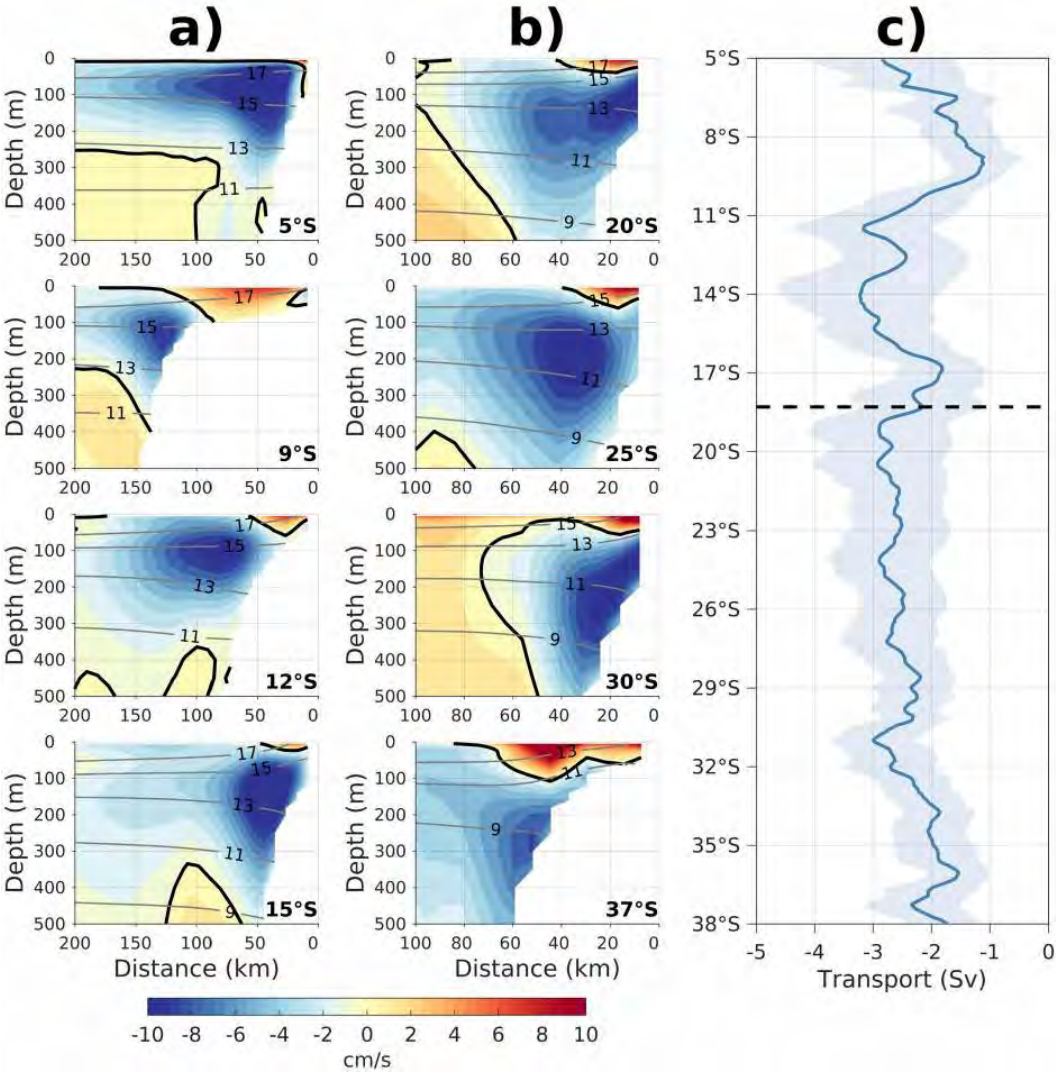

Figure S10. Mean meridional currents from CR simulation over the 1958-2008 period and at different cross-shore sections along the coast of Peru and Chile. a) Peru coast, and b) Chile coast. Equatorward (poleward) currents correspond to positive (negative) values in colors. Gray lines indicate the mean isotherms from 9°C to 17°C. c) Long-term mean value of the simulated Peru-Chile Undercurrent transport (see Methods section). The shading indicates the dispersion, i.e.± the standard deviation of the PCUC transport during the whole period. The horizontal dashed black line corresponds to the limit between Peru (5°S-18°S) and Chile (18°S-38°S) regions. Negative PCUC transport values indicate poleward flux.

Appendix B

UHR-CESM validation

B.1 Surface and subsurface temperature

The mean climatological SST conditions from UHR-CESM PD simulation are compared with observations (ERSST.v5) and CMIP5 multi-models in Figure B.1. The UHR-CESM PD simulation shows significant improvements in contrast to CGCMs. The strong warm bias commonly detected in the EBUS from CGCMs (e.g., **Richter**) is highly reduced, especially in the California and Peru-Chile Upwelling Systems. However, the Peruvian coast and the Benguela Upwelling System are still exhibiting a small warm bias. The 27°C isotherm agrees well with observations, notably in the tropical Atlantic Ocean. In addition, the excessive zonal extension of the "cold tongue" in the eastern Pacific usually seen in CMIP models appears to be reduced in UHR-CESM PD simulation. On the other hand, the "warm pool" located in the western equatorial Pacific is warmer than that of both CGCMs and observations. This region is very sensitive to the development of ENSO events sustained by the strength of the east-west SST gradient (e.g. Fedorov and S. G. Philander, 2000). The warm SST bias in UHR-CESM PD simulation also extends outside of the subtropics to high latitudes in both hemispheres.

In the subsurface layers of the equatorial Pacific region the UHR-CESM PD simulation exhibits a significant warm temperature bias compared with both observations and CESM-LENS (Figure B.2). The equatorial thermocline is too deep and too diffuse, with a temperature bias reaching 3°C between 50-200 m depth in the eastern Pacific and 1.5°C above 100 m depth in the western Pacific (Figure B.2a). This is a common feature from global climate models which is partly due to uncertainties in estimates of vertical diffusivity in models (Jochum, 2009). Current CGCMs typically use a diffusivity coefficient of 0.1 cm^2/s, but theory and observations suggest that this coefficient should not homogeneous in space, with in particular reduced diffusivity values at the equator and increased around 30°N/S (Jochum, 2009). In the UHR-CESM PD simulation the latitudinal variations in vertical diffusivity were not yet implemented, which

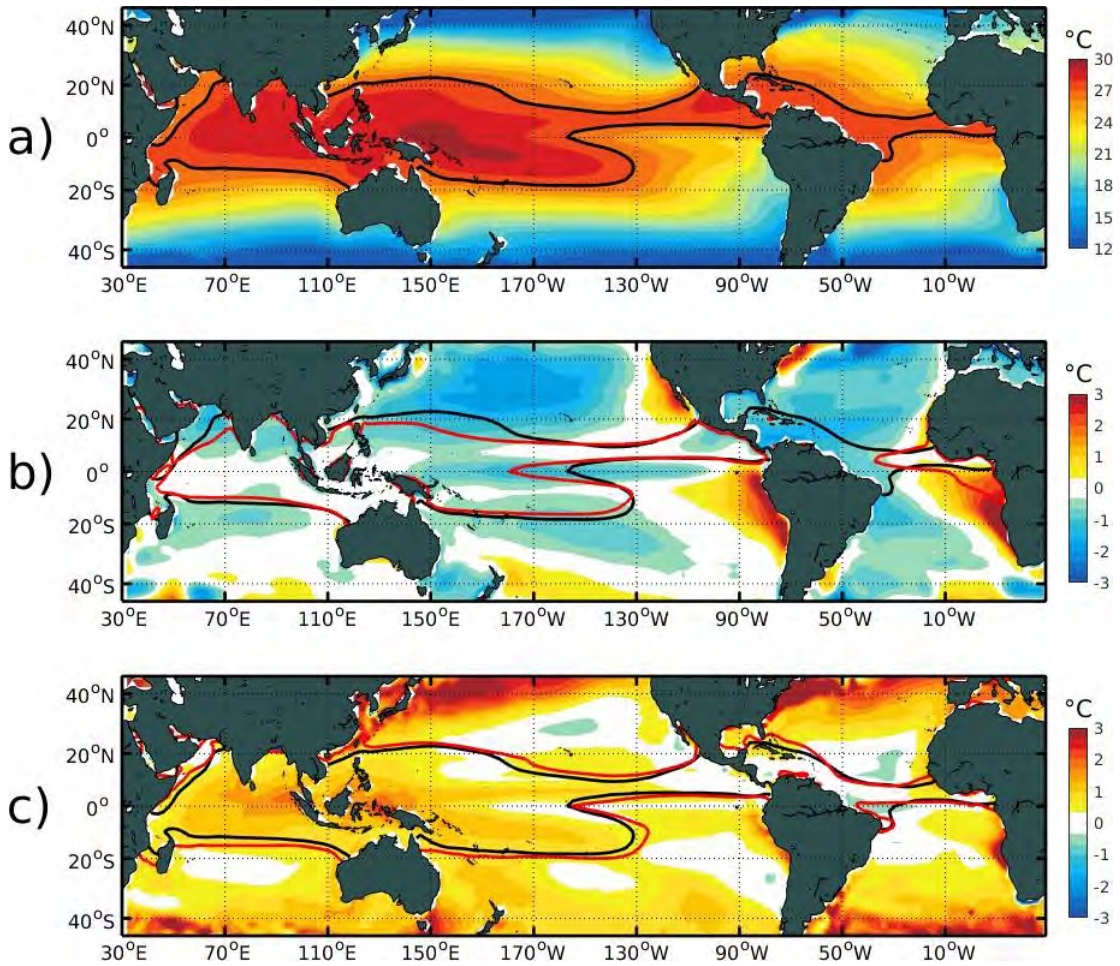

Figure B.1: *a) Mean state of sea surface temperature (SST) of ERSST.v5 over the 1900-2019 period. b-c) SST bias of global coupled models against ERSST.v5. b) CMIP5 27 mean-models (Historical runs, 1900-2005 period), and c) UHR-CESM PD simulation (120-years). The black (red) contour indicates the 27°C isotherm of ERSST.v5 (climate models). The bias is defined as the difference between the global coupled models minus ERSST.v5.*

could explain the subsurface temperature bias in the equatorial Pacific (Small et al., 2014). In fact, this warmer bias is greater than CESM-LENS in both western and eastern equatorial regions, which could overestimate the heat transport by the equatorial current system that is connected with the coastal currents in the EBUS of the Pacific Ocean. In this regard, a strong warm subsurface temperature bias is also found alongshore of the Peru-Chile Current System in the UHR-CESM PD simulation in contrast to a slightly warm temperature bias from CESM-LENS (Figure B.3). This could be related to the warm equatorial Pacific subsurface temperature bias where the Equatorial Undercurrent (EUC) brings warmer waters into the Peru-Chile Undercurrent (PCUC) increasing the stratification and deepening the thermocline (15°C isotherm) along the Peru and Chile coasts.

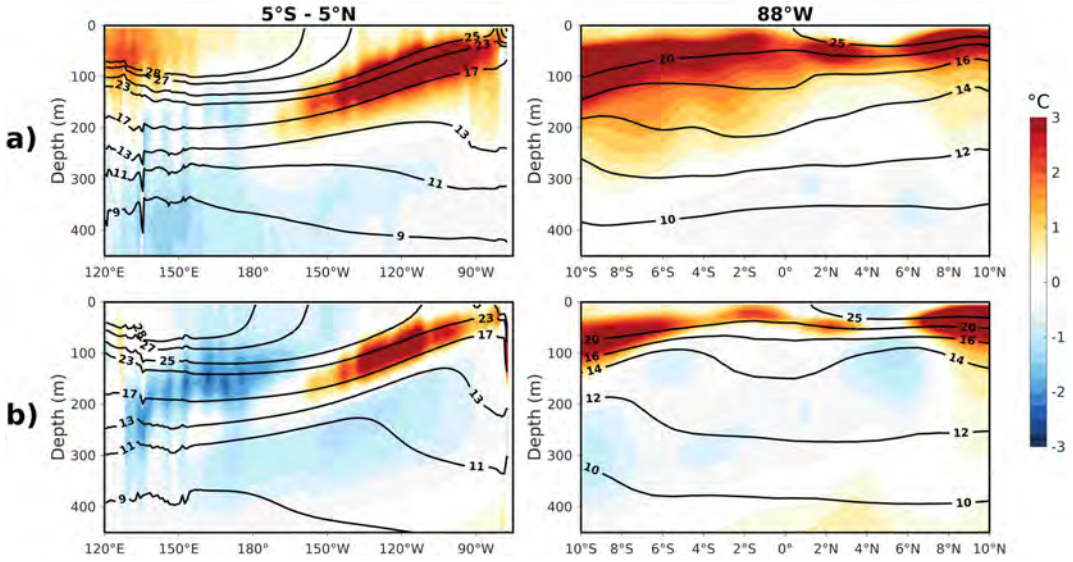

Figure B.2: *Subsurface temperature bias (shading) of global coupled models against observations along the Pacific equator (5°S-5°N, left panels) and latitudinal section at 88°W (right panels). a) UHR-CESM PD simulation, and b) CESM-LENS 40 mean-ensemble. Observations correspond to climatology CARS-2009. The black contour lines correspond to the mean state from each global coupled model. The bias is defined as the difference between the global coupled models minus observations.*

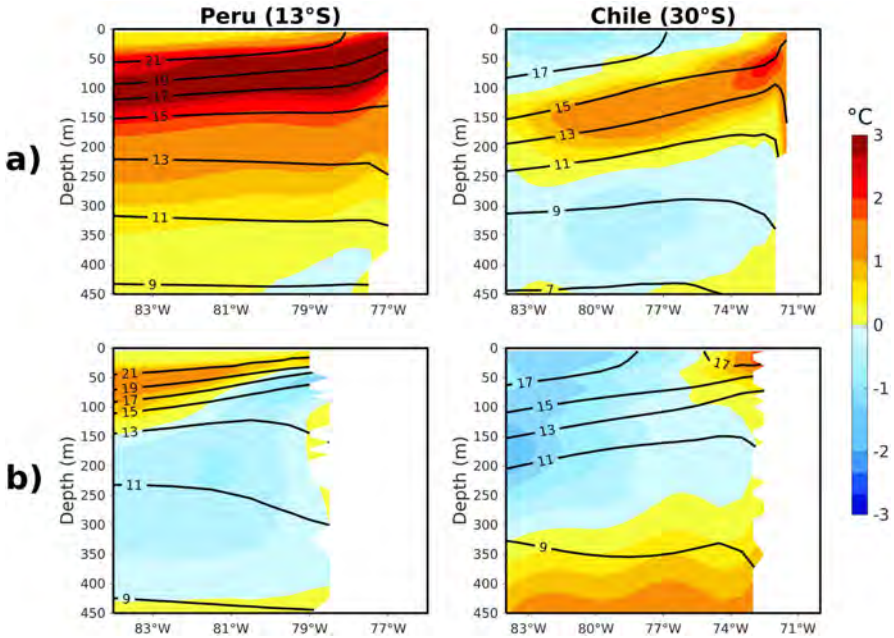

Figure B.3: *Subsurface temperature bias (shading) of global coupled models against observations along the Southeast Pacific coasts for Peru (13°S, left panels) and Chile (30°S, right panels) sections. a) UHR-CESM PD simulation, and b) CESM-LENS 40 mean-ensemble. Observations correspond to climatology CARS-2009. The black contour lines correspond to the mean state from each global coupled model. The bias is defined as the difference between the global coupled models minus observations.*

B.2 Winds in the Peru-Chile Current System

The PCUS is within the year-round influence of the southeast Pacific anticyclone, corresponding in upwelling favorable winds alongshore which intensify near land into a low-level jet parallel to the coast and become trades winds farther offshore (e.g., R. Garreaud and Muñoz, 2005). Figure B.4 represents the wind stress and wind stress curl associated to the PCUS based on satellite products and CGCMs, considering the coarse-to-high spatial resolutions. The intensity and position of the southeast Pacific anticyclone are comparable in all products. However, the alongshore winds in the Chile region are not simulated realistically by the low-resolution products (Figure B.4a-b) in terms of magnitude and latitudinal extension in contrast to the high resolution satellite products (Figure B.4c-d).

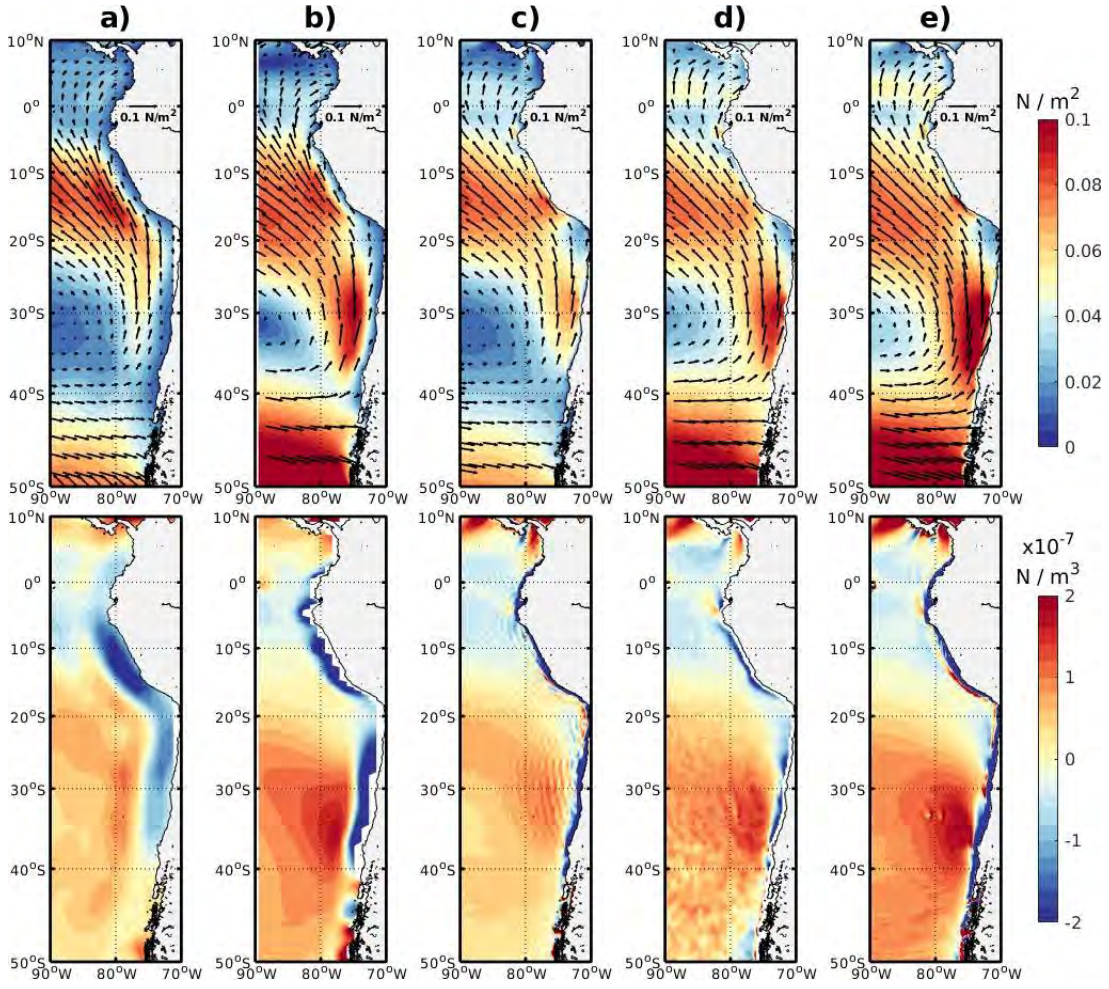

Figure B.4: *Mean state of wind stress (upper panels) and wind stress curl (lower panels) in the Southeast Pacific from a) NCEP-NCAR, b) CESM-LENS 40 mean-ensemble, c) ERA5, d) SCOW, and e) UHR-CESM PD simulation. Shading correspond to wind stress magnitude (upper panels) and wind stress curl (lower panels). Vectors represent the wind stress direction in upper panels. Details of data sets used are indicated in supplementary data.*

The UHR-CESM PD simulation (Figure B.4e) is quite similar to the climatological SCOW product (Figure B.4d), reproducing the low-level jet parallel to the coast as well as the strong intensity winds southward off central Chile corresponding to the Chile Coastal Jet. However, the patch of the strong winds in central Chile (around 30°S) is slightly overestimated by the UHR-CESM PD simulation, in terms of magnitude and spatial extension. Moreover, the wind stress curl estimated by the UHR-CESM agrees fairly well with high-resolution satellite products. This is an important feature for the oceanic circulation because the wind stress curl is commonly associated to the Ekman pumping, which is the result of a cyclonic wind stress curl (negative values) caused mainly by the wind drop-off that extends only tens of kilometers in width along the coast. Low-resolution products cannot reproduce correctly the wind-induced upwelling waters (Figure B.4a-b), that is crucial in the EBUS.

B.3 Peru-Chile and Equatorial Pacific Current System

Currently, CGCMs have problems to reproduce the upwelling dynamics in the EBUS by their low-resolution. As an illustration, we present in Figure B.5 two vertical sections of the simulated oceanic meridional current offshore Peru and Chile from the two versions of the CESM model. The low-resolution CESM-LENS (Figure B.5a) is unable to simulate realistically the PCUC, which is a poleward subsurface current situated in the first 100 km alongshore the Peru-Chile region with values around 10-15 cm/s (e.g., Chaigneau et al., 2013; Pizarro et al., 2001, 2002; Shaffer et al., 1997). While the PCUC is too weak and detached from the continental slope in CESM-LENS, UHR-CESM PD simulates remarkably well the PCUC in terms of magnitude and vertical extension (Figure B.5b), as well as the Coastal Chilean Current (CCC, Shaffer et al., 1999, 1997), which is an equatorial surface current located along the narrow Chilean coasts. In addition, we contrast the UHR-CESM PD simulation with in-situ data from central Chile region at 30°S (Figure B.5c). The PCUC is properly simulated from 50 to 400 m depth, with values in their core of 15 cm/s at 150 m depth.

The equatorial Pacific current system plays an important role in the oceanic teleconnections with the Southeast Pacific transporting water masses properties. Figure B.6 shows a comparison of the equatorial current system at 88°W between two high resolution reanalysis products (ORAS-5 and SODA) and the two versions of the CESM (LENS and UHR). Both CESM-LENS and UHR-CESM PD simulations reproduce an adequate equatorial current system, represented by: Equatorial Undercurrent (EUC), Surface Equatorial Current (SEC), North Equatorial Countercurrent (NECC), and the subsurface Tsuchiya jets around the EUC. However, some differences can be noted.

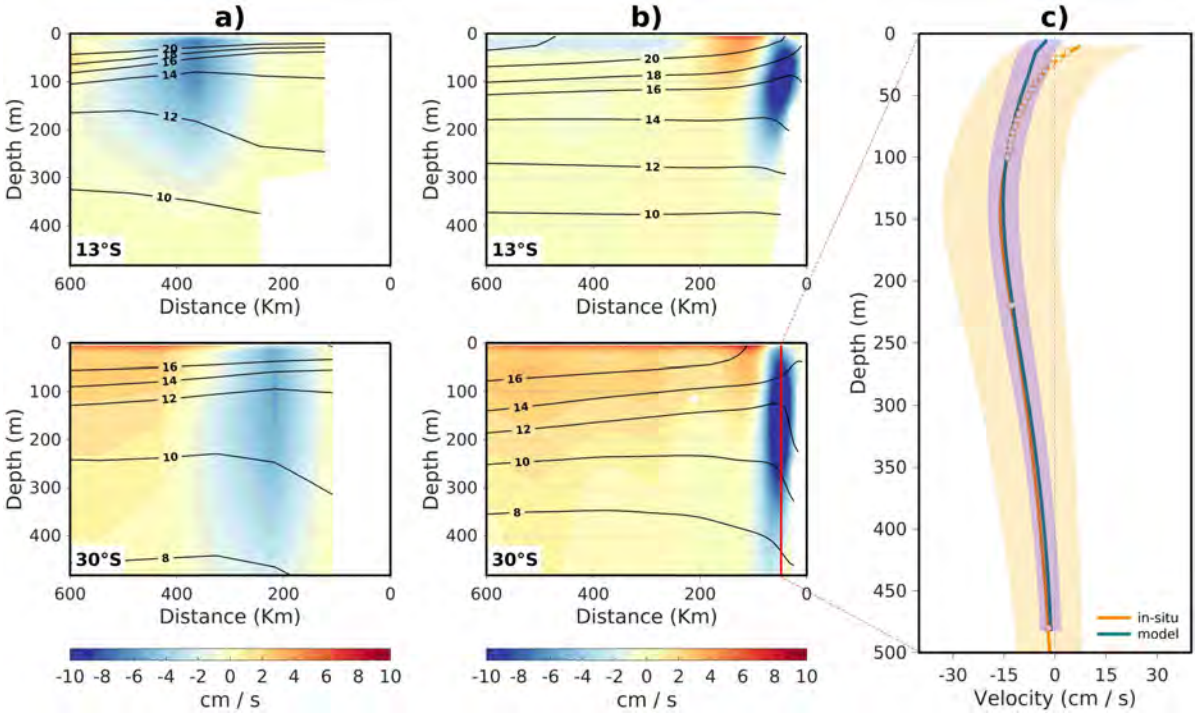

Figure B.5: *Vertical sections of alongshore currents off Peru (13°S) and Chile (30°S). a) CESM-LENS 40 mean-ensemble, b) UHR-CESM PD simulation, and c) comparison between UHR-CESM PD simulation (blue line) and in-situ data (orange line) at 30°S and 50 km offshore. The in-situ data corresponds to COSMOS station during the 2003-2008 period (see Chapter 2). Shadows correspond to the standard deviation. The black contour lines in a-b) correspond to the mean temperature at each vertical section and global model simulation.*

The CESM-LENS simulates weaker surface currents (SEC and NECC), while the UHR-CESM is particularly in good agreement in terms of magnitude and vertical extension with both SODA and ORAS-5 reanalysis products. The EUC in both versions of the CESM tends to have less vertical extension in comparison with SODA, but it is very close to the vertical extension shown by ORAS5. Another interesting remark is that the UHR-CESM PD simulation can reproduce and separate the Tsuchiya jets from the EUC, which is also observed in the SODA reanalysis product.

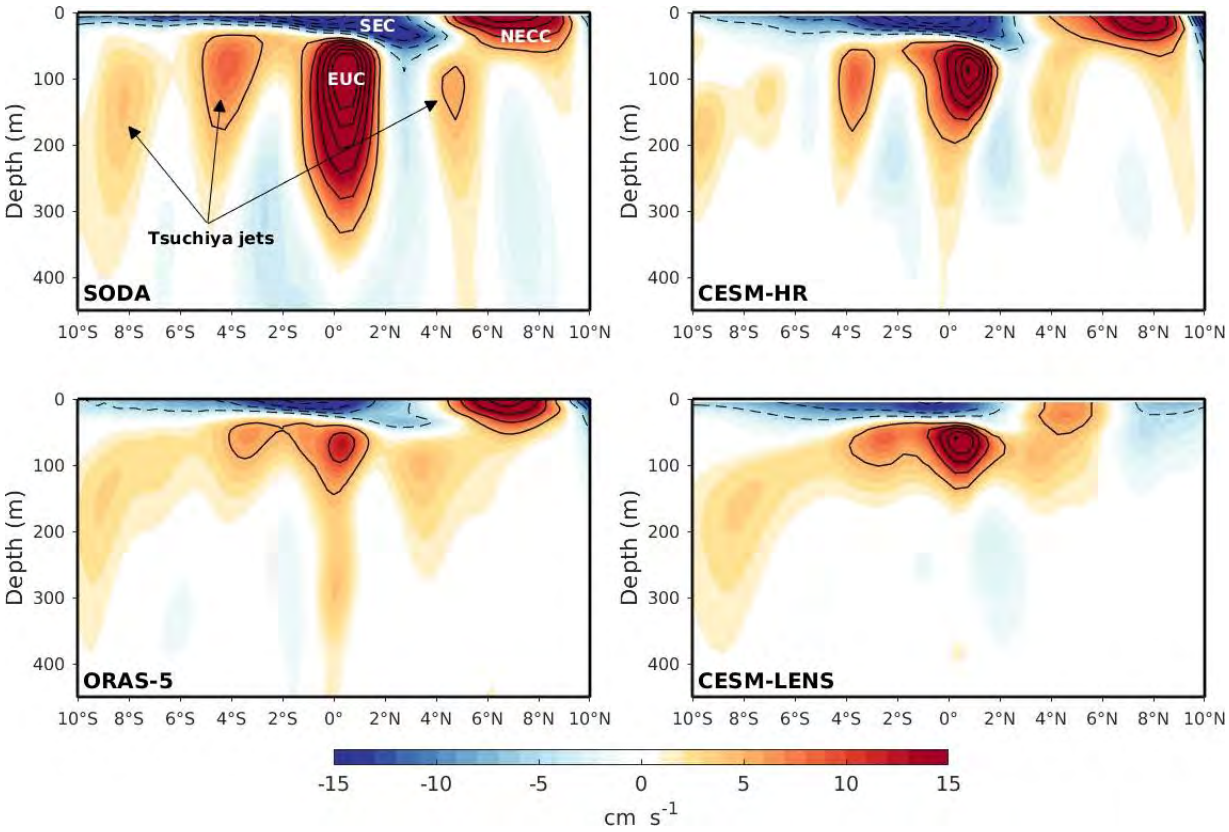

Figure B.6: *Equatorial current system of the Pacific ocean at 88°W from reanalysis products (left panels) and global coupled models (right panels). Positive (negative) values indicate eastward (westward) currents. The black solid (segmented) lines represent the eastward (westward) currents every 5 (-5) cm/s. The equatorial currents correspond to: Equatorial Undercurrent (EUC), Surface Equatorial Current (SEC), North Equatorial Countercurrent (NECC), and the subsurface Tsuchiya jets around the EUC.*

B.4 Mesoscale activity in the South East Pacific

The EKE in the Peru-Chile Upwelling System is compared between satellite altimeter data and the two versions of CESM in Figure B.7. The strong mean EKE values alongshore the Peruvian coast (>100 cm^2/s^2) and offshore central Chile (>70 cm^2/s^2) detected by observations (Figure B.7a) are not simulated by CESM-LENS (Figure B.7b) because of its low-resolution not allowing to resolve eddies. On the other hand, the UHR-CESM PD simulation, which is an eddy-resolving version of CESM, is able to reproduce the mesoscale activity in the PCUS (Figure B.7c) with a remarkably good skill. The high EKE values off Peru (>100 cm^2/s^2) are in good agreement with observations (Figure B.7d), with a slight overestimation southward of the Pisco region at 15°S. In contrast, the patch of observed intense mesoscale activity offshore central Chile is absent in the UHR-CESM PD simulation. Nevertheless, the immense breakthrough to include mesoscale processes in the UHR-CESM PD simulation constitutes a major

achievement to determine the role of ocean eddies in the future climate system.

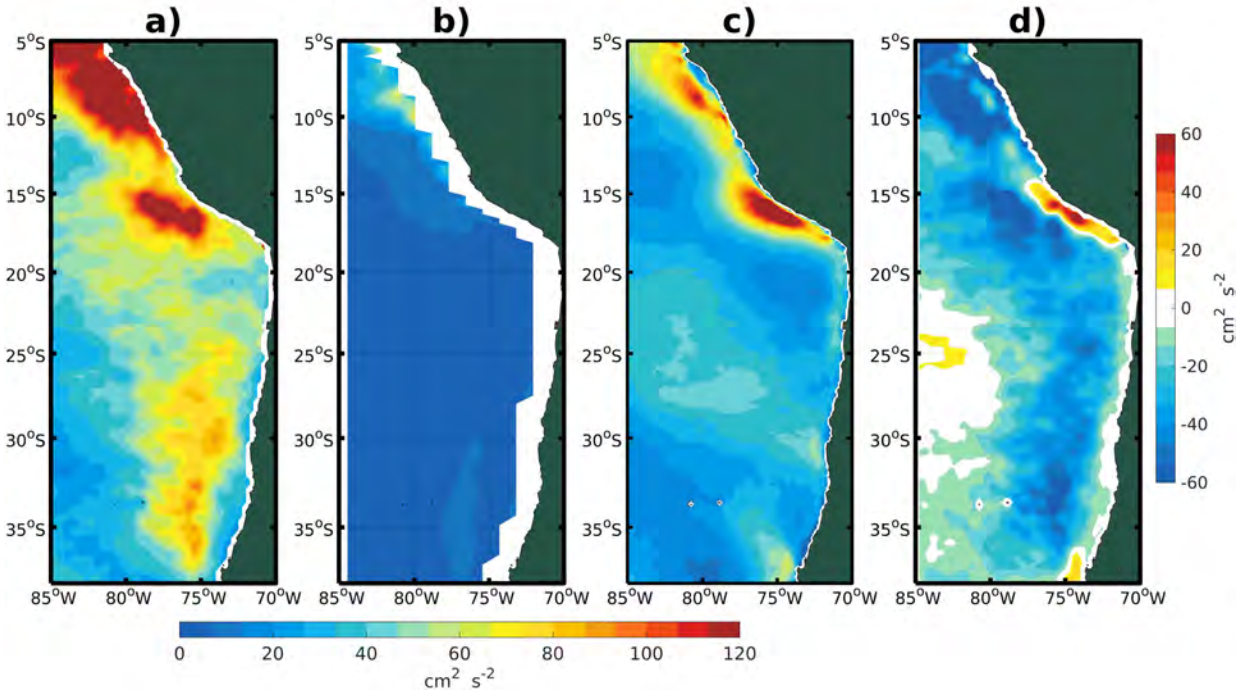

Figure B.7: *Mean eddy kinetic energy (EKE, in cm^2/s^2) in the Peru-Chile Current System. a) Satellite altimetric data (GEKCO), b) CESM-LENS 40 mean-ensemble, c) UHR-CESM PD simulation, and d) bias of UHR-CESM PD simulation minus GEKCO.*

B.5 ENSO diversity

The diversity and complexity of the ocean-atmosphere feedbacks involved into the different types of ENSO events (e.g., Capotondi et al., 2015; Okumura, 2019; Timmermann et al., 2018), make difficult the representation of event-to-event ENSO variability in CGCMs. Enormous efforts have been deployed to improve understanding and modeling the ENSO features in state-of-the-art climate models (Bellenger et al., 2014; Capotondi et al., 2006; Guilyardi, 2006; Guilyardi et al., 2012, 2009; Leloup et al., 2008). Here, the Eastern Pacific (EP) and Central Pacific (CP) El Niño events (Takahashi et al., 2011), including La Niña events, are compared between long-term record from observations (ERSST.v5, 1900-2019 period) and UHR-CESM PD simulation (120 years) in Figures B.8-10. The spatial patterns of the two ENSO regimes are well reproduced by the UHR-CESM PD simulation (Figure B.8). This indicates the ability of the model to realistically simulate the non-linear character of ENSO. The EP El Niño events are largely developed in the eastern equatorial Pacific band, while CP El Niño (or La Niña) events occur in the western-central equatorial Pacific, off the eastern basin. However,

a westward extension in both EP and CP patterns is evidenced in the UHR-CESM PD simulation, principally in the EP El Niño mode.

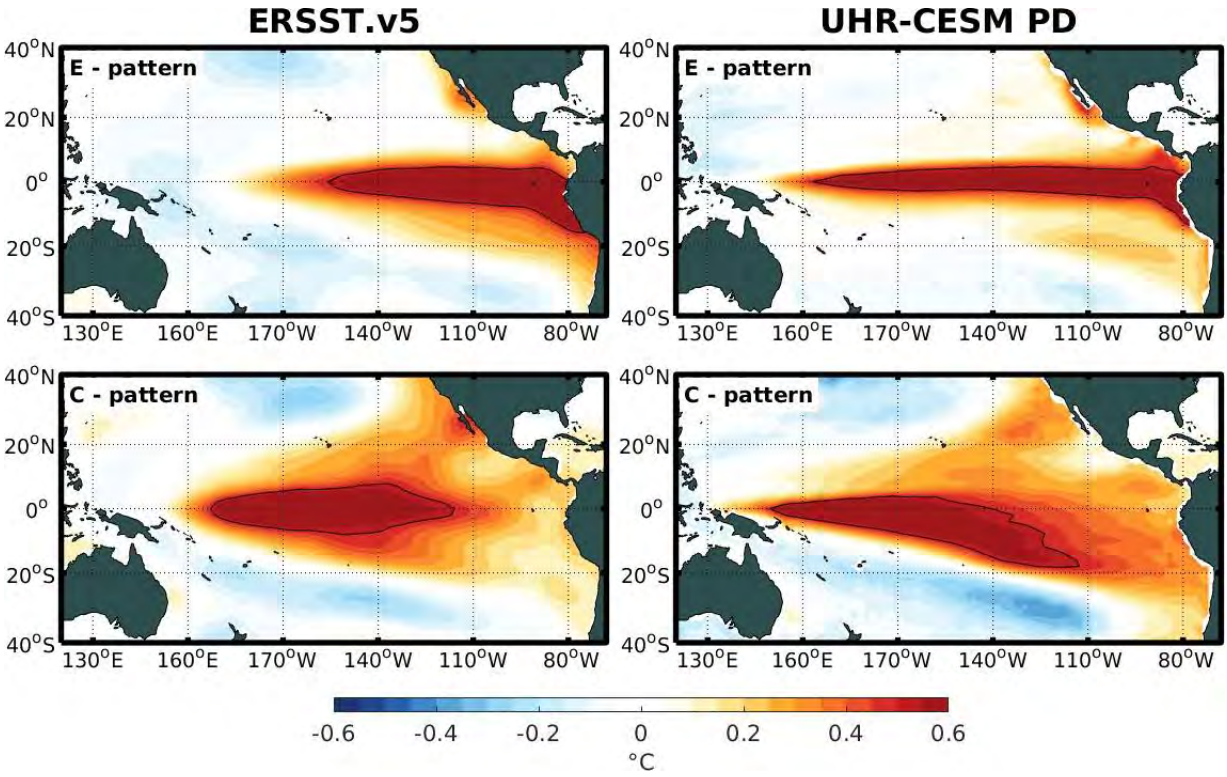

Figure B.8: *ENSO diversity from observations (ERSST.v5, 1900-2019 period) and model simulation (UHR-CESM PD, 120 years). a-b) Spatial pattern of Eastern Pacific (E-pattern) and Central Pacific (C-pattern) El Niño from a) ERSST.v5, and b) UHR-CESM PD simulation. The spatial pattern are expressed as the linear regression coefficients (in °C) between the sea surface temperature anomalies and ENSO indices (E and C). c) Scatter plot between ENSO indices from observations (orange dotes) and model simulation (cyan dotes) over 120 years. Thick black dotes correspond to austral summer season (DJF). The EP (CP) El Niño events are represented when the E-index (C-index) is greater than 1, and La Niña events when the C-index is less than -1.*

The climatology of the standard deviation and skewness corresponding to both EP and CP indices is presented in Figure B.9. The seasonal evolution shows important differences with respect to observations. The peak of the seasonal standard deviation in EP mode occurs during austral winter (JJA) in observations, while in UHR-CESM PD simulation this happens in austral spring-summer (NDJ). On the other hand, the seasonal standard deviation of the CP mode is totally opposite between observations and UHR-CESM PD simulation. The skewness of ENSO regimes reflects the asymmetry in their associated spatial pattern and the physical mechanisms involved (Cai et al., 2018). In this sense, the climatological skewness of the E index reveals that both observations and UHR-CESM PD simulation have a greater amplitude of EP El Niño events

during austral summer (positive skewness values). However, the UHR-CESM PD simulation indicates that cold SST anomalies tend to take place in austral autumn-winter (negative skewness values), which is not evidenced in observations. By contrast, the negative skewness of the C-index in both observations and UHR-CESM PD simulation reflects a stronger amplitude of CP La Niña events than of CP El Niño events. Nonetheless, the seasonal skewness shows that the strong amplitude of CP La Niña events occurs during austral winter (summer) in observations (model).

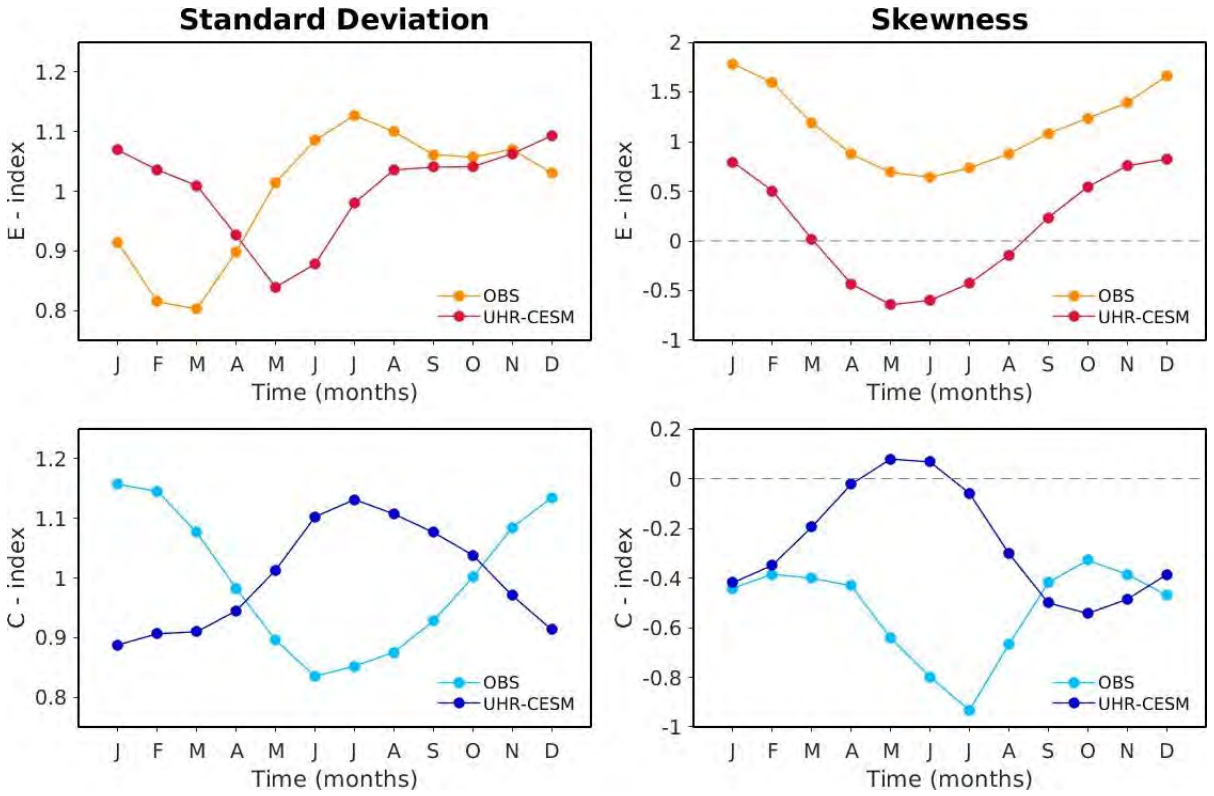

Figure B.9: *ENSO diversity from observations (ERSST.v5, 1900-2019 period) and model simulation (UHR-CESM PD, 120 years). a-b) Spatial pattern of Eastern Pacific (E-pattern) and Central Pacific (C-pattern) El Niño from a) ERSST.v5, and b) UHR-CESM PD simulation. The spatial pattern are expressed as the linear regression coefficients (in °C) between the sea surface temperature anomalies and ENSO indices (E and C). c) Scatter plot between ENSO indices from observations (orange dotes) and model simulation (cyan dotes) over 120 years. Thick black dotes correspond to austral summer season (DJF). The EP (CP) El Niño events are represented when the E-index (C-index) is greater than 1, and La Niña events when the C-index is less than -1.*

The evolution of the ENSO regimes during strong events (represented by exceeding 1 standard deviation from indices) shows realistic ENSO patterns from UHR-CESM PD simulation in comparison to observations (Figure B.10). However, the EP and CP El Niño patterns tend to be quite similar in the model, with an equatorial extension until 160°E, which differs from observations. Another difference found is during La

Niña events, where the peak is during August-September-October around 180°, while in observations the peak occurs in December around 150°W.

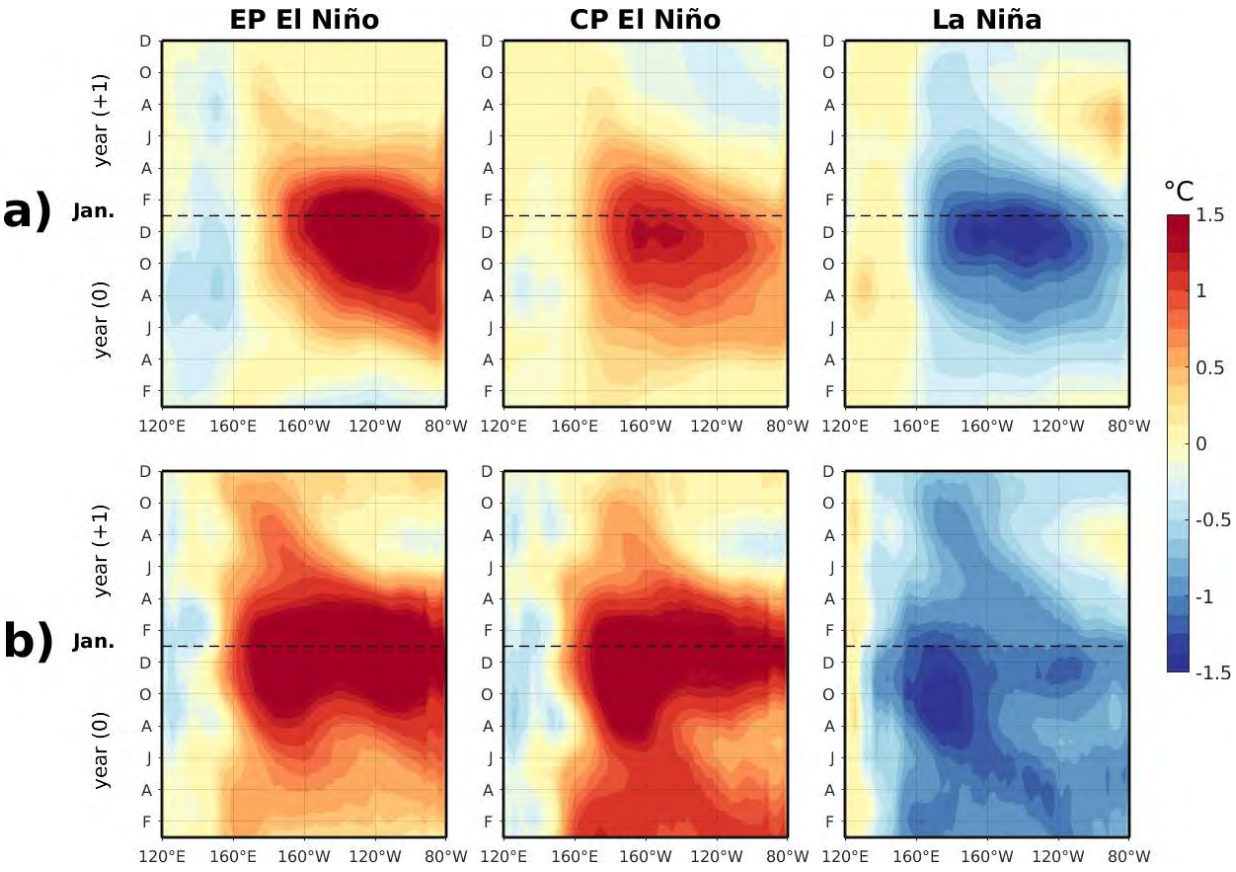

Figure B.10: *Composites of the SST anomalies (in °C) evolution during ENSO diversity events along the equatorial Pacific ocean of a) ERSST.v5 (1900-2019), and b) UHR-CESM PD simulation (120 years). The events were selected when during December (peak of events) of the E-index is greater than 1 for EP El Niño, C-index is greater than 1 for CP El Niño, and C-index is less than -1 for la Niña, in both observations and model simulation. During the whole period, i.e., 120 years, were detected 15 (17) events for EP El Niño, 23 (11) for CP El Niño, and 23 (17) for La Niña in observations (model simulation).*

Appendix C

Impact of climate change in the Chilean island ecoregions

Received: 29 October 2019 | Revised: 7 October 2020 | Accepted: 7 October 2020

DOI: 10.1002/aqc.3506

SPECIAL ISSUE ARTICLE

WILEY

Understanding the impact of climate change on the oceanic circulation in the Chilean island ecoregions

Boris Dewitte[1,2,3,4] | Carlos Conejero[4] | Marcel Ramos[2,3,5] | Luis Bravo[2,3] | Véronique Garçon[4] | Carolina Parada[6,7] | Javier Sellanes[2,3] | Ariadna Mecho[3,8] | Praxedes Muñoz[2,3] | Carlos F. Gaymer[2,3]

[1]Centro de Estudios Avanzados en Zonas Áridas (CEAZA), Coquimbo, Chile

[2]Departamento de Biología Marina, Facultad de Ciencias del Mar, Universidad Católica del Norte, Coquimbo, Chile

[3]Millennium Nucleus for Ecology and Sustainable Management of Oceanic Islands (ESMOI), Coquimbo, Chile

[4]Laboratoire d'Etudes en Géophysique et Océanographie Spatiales, Toulouse, France

[5]Centro de Innovación Acuícola Aquapacifico, Coquimbo, Chile

[6]Departamento de Geofísica, Facultad de Ciencias Físicas y Matemáticas, Universidad de Concepción, Concepción, Chile

[7]Instituto Milenio de Oceanografía, Universidad de Concepción, Concepción, Chile

[8]Laboratoire des Sciences du Climat et l'Environnement (LSCE), Saclay, France

Correspondence
Boris Dewitte, Centro de Estudios Avanzados en Zonas Áridas (CEAZA), Raúl Bitrán #1305, Campus Andrés Bello Universidad de La Serena, La Serena, Coquimbo, Chile.
Email: boris.dewitte@ceaza.cl

Funding information
Fondo Nacional de Desarrollo Científico y Tecnológico, Grant/Award Number: 1190276; Chilean Millennium Initiative ESMOI and IRD; National Chilean Research and Technology Council (CONICYT), Grant/Award Number: 72170554

Abstract

1. The largest changes in the circulation of the South-eastern Pacific resulting from global warming are associated with the southward shift and intensification of the anticyclone and with coastal surface warming. Coastal upwelling is projected to be increase off central Chile, due to an increase in equatorward winds, although increased oceanic stratification and associated enhanced nearshore turbulence will yield an onshore deepening/flattening of the thermocline.
2. The overall increase in south-easterly trade winds of the South-eastern Pacific in a warmer climate are likely to increase the connectivity pattern between Juan Fernandez and Desventuradas islands, and along the Sala y Gomez ridge, through increasing wind-driven mean ocean currents.
3. Deoxygenation associated with the warmer temperatures and changes in ventilation are likely to modify marine habitat and the respiratory barriers of species in the seamounts located in the vicinity of the limits of the minimum oxygen zone.
4. In the South-eastern Pacific, the prevailing 2D understanding of the responses of marine life to climate change needs to be expanded to 3D approaches, integrating the vertical habitat compression of marine organisms as a result of ocean warming and deoxygenation, as climate velocities for temperature and oxygen have contrasting vertical and horizontal patterns.
5. There is a need for regional biogeochemical-coupled modelling studies dedicated to the Chilean islands in order to provide an integrated view of the impact of anthropogenic stressors (e.g. deoxygenation, increased stratification, and climate shift) at the scale required for addressing socio-ecological interactions.
6. A refined understanding of the large-scale biogeography and spatial dynamics of marine populations through experimentation with high-resolution regional ocean models is a prerequisite for scaling-up regional management planning and optimizing the conservation of interconnected marine ecosystems across large scales.

KEYWORDS

Chile, climate variability and change, connectivity patterns, oxygen minimum zone, Pacific Islands

1 | INTRODUCTION

The maritime territory of Chile in the tropical and mid-latitudes includes a large portion of the South-eastern Pacific (SEP), with Easter Island (Rapa Nui) located more than 4,000 km off the Chilean coast, along with Motu Motiro Hiva islet (Salas y Gómez, approx. 400 km eastward off Easter Island), and with the Desventuradas and Juan Fernandez archipelagos situated close to the limit of the coastal transition zone (Hormazabal et al., & Leth, 2004). The three main island systems form a triangle, delineating three ecoregions at the edges that cover about half of the South Pacific anticyclone, which is the main high-pressure system in the mid-latitudes of the South Pacific (see contour plotted with a thick red line in Figure 1). Although for historical reasons the SEP has been one of the least-studied regions in the world ocean since the beginning of the 19th century, it is now considered a key region for understanding the evolution of the global climate system, and this has resulted in some dedicated projects in recent years under the auspice of international research programmes (e.g. VOCALS, Mechoso et al., 2014; TPOS2020, Smith et al., 2019).

The SEP is the region where dry and cold air in the equatorial tropopause descends to near the surface of the ocean in the mid-latitudes to form the South Pacific anticyclone and the descending branch of the Hadley cell. This anticyclone is associated with a large-scale gyre in atmospheric circulation that feeds the trade winds that produce the upwelling along the coast of Peru and Chile. The conjunction of descending dry air and cold surface waters is propitious to the formation of low-level clouds (stratocumulus) by stabilizing the marine boundary layer, yielding the so-called stratocumulus cloud deck, an oceanic region extending from the coasts of Peru and Northern Chile to a few 1,000 km offshore (de Szoeke et al., 2012). This stratocumulus cloud deck blocks solar radiation, which results in positive feedback for maintaining relatively cold and dry conditions over most of the tropical SEP, with associated arid conditions along the coast of Peru and Central Chile. In the mid-latitudes, the eastern edge of the South Pacific convergence zone (SPCZ) and the extra-tropical storms originating from the South Pacific provide more humid conditions. So far state-of-the-art global climate models have had difficulties in realistically simulating these key features (Niznik et al., 2015; Richter, 2015), which has limited

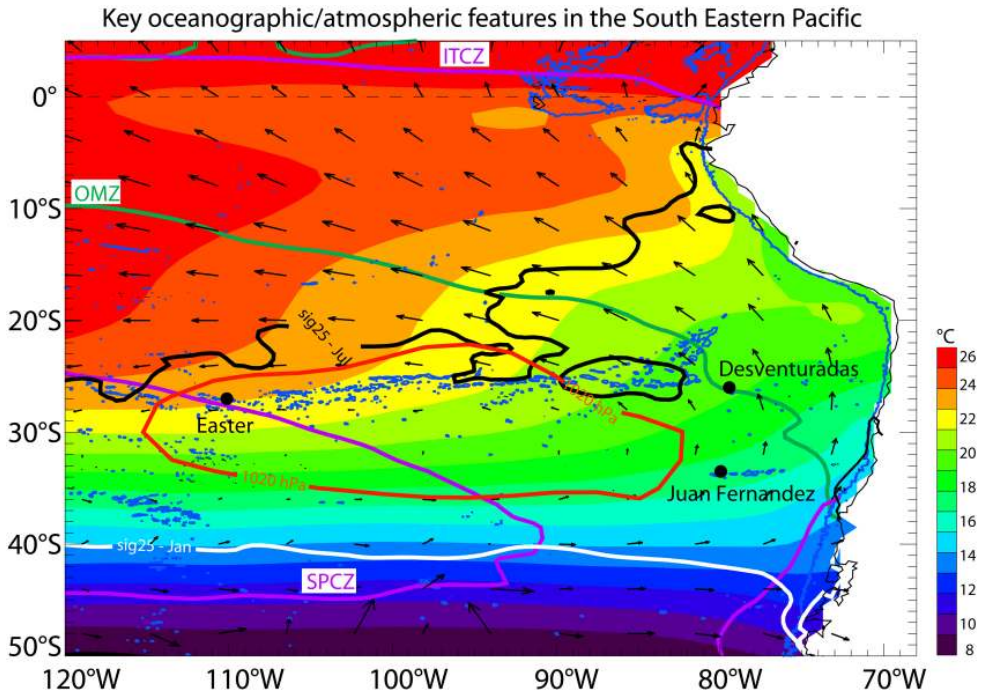

FIGURE 1 Some key features of the mean circulation in the South-eastern Pacific: the shading shows the mean sea surface temperature (SST) from HadISST data, 1950–2018; the arrows indicate mean 10-m winds from WASwind, 1950–2011. The contours in purple indicate the region of mean rainfall larger than 2.5 mm/day, and correspond approximately to the intertropical convergence zone (ITCZ), north of the equator, and the South Pacific convergence zone (SPCZ). The contours in thick white and black indicate the positions of the isopycnal 1,025 kg m^{-3} (i.e $\sigma\theta$ = 25) in July (black) and in January (white), and delineate the region where surface waters can potentially subduct and ventilate the tropical thermocline. The contour in red indicates the mean position of the South Pacific anticyclone and corresponds to the isopleth of 1,020 hPa for surface atmospheric pressures (from NCEP data, mean over 2000–2017). The 2,000-m isobath is also shown in blue to highlight the chain of seamounts between Easter Island and the Desventuradas Archipelago. The contour in green indicates the limit of the oxygen minimum zone (OMZ) at 300 m from CARS data (oxygen concentration lower than 1 ml/L)

our understanding of the oceanic circulation in this region and its role on the climate system.

The SEP also hosts one of the largest oxygen minimum zones (OMZs) in the world, a layer below the surface of near-stagnant oxygen-depleted waters (Paulmier & Ruiz-Pino, 2009), associated with the combined effect of the thermocline ventilation forming a shadow zone in the eastern tropics (Luyten et al., 1983) and of the high respiration rates of exported organic matter (Wyrtki, 1962). The OMZ that represents a respiratory barrier for most pelagic (Wishner et al., 1995) and benthic (Levin, 2003; Quiroga et al., 2009; Sellanes et al., 2010) marine species has its western limit located near the Desventuradas and Juan Fernandez archipelagos (Fuenzalida et al., 2009), representing a potential threat for benthic communities on the surrounding seamounts. The occurrence of hypoxic conditions can, for instance, trigger a reduction of macrobenthos in the benthic zone, affecting production and restocking processes (Arntz et al., 2006; Yáñez et al., 2017). Tolerance to hypoxic conditions varies between different ontogenetic stages and reproductive conditions and depends on species-specific abilities to tolerate low oxygen levels (Gallardo et al., 2017). Experiments developed on squat lobster populations suggest that episodic low oxygen and high temperature oscillations might affect brood development and impact the long-term survival of ovigerous females, potentially affecting recruitment success, given a potential synergistic effect acting at the metabolic level (Gallardo et al., 2019). The main process by which the OMZ can expand or shrink is through the ventilation of the thermocline, modulated by variability in biogeochemical demand. Variation in wind stress curl and atmospheric fluxes in the mid-latitudes in particular can modulate the transport of oxygenated waters from the region where the thermocline outcrops (approximately at the 15°C isotherm or sigma-25 isopleth, cf. Figure 1). This is a seasonal event linked to large climatological variations in atmospheric forcing there (Yeager & Large, 2004) but can operate at lower frequency timescales (i.e., interannual to centennial periods), providing a mechanism by which the OMZ can be impacted by climate variability (Oschlies et al., 2018). The other mechanism by which the OMZ can experience fluctuations in its characteristics (volume, extension) is through the connection of the equatorial current systems (equatorial undercurrent and Tsuchiya jets) that transport oxygen-enriched waters with the Peru–Chile undercurrent that flows poleward along the coast at latitudes as far as 40°S (Montes et al., 2014; Pizarro-Koch et al., 2018). These mechanisms have been the basis for interpreting past variability in palaeo proxies for oxygenation and productivity from sediment cores along the coast of South America, suggesting significant variability in the OMZ linked to climate variability over the last 25,000 years (Muñoz et al., 2020; Salvatteci et al., 2016). Although the OMZ is most intense at the eastern boundary of the basin, which is near the South American coastline, westward propagating eddies can spread OMZ waters to the island and seamount systems (Cornejo D'Ottone et al., 2016), and thus represent a key oceanographic feature in the SEP for understanding insular marine ecosystems.

Broadly, owing to the small size of the islands the oceanic circulation around the islands can be, to a large extent, interpreted as resulting from the large-scale circulation of the SEP. The presence of an island within a large-scale oceanic flow, however, produces a process referred to as the island mass effect (Doty & Oguri, 1956), which consists of a dynamical adjustment of the flow under localized frictional forces, generally observed from remotely sensed ocean colour data, as it produces a bloom in phytoplankton in the wake of the island (Andrade et al., 2014) or sometimes far from the island (Messié et al., 2020). Several physical processes can be involved in the island mass effect, such as coastal upwelling, Ekman pumping, eddies, or internal waves (Andrade et al., 2014; Barton, 2001; Heywood et al., 1990; Heywood et al., 1996; Palacios, 2002). Prominent (high-altitude) orographic features on the islands can also produce localized wind stress curl patches, which in turn can force an oceanic circulation that can extend far from the island, a feature known as a beta-plume (Stommel, 1982). The beta-plume effect can, for instance, produce time-mean zonal jets of approximately 10 cm/s extending as far as approximately 20° to the west of the island of Hawaii (Belmadani et al., 2013). As the SEP is also characterized by the presence of several mid-oceanic ridges, in particular with a complicated chain of high seamounts between Easter Island and the Desventuradas Archipelago (see contours in blue in Figure 1 that correspond to the 2,000-m isobaths), topography also represents a significant source of vorticity for the small-scale deep circulation (i.e. mixing), which in turn can alter the large-scale mean flow (Vic et al., 2019). These processes are poorly (and most of the time not) resolved by current-generation global climate models, owing to their resolutions being too coarse and the imperfect realism of topographic features, although they are key for understanding local cultural practices (e.g. artisanal fisheries) and connectivity patterns of some marine species between the islands and seamounts. Certainly, these local processes are also modulated by large-scale variability that covers a wide range of frequencies, from intraseasonal to centennial.

This paper provides an overview of key oceanic processes for understanding the ecosystem structure around the Chilean islands. Although changes in the circulation and biogeochemical environment discussed here have the potential to impact all faunistic groups present in the island systems, our focus is on benthic communities, the most abundant in the region, with less mobility than pelagic communities, and considering current uncertainties in the degree of connectivity between the island systems for this particular group. In particular, in intermediate waters within the Chilean exclusive economic zone (EEZ), Mecho et al. (2020) compiled a data set of 68 operational taxonomic units (OTUs) of echinoderms, comprising 35 families and four classes, from mesophotic depths (540–400 m) of the Nazca Ridge, the eastern extent of the Salas y Gómez Ridge, and the Desventuradas and Juan Fernandez photic depths archipelagos. While several of these species, e.g. *Clypeaster isolatus*, *Scrippsechinus fisheri*, and *Stereocidaris nascaensis*, are apparently endemic to the Salas y Gómez and Nazca ridges, none of them were found at Easter Island, located only 800 km westwards. In fact, of the 18 echinoderm OTUs observed on Easter Island at mesophotic depths, only two were shared with the central portion of the Salas y Gómez ridge, suggesting a potential faunal break east of Salas y Gómez for this faunistic group

(Mecho et al., 2020). For other groups, however, as for fishes and corals (Easton et al., 2019), some species are shared between the Salas y Gómez Ridge and Easter Island, even if relatively high rates of endemism (15–30%) have been described for the eastern seamounts (Friedlander et al., 2013). Seventy-eight per cent of Salas y Gómez species were reported at Easter Island, whereas only 14% of Easter Island species were reported at Salas y Gómez Ridge (Easton et al., 2019). The data available for the region remain scarce, however, and more biological information is needed to support any conclusion of potential biological breaks for all groups. Thus, with this in mind, the motivation here is to highlight the complex of pathways by which large-scale oceanic and atmospheric variability can modulate processes at fine scales in the vicinity of the islands and seamount systems, which as yet has hardly been addressed owing to limitations in climate models and the observations in this region of the world. We then review the current understanding of the effect of ocean warming on marine life based on global climate model projections, illustrating limitations in the use of climate velocity as a metric to gain insights into the potential scope of species range-shift responses to global warming. As a perspective, this article points to necessary research initiatives in order to better constrain current uncertainties and improve the guidance for resource management and conservation plans in this region.

2 | MATERIALS AND METHODS

2.1 | Observations

The sea surface temperature data (SSTs) analysed in this study were taken from the HadISST v1.1. dataset on a $1^\circ \times 1^\circ$ regular grid covering the period 1950–2016 and originally released by the Met Office Hadley Centre (Rayner et al., 2003). Sea surface height data, from the GEKCO (Geostrophic and Ekman Current Observatory) product (Sudre et al., 2013), were used to estimate the surface geostrophic eddy kinetic energy (EKE) (see section 2.3). This dataset is based on altimetric data from the DUACS (Data Unification and Altimeter Combination System) of AVISO (Archiving, Validation and Interpretation of Satellite Oceanographic data). Data are globally gridded from 1993 to the present as daily values with a spatial resolution of 0.25°. The 10-m winds are from ship-based measurements (anemometer) from Tokinaga and Xie (2011) (Figure 1), and the mean surface current data (1975–2015) are taken from drifter data published by Laurindo et al. (2017) (Figure 2). Observations of mean temperature, salinity, and oxygen concentration were obtained from the global 3D CSIRO (Commonwealth Scientific and Industrial Research Organisation) Atlas of Regional Seas (CARS) climatology (2009 version). CARS climatology combines all the available oceanographic data from the World Ocean Database over the last 50 years, along with the Array for Real-Time Geostrophic Oceanography (ARGO) buoy profiles (Dunn & Ridgway, 2002). Precipitation data (Figure 1) are from CPC Merged Analysis of Precipitation (Xie & Arkin, 1997). The 10-m wind data from the National Centers for Environmental Prediction/National Center for Atmospheric Science (NCEP/NCAR) reanalysis data (Kalnay et al., 1996) for the period 1950–2018 are also used to derive the South Pacific meridional mode (SPMM) pattern (see section 2.3). The bathymetry data were obtained from the General Bathymetric Chart of the Oceans (GEBCO), version 2019.

2.2 | Model outputs

In order to diagnose the climate change patterns in the SEP, we use an unprecedented model data resource made available to the community, i.e. the long-term simulations of the NCAR Community Earth System Model Large Ensemble Project (CESM-LE) (Kay et al., 2015; Lovenduski et al., & Lindsay, 2015), which is derived from the Community Earth System Model, version 1, with the Community Atmosphere Model, version 5 (CESM1(CAM5); Hurrell et al., 2013). The CESM-LE simulations include land and ocean biogeochemistry, and are amongst the few Earth system models participating in CMIP5 (Kwiatkowski et al., 2017) and the only one amongst this subgroup with such a large ensemble (42 members for the physics and 36 members for the ocean biogeochemistry for historical runs). Although presenting classical biases of current-generation global climate models, in particular a warm bias in the eastern tropical Pacific, CESM reasonably simulates the tropical variability, including the El Niño–Southern Oscillation (ENSO) (Deser et al., 2012; Dewitte & Takahashi, 2017; Karamperidou et al., 2016) and some key aspects of the sensitivity of the carbon cycle to climate variability (Long et al., 2013). Although CESM tends to overestimate the volume and spatial extents of the OMZs in the tropical Pacific (Moore et al., 2013), it captures the large-scale spatial pattern distribution of dissolved oxygen properly (Long et al., 2016) and exhibits the closest match to observations in the tropical Pacific across models (Cabré et al., 2015). The 42 (40) available members of the historical (RCP8.5) runs, covering the period 1920–2005 (2006–2100), are used for temperature, whereas 36 and 34 members are used for pH and dissolved oxygen, respectively, for the historical and RCP8.5 runs. The climate change pattern is diagnosed as the difference between the mean over the 2050–2100 period and the mean over the 1950–2005 period.

2.3 | Methods

In order to diagnose the magnitude of mesoscale activity in the statistical sense, the classical approach that consists in estimating the mean EKE of the surface circulation was used. The mean EKE was obtained here from 5-day mean detrended surface geostrophic current anomalies (u'_g, v'_g), which are derived from sea surface height. Then the quantity EKE = $(u'_g{}^2 + v'_g{}^2)/2$ is derived. Surface geostrophic current anomalies were computed from 5-day mean outputs removing the monthly climatology interpolated at a 5-day temporal resolution. The mean EKE over 3-month running windows followed by a monthly average is then estimated, providing a series of monthly mean EKE values. The seasonal cycle from monthly mean EKE values was

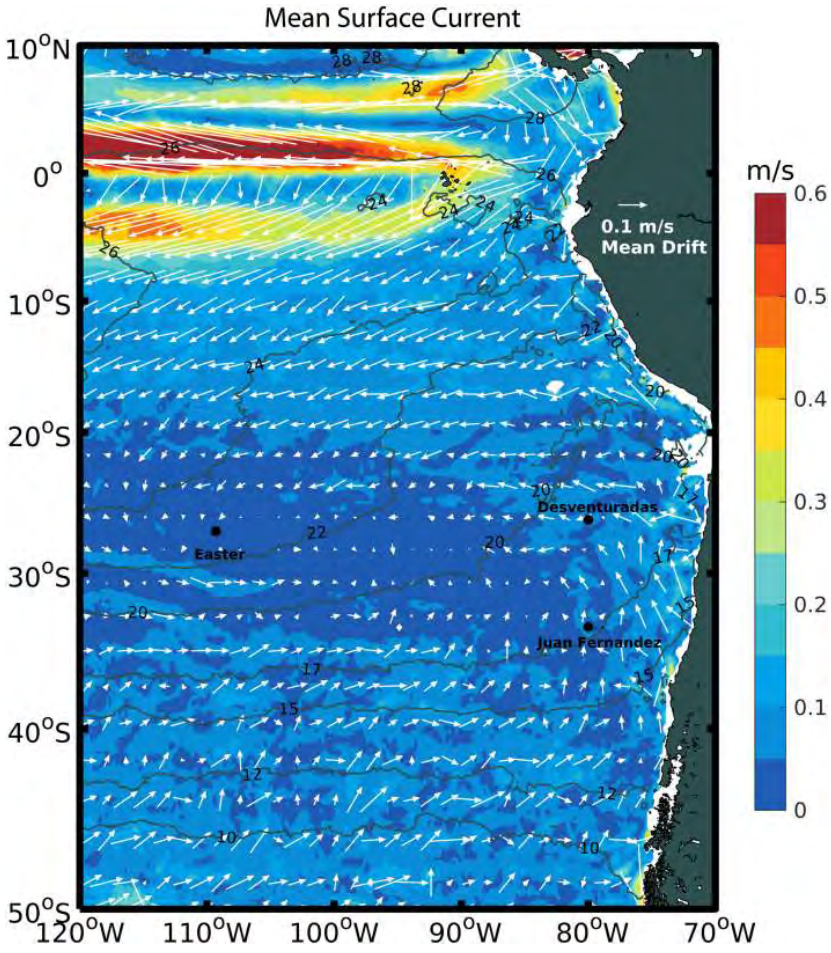

FIGURE 2 Mean surface current from drifter data (Laurindo et al., 2017) for the period 1975–2015. Shading is for amplitude and vectors provide the direction (reference length given in the upper right of the panel). Contours in grey correspond to the mean sea surface temperature. Black dots indicate the locations of Juan Fernandez Islands, Desventuradas Islands, and Easter Island

removed and a 1-year running mean filter was then applied to ensure that any seasonal variability was removed. The field obtained was then analysed through empirical orthogonal function (EOF) decomposition (Figure 3).

Mean vertical current are estimated from integrating dynamic height (from CARS) with a reference depth at 1000m and thereby assuming geostrophic balance (Figure 4).

In order to diagnose the ENSO patterns in the SEP, the E and C indices defined by Takahashi, Montecinos, Goubanova, and Dewitte (2011) as E = (PC1 − PC2)/√2 and C = (PC1 + PC2)/√2, where PC1 and PC2 are the normalized principal components of the first two EOF modes of SST anomalies in the tropical Pacific (120°E–290°E, 10°S–10°N) were used. A bilinear regression of SST anomalies in each grid point onto the E and C indices is then estimated, which provides the spatial patterns of SST anomalies associated with each index, i.e., the E and C modes, respectively (Figure 5a).

To derive the SPMM pattern (Figure 5b), we follow Chiang and Vimont (2004) and use singular value decomposition (SVD) analysis (Bretherton et al., 1992) to derive the eigenvectors and eigenvalues of the covariance matrix between 10-m winds and SST anomalies that have been previously filtered out from ENSO influence (i.e., removing the contribution of both the E and C indices from the SST and 10-m wind fields through bilinear regression). The SVD decomposition was performed over the domain (140°W–90°W, 40°S–0°).

A simple climate–landscape metric was also used that allows an assessment of the exposure of species to climate change, i.e., the 'velocity of climate change' or 'climate velocity' that represents the rate of movement of climatic isopleths across a landscape or seascape (Loarie et al., 2009; Pinsky et al., 2013). Although lacking explicit ecological or biological grounding, this metric is one of the most widely used in climate-change ecology and conservation (for a review, see García Molinos et al., 2019) and is referred to in policy documents (IPCC, 2014; MCCIP, 2015). The velocity of climate change provides the speed and direction with which hypothetical species would need to move to remain at the same value of an environmental parameter (usually temperature or precipitation), experienced today at a particular location, in the future (Burrows et al., 2011). For temperature, it is estimated as the ratio of temporal (°C/yr) and spatial (°C/km) gradients of mean annual near-surface temperature. The temporal gradient corresponds here to the ensemble mean of the long-term linear trend of the CESM simulations of the representative concentration pathway 8.5 (RCP8.5) scenario (2006–2100), whereas the spatial gradients are

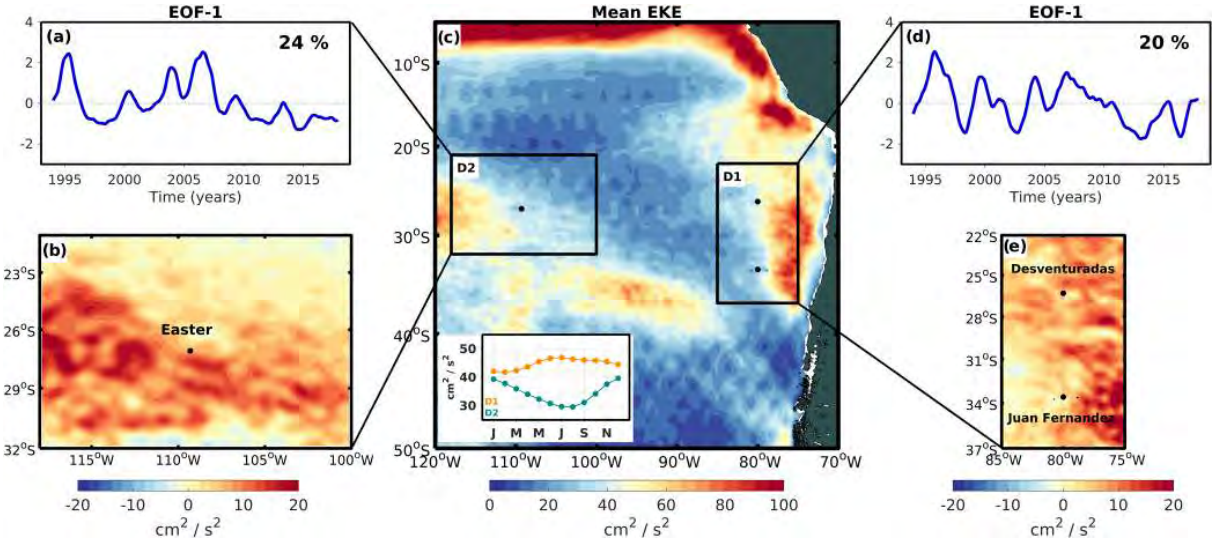

FIGURE 3 Mean eddy kinetic energy (EKE) calculated from satellite altimeter data for the 1993–2018 period. The mean EKE is a proxy of the intensity of the turbulent flow, mostly accounted for by eddies. (a, b) First empirical orthogonal function (EOF) mode of the interannual EKE variability over Easter Island (domain D2), corresponding to the principal component (a) and the spatial pattern (b). (c) Mean EKE. The seasonal cycle of the domains D1 and D2 is indicated to the lower left of the map. (d–e) First EOF mode of the interannual EKE variability over the Desventuradas and Juan Fernandez islands (domain D1), corresponding to the principal component (d) and the spatial pattern (e). The explained variance is indicated at the upper right of the principal component panels (a, d). Black dots indicate the locations of Juan Fernandez Islands, Desventuradas Islands, and Easter Island

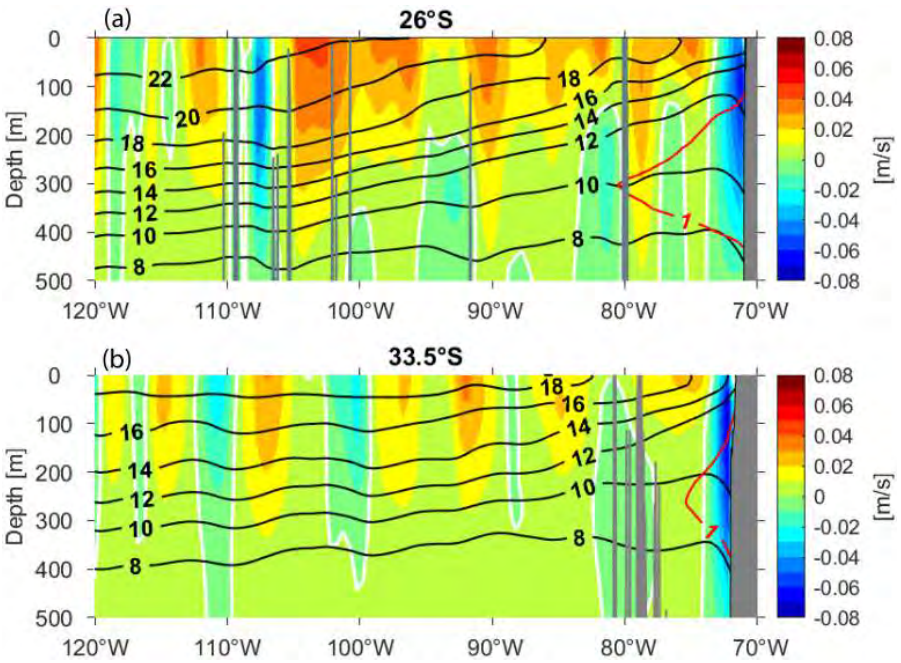

FIGURE 4 Mean zonal sections of temperature (black contours) and meridional geostrophic current referenced to a depth of 1,000 m (red, northward; blue, southward) at 26°S (a) and 33.5°S (b). The contours in red indicate the limit of the oxygen minimum zone (OMZ; isolepth 1 ml/L). Data are from CARS

derived from the CARS data. The direction (angle) of the velocity is oriented along the direction of the spatial gradient. Velocity angles have an opposite direction to the spatial climatic gradient if warming and have the same direction if cooling. Here, conversely to previous studies that focus on surface temperature, we take advantage of the CARS data that provide the 3D observed temperature to calculate the climate velocity at different depths. In addition, we also estimate a climate velocity associated with dissolved oxygen concentration,

defining it as the ratio of the ensemble mean of the long-term linear trend in modelled dissolved oxygen concentration of the NCAR CESM-LE simulations of the RCP8.5 scenario (2006–2100) and of the spatial gradient derived from the oxygen concentration CARS data. For oxygen, the angle has opposite direction to the spatial climatic gradient if the ocean loses oxygen (deoxygenation trend) and the same direction if it gains oxygen (oxygenation trend).

3 | MEAN OCEANIC SURFACE CIRCULATION IN THE SEP

The mean surface oceanic circulation in the SEP can be roughly understood as resulting from the gyre anticyclonic atmospheric circulation that forces the surface Ekman current. It thus follows approximately the direction of the south-east trade winds, with a tendency to converge in the region centred around (26°S, 110°W), where the mean currents are weak (Figure 2). To the south of the region, the currents are mostly eastward, however, with large longitudinal variability in their direction as a result of the relatively intense mesoscale activity there. This mesoscale activity originates partly from the Austral winter storms that propagate eastwards, as they are underneath the so-called extratropical storm track of the South Pacific (Trenberth, 1991). There is a dominant northward flow from the Juan Fernandez Archipelago to the Desventuradas Archipelago that curves towards the west in the direction of Easter Island. To the north, the mean circulation feeds the south equatorial current near 5°S, a powerful current of amplitude larger than 1 m/s. The latitude of the Sala y Gomez Ridge (approx. 26°S) corresponds to the intersection of several water masses originating from the four cardinal directions: In the surface layer (approx. 0–200 m), to the west, there is Subtropical water (STW) and, to the east, sub-Antarctic water (SAAW). Below 200 m, a tongue of low-oxygen waters extending beyond the OMZ is rather clearly associated with a tongue of high-salinity water associated with equatorial subsurface water (ESSW) and both are largely reduced to the south of Juan Fernandez island by mixing with low-salinity and well-ventilated Antarctic intermediate water (AAIW) and SAAW (Llanillo et al., 2012; Silva et al., 2009).

Superimposed on this mean circulation, there is a relatively energetic mesoscale circulation (Figure 3). Its amplitude is greatest near the equator and along the coast of Peru and Central Chile, and results from the instability of the mean currents, a situation when a slight change in the mean circulation is suddenly amplified, resulting in the development of eddies. In particular, near the coast, the vertical shear between the dominant northward surface current and the subsurface southward current (i.e. the Peru–Chile undercurrent) produces so-called baroclinic instability, which is the mechanism by which mean current can transfer available potential energy to the turbulent flow (Capet et al., 2008). Eddies generated along the coast have a complex vertical structure, with some eddies having the strongest currents near the surface (mostly cyclonic eddies) and with some others having maximum amplitude in the subsurface, near a depth of approximately 300 m (mostly anticyclonic eddies; (Hormazabal et al., 2013). They can transport water mass properties (heat, salt, oxygen, nutrients) from the coast to the offshore ocean up to the Desventuradas and Juan Fernandez archipelagos (Cornejo D'Ottone et al., 2016; Combes et al., 2015). The mean EKE is also strong to the west and south of Easter Island. Considering the relatively weak mean circulation, eddies are salient features of the circulation as they can influence the mean transport of the water mass properties (Pizarro-Koch et al., 2018; Vergara et al., 2016).

These features undergo seasonal variability resulting in part from the seasonal meridional migration of the South Pacific anticyclone, the resulting change in solar radiation (cloud cover), and from the forcing of extratropical Rossby waves. The latter are, in particular, forced locally by the change in wind stress curl associated with the southward shift of the pressure system in the Austral summer, but are also forced along the coast by the seasonal equatorial Kelvin wave (Dewitte et al., 2008; Ramos et al., 2006). These Rossby waves can propagate vertically and can eventually reverse the weak mean subsurface circulation; however, the mean circulation at subsurface is largely undocumented because of the lack of observations. So far only estimates of subsurface circulation can be obtained from historical hydrological observations (of temperature and salinity) by assuming geostrophic balance. The vertical sections of the mean geostrophic currents at 26°S and 33.5°S (Figure 4) show characteristic circulation patterns of an eastern boundary current system, with an intense poleward subsurface flow near the shelf and continental slope, and with a mean northward flow away from the coast, which notoriously become more intense at 26°S above 350 m. Near Easter Island a reversing current from both sides of the island is indicative of a sustained recirculation around the island or the effect of mesoscale activity (see Figure 3).

4 | NATURAL INTERANNUAL AND DECADAL VARIABILITY

The dominant climate fluctuation in the eastern tropical Pacific is the ENSO. El Niño, in its emblematic form, represents a substantial surface warming of the eastern equatorial Pacific that induces a shift in the climatic conditions along the coast of Peru and Chile through producing anomalous wetter conditions along the normally dry coastal regions of Peru and northern Chile. Extreme El Niño events are in particular associated with heavy rainfall in the northern coastal region of Peru, which is associated with a southward migration of the intertropical convergence zone (ITCZ). Recent research has shown that these extreme El Niño events, which are very few over the observational record (only two events of this kind took place over the last 50 years, in 1982/83 and 1997/98), belong to a certain class of events characterized in particular by peak SST anomalies developing in the far Eastern Pacific and along the coast of Peru (Takahashi et al., 2011). The majority of the events can be classified as weak or moderate events and have been named Eastern Pacific and Central Pacific El Niño events, depending upon whether their peak SST anomalies are found in the Eastern or the Central Equatorial Pacific (Dewitte & Takahashi, 2017, 2018).

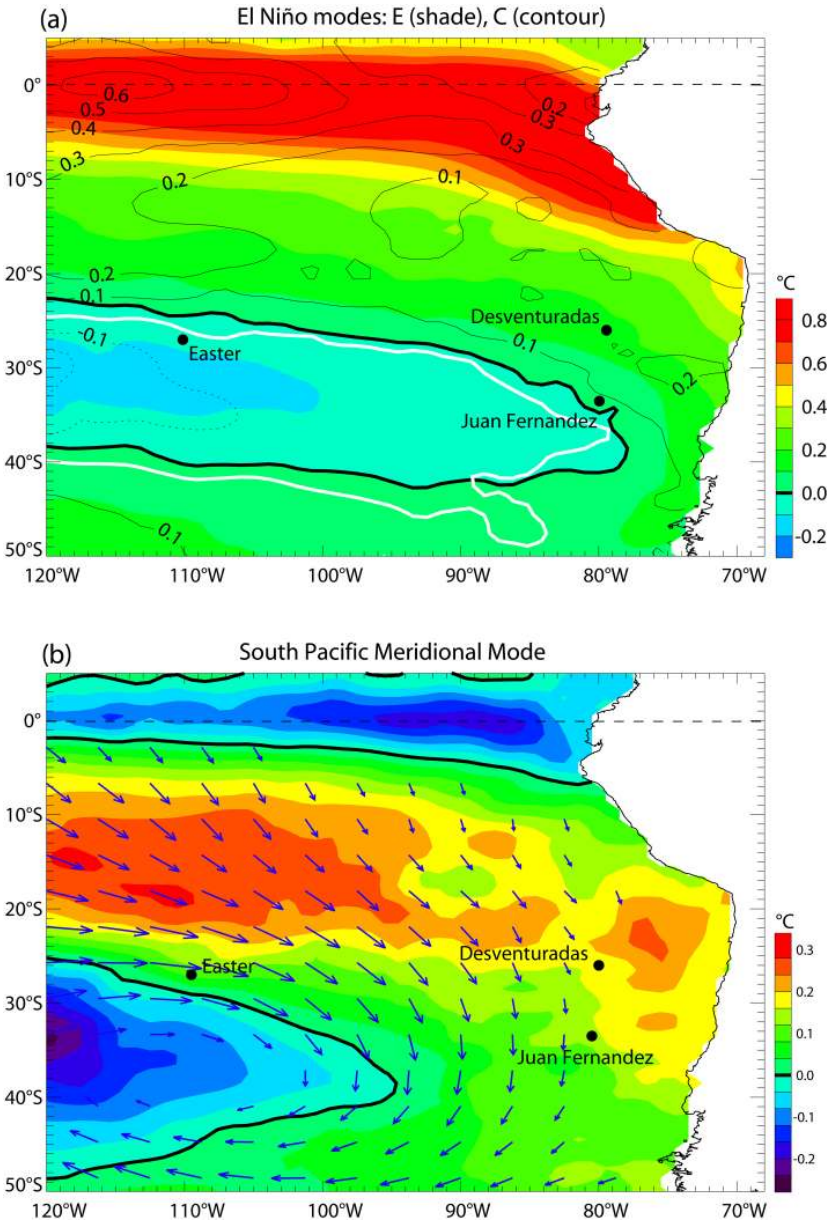

FIGURE 5 Spatial patterns of: (a) the two dominant El Niño–Southern Oscillation (ENSO) modes (E and C modes) and (b) the South Pacific meridional mode (see section 2). The contour in white in (a) is the zero contour for the C mode. The arrows in (b) correspond to the wind pattern associated with the South Pacific meridional mode (SPMM)

These two classes of events or ENSO 'regimes' can be well accounted for by the first two rotated EOFs of SST anomalies in the tropical Pacific (Takahashi et al., 2011; see section 2.3), and have been popularized under the concept of ENSO diversity in the recent literature (for a review, see Capotondi et al., 2015). Figure 5a presents the patterns of these two rotated EOFs of SST anomalies, referred as E and C modes following Takahashi et al. (2011). The E mode accounts for the Eastern Pacific (hereafter EP) El Niño events, which are associated with a strong loading (warming) along the coast of Peru and northern Chile, whereas the C mode accounts for Central Pacific (hereafter CP) El Niño and La Niña events, depending on the sign of the C index, and has a centre of action located approximately 160°W along the equator. Note that La Niña events are essentially of the CP type (Kug & Ham, 2011). Although these two modes are associated with perturbations of mean conditions in the near coastal regions of the SEP, they have relatively little impact on SST to the south of 15°S in the open ocean. In fact, both Easter Island and Juan Fernandez are close to the zero contours of these two modes, meaning that these regions experience very little variation in SST at the peak phase of El Niño events. During the development of extreme El Niño events (e.g. 1982/83 and 1997/98), however, movements in the main convective centres (i.e., the ITCZ and the SPCZ, see Figure 1) can drastically modify the local atmospheric circulations, producing, in particular, intense precipitation events. During such events, the swings

of the SPCZ to a more zonal alignment closer to the equator (Cai et al., 2012; Vincent et al., 2011) are favourable to more intense rainfall at Easter Island, whereas extreme La Niña events would tend to result in dryer conditions. This can impact the marine ecosystems there by either modulating the regional oceanic circulation through changes in buoyancy fluxes or by directly affecting photosynthesis and UV tolerance of the organisms (both benthic and pelagic) living within euphotic depths through changes in solar radiation. The local atmospheric conditions near the Desventuradas Archipelago are also likely to be impacted during strong EP El Niño events, with anomalies reaching approximately 1°C during the extreme 1997/98 El Niño, for instance, which has the potential to enhance mixing in the otherwise well-stabilized marine boundary layer there. This means that oceanic and atmospheric variability in the SEP (at least south of 15°S) cannot be explained in a straightforward manner by ENSO but instead has to result from other large-scale environmental forcing or indirect consequences of El Niño. The processes by which El Niño can remotely influence the SEP circulation are referred to as oceanic and atmospheric teleconnections, dependent on whether they involve an oceanic or atmospheric pathway. For instance, eddy activity can be modulated by oceanographic conditions produced by El Niño along the coast of Chile (Combes et al., 2015; Conejero et al., 2020), which in turn can influence SST and oceanographic conditions in the vicinity of the islands as eddies propagate westwards from the coastal region.

The second mode of interannual variability in the SEP that is not linearly related to ENSO at lag zero is the SPMM (Zhang et al., 2014). The SPMM results from the low-level atmospheric response to warm SST anomalies occurring underneath the south-eastern branch of the trade winds, which tends to reduce evaporation and produces a positive feedback for SST anomalies, along with favouring its propagation in the direction of the trade winds (Figure 5b). This mode is connected to episodic warm oceanic conditions developing along the coast of Central Chile, which have been referred to recently as 'Chilean El Niño events' (Xue et al., 2020). This mode has a relatively strong loading in the Desventuradas region, meaning that during its positive phase warming is expected there, associated with a reduction of the trade winds. Interestingly, Easter Island is also weakly impacted by this mode, suggesting that it is relatively protected from SST fluctuations at interannual timescales. As it is located towards the northern edge of the SPCZ (cf. Figure 1), however, any small changes in SST can have a large impact on convective conditions and have the potential to move the SPCZ to the north. Such a situation can, in particular, take place at decadal timescales during the positive phase of the interdecadal Pacific oscillation (IPO) (Folland et al., 2002; Henley et al., 2015), as occurred from the late 70s until the early 2000s. The IPO is also influential on the oceanic circulation in this region. In particular, stronger trade winds occur during a negative phase of the IPO, which causes a shoaling of the eastern thermocline of the tropical and subtropical Pacific Ocean (Miller et al., 1994). Simultaneously, in the tropical regions the zonal volume transport by the equatorial current system increases as well as the meridional transport by the subtropical cells (STCs) (Hong et al., 2014), which connect the subtropics to the tropics (McCreary & Lu, 1994). Stronger trade winds also tend to increase the subduction volume of the South Pacific eastern subtropical mode water (Luo et al., 2011). Since the 1990s an increase in equatorward meridional winds in the SEP has also been observed (England et al., 2014), which has been suggested to be partly caused by the warming of the Northern Atlantic, as part of the Atlantic multidecadal oscillation, producing an interhemispheric SST gradient in the Pacific (Hu & Fedorov, 2018).

Another source of natural variability in the island and seamount systems comes from the chaotic nature of the circulation associated with the nonlinear ocean dynamics. Mesoscale to submesoscale circulation can be generated through instability processes that can modulate the circulation at low frequencies, even in the absence of coherent atmospheric or buoyancy forcings (Sérazin et al., 2015). The contribution of this intrinsic (nondeterministic) variability to the fluxes of water mass properties can be as important as that associated with the mean circulation in the SEP (for dissolved oxygen, see Bettencourt et al., 2015). As the Chilean island systems are located in the vicinity of 'hot spots' of mesoscale activity (Figure 3c), they can experience changes in the neighbourhood circulation associated with low-frequency eddy-induced flow. Figure 3 displays estimates of such changes at interannual timescales, as inferred from the dominant EOF mode of mesoscale activity in two subregions encompassing the island systems (Desventuradas and Juan Fernandez archipelagos (D1) versus Easter Island (D2)). Results indicate that the largest fluctuations (i.e., peak loading of the mode pattern) in mesoscale activity take place to the south of Easter Island and to the east of the Desventuradas and Juan Fernandez archipelagos. These fluctuations do not have clear linear relationships with El Niño and the SPPM. The largest correlation values (absolute) are found with the E index that account for extreme EP El Niño events: $c = -0.35$ at lag = +4 months for D1 and $c = -42$ at lag = −7 months for D2 (not shown) (a positive lag corresponds to PC time series ahead the E index). Note that the result for D1 is consistent with Conejero et al. (2020), indicating that mesoscale activity off Central Chile tends to reduce prior to the peak of EP El Niño events. The low-frequency eddy-induced circulation and its role on water mass properties in the island systems remains to be investigated, and potentially has important effects on the transport of water mass properties (heat, dissolved oxygen, and nutrients) that could influence habitats. The Desventuradas and Juan Fernandez seamount systems are located in the route of westward-propagating eddies generated along the coast of Central Chile and forming a so-called striation in the eddy field (Belmadani et al., 2017). Such eddies can also transport low-oxygen waters in their core far beyond the longitude of these island systems (Cornejo D'Ottone et al., 2016).

5 | DISCUSSION

The observed increase of atmospheric CO_2 and the observed changes in the physical properties of the ocean have profound impacts on marine biogeochemical cycles, by changing the solubility and chemical equilibration of gases and by altering circulation patterns. The circulation patterns redistribute biologically relevant

variables, such as oxygen, pH, planktonic distribution, and primary productivity (Bopp et al., 2013; Chust et al., 2014), and also temperature and salinity. Here, we first discuss expected changes in the physical and biogeochemical properties of the ocean that may have impacts on the circulation and environmental conditions in the island systems, and then synthesize the relevant existing literature to point out knowledge gaps and limitations for inferring, with confidence, the overall effect of the changes in circulation on marine ecosystems.

5.1 | The 'climate change pattern' in the SEP

It is now established that global warming will have significant impacts on the circulation in the SEP (Figure 6), although the underlying processes associated with these changes remain under debate. A well-known paradigm for global warming-induced mean circulation changes in the eastern boundary current systems was presented by Bakun (1990), who proposed that the differential warming between the continent and the ocean will yield a pressure gradient that will increase the upwelling-favourable winds through geostrophic dynamical adjustment. The study by Bakun (1990) has, however, two caveats. First, it used ship-based measurements of sea surface wind speed that had a spurious upward trend because of increases in anemometer height in the 1960s (Tokinaga & Xie, 2011). Corrected winds do not present a positive trend in the upwelling-favourable/along-shore winds off Peru (Belmadani et al., 2014, their figure 1), as was found in Bakun (1990). Second, model experiments only suggest an approximate geostrophic balance in the steady-state off Peru and Chile (Belmadani et al., 2014; Muñoz & Garreaud, 2005), meaning that frictional processes associated with the presence of the Andes in particular are certainly more important than was implicitly hypothesized by Bakun (1990). In fact, only indirect evidence for a possible strengthening of the upwelling-favourable winds has been provided by a negative trend in coastal SST, which has been observed off northern Chile since 1979 (Falvey & Garreaud, 2009) and off central–southern Peru since the mid-20th century (Gutiérrez et al., 2011). In addition, climate models, although predicting an increase in upwelling-favourable winds along the coast of Chile (Rykaczewski et al., 2015), do simulate a warming trend of SST along the coast, resulting in a marked increase in vertical stratification because the surface layers warm faster than the subthermocline waters (Figures 7a and 8a). The increased stratification along the coast may actually reduce upwelling through flattening the isotherms and deepening the permanent thermocline along the coast. Still, the results of downscaling experiments from a regional ocean model of projections from a climate model under abrupt CO_2 forcing suggest that, off Central Chile, the increase in upwelling-favorable winds will likely yield a significant increase of coastal upwelling (Echevin et al., 2012) despite the deepening/sharpening of the thermocline along the coast, and the associated coastal SST warming. Over the last decades however, SST along the coast has had a tendency to cool down along the coast of Peru and Northen Chile, which could be due to natural variability. Through the equatorial oceanic teleconnection along the coast of South America, natural variability in the tropical Pacific has in particular the potential to modulate SST at low frequency (i.e., decadal) along the coast with a magnitude comparable with that of the observations (Dewitte et al., 2012).

Although current-generation global models cannot resolve coastal upwelling dynamics and the eddy flow realistically, they can still inform on the likely changes in the basin-scale mean circulation pattern in the SEP. Figure 6 shows the projected change in mean SST and wind stress in the SEP as simulated by a state-of-the-art Earth system model (ESM) (see section 2.2). The peak warming trend extends from the equatorial region to along the coast of Peru and Chile, forming an El Niño-like pattern with a warming of appromimately 2–3°C by the end of the 21st century (for the ensemble mean of the models of the CMIP5 data base, see also Karamperidou et al., 2016). In the more oligotrophic offshore ocean the warming will not be as severe because of the increased latent heat cooling associated with wind intensification (Lu & Zhao, 2012; Xie et al., 2010). The increased equatorward winds in the warming climate are induced by the southward shift of the anticyclone (Li et al., 2013) resulting from the expansion of the Hadley cell (Lu et al., 2007). Although the warming trend is confined to the upper thermocline in the offshore ocean, it extends to the subthermocline, reaching depths of approximately 400 m to the

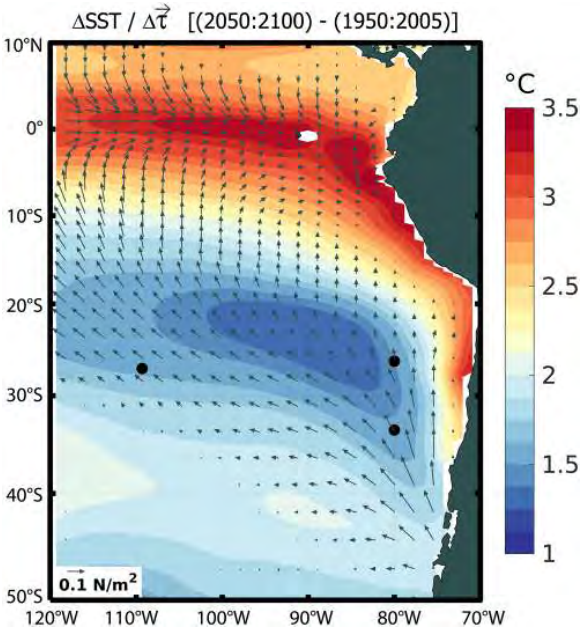

FIGURE 6 Variation in mean sea surface temperature (SST, shading) and wind stress (vectors) from the present climate to the future climate, as simulated by the CESM model. Difference presented between 2050–2100 (RCP8.5 scenario, future climate) and 1950–2005 (historical scenario, present climate). Only significant values are showed by a Wilcoxon rank sum test. Black dots indicate the locations of Juan Fernandez Islands, Desventuradas Islands, and Easter Island

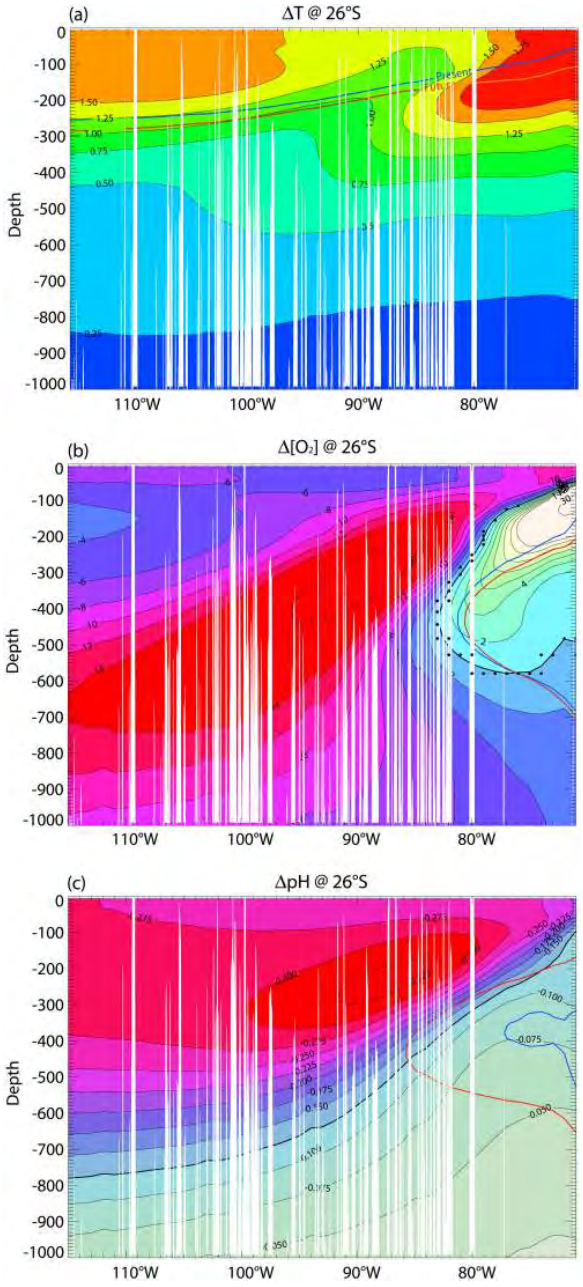

FIGURE 7 Effect of climate change on the oceanic conditions along a section at 26°S (Salas y Gómez Ridge), as simulated by the CESM model: difference in mean conditions between the present (1950–2005, 'historical' scenario) and the future (2050–2100, RCP8.5 scenario) for (a) temperature, (b) dissolved oxygen, and (c) pH. The blue and red lines stand for the 15°C isotherms in (a), for the oxygen minimum zone limit, $[O_2]$ < 1 ml/L, in (b), and for the pH isopleth of 7.35 in (c) for the (blue) present and (red) future climates. Note the deepening of the 15°C isotherm (a proxy for thermocline depth) by approximately 40 m in the warmer climate and the increase in oxygen content in the vicinity of the oxycline (orange colour, approx. 30 μmol/kg). The model also indicates an overall decrease in pH more pronounced in the surface layer (red–pink colour, approx. 0.3 unit). The black dots in (b) correspond to the locations where the change in oxygen concentration is not significant at the 99% level according to a Wilcoxon rank sum test. Topography from observed data corresponds to the seamounts and islands within ±1° around 26°S

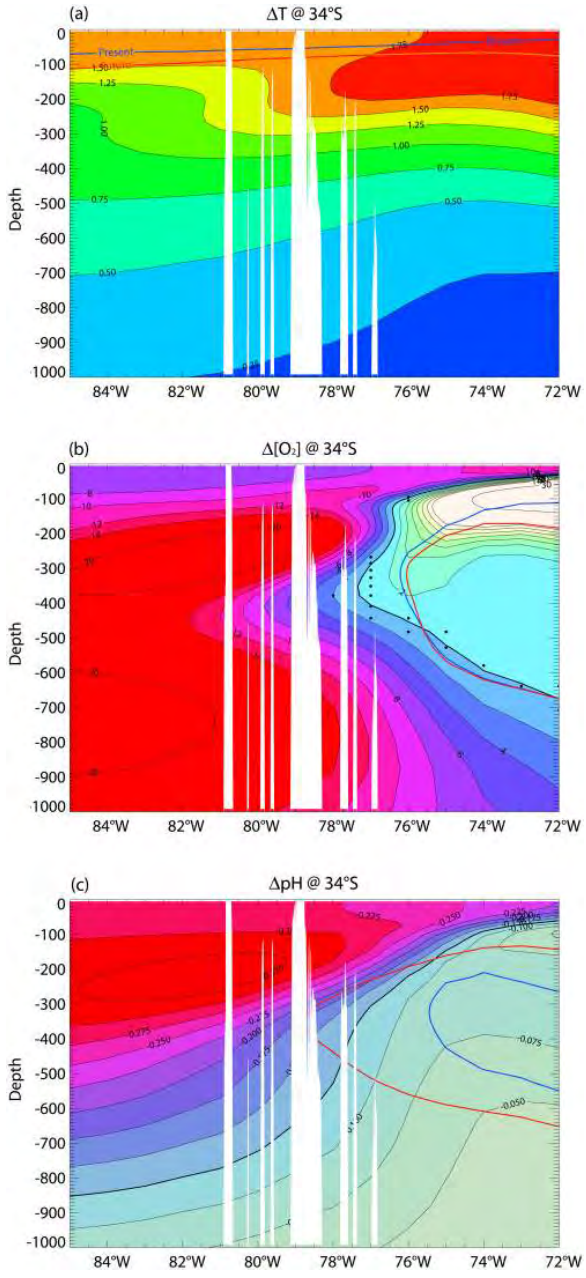

FIGURE 8 As in Figure 7, but for a section at 34°S (Juan Fernandez Archipelago)

east of the Desventuradas and Juan Fernandez archipelagos (Figures 7a and 8a).

Besides mean state changes, global warming will also induce an increased variability in EP El Niño events (Cai et al., 2018) and possibly an increased variance in the SPMM, as found for the Northern hemisphere pacific meridional mode (Liguori & Di Lorenzo, 2018).

5.2 | Overall effect of changing oceanic conditions on marine ecosystems

Various factors must be considered for predicting the impact of changing oceanic conditions on the island and seamount marine ecosystems in the SEP, which are difficult to rank in importance, considering the current knowledge gaps and uncertainties. Among those factors, connectivity patterns and the environmental tolerance of species are certainly at the top of the list. The changes in mean circulation are likely to modulate connectivity patterns between regions in the SEP (for the connectivity between the central Chile coast and Easter Island ecoregion, see Jan van Gennip et al., 2019), and between seamounts within subsystems, although this can be offset by changes in mesoscale activity at basin-scale and/or fine-scale recirculation processes associated with the interaction between mean circulation and topography. For instance, the projected increase in equatorward winds off central Chile in the warmer climate would be favourable for the connectivity from the Juan Fernandez Archipelago towards the Desventuradas Archipelago through enhancing the Ekman-driven surface current. The increased stratification along the coast may also be favourable for an increase in mesoscale activity (Echevin et al., 2012) that, although having the potential to increase larval retention over the continental shelf (Brochier et al., 2013), can yield a more dissipative northward transport in the open ocean, and in turn reduce the effectiveness of the connectivity. Compensating effects may thus take place that are yet to be investigated.

So far, most efforts relevant for the SEP region have focused on analysing low-resolution global ESMs that although incorporating ecological complexity still suffer large uncertainties. The approach has mostly relied on temperature changes alone as the main driver of the reorganization of species diversity patterns, in particular estimating 'the velocity of climate change' or 'climate velocity', which is the rate and direction that isotherms shift through space (see section 2.3). From this approach, Burrows et al. (2014) characterized climate zones that mark disconnection milestone regions (climate trajectories based on isotherms tracking divergence) where spatial local conditions (isotherms) are new or have been lost. Thus, climate sources are regions where locally novel conditions are not connected to areas in which similar climates have previously occurred (and are thereby inaccessible to climate migrants tracking isotherms) and climate sinks are regions where climate conditions have disappeared locally. Coastlines are acting as barriers and cooler oceanic areas are acting as attractors for trajectories (i.e. streamlines associated with climate velocity), creating source and sink areas for local climatic conditions. In the Chilean oceanic ecoregions, slow-moving cells (i.e., with weak climate velocities caused by sharp changes in temperature gradient or by weak temperature trends) are represented (for a result from one climate model under the RCP8.5 scenario, see their Figure 4c). The Easter Island ecoregion sits on the border of a swift convergence zone. Convergence areas and some divergence cells are also present in the Chilean upwelling system. Some coastal sinks are observed along the Chilean coast. For the last 50 years (1960–2009), Burrows et al. (2014) reported slow-moving cells south of 30°S (their Figure 2b), meaning

that climate change did not propagate rapidly across the surface, and so there was little or slow change in species distributions based on this metric over the last five decades. For the 21st century, under the RCP8.5 scenario, climate trajectories for SST using an ensemble of global models predicted different patterns of shifting climates in the SEP (for one model, see their Figure 4c). Slow-moving cells and coastal sinks have disappeared in the SEP. Climate sources are still present all along the Chilean coast, from 20°S to 30°S. South of 30°S, offshore southern Chilean convergence regions are predicted. The Easter Island ecoregion is located on the border of climate corridors witnessing either stable or increased species richness. In these regions, spatial and temporal dynamics in habitat together with the ambient trophic structure will ultimately regulate fish distributions (e.g. along the coast of Peru, sardine benefits from a more oxygenated and deeper habitat, whereas anchovies, with lower respiration rates, survive in a very shallow oxycline). Overall, the study by Burrows et al. (2014) suggests that the SEP could experience a significant reorganization in patterns of species diversity driven just by changes in mean SST as a result of climate change.

This is without considering the effects of ocean deoxygenation and acidification on the marine biota. These are a direct consequence of the warming of the surface waters and increase in atmospheric CO_2 that, respectively, decrease the oxygen solubility of sea water and increase the carbon dioxide uptake by the ocean. Trajectories of oxygen concentrations and pH might be instrumental for predicting the evolution of the marine fauna and its assemblage in the SEP. Mecho et al. (2020) indicate in particular that oxygen gradients were key to explaining the spatial changes in the echinoderm community composition in the mesophotic systems of the SEP. Furthermore, among benthic taxa, echinoderms have been reported as being among the most sensitive taxa to hypoxia (Levin, 2003). An interesting feature of the SEP is that, despite the fact that the global ocean will lose oxygen in the future, the already deoxygenated (hypoxic) waters of the OMZ may become better ventilated through enhanced mixing in the upper ocean, which might preserve habitats for species having developed a tolerance to oxygen changes in a region of marked mean gradients, as found in the Desventuradas and Juan Fernandez archipelagos, which border the OMZ limit (see red line in Figure 4). Off Chile, near the coast, the CESM model simulates an oxygenation of the OMZ at the oxycline level without offshore expansion of the OMZ limit. In the vicinity of the seamounts and island systems, to the west of the OMZ limit, however, ocean deoxygenation will take place with a peak amplitude at a depth of approximately 200 m near the Juan Fernandez and Desventuradas archipelagos (Figure 7b), and at a depth of approximately 600 m along the Salas y Gomez ridge, up to Easter Island (Figure 8b). Changes in pH also exhibit a pattern that exposes the seamounts to significant increases in acidity, as minimum values of pH changes (approx. – 0.3 units) between the future and present climates are found in the depth range between 150 and 350 m along 26°S and 34°S (Figures 7c and 8c). These changes are likely to have profound impacts on marine species, in particular in the weakly mobile benthic fauna of the seamounts of the Desventuradas and Juan Fernandez archipelagos, where the severity of the deoxygenation and acidification trends combines to produce maximum physiological stress (Breitburg et al., 2018) and life-cycle alterations for some benthic groups (i.e., echinoderms), such as stage-specific developmental phenomena, which may drive the whole-species responses (Dupont et al., 2010). For instance, the ability to withstand low-oxygen conditions of the squat lobster, *Pleuroncodes monodon*, a conspicuous inhabitant of the SEP OMZ, is severely affected in warmer waters (Gallardo et al., 2019). Also related to synergistic deleterious effects of changes in abiotic conditions, the combination of rising temperatures and decreasing pH levels has been proven to severely affect the physiology of the widespread cold-water scleractinian coral *Desmophyllum dianthus* (Gori et al., 2016), and species that also occur in seamounts of the Nazca and Salas y Gómez ridges. The adaptive capacities of species should also be taken into account, however. It is known that the physiological tolerance of local populations within a species range can in particular vary widely through adaptation and acclimatization to local environmental conditions (Gallardo et al., 2019; Steckbauer et al., 2015; Valladares et al., 2014). It can also be hypothesized that benthic fauna in the Desventuradas and Juan Fernandez archipelagos may have adapted to episodic or prolonged decreases in dissolved oxygen concentration, as the OMZ characteristics (volume and extension) are modulated by climate variability (Garçon et al., 2019). In the same way that marine organisms encounter limitations to their displacement in response to climate change-induced temperature variations, however, they can also meet constraints in their capacity to migrate because of the presence of poorly oxygenated waters, as in the neighbourhood of the OMZ (Breitburg et al., 2018; Brown & Thatje, 2015; Stramma et al., 2012). This is particularly important for fish, which, in general, are very sensitive to hypoxia (Levin, 2003). As both the rate of change in oxygen and its spatial gradient (horizontally and vertically) differ from that of temperature, this implies that distinct climate velocities are found for oxygen and temperature. As an illustration, Figures 9 and 10 display estimates of climate velocity for temperature and dissolved oxygen, respectively, at three different depths within the euphotic layer. For temperature, climate velocity is always positive, whereas for dissolved oxygen, the climate velocity can be negative and positive. The results indicate that both the pattern and amplitude of the climate velocities are quite distinct, with the differences in patterns increasing with depth. At the surface, the oxygen changes tend to mirror the warming trend as surface waters absorb less atmospheric oxygen through reduced solubility, whereas at the subsurface, the circulation (ventilation) and the biogeochemical processes combine to shape the oxygen patterns and gradients. Note that along the coast of South America the climate velocity associated with surface temperature is weak because the zonal gradients are large as a result of coastal upwelling, whereas at depths of 100 m, where gradients are reduced owing to the flatter isotherms (thermocline), the climate velocity increases sharply, with a pattern mimicking the long-term SST trend (Figure 6). At depths of 200 m, the maximum velocities are found further offshore, consistent with the subsurface penetration of the warming trend (Figures 7a and 8a). The large values of climate velocity at the subsurface (depths of 200 m) suggest a potentially

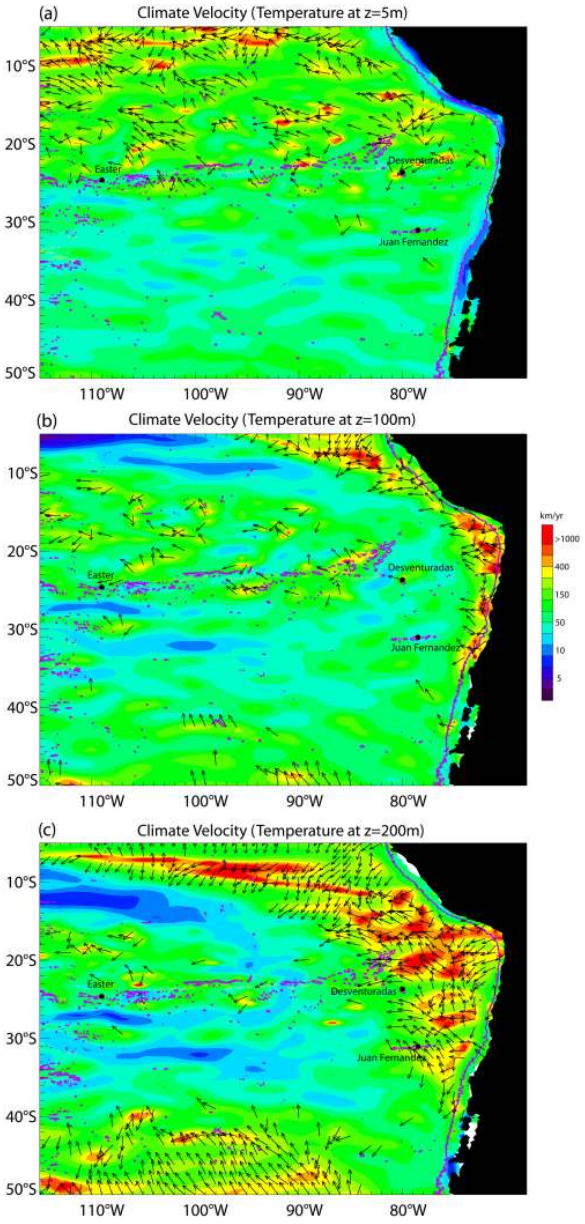

FIGURE 9 Climate velocity (amplitude (contour); direction (arrows)) associated with temperature for the RCP8.5 scenario (2005–2100) of the CESM model at depths of (a) 5 m, (b) 100 m, and (c) 200 m. Only directions for amplitudes greater than 150 km/yr are plotted. The line in pink indicates the 2,000-m isobath and helps to visualize the chains of seamounts along the Nazca and Salas y Gomez ridges

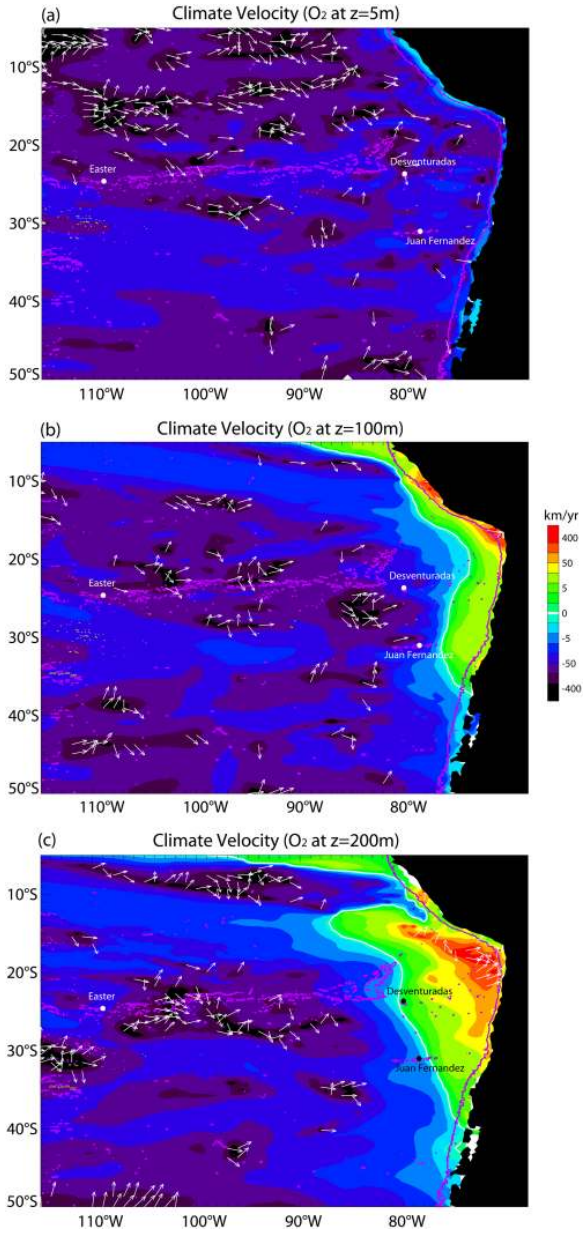

FIGURE 10 As in Figure 9, but for the climate velocity associated with dissolved oxygen

large impact on benthic fauna on the seamount systems of the Desventuradas and Juan Fernandez archipelagos. Regarding the climate velocity associated with dissolved oxygen (Figure 10), it is interesting to note that this becomes positive (i.e. increased oxygenation) at the subsurface along the coast of Peru and Chile, within the OMZ, suggesting a compensating effect of the warming temperature on marine species. From the Nazca Ridge up to the Sala y Gomez Ridge, however, the estimate of climate velocity suggests a potentially negative effect on biota. Although the interpretation of these results needs to be taken with caution because of limitations associated with data and model biases, it indicates that, for the SEP, the prevailing 2D understanding of the responses of marine life to climate change needs to be expanded to 3D approaches, integrating the vertical habitat compression of marine organisms with ocean warming (Jorda et al., 2020), but also with oxygen content. Depth-range compression

of organisms occupying benthic habitats is of particular concern as it also involves a 2D compression of the habitat. This is because these organisms – unlike pelagic species – cannot occupy the full 3D extent of the water column, as the area that they potentially occupy is progressively pushed downslope. Along the coast of Chile, which represents a hot spot of vertical isotherm migration (Jorda et al., 2020), the potential for poleward horizontal migration in these regions (associated in particular with the poleward Peru–Chile undercurrent) may offset the physiological challenges associated with vertical migration (for example, light, hydrostatic pressure, and oxygen-limitation capacity). In the open ocean seamounts and island systems of the SEP, however, poleward horizontal migration may be more challenging, requiring the fauna to physiologically adapt to depth-related environmental stressors or to take advantage of the intricate and dense assemblage of seamounts to respond to climate change through both horizontal and vertical migration.

6 | CONCLUDING REMARKS

The Chilean islands and seamounts of the SEP form a unique system in which the Easter Island ecoregion, extending up to Salas y Gómez Island, is centred in the most oligotrophic and biomass-poor waters in the world, whereas the Desventuradas and Juan Fernandez archipelagos border, to their eastern flank, one of the most productive regions of the planet. Inferring a general mechanistic model that quantifies how changing environmental conditions, which are diverse, will alter the marine environment surrounding the Chilean islands is thus a challenging task. Various factors come into play, and it is not possible to rank these by importance because of numerous knowledge gaps. These can be divided into two broad classes: (i) the fine-scale ocean dynamics in the SEP are not yet accessible from climate change projections; and (ii) the physiological tolerance and adaptive capacity of marine species to the global warming-induced changes in temperature, oxygen, and pH are still poorly known for this region of the world. This limits our understanding of how climate change can alter the growth, mortality, reproduction, mobility, fitness, phenology, and interactions of individuals, and thus the overall structure and functioning of the ecosystems and food-web dynamics.

Broadly, increased metabolic rates as a result of rising temperatures are likely to restrict organismal aerobic capacities, as in other regions of the world. The chain of seamounts potentially favouring connectivity between regions, both horizontally and vertically, could help mitigate the negative effects of temperature increase in the surface layer. The physiology of hypoxic, acidic, and thermal tolerance of key marine species, in particular echinoderms, in the island systems remains to be evaluated. The tolerance of marine species to warming and oxygen loss are physiologically related and can be represented in a single metric: the ratio of temperature-dependent oxygen supply and demand rates. This ratio, called the metabolic index (φ), measures the environmental scope for aerobic activity and is governed by ocean conditions as well as thermal and hypoxia sensitivity traits that vary across species (Deutsch et al., 2015). If climate warming and oxygen loss reduce φ below the species-specific minimum requirement for sustained ecological activity (φ_{crit}), the ocean would no longer support active aerobic metabolism and, by extension, long-term population persistence (Howard et al., 2020). Climate velocities of metabolic indexes for the major marine species in the SEP could inform on the fate of the available aerobic habitat volume under a warmer climate.

Global model projections only provide a broad view of the likely compression of habitats in that region based on changes in temperature, pH, oxygen, and net primary production (NPP). In general, the amplitude of the changes in these variables is relatively smaller in the SEP than in any other regions of the world. For instance, although NPP by marine phytoplankton will decrease substantially over most of the tropical Pacific, because the increased stratification (Capotondi et al., 2012) prevents nutrients found at depth from making their way to the surface where they are needed for photosynthesis, the decreasing trend in the SEP is predicted to be relatively weak, with even the region between Easter Island and the Desventuradas Archipelago exhibiting a positive trend (see Figure 5d of Bopp et al., 2013). The relatively 'mild' environmental stress that will be experienced in the SEP, compared with other regions of the world, does not mean that the structure and function of both pelagic and benthic communities will not be drastically impacted because of the nonlinear internal dynamics of the ecosystem, associated with the multiple physical processes at work and the complexity of the food web (Lett et al., 2010; Payne et al., 2016; Rose et al., 2010). This can only be evaluated by improving our knowledge of the structure of biota assemblages, the physiology of key marine species, and incorporating more complexity in the ESMs used for climate projections.

Considering including more physics in the models, through increased resolution (i.e., taking into account the details of topographic features, such as the chain of seamounts), for simulating more realistically the dispersal and connectivity of larva among the islands, and between the islands and the continent, appears a prerequisite. Although only integrating the lowest end of the food web, biophysical modelling based on Lagrangian tools has been a powerful approach for understanding ecosystem dynamics (Dubois et al., 2016; Lett et al., 2010), and its application has been limited, so far, by the availability of hydrodynamical model simulations at an adequate resolution for resolving the physical processes relevant for larvae dispersal (i.e., processes associated with mesoscale to submesoscale dynamics). Challenges also remain in downscaling global ESMs in this region because of persistent biases both in physical and biogeochemical features (Cabré et al., 2015; Richter, 2015). Climate change could affect the Chilean oceanic island ecoregions to different extents. The strengthening (weakening) of large-scale South Pacific current patterns will have a direct impact on the transport and dispersal of early life stages of planktonic species associated with the island systems, subsequently affecting connectivity between populations (Cowen et al., 2000; Cowen et al., 2006; Dubois et al., 2016) and the distribution between ecoregions. In fact, dispersal and connectivity patterns have hardly been documented for the contemporary climate in this region. Fish assemblage studies have revealed stronger links between

the Desventuradas Islands and the Western Pacific rather than the South American coast (Pequeño & Lamilla, 2000). Thus, the Desventuradas Islands appear to be linked to the Salas y Gomez islet, and further to Easter Island, through an extended chain of seamounts and submarine volcanoes that depart from the Nazca Ridge (Rodrigo et al., 2014), forming a submarine alignment that could act as a biological corridor through facilitating connectivity between island systems. A recent large-scale microplastic dispersal study based on global eddy-resolving model simulations supports the likely existence of a biological connection between the Desventuradas Islands and Easter Island along the Nazca Ridge (Jan van Gennip et al., 2019). Using a high-resolution ocean model simulation combined with genetic data, Meerhoff et al. (2018) suggest that the connectivity pattern for the endemic lobster *Panulirus pascuensis* between the Salas y Gomez islet (Motu Motiro Hiva) and Easter Island is asymmetric, with 3% of the adults from Easter Island coming from Salas y Gómez and only 0.02% moving in the opposite direction. A similar feature was also encountered for the rudderfish *Kyphosus sandwicensis* by Valencia et al. (this issue). A similar connectivity study for the Juan Fernández lobster *Jasus frontalis* also suggested asymmetric connectivity between the Juan Fernandez and Desventuradas archipelagos, with an important flux of particles toward the Desventuradas Archipelago, which could contribute and possibly maintain some of the Desventuradas population (Porobić et al., 2012). Genetic Bayesian studies have found, in particular, that a lobster population was first established in the Juan Fernández Archipelago and then expanded towards the Desventuradas Islands by contemporary and historical oceanographic processes (Porobić et al., 2013).

The broad view of the changes in circulation caused by a warming climate, consisting in a southward migration of the South Pacific anticyclone that will increase the equatorward-westward winds off Central Chile (see Figure 6), yields the expectation that the effectiveness of the 'physical' connectivity will increase both between the Salas y Gomez islet and Easter Island and between the Juan Fernandez and Desventuradas archipelagos. Such a null hypothesis would need to be tested from a hierarchy of model systems, from biophysical models (i.e. individual-based models coupled to high-resolution hydrodynamical models) applied to early life-history stages of key species to food-web and end-to-end models, as a basis for developing strategies for resources management. Although Chile has already created several large-scale marine protected areas (MPAs) around these archipelagos, protecting both ends of the Salas y Gómez Ridge (the Nazca-Desventuradas and Motu Motiro Hiva marine parks and the Easter Island Multiple Uses MPA, three large-scale MPAs that total more than 1,000,000 km^2 of protection within the Chilean EEZ; Paredes et al., 2019), the expected large-scale change in the circulation discussed here, combined with exposure to environmental stressors such as ocean deoxygenation and acidification, calls for the unification of these MPAs through a blue corridor along the Salas y Gómez and Nazca ridges, in order to enhance the resilience of the overall ecosystem function and preserve the biota structure while knowledge gaps in our understanding of the connectivity patterns amongst the assemblages between the different island systems are filled. Such an initiative could be inspired by the Eastern Tropical Pacific Seascape (ETPS), an area of more than 2,000,000 km^2 resulting from a partnership between the governments of Colombia, Costa Rica, Equator, and Panamá, established under the auspices of UNESCO (United Nations Educational, Scientific and Cultural Organization), forming an ecologically representative network of marine protected areas aimed at preserving migratory routes for whales, fur seals, sea lions, sharks, turtles, and seabirds (Bessudo et al., 2011; Ketchum et al., 2014). Although no effective protection is in place in the area beyond national jurisdiction (ABNJ) at the Salas y Gómez and Nazca ridges, both ridges were declared ecologically or biologically significant marine areas (EBSAs) by the Convention on Biological Diversity (CBD) at the 12th Conference of the Parties (COP 12) in 2014 (CBD, 2014). Several recent international collaborative research efforts are aiming to explore the Salas y Gómez Ridge (Easton et al., 2019; Mecho et al., 2019), in order to collect the necessary information for understanding the processes that determine the observed biodiversity patterns. This represents a keystone for implementing integrated ecosystem management tools and ecosystem-based management (EBM), taking into account climate projections, as a basis for designing effective protection measures (e.g. MPAs) in this EBSA (Wagner et al., 2020).

ACKNOWLEDGEMENTS

The authors would like to thank the two anonymous reviewers for their constructive comments that helped improve the original manuscript. We also thank Dr Laura Ramajo for fruitfull discussions. Carlos Conejero was supported by a doctoral scholarship from the National Chilean Research and Technology Council (CONICYT) through the programme Becas Chile (scholarship 72170554). Boris Dewitte acknowledges support from FONDECYT (project N° 1190276). Luis Bravo acknowledges support from FONDECYT (project N° 11190918). This research was also supported by the Chilean Millennium Initiative ESMOI and IRD (Research Institute for Development, France).

AUTHOR CONTRIBUTIONS

B.D. led the study and wrote the initial manuscript. B.D., C.C. and M. R. performed the analyses and generated the final figures. All co-authors participated in discussion of the results and contributed to the manuscript.

CONFLICT OF INTEREST

The authors declare no conflict of interest.

ORCID

Boris Dewitte https://orcid.org/0000-0003-3817-8691
Véronique Garçon https://orcid.org/0000-0002-4041-1379
Carolina Parada https://orcid.org/0000-0003-1311-5563
Ariadna Mecho https://orcid.org/0000-0001-7361-815X
Carlos F. Gaymer https://orcid.org/0000-0003-4395-9505

REFERENCES

Andrade, I., Sangrà, P., Hormazábal, S. E., & Correa-Ramírez, M. A. (2014). Island mass effect in the Juan Fernández Archipelago (33°S), Southeastern Pacific. *Deep Sea Research Part I: Oceanographic Reseach Papers*, *84*, 86–99. https://doi.org/10.1016/j.dsr.2013.10.009

Arntz, W. E., Gallardo, V. A., Gutiérrez, D., Isla, E., Levin, L. A., Mendo, J., … Wolff, M. (2006). El Niño and similar perturbation effects on the benthos of the Humboldt, California, and Benguela Current upwelling ecosystems. *Advances in Geosciences*, *6*, 243–265. https://doi.org/10.5194/adgeo-6-243-2006

Bakun, A. (1990). Global climate change and intensification of coastal upwelling. *Science*, *247*, 198–201. https://doi.org/10.1126/science.247.4939.198

Barton, E. D. (2001). Island wakes. *Encyclopedia of Ocean Sciences*, 1397–1403. https://doi.org/10.1006/rwos.2001.0140

Belmadani, A., Concha, E., Donoso, D., Chaigneau, A., Colas, F., Maximenko, N. A., & Di Lorenzo, E. (2017). Striations and preferred eddy tracks triggered by topographic steering of the background flow in the eastern South Pacific. *Journal of Geophysical Research: Oceans*, *122*, 2847–2870. https://doi.org/10.1002/2016JC012348.IPRC-1243

Belmadani, A., Echevin, V., Codron, F., Takahashi, K., & Junquas, C. (2014). What dynamics drive future wind scenarios for coastal upwelling off Peru and Chile? *Climate Dynamics*, *43*, 1893–1914. https://doi.org/10.1007/s00382-013-2015-2

Belmadani, A., Maximenko, N. A., Mccreary, J. P., Furue, R., Melnichenko, O. V., Schneider, N., & Lorenzo, E. D. (2013). Linear Wind-Forced Beta Plumes with Application to the Hawaiian Lee Countercurrent. *Journal of Physical Oceanography*, *43*, 2071–2094. https://doi.org/10.1175/JPO-D-12-0194.1

Bessudo, S., Soler, G. A., Klimley, A. P., Ketchum, J. T., Hearn, A., & Arauz, R. (2011). Residency of the scalloped hammerhead shark (*Sphyrna lewini*) at Malpelo Island and evidence of migration to other islands in the Eastern Tropical Pacific. *Environmental Biology of Fishes*, *91*, 165–176. https://doi.org/10.1007/s10641-011-9769-3

Bettencourt, J., Lopez, C., Hernandez-Garcia, E., Montes, I., Sudre, J., Dewitte, B., … Garçon, V. (2015). Boundaries of the Oxygen Minimum Zone shaped by coherent mesoscale dynamics. *Nature Geoscience*, *8*, 937–940. https://doi.org/10.1038/NGEO2570

Bopp, L., Resplandy, L., Orr, J. C., Doney, S. C., Dunne, J. P., Gehlen, M., … Vichi, M. (2013). Multiple stressors of ocean ecosystems in the 21st century: Projections with CMIP5 models. *Biogeosciences*, *10*, 6225–6245. https://doi.org/10.5194/bg-10-6225-2013

Breitburg, D., Levin, L. A., Oschlies, A., Grégoire, M., Chavez, F. P., Conley, D. J., … Zhang, J. (2018). Declining oxygen in the global ocean and coastal waters. *Science*, *359*, eaam7240. https://doi.org/10.1126/science.aam7240

Bretherton, C. S., Smith, C., & Wallace, J. M. (1992). An intercomparison of methods for finding coupled patterns in climate data. *Journal of Climate*, *5*, 541–560. https://doi.org/10.1175/1520-0442(1992)005<0541:AIOMFF>2.0.CO;2

Brochier, T., Echevin, V., Tam, J., Chaigneau, A., Goubanova, K., & Bertrand, A. (2013). Climate change scenarios experiments predict a future reduction in small pelagic fish recruitment in the Humboldt Current system. *Global Change Biology*, *19*, 1841–1853. https://doi.org/10.1111/gcb.12184

Brown, A., & Thatje, S. (2015). The effects of changing climate on faunal depth distributions determine winners and losers. *Global Change Biology*, *21*, 173–180. https://doi.org/10.1111/gcb.12680

Burrows, M. T., Schoeman, D. S., Buckley, L. B., Moore, P., Poloczanska, E. S., Brander, K. M., … Richardson, A. J. (2011). The pace of shifting climate in marine and terrestrial ecosystems. *Science*, *334*, 652–655. https://doi.org/10.1126/science.1210288

Burrows, M. T., Schoeman, D. S., Richardson, A. J., Molinos, J. G., Hoffmann, A., Buckley, L. B., … Poloczanska, E. S. (2014). Geographical limits to species-range shifts are suggested by climate velocity. *Nature*, *507*, 492–495. https://doi.org/10.1038/nature12976

Cabré, A., Marinov, I., Bernardello, R., & Bianchi, D. (2015). Oxygen minimum zones in the tropical Pacific across CMIP5 models: Mean state differences and climate change trends. *Biogeosciences*, *12*, 5429–5454. https://doi.org/10.5194/bg-12-5429-2015

Cai, W., Lengaigne, M., Borlace, S., Collins, M., Cowan, T., McPhaden, M. J., … Widlansky, M. J. (2012). More extreme swings of the South Pacific convergence zone due to greenhouse warming. *Nature*, *488*, 365–369. https://doi.org/10.1038/nature11358

Cai, W., Wang, G., Dewitte, B., Wu, L., Santoso, A., Takahashi, K., … McPhaden, M. J. (2018). Increased variability of eastern Pacific El Niño under greenhouse warming. *Nature*, *564*, 201–206. https://doi.org/10.1038/s41586-018-0776-9

Capet, X., Colas, F., McWilliams, J. C., Penven, P., & Marchesiello, P. (2008). Eddies in eastern boundary subtropical upwelling systems. Ocean Modeling in an Eddying Regime. *Geophysical Monograph Series*, *177*, 131–147. https://doi.org/10.1029/177gm10

Capotondi, A., Alexander, M. A., Bond, N. A., Curchitser, E. N., & Scott, J. D. (2012). Enhanced upper ocean stratification with climate change in the CMIP3 models. *Journal Geophysical Research: Oceans*, *117*, C04031. https://doi.org/10.1029/2011JC007409

Capotondi, A., Wittenberg, A. T., Newman, M., Di Lorenzo, E., Yu, J. Y., Braconnot, P., … Yeh, S.-W. (2015). Understanding ENSO diversity. *Bulletin of the American Meteorological Society*, *96*, 921–938. https://doi.org/10.1175/BAMS-D-13-00117.1

CBD. (2014). Decision adopted by the Conference of the Parties to the Convention on Biological Diversity. Conference of the Parties to the Convention on Biological Diversity Twelfth Meeting. Pyeongchang, Republic of Korea, 6–17 October 2014. Agenda Item 21. 59 pp.

Chiang, J. C., & Vimont, D. J. (2004). Analogous Pacific and Atlantic meridional modes of tropical atmosphere–ocean variability. *Journal of Climate*, *17*, 4143–4158. https://doi.org/10.1175/JCLI4953.1

Chust, G., Icarus Allen, J., Bopp, L., Schrum, C., Holt, J., Tsiaras, K., … Irigoien, X. (2014). Biomass changes and trophic amplification of plankton in a warmer ocean. *Global Change Biology*, *20*, 2124–2139. https://doi.org/10.1111/gcb.12562

Combes, V., Hormazabal, S., & Di Lorenzo, E. (2015). Interannual variability of the subsurface eddy field in the Southeast Pacific. *Journal of Geophysical Research: Oceans*, *120*, 4907–4924. https://doi.org/10.1002/2014jc010265

Conejero, C., Dewitte, B., Garçon, V., Sudre, J., & Montes, I. (2020). ENSO diversity driving low-frequency change in mesoscale activity off Peru and Chile. *Scientific Reports*, *10*, 17902. https://doi.org/10.1038/s41598-020-74762-x

Cornejo D'Ottone, M., Bravo, L., Ramos, M., Pizarro, O., Karstenssen, J., Gallegos, M., … Karp-Boss, L. (2016). Biogeochemical characteristics of a long-lived anticyclonic eddy in the eastern South Pacific Ocean. *Biogeosciences*, *13*, 2971–2979. https://doi.org/10.5194/bg-13-2971-2016

Cowen, R. K., Lwiza, K. M. M., Sponaugle, S., Paris, C. B., & Olson, D. B. (2000). Connectivity of marine populations: Open or closed? *Science*, *287*, 857–859. https://doi.org/10.1126/science.287.5454.857

Cowen, R. K., Paris, C. B., & Srinivasan, A. (2006). Scaling of connectivity in Marine Populations. *Science*, *311*, 522–527. https://doi.org/10.1126/science.1122039

de Szoeke, S. P., Yuter, S. E., Mechem, D., Fairall, C. W., Burleyson, C. D., & Zuidema, P. (2012). Observations of stratocumulus and their effect on the eastern Pacific surface heat budget along 20°S. *Journal of Climate*, *25*, 8542–8567. https://doi.org/10.1175/JCLI-D-11-00618.1

Deser, C., Phillips, A. S., Tomas, R. A., Okumura, Y. M., Alexander, A., Capotondi, A., … Ohba, M. (2012). ENSO and Pacific decadal variability

in Community Climate System Model version 4. *Journal of Climate*, *25*, 2622–2651. https://doi.org/10.1175/JCLI-D-11-00301.1

Deutsch, C., Ferrel, A., Seibel, B. A., Portner, H.-O., & Huey, R. B. (2015). Climate change tightens a metabolic constraint on marine habitat. *Science*, *348*, 1132–1135. https://doi.org/10.1126/science.aaa1605

Dewitte, B., Ramos, M., Echevin, V., Pizarro, O., & duPenhoat, Y. (2008). Vertical structure variability in a seasonal simulation of a medium-resolution regional model simulation of the South Eastern Pacific. *Progress in Oceanography*, *79*, 120–137. https://doi.org/10.1016/j.pocean.2008.10.014

Dewitte, B., & Takahashi, K. (2017). Diversity of moderate El Niño events evolution: Role of air-sea interactions in the eastern tropical Pacific. *Climate Dynamics*, *52*, 7455–7476. https://doi.org/10.1007/s00382-017-4051-9

Dewitte, B., & Takahashi, K. (2018). Extreme El Niño events. In V. Vuruputur, J. Sukhatme, R. Murtugudde, & R. Roca (Eds.), *Tropical extremes: natural variability and trends*. Amsterdam, Netherlands: Elsevier. https://doi.org/10.1016/B978-0-12-809248-4.00006-6

Dewitte, B., Vazquez-Cuervo, J., Goubanova, K., Illig, S., Takahashi, K., Cambon, G., … Ortlieb, L. (2012). Change in El Niño flavours over 1958–2008: Implications for the long-term trend of the upwelling off Peru. *Deep Sea Research Part II: Topical Studies in Oceanography*, *77-80*, 143–156. https://doi.org/10.1016/j.dsr2.2012.04.011

Doty, M. S., & Oguri, M. (1956). The island mass effect. *ICES Journal of Marine Science*, *22*, 33–37. https://doi.org/10.1093/icesjms/22.1.33

Dubois, M., Rossi, V., Ser-Giacomi, E., Arnaud-Haond, S., López, C., & Hernández-García, E. (2016). Linking oceanography, larval connectivity and population dynamics for the management of marine ecosystems. *Global Ecology and Biogeography*, *25*, 503–515. https://doi.org/10.1111/geb.12431

Dunn, J. R., & Ridgway, K. R. (2002). Mapping ocean properties in regions of complex topography. *Deep Sea Research Part I: Oceanographic Research Papers*, *49*, 591–604. https://doi.org/10.1016/S0967-0637(01)00069-3

Dupont, S., Ortega-Martínez, O., & Thorndyke, M. (2010). Impact of near-future ocean acidification on echinoderms. *Ecotoxicology*, *19*, 449–462. https://doi.org/10.1007/s10646-010-0463-6

Easton, E. E., Gorny, M., Mecho, A., Sellanes, J., Gaymer, C. F., Spalding, H. L., & Aburto, J. (2019). Chile and the Salas y Gómez ridge. In Y. Loya, K. Puglise, & T. Bridge (Eds.), *Mesophotic coral ecosystems* (Vol. 12). Coral Reefs of the World. (pp. 477–490). Cham: Springer.

Echevin, V., Goubanova, K., Belmadani, A., & Dewitte, B. (2012). Sensitivity of the Humboldt current system to global warming: A downscaling experiment with the IPSL_CM4 model. *Climate Dynamics*, *38*, 761–774. https://doi.org/10.1007/s00382-011-1085-2, https://doi.org/10.1007/s00382-011-1085-2

England, M. H., McGregor, S., Spence, P., Meehl, G. A., Timmermann, A., Cai, W., … Santoso, A. (2014). Recent intensification of wind-driven circulation in the Pacific and the ongoing warming hiatus. *Nature Climate Change*, *4*, 222–227. https://doi.org/10.1038/nclimate2106

Falvey, M., & Garreaud, R. D. (2009). Regional cooling in a warming world: Recent temperature trends in the southeast Pacific and along the west coast of subtropical South America (1979–2006). *Journal of Geophysical Research: Atmospheres*, *114*, D04102. https://doi.org/10.1029/2008JD010519

Folland, C. K., Renwick, J. A., Salinger, M. J., & Mullan, A. B. (2002). Relative influences of the interdecadal Pacific oscillation and ENSO on the South Pacific convergence zone. *Geophysical Research Letters*, *29*, 21–1–21-4. https://doi.org/10.1136/bjsm.36.5.370

Friedlander, A. M., Ballesteros, E., Beets, J., Berkenpas, E., Gaymer, C. F., Gorny, M., & Sala, E. (2013). Effects of isolation and fishing on the marine ecosystems of Easter Island and Salas y Gómez, Chile. *Aquatic Conservation: Marine and Freshwater Ecosystems*, *23*, 515–531. https://doi.org/10.1002/aqc.2333

Fuenzalida, R., Schneider, W., Garcés-Vargas, J., Bravo, L., & Lange, C. (2009). Vertical and horizontal extension of the oxygen minimum zone in the eastern South Pacific Ocean. *Deep Sea Research Part II: Topical Studies in Oceanography*, *56*, 992–1003. https://doi.org/10.1016/j.dsr2.2008.11.001

Gallardo, M. A., Gonzalez, A. E., Ramos, M., Mujica, A., Muñoz, P., Sellanes, J., … Yannicelli, B. (2017). Reproductive patterns in demersal crustaceans from the upper boundary of the OMZ off north-central Chile. *Continental Shelf Research*, *141*, 26–37. https://doi.org/10.1016/j.csr.2017.04.011

Gallardo, M. A., Nuñez, V., Thiel, M., Yannicelli, B., Brokordt, K., & Rojas, I. (2019). Life on the edge: Incubation behaviour and physiological performance of squat lobsters in oxygen-minimum conditions. *Marine Ecology Progress Series*, *623*, 51–70. https://doi.org/10.3354/meps12984

García Molinos, J., Schoeman, D. S., Brown, C. J., & Burrows, M. T. (2019). VoCC: The Velocity of Climate Change and related climatic metrics. R Package Version 1.0.0. https://doi.org/10.5281/zenodo.3382092

Garçon, V., Dewitte, B., Montes, I., & Goubanova, K. (2019). Land-Sea-Atmosphere interactions exacerbating ocean deoxygenation in Eastern Boundary Upwelling Systems (EBUS). In D. Laffoley & J. M. Baxter (Eds.), *Ocean deoxygenation: Everyone's problem, causes, impacts, consequences and solutions* (pp. 171–186). Gland, Switzerland: IUCN (International Union for Conservation of Nature and Natural Resources Report. https://doi.org/10.2305/IUCN.CH.2019.13.en

Gori, A., Ferrier-Pages, C., Hennige, S. J., Murray, F., Rottier, C., Wicks, L. C., & Roberts, M. J. (2016). Physiological response of the cold-water coral *Desmophyllum dianthus* to thermal stress and ocean acidification. *PeerJ*, *4*, e1606. https://doi.org/10.7717/peerj.1606

Goubanova, K., Echevin, V., Dewitte, B., Codron, F., Takahashi, K., Terray, P., & Vrac, M. (2011). Statistical downscaling of sea-surface wind over the Peru-Chile upwelling region: Diagnosing the impact of climate change from the IPSL-CM4 model. *Climate Dynamics*, *36*, 1365–1378. https://doi.org/10.1007/s00382-010-0824-0

Gutiérrez, D., Bouloubassi, I., Sifeddine, A., Purca, S., Goubanova, K., Graco, M., … Ortlieb, L. (2011). Coastal cooling and increased productivity in the main upwelling zone off Peru since the mid-twentieth century. *Geophysical Research Letters*, *38*, L07603. https://doi.org/10.1029/2010GL046324

Henley, B. J., Gergis, J., Karoly, D. J., Power, S. B., Kennedy, J., & Folland, C. K. (2015). A tripole index for the interdecadal pacific oscillation. *Climate Dynamics*, *45*, 3077–3090. https://doi.org/10.1007/s00382-015-2525-1

Heywood, K. J., Barton, E. D., & Simpson, J. H. (1990). The effects of flow disturbance by an oceanic island. *Journal of Marine Research*, *48*, 55–73. https://doi.org/10.1357/002224090784984623

Heywood, K. J., Stevens, D. P., & Bigg, G. R. (1996). Eddy formation behind the tropical island of Aldabra. *Deep Sea Research Part I: Oceanographic Research Papers*, *43*, 555–578. https://doi.org/10.1016/0967-0637(96)00097-0

Hong, L., Zhang, L., Chen, Z., & Wu, L. (2014). Linkage between the Pacific Decadal Oscillation and the low frequency variability of the Pacific Subtropical Cell. *Journal of Geophysical Research: Oceans*, *119*, 3464–3477. https://doi.org/10.1002/2013jc009650

Hormazabal, S., Combes, V., Morales, C. E., Correa-Ramirez, M. A., Di Lorenzo, E., & Nunez, S. (2013). Intrathermocline eddies in the coastal transition zone off central Chile (31–41° S). *Journal of Geophysical Research-Oceans*, *118*, 4811–4821. https://doi.org/10.1002/jgrc.20337

Hormazabal, S., Shaffer, G., & Leth, O. (2004). Coastal transition zone off Chile. *Journal of Geophysical Research: Oceans*, *109*, C01021. https://doi.org/10.1029/2003JC001956

Howard, E., Penn, J., Frenzel, H., Seibel, B., Bianchi, D., Renault, L., … Deutsch, C. (2020). Climate-driven aerobic habitat loss in the California Current System. *Science Advances*, *6*, eaay3188. https://doi.org/10.1126/sciadv.aay3188

Hu, S., & Fedorov, A. V. (2018). Cross-equatorial winds control El Niño diversity and change. *Nature Climate Change*, *8*, 798–802. https://doi.org/10.1038/s41558-018-0248-0

Hurrell, J. W., Holland, M. M., Gent, P. R., Ghan, S., Kay, J. E., Kushner, P. J., … Marshall, S. (2013). The Community Earth System Model: A framework for collaborative research. *Bulletin of the American Meteorological Society*, *94*, 1339–1360. https://doi.org/10.1175/BAMS-D-12-00121.1

IPCC (2014). In C. B. Field, V. R. Barros, D. J. Dokken, K. J. Mach, M. D. Mastrandrea, T. E. Bilir, et al. (Eds.), *Climate change 2014: Impacts, adaptation, and vulnerability. Part A: Global and sectoral aspects. Contribution of Working Group II to the Fifth Assessment Report of the Intergovernmental Panel on Climate Change*. Cambridge, UK and New York, NY, USA: Cambridge University Press.

Jan van Gennip, S., Dewitte, B., Garçon, V., Thiel, M., Popova, E., Drillet, Y., … Gaymer, C. F. (2019). In search for the sources of plastic marine litter that contaminates the Easter Island Ecoregion. *Scientific Reports*, *9*, 19662. https://doi.org/10.1038/s41598-019-56012-x

Jorda, G., Marba, N., Bennett, S., Santana-Garcon, J., Agusti, S., & Duarte, C. (2020). Ocean warming compresses the three-dimensional habitat of marine life. *Nature Ecology and Evolution*, *4*, 109–114. https://doi.org/10.1038/s41559-019-1058-0

Kalnay, E., Kanamitsu, M., Kistler, R., Collins, W., Deaven, D., Gandin, L., … Joseph, D. (1996). The NCEP/NCAR 40-Year Reanalysis Project. *Bulletin of the American Meteorological Society*, *77*, 437–472. https://doi.org/10.1175/1520-0477(1996)077<0437:TNYRP>.0.CO;2

Karamperidou, C., Jin, F.-F., & Conroy, J. L. (2016). The Importance of ENSO Nonlinearities in Tropical Pacific Response to External Forcing. *Climate Dynamics*, *49*, 2695–2704. https://doi.org/10.1007/s00382-016-3475-y

Kay, J. E., Deser, C., Phillips, A., Mai, A., Hannay, C., Strand, G., … Vertenstein, M. (2015). The Community Earth System Model (CESM) Large Ensemble Project: A Community Resource for Studying Climate Change in the Presence of Internal Climate Variability. *Bulletin of the American Meteorological Society*, *96*, 1333–1349. https://doi.org/10.1175/BAMS-D-13-00255.1

Ketchum, J. T., Hearn, A., Klimley, A. P., Peñaherrera, C., Espinoza, E., Bessudo, S., … Arauz, R. (2014). Inter-island movements of scalloped hammerhead sharks (*Sphyrna lewini*) and seasonal connectivity in a marine protected area of the eastern tropical Pacific. *Marine Biology*, *161*, 939–951. https://doi.org/10.1007/s00227-014-2393-y

Kug, J.-S., & Ham, Y.-G. (2011). Are there two types of La Nina events? *Geophysical Research Letters*, *38*, L16704. https://doi.org/10.1029/2011GL048237

Kwiatkowski, L., Bopp, L., Aumont, O., Clais, P., Cox, P. M., Laufkötter, C., … Séférian, R. (2017). Emergent constraints on projections of declining primary production in the tropical oceans. *Nature Climate Change*, *7*, 355–358. https://doi.org/10.1038/nclimate3265

Laurindo, L., Mariano, A., & Lumpkin, R. (2017). An improved near-surface velocity climatology for the global ocean from drifter observations. *Deep Sea Research Part I: Oceanographic Research Papers*, *124*, 73–92. https://doi.org/10.1016/j.dsr.2017.04.009

Lett, C., Ayata, S.-D., Huret, M., & Irisson, J.-O. (2010). Biophysical modelling to investigate the effects of climate change on marine population dispersal and connectivity. *Progress in Oceanography*, *87*, 106–113. https://doi.org/10.1016/j.pocean.2010.09.005

Levin, L. A. (2003). Oxygen minimum zone benthos: Adaptation and community response to hypoxia. *Oceanography and Marine Biology. Annual Review*, *41*, 1–45.

Li, W., Li, L., Ting, M., Deng, Y., Kushnir, Y., Liu, Y., … Zhang, P. (2013). Intensification of the Southern Hemisphere summertime subtropical anticyclones in a warming climate. *Geophysical Research Letters*, *40*, 5959–5964. https://doi.org/10.1002/2013GL058124

Liguori, G., & Di Lorenzo, E. (2018). Meridional modes and increasing Pacific decadal variability under anthropogenic forcing. *Geophysical Research Letters*, *45*, 983–991. https://doi.org/10.1002/2017gl076548

Llanillo, P. J., Pelegrí, J. L., Duarte, C. M., Emelianov, M., Gasser, M., Gourrion, J., & Rodrıguez-Santana, A. (2012). Meridional and zonal changes in water properties along the continental slope off central and northern Chile. *Ciencias Marinas*, *38*, 307–332. https://doi.org/10.7773/cm.v38i1B.1814

Loarie, S. R., Duffy, P. B., Hamilton, H., Asner, G. P., Field, C. B., & Ackerly, D. D. (2009). The velocity of climate change. *Nature*, *462*, 1052–1055. https://doi.org/10.1038/nature08649

Long, M. C., Deutsch, C. A., & Ito, T. (2016). Finding forced trends in oceanic oxygen. *Global Biogeochemical Cycles*, *30*, 381–397. https://doi.org/10.1002/2015GB005310

Long, M. C., Lindsay, K., Peacock, S., Moore, J. K., & Doney, S. C. (2013). Twentieth century oceanic carbon uptake and storage in CESM1 (BGC). *Journal of Climate*, *26*, 6775–6800. https://doi.org/10.1175/JCLI-D-12-00184.1

Lovenduski, N. S., Long, M. C., & Lindsay, K. (2015). Natural variability in the surface ocean carbonate ion concentration. *Biogeosciences*, *12*, 6321–6335. https://doi.org/10.5194/bg-12-6321-2015

Lu, J., Vecchi, G. A., & Reichler, T. (2007). Expansion of the Hadley cell under global warming. *Geophysical Research Letters*, *34*, L06805. https://doi.org/10.1029/2006GL028443

Lu, J., & Zhao, B. (2012). The role of oceanic feedback in the climate response to doubling CO_2. *Journal of Climate*, *25*, 7544–7563. https://doi.org/10.1175/JCLI-D-11-00712.1

Luo, Y., Liu, Q., & Rothstein, L. M. (2011). Increase of South Pacific eastern subtropical mode water under global warming. *Geophysical Research Letters*, *38*, L01601. https://doi.org/10.1029/2010GL045878

Luyten, J. R., Pedlosky, J., & Stommel, H. (1983). The ventilated thermocline. *Journal of Physical Oceanography*, *13*, 292–309. https://doi.org/10.1175/1520-0485(1983)013<0292:TVT>2.0.CO;2

MCCIP. (2015). In M. Frost, G. Bayliss-Brown, P. Buckley, M. Cox, B. Stoker, & N. Withers Harvey (Eds.), *Marine climate change impacts: Implications for the implementation of marine biodiversity legislation. Summary Report*. Lowestoft: MCCIP. 16pp. https://doi.org/10.14465/2015.mbl00.001-016

McCreary, J. P., & Lu, P. (1994). On the interaction between the subtropical and equatorial ocean circulation: The Subtropical Cell. *Journal of Physical Oceanography*, *24*, 466–497. truhttps://doi.org/10.1175/1520-0485(1994)024<0466:ibtsae>2.0.co;2

Mecho, A., Dewitte, B., Sellanes, J., Van Gennip, S., Easton, E. E., & Gusmao, J. B. (2020). Environmental factors describing echinoderm assemblages of southeastern Pacific Ocean mesophotic systems. *Frontiers in Marine Science - Deep-Sea Environments and Ecology*. (accepted upon minor revisions)

Mecho, A., Easton, E. E., Sellanes, J., Gorny, M., & Mah, C. (2019). Unexplored diversity of the mesophotic echinoderm fauna of the Easter Island ecoregion. *Marine Biology*, *166*, 91. https://doi.org/10.1007/s00227-019-3537-x

Mechoso, C. R., Wood, R., Bretherton, C. S., Clarke, A. D., Coe, H., Fairall, C., … Zuidema, P. (2014). Ocean–Cloud–Atmosphere–Land Interactions in the Southeastern Pacific: The VOCALS Program. *Bulletin of the American Meteorological Society*, *95*, 357–375. https://doi.org/10.1175/BAMS-D-11-00246.1

Meerhoff, E., Yannicelli, B., Dewitte, B., Diaz-Cabrera, E., Vega-Retter, C., Ramos, M., … Véliz, D. (2018). Asymmetric connectivity of the lobster *Panulirus pascuensis* in remote islands of the southern Pacific:

Importance for its management and conservation. *Bulletin of Marine Science*, *94*, 753–774. https://doi.org/10.5343/bms.2017.1114

Messié, M., Petrenko, A., Doglioli, A. M., Aldebert, C., Martinez, E., Koenig, G., … Moutin, T. (2020). The delayed island mass effect: How islands can remotely trigger blooms in the oligotrophic ocean. *Geophysical Research Letters*, *47*, e2019GL085282. https://doi.org/10.1029/2019GL085282

Miller, A. J., Cayan, D. R., Barnett, T. P., Graham, N. E., & Oberhuber, J. M. (1994). Interdecadal variability of the Pacific Ocean: Model response to observed heat flux and wind stress anomalies. *Climate Dynamics*, *9*, 287–302. https://doi.org/10.1007/bf00204744

Montes, I., Dewitte, B., Gutknecht, E., Paulmier, A., Dadou, I., Oschlies, A., & Garçon, V. (2014). High resolution modeling of the eastern tropical Pacific oxygen minimum zone: Sensitivity to the tropical oceanic circulation. *Journal of Geophysical Research*, *Oceans*, *119*, 5515–5532. https://doi.org/10.1002/2014JC009858

Moore, J. K., Lindsay, K., Doney, K. S., Long, M. C., & Misumi, K. (2013). Marine ecosystem dynamics and biogeochemical cycling in the Community Earth System Model [CESM1(BGC)]: Comparison of the 1990s with the 2090s under the RCP4.5 and RCP8.5 scenarios. *Journal of Climate*, *26*, 9291–9312. https://doi.org/10.1175/jcli-d-12-00566.1

Muñoz, P., Rebolledo, L., Dezileau, L., Maldonado, A., Mayr, C., Cárdenas, P., … Ramos, M. (2020). Reconstructing past variations in environmental conditions and paleoproductivity over the last ∼8000 years off north-central Chile (30° S). *Biogeosciences*. https://doi.org/10.5194/bg-2018-396. in press.

Muñoz, R. C., & Garreaud, R. D. (2005). Dynamics of the low-level jet off the west coast of subtropical South America. *Monthly Weather Review*, *133*, 3661–3677. https://doi.org/10.1175/MWR3074.1

Niznik, M. J., Lintner, B. R., Matthews, A. J., & Widlansky, M. J. (2015). The role of tropical–extratropical interaction and synoptic variability in maintaining the south pacific convergence zone in CMIP5 models. *Journal of Climate*, *28*, 3353–3374. https://doi.org/10.1175/JCLI-D-14-00527.1

Oschlies, A., Brandt, P., Stramma, L., & Schmidtko, S. (2018). Drivers and mechanisms of ocean deoxygenation. *Nature Geoscience*, *11*, 467–473. https://doi.org/10.1038/s41561-018-0152-2

Palacios, D. M. (2002). Factors influencing the island-mass effect of the Galápagos Archipelago. *Geophysical Research Letters*, *29*, 1–4. https://doi.org/10.1029/2002GL016232

Paredes, F., Flores, D., Figueroa, A., Gaymer, C. F., & Aburto, J. A. (2019). Science, capacity building and conservation knowledge: The empowerment of the local community for marine conservation in Rapa Nui. *Aquatic Conservation: Marine and Freshwater Ecosystems*, *29*, 130–137. https://doi.org/10.1002/aqc.3114

Paulmier, A., & Ruiz-Pino, D. (2009). Oxygen minimum zones (OMZs) in the modern ocean. *Progress in Oceanography*, *80*, 113–128. https://doi.org/10.1016/j.pocean.2008.08.001

Payne, M., Barange, M., Cheung, W. W. L., MacKenzie, B., Batchelder, H. P., Cormon, X., … Paula, J. R. (2016). Uncertainties in projecting climate-change impacts in marine ecosystems. *ICES Journal of Marine Science*, *73*, 1272–1282. https://doi.org/10.1093/icesjms/fsv231

Pequeño, G., & Lamilla, J. (2000). The littoralfish assemblage of the Desventuradas Islands (Chile) has zoogeographical affinities with the Western Pacific. *Global Ecology and Biogeography*, *9*, 431–437. https://doi.org/10.1046/j.1365-2699.2000.00207.x

Pinsky, M. L., Worm, B., Fogarty, M. J., Sarmiento, J. L., & Levin, S. A. (2013). Marine taxa track local climate velocities. *Science*, *341*, 1239–1242. https://doi.org/10.1126/science.1239352

Pizarro-Koch, M., Pizarro, O., Dewitte, B., Montes, I., Ramos, M., Paulmier, A., & Garçon, V. (2018). Seasonal variability of the southern tip of the Oxygen Minimum Zone in the Eastern South Pacific (30°–38°S): A modeling study. *Journal of Geophysical Research-Oceans*, *124*, 8574–8604. https://doi.org/10.1029/2019JC015201

Porobić, J., Canales-Aguirre, C. B., Ernst, B., Galleguillos, R., & Hernández, C. E. (2013). Biogeography and historical demography of the Juan Fernández Rock Lobster, *Jasus frontalis* (Milne Edwards, 1837). *Journal of Heredity*, *104*, 223–233. https://doi.org/10.1093/jhered/ess141

Porobić, J., Parada, C., Ernst, B., Hormazábal, S. E., & Combes, V. (2012). Modeling the connectivity of Juan Fernández rock lobster (*Jasus frontalis*), subpopulations through a biophysical model. *Latin American Journal of Aquatic Research*, *40*, 613–632.

Quiroga, E., Sellanes, J., Arntz, W., Gerdes, D., Gallardo, V. A., & Hebbeln, D. (2009). Benthic megafaunal and demersal fish assemblages on the Chilean continental margin: The influence of the oxygen minimum zone on bathymetric distribution. *Deep Sea Research Part II: Topical Studies in Oceanography*, *56*, 1112–1123. https://doi.org/10.1016/j.dsr2.2008.09.010

Ramos, M., Pizarro, O., Bravo, L., & Dewitte, B. (2006). Seasonal variability of the permanent thermocline off northern Chile. *Geophysical Research Letters*, *33*, L09608. https://doi.org/10.1038/s41598-020-73874-8

Rayner, N. A., Parker, D. E., Horton, E. B., Folland, C. K., Alexander, L. V., Rowell, D. P., … Kaplan, A. (2003). Global analyses of sea surface temperature, sea ice, and night marine air temperature since the late nineteenth century. *Journal of Geophysical Research*, *108*, 4407. https://doi.org/10.1029/2002JD002670

Richter, I. (2015). Climate model biases in the eastern tropical oceans: Causes, impacts and ways forward. *WIREs Climate Change*, *6*, 345–358. https://doi.org/10.1002/wcc.338

Rodrigo, C., Díaz, J., & González-Fernández, A. (2014). Origin of the Easter Submarine Alignment: Morphology and structural lineaments. *Latin American Journal of Aquatic Research*, *42*, 857–870. https://doi.org/10.3856/vol42-issue4-fulltext-12

Rose, K. A., Allen, J. I., Artioli, Y., Barange, M., Blackford, J., Carlotti, F., … Zhou, M. (2010). End-to-end models for the analysis of marine ecosystems: Challenges, issues, and next steps. *Marine and Coastal Fisheries*, *2*, 115–130. https://doi.org/10.1577/C09-059.1

Rykaczewski, R. R., Dunne, J. P., Sydeman, W. J., García-Reyes, M., Black, B. A., & Bograd, S. J. (2015). Poleward displacement of coastal upwelling-favorable winds in the ocean's eastern boundary currents through the 21st century. *Geophysical Research Letters*, *42*, 6424–6431. https://doi.org/10.1002/2015GL064694

Salvatteci, R., Gutiérrez, D., Sifeddine, A., Ortlieb, L., Druffel, E., Boussafir, M., & Schneider, R. (2016). Centennial to millennial-scale changes in oxygenation and productivity in the Eastern Tropical South Pacific during the last 25,000 years. *Quaternary Science Reviews*, *131*, 102–117. https://doi.org/10.1016/j.quascirev.2015.10.044

Sellanes, J., Neira, C., Quiroga, E., & Teixido, N. (2010). Diversity patterns along and across the Chilean margin: A continental slope encompassing oxygen gradients and methane seep benthic habitats. *Marine Ecology*, *31*, 111–124. https://doi.org/10.1111/j.1439-0485.2009.00332.x

Sérazin, G., Penduff, T., Grégorio, S., Barnier, B., Molines, J.-M., & Terray, L. (2015). Intrinsic variability of sea level from global ocean simulations: Spatiotemporal scales. *Journal of Climate*, *28*, 4279–4292. https://doi.org/10.1175/JCLI-D-14-00554.1

Silva, N., Rojas, N., & Fedele, A. (2009). Water masses in the Humboldt Current System: Properties, distribution, and the nitrate deficit as a chemical water mass tracer for equatorial subsurface water off Chile. *Deep Sea Research Part II: Topical Studies in Oceanography*, *56*, 1004–1020. https://doi.org/10.1016/j.dsr2.2008.12.013

Smith, N., Kessler, W. S., Cravatte, S., Sprintall, S., Wijffels, S., Cronin, M. F., … Brunner, S. (2019). Tropical pacific observing system. *Frontiers in Marine Research*, *6*, 1–26. https://doi.org/10.3389/fmars.2019.00031

Steckbauer, A., Ramajo, L., Hendriks, I. E., Fernandez, M., Lagos, N. A., Prado, L., & Duarte, C. M. (2015). Synergistic effects of hypoxia and increasing CO_2 on benthic invertebrates of the central Chilean coast. *Frontiers in Marine Science*, *2*, 49. https://doi.org/10.3389/fmars.2015.00049

Stommel, H. M. (1982). Is the South Pacific helium-3 plume dynamically active? *Earth and Planetary Science Letters*, *61*, 63–67. https://doi.org/10.1016/0012-821x(82)90038-3

Stramma, L., Prince, E. D., Schmidtko, S., Luo, J., Hoolihan, J. P., Visbeck, M., … Körtzinger, A. (2012). Expansion of oxygen minimum zones may reduce available habitat for tropical pelagic fishes. *Nature Climate Change*, *2*, 33–37. https://doi.org/10.1038/nclimate1304

Sudre, J., Maes, C., & Garçon, V. (2013). On the global estimates of geostrophic and Ekman surface currents. *Limnology and Oceanography: Fluids and Environments*, *3*, 1–20. https://doi.org/10.1215/21573689-2071927

Takahashi, K., Montecinos, A., Goubanova, K., & Dewitte, B. (2011). ENSO regimes: Reinterpreting the canonical and Modoki El Niño. *Geophysical Research Letters*, *38*, L10704. https://doi.org/10.1029/2011GL047364

Tokinaga, H., & Xie, S.-P. (2011). Wave and anemometer-based sea-surface wind (WASWind) for climate change analysis. *Journal of Climate*, *24*, 267–285. https://doi.org/10.1175/2010JCLI3789.1

Trenberth, K. E. (1991). Storm tracks in the Southern Hemisphere. *Journal of Atmospheric Science*, *48*, 2159–2178. https://doi.org/10.1175/1520-0469(1991)048<2159:STITSH>2.0.CO;2

Valladares, F., Matesanz, S., Guilhaumon, F., Araújop, M. B., Balaguer, L., Benito-Garzón, M., … Zavala, M. A. (2014). The effects of phenotypic plasticity and local adaptation on forecasts of species range shifts under climate change. *Ecology Letters*, *17*, 1351–1364. https://doi.org/10.1111/ele.12348

Vergara, O., Dewitte, B., Montes, I., Garçon, V., Ramos, M., Paulmier, A., & Pizarro, O. (2016). Seasonal variability of the oxygen minimum zone off Peru in a high-resolution regional coupled model. *Biogeosciences*, *13*, 4389–4410. https://doi.org/10.5194/bg-13-4389-2016

Vic, C., Naveira Garabato, A. C., Green, J. A. M., Waterhouse, A. F., Zhao, Z., Melet, A., … Stephenson, G. R. (2019). Deep-ocean mixing driven by small-scale internal tides. *Nature Communications*, *10*, 2099. https://doi.org/10.1038/s41467-019-10149-5

Vincent, E. M., Lengaigne, M., Menkes, C. E., Jourdain, N. C., Marchesiello, P. M., & Madec, G. (2011). Interannual variability of the South Pacific Convergence Zone and implications for tropical cyclone genesis. *Climate Dynamics*, *36*, 1881–1896. https://doi.org/10.1007/s00382-009-0716-3

Wagner, D., van der Meer, L., Gorny, M., Sellanes, J., Gaymer, C. F., Soto, E. H. … Morgan, L. E.(2020) The Salas y Gómez and Nazca ridges: challenges and opportunities for protecting a global diversity hotspot on the high seas. *Marine Policy*.

Wishner, K. F., Ashjian, J., Gelfman, C., Gowing, M. M., Kann, L., Levin, L. A., … Salzman, J. (1995). Pelagic and benthic ecology of the lower interface of the Eastern Tropical Pacific oxygen minimum zone. *Deep Sea Research Part 1: Oceanographic Research Papers*, *42*, 93–115. https://doi.org/10.1016/0967-0637(94)00021-j

Wyrtki, K. (1962). The oxygen minima in relation to ocean circulation. *Deep Sea Research and Oceanographic Abstracts*, *9*, 11–23. https://doi.org/10.1016/0011-7471(62)90243-7

Xie, P., & Arkin, P. A. (1997). Global precipitation: A 17-year monthly analysis based on gauge observations, satellite estimates, and numerical model outputs. *Bulletin of the American Meteorological Society*, *78*, 2539–2558. https://doi.org/10.1175/1520-0477(1997)078<2539:GPAYMA>2.0.CO;2

Xie, S. P., Deser, C., Vecchi, G. A., Ma, J., Teng, H., & Wittenberg, A. T. (2010). Global warming pattern formation: Sea surface temperature and rainfall. *Journal of Climate*, *23*, 966–986. https://doi.org/10.1175/2009JCLI3329.1

Xue, J., Luo, J.-J., Yuan, C., & Yamagata, T. (2020). Discovery of Chile Niño/Niña. *Geophysical Research Letters*, *47*, e2019GL086468. https://doi.org/10.1029/2019GL086468

Yáñez, E., Lagos, N. A., Norambuena, R., Silva, C., Letelier, J., Muck, K. P., … Böhm, G. (2017). Impacts of climate change on marine fisheries and aquaculture in Chile. In B. Phillips & M. Pérez-Ramírez (Eds.), *Climate change impacts on fisheries and aquaculture: A global analysis*. Hoboken, NJ, USA: Wiley- Blackwell. https://doi.org/10.1590/0001-3765201720170400

Yeager, G. S., & Large, W. G. (2004). Late-winter generation of spiciness on subducted isopycnals. *Journal of Physical Oceanography*, *34*, 1528–1547. https://doi.org/10.1175/1520-0485(2004)034<1528:LGOSOS>2.0.CO;2

Zhang, H., Clement, A., & DiNezio, P. (2014). The South Pacific Meridional Mode: A mechanism for ENSO-like variability. *Journal of Climate*, *27*, 769–783. https://doi.org/10.1175/JCLI-D-13-00082.1

How to cite this article: Dewitte B, Conejero C, Ramos M, et al. Understanding the impact of climate change on the oceanic circulation in the Chilean island ecoregions. *Aquatic Conserv: Mar Freshw Ecosyst*. 2021;1–21. https://doi.org/10.1002/aqc.3506

References

Abram, N. J., M. K. Gagan, M. T. McCulloch, J. Chappell, and W. S. Hantoro (2003). "Coral reef death during the 1997 Indian Ocean Dipole linked to Indonesian wildfires". In: *Science* 301.5635, pp. 952–955.

Adam, O., T. Schneider, and F. Brient (2018). "Regional and seasonal variations of the double-ITCZ bias in CMIP5 models". In: *Climate dynamics* 51.1, pp. 101–117.

Aguirre, C., M. Rojas, R. D. Garreaud, and D. A. Rahn (2019). "Role of synoptic activity on projected changes in upwelling-favourable winds at the ocean's eastern boundaries". In: *npj Climate and Atmospheric Science* 2.1, pp. 1–7.

Alexander, M. A., I. Bladé, M. Newman, J. R. Lanzante, N.-C. Lau, and J. D. Scott (2002). "The atmospheric bridge: The influence of ENSO teleconnections on air–sea interaction over the global oceans". In: *Journal of climate* 15.16, pp. 2205–2231.

Alexander, M. A., D. J. Vimont, P. Chang, and J. D. Scott (2010). "The impact of extratropical atmospheric variability on ENSO: Testing the seasonal footprinting mechanism using coupled model experiments". In: *Journal of Climate* 23.11, pp. 2885–2901.

Allen, M., W. S. O. Dube, W. C. F. Aragón-Durand, M. K. S. Humphreys, N. M. J. Kala, R. P. Y. Mulugetta, M.Wairiu, and K. Zickfeld (2018). "Framing and Context". In: *Global Warming of 1.5°C. An IPCC Special Report on the impacts of global warming of 1.5°C above pre-industrial levels and related global greenhouse gas emission pathways, in the context of strengthening the global response to the threat of climate change, sustainable development, and efforts to eradicate poverty*. In Press.

Allen, M. R. and W. J. Ingram (2002). "Constraints on future changes in climate and the hydrologic cycle". In: *Nature* 419.6903, pp. 228–232.

Archer, C. L. and K. Caldeira (2008). "Historical trends in the jet streams". In: *Geophysical Research Letters* 35.8.

Ashok, K., S. K. Behera, S. A. Rao, H. Weng, and T. Yamagata (2007). "El Niño Modoki and its possible teleconnection". In: *Journal of Geophysical Research: Oceans* 112.C11.

Ashok, K. and T. Yamagata (2009). "The El Niño with a difference". In: *Nature* 461.7263, pp. 481–484.

Bakun, A. (1990). "Global climate change and intensification of coastal ocean upwelling". In: *Science* 247.4939, pp. 198–201.

Bakun, A., B. A. Black, S. J. Bograd, M. Garcia-Reyes, A. J. Miller, R. R. Rykaczewski, and W. J. Sydeman (2015). "Anticipated effects of climate change on coastal upwelling ecosystems". In: *Current Climate Change Reports* 1.2, pp. 85–93.

Bayr, T., D. Dommenget, T. Martin, and S. B. Power (2014). "The eastward shift of the Walker circulation in response to global warming and its relationship to ENSO variability". In: *Climate dynamics* 43.9-10, pp. 2747–2763.

Beaugrand, G. et al. (2019). "Prediction of unprecedented biological shifts in the global ocean". In: *Nature Climate Change* 9.3, pp. 237–243.

Bellenger, H., É. Guilyardi, J. Leloup, M. Lengaigne, and J. Vialard (2014). "ENSO representation in climate models: From CMIP3 to CMIP5". In: *Climate Dynamics* 42.7, pp. 1999–2018.

Belmadani, A., E. Concha, D. Donoso, A. Chaigneau, F. Colas, N. Maximenko, and E. Di Lorenzo (2017). "Striations and preferred eddy tracks triggered by topographic steering of the background flow in the eastern S outh P acific". In: *Journal of Geophysical Research: Oceans* 122.4, pp. 2847–2870.

Belmadani, A., V. Echevin, F. Codron, K. Takahashi, and C. Junquas (2014). "What dynamics drive future wind scenarios for coastal upwelling off Peru and Chile?" In: *Climate dynamics* 43.7-8, pp. 1893–1914.

Belmadani, A., V. Echevin, B. Dewitte, and F. Colas (2012). "Equatorially forced intraseasonal propagations along the Peru-Chile coast and their relation with the nearshore eddy activity in 1992–2000: A modeling study". In: *Journal of Geophysical Research: Oceans* 117.C4.

Bender, F. A., V. Ramanathan, and G. Tselioudis (2012). "Changes in extratropical storm track cloudiness 1983–2008: Observational support for a poleward shift". In: *Climate Dynamics* 38.9, pp. 2037–2053.

Bilbao, R. A., J. M. Gregory, and N. Bouttes (2015). "Analysis of the regional pattern of sea level change due to ocean dynamics and density change for 1993–2099 in observations and CMIP5 AOGCMs". In: *Climate Dynamics* 45.9, pp. 2647–2666.

Bjerknes, J. (1969). "Atmospheric teleconnections from the equatorial Pacific". In: *Monthly weather review* 97.3, pp. 163–172.

Bopp, L. et al. (2013). "Multiple stressors of ocean ecosystems in the 21st century: projections with CMIP5 models". In: *Biogeosciences* 10.10, pp. 6225–6245.

Brandt, P., A. Funk, V. Hormann, M. Dengler, R. J. Greatbatch, and J. M. Toole (2011). "Interannual atmospheric variability forced by the deep equatorial Atlantic Ocean". In: *Nature* 473.7348, pp. 497–500.

Breitburg, D. et al. (2018). "Declining oxygen in the global ocean and coastal waters". In: *Science* 359.6371.

Bryan, F. O., M. W. Hecht, and R. D. Smith (2007). "Resolution convergence and sensitivity studies with North Atlantic circulation models. Part I: The western boundary current system". In: *Ocean Modelling* 16.3-4, pp. 141–159.

Cai, W., T. Cowan, and M. Raupach (2009). "Positive Indian Ocean dipole events precondition southeast Australia bushfires". In: *Geophysical Research Letters* 36.19.

Cai, W. et al. (2019). "Pantropical climate interactions". In: *Science* 363.6430.

Cai, W., B. Ng, T. Geng, L. Wu, A. Santoso, and M. J. McPhaden (2020). "Butterfly effect and a self-modulating El Niño response to global warming". In: *Nature* 585.7823, pp. 68–73.

Cai, W., G. Wang, B. Dewitte, L. Wu, A. Santoso, K. Takahashi, Y. Yang, A. Carréric, and M. J. McPhaden (2018). "Increased variability of eastern Pacific El Niño under greenhouse warming". In: *Nature* 564.7735, pp. 201–206.

Cai, W., X.-T. Zheng, E. Weller, M. Collins, T. Cowan, M. Lengaigne, W. Yu, and T. Yamagata (2013). "Projected response of the Indian Ocean Dipole to greenhouse warming". In: *Nature geoscience* 6.12, pp. 999–1007.

Capet, X., F. Colas, J. C. McWilliams, P. Penven, and P. Marchesiello (2008). "Eddies in eastern boundary subtropical upwelling systems". In: *Ocean Modeling in an Eddying Regime, Geophys. Monogr. Ser* 177, pp. 131–147.

Capotondi, A. et al. (2015). "Understanding ENSO diversity". In: *Bulletin of the American Meteorological Society* 96.6, pp. 921–938.

Capotondi, A., A. Wittenberg, and S. Masina (2006). "Spatial and temporal structure of tropical Pacific interannual variability in 20th century coupled simulations". In: *Ocean Modelling* 15.3-4, pp. 274–298.

Carréric, A., B. Dewitte, W. Cai, A. Capotondi, K. Takahashi, S.-W. Yeh, G. Wang, and V. Guémas (2019). "Change in strong eastern Pacific El Niño events dynamics in the warming climate". In: *Climate Dynamics* 54.1, pp. 901–918.

Chadwick, R., I. Boutle, and G. Martin (2013). "Spatial patterns of precipitation change in CMIP5: Why the rich do not get richer in the tropics". In: *Journal of climate* 26.11, pp. 3803–3822.

Chaigneau, A., N. Dominguez, G. Eldin, L. Vasquez, R. Flores, C. Grados, and V. Echevin (2013). "Near-coastal circulation in the Northern Humboldt Current System from shipboard ADCP data". In: *Journal of Geophysical Research: Oceans* 118.10, pp. 5251–5266.

Chaigneau, A., G. Eldin, and B. Dewitte (2009). "Eddy activity in the four major upwelling systems from satellite altimetry (1992–2007)". In: *Progress in Oceanography* 83.1-4, pp. 117–123.

Chaigneau, A. and O. Pizarro (2005). "Eddy characteristics in the eastern South Pacific". In: *Journal of Geophysical Research: Oceans* 110.C6.

Chang, P., L. Ji, and H. Li (1997). "A decadal climate variation in the tropical Atlantic Ocean from thermodynamic air-sea interactions". In: *Nature* 385.6616, pp. 516–518.

Chavez, F. P., A. Bertrand, R. Guevara Carrasco, P. Soler, and J. Csirke (2008). "The northern Humboldt Current System: Brief history, present status and a view towards the future". In: *Progress in Oceanography* 79.special issue 2-4, pp. 95–105.

Chavez, F. P. and M. Messié (2009). "A comparison of eastern boundary upwelling ecosystems". In: *Progress in Oceanography* 83.1-4, pp. 80–96.

Chelton, D. B., M. G. Schlax, M. H. Freilich, and R. F. Milliff (2004). "Satellite measurements reveal persistent small-scale features in ocean winds". In: *science* 303.5660, pp. 978–983.

Chelton, D. B., M. G. Schlax, and R. M. Samelson (2011). "Global observations of nonlinear mesoscale eddies". In: *Progress in oceanography* 91.2, pp. 167–216.

Chiang, J. C. and D. J. Vimont (2004). "Analogous Pacific and Atlantic meridional modes of tropical atmosphere–ocean variability". In: *Journal of Climate* 17.21, pp. 4143–4158.

Chou, C. and C.-A. Chen (2010). "Depth of convection and the weakening of tropical circulation in global warming". In: *Journal of Climate* 23.11, pp. 3019–3030.

Chou, C., J. D. Neelin, C.-A. Chen, and J.-Y. Tu (2009). "Evaluating the "rich-get-richer" mechanism in tropical precipitation change under global warming". In: *Journal of Climate* 22.8, pp. 1982–2005.

Christensen, J. H. et al. (2013). "Climate phenomena and their relevance for future regional climate change". In: *Climate change 2013 the physical science basis: Working group I contribution to the fifth assessment report of the intergovernmental panel on climate change*. Cambridge University Press, pp. 1217–1308.

Chu, J.-E., S.-S. Lee, A. Timmermann, C. Wengel, M. F. Stuecker, and R. Yamaguchi (2020). "Reduced tropical cyclone densities and ocean effects due to anthropogenic greenhouse warming". In: *Science Advances* 6.51, eabd5109.

Church, J. et al. (2013). "Chapter 13: Sea Level Change". In: *Climate Change 2013: The Physical Science Basis: Contribution of Working Group I to the Fifth Assessment Report of the Intergovernmental Panel on Climate ChangeIntergovernmental Panel on Climate Change*. Cambridge University Press, Cambridge, United Kingdom and New York, NY, USA.

Church, J. A. and N. J. White (2011). "Sea-level rise from the late 19th to the early 21st century". In: *Surveys in geophysics* 32.4, pp. 585–602.

Colas, F., X. Capet, J. C. McWilliams, and Z. Li (2013). "Mesoscale eddy buoyancy flux and eddy-induced circulation in Eastern Boundary Currents". In: *Journal of Physical Oceanography* 43.6, pp. 1073–1095.

Colas, F., J. C. McWilliams, X. Capet, and J. Kurian (2012). "Heat balance and eddies in the Peru-Chile current system". In: *Climate dynamics* 39.1, pp. 509–529.

Combes, V., S. Hormazabal, and E. Di Lorenzo (2015). "Interannual variability of the subsurface eddy field in the Southeast P acific". In: *Journal of Geophysical Research: Oceans* 120.7, pp. 4907–4924.

Crook, J. A. and P. M. Forster (2011). "A balance between radiative forcing and climate feedback in the modeled 20th century temperature response". In: *Journal of Geophysical Research: Atmospheres* 116.D17.

Dai, A., J. C. Fyfe, S.-P. Xie, and X. Dai (2015). "Decadal modulation of global surface temperature by internal climate variability". In: *Nature Climate Change* 5.6, pp. 555–559.

Danabasoglu, G. and P. R. Gent (2009). "Equilibrium climate sensitivity: Is it accurate to use a slab ocean model?" In: *Journal of Climate* 22.9, pp. 2494–2499.

Delorme, B. and Y. Eddebbar (2016). "Ocean Circulation and Climate: an Overview". In: *Ocean and Climate, 2016 – Scientific Notes, Second edition* 2, p. 92.

Deppenmeier, A.-L., R. J. Haarsma, and W. Hazeleger (2016). "The Bjerknes feedback in the tropical Atlantic in CMIP5 models". In: *Climate Dynamics* 47.7, pp. 2691–2707.

Deser, C., M. A. Alexander, S.-P. Xie, and A. S. Phillips (2010). "Sea surface temperature variability: Patterns and mechanisms". In: *Annual review of marine science* 2, pp. 115–143.

Deser, C., A. Phillips, V. Bourdette, and H. Teng (2012). "Uncertainty in climate change projections: the role of internal variability". In: *Climate dynamics* 38.3, pp. 527–546.

Dewitte, B. et al. (2012). "Change in El Niño flavours over 1958–2008: Implications for the long-term trend of the upwelling off Peru". In: *Deep Sea Research Part II: Topical Studies in Oceanography* 77, pp. 143–156.

Dewitte, B., G. Reverdin, and C. Maes (1999). "Vertical structure of an OGCM simulation of the equatorial Pacific Ocean in 1985–94". In: *Journal of Physical Oceanography* 29.7, pp. 1542–1570.

Dewitte, B. and K. Takahashi (2017). "Diversity of moderate El Niño events evolution: role of air–sea interactions in the eastern tropical Pacific". In: *Climate Dynamics* 52.12, pp. 7455–7476.

Dhame, S., A. S. Taschetto, A. Santoso, and K. J. Meissner (2020). "Indian Ocean warming modulates global atmospheric circulation trends". In: *Climate Dynamics* 55.7, pp. 2053–2073.

DiNezio, P. N., A. C. Clement, G. A. Vecchi, B. J. Soden, B. P. Kirtman, and S.-K. Lee (2009). "Climate response of the equatorial Pacific to global warming". In: *Journal of Climate* 22.18, pp. 4873–4892.

DiNezio, P. N., G. A. Vecchi, and A. C. Clement (2013). "Detectability of changes in the Walker circulation in response to global warming". In: *Journal of Climate* 26.12, pp. 4038–4048.

Ding, H., N. S. Keenlyside, and M. Latif (2012). "Impact of the equatorial Atlantic on the El Niño southern oscillation". In: *Climate dynamics* 38.9-10, pp. 1965–1972.

Ding, R., J. Li, and Y.-h. Tseng (2015). "The impact of South Pacific extratropical forcing on ENSO and comparisons with the North Pacific". In: *Climate Dynamics* 44.7-8, pp. 2017–2034.

Dong, C., J. C. McWilliams, Y. Liu, and D. Chen (2014). "Global heat and salt transports by eddy movement". In: *Nature communications* 5.1, pp. 1–6.

Dong, L. and M. J. McPhaden (2017). "Why has the relationship between Indian and Pacific Ocean decadal variability changed in recent decades?" In: *Journal of climate* 30.6, pp. 1971–1983.

Du, Y. and S.-P. Xie (2008). "Role of atmospheric adjustments in the tropical Indian Ocean warming during the 20th century in climate models". In: *Geophysical Research Letters* 35.8.

Dufresne, J.-L. and S. Bony (2008). "An assessment of the primary sources of spread of global warming estimates from coupled atmosphere–ocean models". In: *Journal of Climate* 21.19, pp. 5135–5144.

Echevin, V., K. Goubanova, A. Belmadani, and B. Dewitte (2012). "Sensitivity of the Humboldt Current system to global warming: a downscaling experiment of the IPSL-CM4 model". In: *Climate Dynamics* 38.3, pp. 761–774.

England, M. H. et al. (2014). "Recent intensification of wind-driven circulation in the Pacific and the ongoing warming hiatus". In: *Nature climate change* 4.3, pp. 222–227.

Fairall, C. W., E. F. Bradley, D. P. Rogers, J. B. Edson, and G. S. Young (1996). "Bulk parameterization of air-sea fluxes for tropical ocean-global atmosphere coupled-ocean atmosphere response experiment". In: *Journal of Geophysical Research: Oceans* 101.C2, pp. 3747–3764.

Falvey, M. and R. D. Garreaud (2009). "Regional cooling in a warming world: Recent temperature trends in the southeast Pacific and along the west coast of subtropical South America (1979–2006)". In: *Journal of Geophysical Research: Atmospheres* 114.D4.

Fedorov, A. V. and S. G. Philander (2000). "Is El Niño changing?" In: *Science* 288.5473, pp. 1997–2002.

Flato, G. et al. (2013). "Evaluation of Climate Models". In: *Climate Change 2013: The Physical Science Basis. Contribution of Working Group I to the Fifth Assessment Report of the Intergovernmental Panel on Climate Change*. Cambridge University Press, Cambridge, United Kingdom and New York, NY, USA.

Foltz, G. R. and M. J. McPhaden (2010). "Abrupt equatorial wave-induced cooling of the Atlantic cold tongue in 2009". In: *Geophysical Research Letters* 37.24.

Frankignoul, C. and K. Hasselmann (1977). "Stochastic climate models, Part II Application to sea-surface temperature anomalies and thermocline variability". In: *Tellus* 29.4, pp. 289–305.

Frenger, I., N. Gruber, R. Knutti, and M. Münnich (2013). "Imprint of Southern Ocean eddies on winds, clouds and rainfall". In: *Nature geoscience* 6.8, pp. 608–612.

García-Reyes, M., W. J. Sydeman, D. S. Schoeman, R. R. Rykaczewski, B. A. Black, A. J. Smit, and S. J. Bograd (2015). "Under pressure: Climate change, upwelling, and eastern boundary upwelling ecosystems". In: *Frontiers in Marine Science* 2, p. 109.

Garreaud, R. and R. C. Muñoz (2005). "The low-level jet off the west coast of subtropical South America: Structure and variability". In: *Monthly Weather Review* 133.8, pp. 2246–2261.

Gaube, P., D. B. Chelton, P. G. Strutton, and M. J. Behrenfeld (2013). "Satellite observations of chlorophyll, phytoplankton biomass, and Ekman pumping in nonlinear mesoscale eddies". In: *Journal of Geophysical Research: Oceans* 118.12, pp. 6349–6370.

Gent, P. R. (2013). "Coupled models and climate projections". In: *International Geophysics*. Vol. 103. Elsevier, pp. 609–623.

Goubanova, K., V. Echevin, B. Dewitte, F. Codron, K. Takahashi, P. Terray, and M. Vrac (2011). "Statistical downscaling of sea-surface wind over the Peru–Chile upwelling region: diagnosing the impact of climate change from the IPSL-CM4 model". In: *Climate Dynamics* 36.7-8, pp. 1365–1378.

Gruber, N., Z. Lachkar, H. Frenzel, P. Marchesiello, M. Münnich, J. C. McWilliams, T. Nagai, and G.-K. Plattner (2011). "Eddy-induced reduction of biological production in eastern boundary upwelling systems". In: *Nature geoscience* 4.11, pp. 787–792.

Guilyardi, E. (2006). "El Niño–mean state–seasonal cycle interactions in a multi-model ensemble". In: *Climate Dynamics* 26.4, pp. 329–348.

Guilyardi, E., W. Cai, M. Collins, A. Fedorov, F.-F. Jin, A. Kumar, D.-Z. Sun, and A. Wittenberg (2012). "New strategies for evaluating ENSO processes in climate models". In: *Bulletin of the American Meteorological Society* 93.2, pp. 235–238.

Guilyardi, E., A. Wittenberg, A. Fedorov, M. Collins, C. Wang, A. Capotondi, G. J. Van Oldenborgh, and T. Stockdale (2009). "Understanding El Niño in ocean–atmosphere

general circulation models: Progress and challenges". In: *Bulletin of the American Meteorological Society* 90.3, pp. 325–340.

Hartmann, D., A. K. Tank, L. A. M. Rusticucci, Y. C. S. Brönnimann, E. D. F.J. Dentener, A. K. D. Easterling, P. T. B. Soden, M. Wild, and P. Zhai (2013). "Observations: Atmosphere and Surface". In: *Climate Change 2013: The Physical Science Basis: Contribution of Working Group I to the Fifth Assessment Report of the Intergovernmental Panel on Climate ChangeIntergovernmental Panel on Climate Change*. Cambridge University Press, Cambridge, United Kingdom and New York, NY, USA.

Hawkins, E. and R. Sutton (2009). "The potential to narrow uncertainty in regional climate predictions". In: *Bulletin of the American Meteorological Society* 90.8, pp. 1095–1108.

Hay, C. C., E. Morrow, R. E. Kopp, and J. X. Mitrovica (2015). "Probabilistic reanalysis of twentieth-century sea-level rise". In: *Nature* 517.7535, pp. 481–484.

He, J. and B. J. Soden (2015). "Anthropogenic weakening of the tropical circulation: The relative roles of direct CO2 forcing and sea surface temperature change". In: *Journal of Climate* 28.22, pp. 8728–8742.

Heede, U. K., A. V. Fedorov, and N. J. Burls (2020). "Time scales and mechanisms for the tropical pacific response to global warming: A tug of war between the ocean thermostat and weaker walker". In: *Journal of Climate* 33.14, pp. 6101–6118.

Held, I. M. and B. J. Soden (2000). "Water vapor feedback and global warming". In: *Annual review of energy and the environment* 25.1, pp. 441–475.

Held, I. M. and B. J. Soden (2006). "Robust responses of the hydrological cycle to global warming". In: *Journal of climate* 19.21, pp. 5686–5699.

Hersbach, H. et al. (2020). "The ERA5 global reanalysis". In: *Quarterly Journal of the Royal Meteorological Society* 146.730, pp. 1999–2049.

Hormazabal, S., V. Combes, C. E. Morales, M. A. Correa-Ramirez, E. Di Lorenzo, and S. Nuñez (2013). "Intrathermocline eddies in the coastal transition zone off central Chile (31–41 S)". In: *Journal of Geophysical Research: Oceans* 118.10, pp. 4811–4821.

Hu, A. and S. C. Bates (2018). "Internal climate variability and projected future regional steric and dynamic sea level rise". In: *Nature communications* 9.1, pp. 1–11.

Hu, A. and C. Deser (2013). "Uncertainty in future regional sea level rise due to internal climate variability". In: *Geophysical Research Letters* 40.11, pp. 2768–2772.

Hu, Y. and Q. Fu (2007). "Observed poleward expansion of the Hadley circulation since 1979". In: *Atmospheric Chemistry and Physics* 7.19, pp. 5229–5236.

Huang, B. et al. (2017). "Extended reconstructed sea surface temperature, version 5 (ERSSTv5): upgrades, validations, and intercomparisons". In: *Journal of Climate* 30.20, pp. 8179–8205.

Huang, P., S.-P. Xie, K. Hu, G. Huang, and R. Huang (2013). "Patterns of the seasonal response of tropical rainfall to global warming". In: *Nature Geoscience* 6.5, pp. 357–361.

Hurrell, J. W. et al. (2013). "The community earth system model: a framework for collaborative research". In: *Bulletin of the American Meteorological Society* 94.9, pp. 1339–1360.

IPCC (2013). "Climate Change 2013: The Physical Science Basis". In: *Contribution of Working Group I to the Fifth Assessment Report of the Intergovernmental Panel on Climate Change*. Cambridge University Press, United Kingdom and New York, NY, USA, 1535 pp.

Izumo, T. (2005). "The equatorial undercurrent, meridional overturning circulation, and their roles in mass and heat exchanges during El Niño events in the tropical Pacific Ocean". In: *Ocean Dynamics* 55.2, pp. 110–123.

Jia, F. and L. Wu (2013). "A study of response of the equatorial Pacific SST to doubled-CO2 forcing in the coupled CAM–1.5-layer reduced-gravity ocean model". In: *Journal of physical oceanography* 43.7, pp. 1288–1300.

Jochum, M. (2009). "Impact of latitudinal variations in vertical diffusivity on climate simulations". In: *Journal of Geophysical Research: Oceans* 114.C1.

Jouanno, J., F. Marin, Y. Du Penhoat, J. Sheinbaum, and J.-M. Molines (2011). "Seasonal heat balance in the upper 100 m of the equatorial Atlantic Ocean". In: *Journal of Geophysical Research: Oceans* 116.C9.

Kalnay, E. et al. (1996). "The NCEP/NCAR 40-year reanalysis project". In: *Bulletin of the American meteorological Society* 77.3, pp. 437–472.

Kang, S. M. and J. Lu (2012). "Expansion of the Hadley cell under global warming: Winter versus summer". In: *Journal of Climate* 25.24, pp. 8387–8393.

Kaplan, A., M. A. Cane, Y. Kushnir, A. C. Clement, M. B. Blumenthal, and B. Rajagopalan (1998). "Analyses of global sea surface temperature 1856–1991". In: *Journal of Geophysical Research: Oceans* 103.C9, pp. 18567–18589.

Karl, T. R., A. Arguez, B. Huang, J. H. Lawrimore, J. R. McMahon, M. J. Menne, T. C. Peterson, R. S. Vose, and H.-M. Zhang (2015). "Possible artifacts of data biases in the recent global surface warming hiatus". In: *Science* 348.6242, pp. 1469–1472.

Kaufmann, R. K., H. Kauppi, M. L. Mann, and J. H. Stock (2011). "Reconciling anthropogenic climate change with observed temperature 1998–2008". In: *Proceedings of the National Academy of Sciences* 108.29, pp. 11790–11793.

Kay, J. E. et al. (2015). "The Community Earth System Model (CESM) large ensemble project: A community resource for studying climate change in the presence of

internal climate variability". In: *Bulletin of the American Meteorological Society* 96.8, pp. 1333–1349.

Keenlyside, N. S. and M. Latif (2007). "Understanding equatorial Atlantic interannual variability". In: *Journal of climate* 20.1, pp. 131–142.

Kennedy, J., N. Rayner, R. Smith, D. Parker, and M. Saunby (2011). "Reassessing biases and other uncertainties in sea surface temperature observations measured in situ since 1850: 1. Measurement and sampling uncertainties". In: *Journal of Geophysical Research: Atmospheres* 116.D14.

Kennedy, J. J., N. A. Rayner, R. O. Smith, D. E. Parker, and M. Saunby (2011). "Reassessing biases and other uncertainties in sea surface temperature observations measured in situ since 1850: 2. Biases and homogenization". In: *Journal of Geophysical Research: Atmospheres* 116.D14.

Kent, E. C. et al. (2017). "A call for new approaches to quantifying biases in observations of sea surface temperature". In: *Bulletin of the American Meteorological Society* 98.8, pp. 1601–1616.

Kiehl, J. T. and K. E. Trenberth (1997). "Earth's annual global mean energy budget". In: *Bulletin of the American Meteorological Society* 78.2, pp. 197–208.

Knutson, T. R., T. Delworth, K. Dixon, I. Held, J. Lu, V. Ramaswamy, M. Schwarzkopf, G. Stenchikov, and R. Stouffer (2006). "Assessment of twentieth-century regional surface temperature trends using the GFDL CM2 coupled models". In: *Journal of Climate* 19.9, pp. 1624–1651.

Knutson, T. R. and S. Manabe (1995). "Time-mean response over the tropical Pacific to increased C02 in a coupled ocean-atmosphere model". In: *Journal of Climate* 8.9, pp. 2181–2199.

Knutti, R. (2008). "Why are climate models reproducing the observed global surface warming so well?" In: *Geophysical Research Letters* 35.18.

Kosaka, Y. and S.-P. Xie (2013). "Recent global-warming hiatus tied to equatorial Pacific surface cooling". In: *Nature* 501.7467, pp. 403–407.

Kug, J.-S., F.-F. Jin, and S.-I. An (2009). "Two types of El Niño events: cold tongue El Niño and warm pool El Niño". In: *Journal of Climate* 22.6, pp. 1499–1515.

Lagerloef, G. S., G. T. Mitchum, R. B. Lukas, and P. P. Niiler (1999). "Tropical Pacific near-surface currents estimated from altimeter, wind, and drifter data". In: *Journal of Geophysical Research: Oceans* 104.C10, pp. 23313–23326.

Latif, M. and T. P. Barnett (1995). "Interactions of the tropical oceans". In: *Journal of Climate* 8.4, pp. 952–964.

Lawrence, D. M., K. W. Oleson, M. G. Flanner, C. G. Fletcher, P. J. Lawrence, S. Levis, S. C. Swenson, and G. B. Bonan (2012). "The CCSM4 land simulation, 1850–2005:

Assessment of surface climate and new capabilities". In: *Journal of Climate* 25.7, pp. 2240–2260.

Leloup, J. and A. Clement (2009). "Why is there a minimum in projected warming in the tropical North Atlantic Ocean?" In: *Geophysical research letters* 36.14.

Leloup, J., M. Lengaigne, and J.-P. Boulanger (2008). "Twentieth century ENSO characteristics in the IPCC database". In: *Climate Dynamics* 30.2-3, pp. 277–291.

Leth, O. and J. F. Middleton (2004). "A mechanism for enhanced upwelling off central Chile: Eddy advection". In: *Journal of Geophysical Research: Oceans* 109.C12.

Leth, O. and G. Shaffer (2001). "A numerical study of the seasonal variability in the circulation off central Chile". In: *Journal of Geophysical Research: Oceans* 106.C10, pp. 22229–22248.

Li, G. and S.-P. Xie (2014). "Tropical biases in CMIP5 multimodel ensemble: The excessive equatorial Pacific cold tongue and double ITCZ problems". In: *Journal of Climate* 27.4, pp. 1765–1780.

Li, G., L. Cheng, J. Zhu, K. E. Trenberth, M. E. Mann, and J. P. Abraham (2020). "Increasing ocean stratification over the past half-century". In: *Nature Climate Change* 10.12, pp. 1116–1123.

Li, X., S.-P. Xie, S. T. Gille, and C. Yoo (2016). "Atlantic-induced pan-tropical climate change over the past three decades". In: *Nature Climate Change* 6.3, pp. 275–279.

Limpasuvan, V. and D. L. Hartmann (1999). "Eddies and the annular modes of climate variability". In: *Geophysical Research Letters* 26.20, pp. 3133–3136.

Lin, J.-L. (2007). "The double-ITCZ problem in IPCC AR4 coupled GCMs: Ocean–atmosphere feedback analysis". In: *Journal of Climate* 20.18, pp. 4497–4525.

Lindsay, K. et al. (2014). "Preindustrial-control and twentieth-century carbon cycle experiments with the Earth System Model CESM1 (BGC)". In: *Journal of Climate* 27.24, pp. 8981–9005.

Liu, W., J. Lu, and S.-P. Xie (2015). "Understanding the Indian Ocean response to double CO 2 forcing in a coupled model". In: *Ocean Dynamics* 65.7, pp. 1037–1046.

Liu, Z. and M. Alexander (2007). "Atmospheric bridge, oceanic tunnel, and global climatic teleconnections". In: *Reviews of Geophysics* 45.2.

Liu, Z., S. Vavrus, F. He, N. Wen, and Y. Zhong (2005). "Rethinking tropical ocean response to global warming: The enhanced equatorial warming". In: *Journal of Climate* 18.22, pp. 4684–4700.

Long, M. C., K. Lindsay, S. Peacock, J. K. Moore, and S. C. Doney (2013). "Twentieth-century oceanic carbon uptake and storage in CESM1 (BGC)". In: *Journal of Climate* 26.18, pp. 6775–6800.

Losada, T., B. Rodrıguez-Fonseca, I. Polo, S. Janicot, S. Gervois, F. Chauvin, and P. Ruti (2010). "Tropical response to the Atlantic Equatorial mode: AGCM multimodel approach". In: *Climate Dynamics* 35.1, pp. 45–52.

Lu, J., G. Chen, and D. M. Frierson (2008). "Response of the zonal mean atmospheric circulation to El Niño versus global warming". In: *Journal of Climate* 21.22, pp. 5835–5851.

Lu, J., C. Deser, and T. Reichler (2009). "Cause of the widening of the tropical belt since 1958". In: *Geophysical Research Letters* 36.3.

Lu, J., G. A. Vecchi, and T. Reichler (2007). "Expansion of the Hadley cell under global warming". In: *Geophysical Research Letters* 34.6.

Lu, J. and B. Zhao (2012). "The role of oceanic feedback in the climate response to doubling CO2". In: *Journal of Climate* 25.21, pp. 7544–7563.

Lu, P., J. P. McCreary Jr, and B. A. Klinger (1998). "Meridional circulation cells and the source waters of the Pacific Equatorial Undercurrent". In: *Journal of Physical Oceanography* 28.1, pp. 62–84.

Lübbecke, J. F. and M. J. McPhaden (2012). "On the inconsistent relationship between Pacific and Atlantic Niños". In: *Journal of Climate* 25.12, pp. 4294–4303.

Luo, Y., J. Lu, F. Liu, and W. Liu (2015). "Understanding the El Niño-like oceanic response in the tropical Pacific to global warming". In: *Climate Dynamics* 45.7, pp. 1945–1964.

Luo, Y., J. Lu, F. Liu, and X. Wan (2016). "The positive Indian Ocean dipole–like response in the tropical Indian Ocean to global warming". In: *Advances in Atmospheric Sciences* 33.4, pp. 476–488.

Lyu, K., X. Zhang, J. A. Church, A. B. Slangen, and J. Hu (2014). "Time of emergence for regional sea-level change". In: *Nature Climate Change* 4.11, pp. 1006–1010.

Ma, J. and S.-P. Xie (2013). "Regional patterns of sea surface temperature change: A source of uncertainty in future projections of precipitation and atmospheric circulation". In: *Journal of climate* 26.8, pp. 2482–2501.

Ma, J., S.-P. Xie, and Y. Kosaka (2012). "Mechanisms for tropical tropospheric circulation change in response to global warming". In: *Journal of Climate* 25.8, pp. 2979–2994.

Mantua, N. J., S. R. Hare, Y. Zhang, J. M. Wallace, and R. C. Francis (1997). "A Pacific interdecadal climate oscillation with impacts on salmon production". In: *Bulletin of the american Meteorological Society* 78.6, pp. 1069–1080.

Marchesiello, P. and P. Estrade (2010). "Upwelling limitation by onshore geostrophic flow". In: *Journal of Marine Research* 68.1, pp. 37–62.

Marchesiello, P., J. C. McWilliams, and A. Shchepetkin (2003). "Equilibrium structure and dynamics of the California Current System". In: *Journal of physical Oceanography* 33.4, pp. 753–783.

Marshall, J., H. Johnson, and J. Goodman (2001). "A study of the interaction of the North Atlantic Oscillation with ocean circulation". In: *Journal of Climate* 14.7, pp. 1399–1421.

McGillicuddy, D. J. et al. (2007). "Eddy/wind interactions stimulate extraordinary mid-ocean plankton blooms". In: *Science* 316.5827, pp. 1021–1026.

McGregor, S., A. Timmermann, M. F. Stuecker, M. H. England, M. Merrifield, F.-F. Jin, and Y. Chikamoto (2014). "Recent Walker circulation strengthening and Pacific cooling amplified by Atlantic warming". In: *Nature Climate Change* 4.10, pp. 888–892.

Meehl, G. A., J. M. Arblaster, J. T. Fasullo, A. Hu, and K. E. Trenberth (2011). "Model-based evidence of deep-ocean heat uptake during surface-temperature hiatus periods". In: *Nature Climate Change* 1.7, pp. 360–364.

Meehl, G. A., A. Hu, J. M. Arblaster, J. Fasullo, and K. E. Trenberth (2013). "Externally forced and internally generated decadal climate variability associated with the Interdecadal Pacific Oscillation". In: *Journal of Climate* 26.18, pp. 7298–7310.

Meehl, G. A., A. Hu, B. D. Santer, and S.-P. Xie (2016). "Contribution of the Interdecadal Pacific Oscillation to twentieth-century global surface temperature trends". In: *Nature Climate Change* 6.11, pp. 1005–1008.

Meehl, G. A., H. Teng, and J. M. Arblaster (2014). "Climate model simulations of the observed early-2000s hiatus of global warming". In: *Nature Climate Change* 4.10, pp. 898–902.

Meehl, G. A. et al. (2006). "Climate change projections for the twenty-first century and climate change commitment in the CCSM3". In: *Journal of climate* 19.11, pp. 2597–2616.

Meehl, G. A. et al. (2007). "Global climate projections. Chapter 10". In: *Climate Change 2007: The Physical Science Basis. Contribution of Working Group I to the Fourth Assessment Report of the Intergovernmental Panel on Climate Change*. Cambridge University Press.

Meurs, P. van and P. P. Niiler (1997). "Temporal variability of the large-scale geostrophic surface velocity in the northeast Pacific". In: *Journal of physical oceanography* 27.10, pp. 2288–2297.

Min, Q., J. Su, and R. Zhang (2017). "Impact of the South and North Pacific meridional modes on the El Niño–Southern Oscillation: Observational analysis and comparison". In: *Journal of Climate* 30.5, pp. 1705–1720.

Montes, I., F. Colas, X. Capet, and W. Schneider (2010). "On the pathways of the equatorial subsurface currents in the eastern equatorial Pacific and their contributions to the Peru-Chile Undercurrent". In: *Journal of Geophysical Research: Oceans* 115.C9.

Moore, J. K., K. Lindsay, S. C. Doney, M. C. Long, and K. Misumi (2013). "Marine ecosystem dynamics and biogeochemical cycling in the Community Earth System Model [CESM1 (BGC)]: Comparison of the 1990s with the 2090s under the RCP4. 5 and RCP8. 5 scenarios". In: *Journal of Climate* 26.23, pp. 9291–9312.

Moss, R. H. et al. (2010). "The next generation of scenarios for climate change research and assessment". In: *Nature* 463.7282, pp. 747–756.

Nguyen, H., C. Lucas, A. Evans, B. Timbal, and L. Hanson (2015). "Expansion of the Southern Hemisphere Hadley cell in response to greenhouse gas forcing". In: *Journal of Climate* 28.20, pp. 8067–8077.

Nicholls, R. J. and A. Cazenave (2010). "Sea-level rise and its impact on coastal zones". In: *science* 328.5985, pp. 1517–1520.

Nnamchi, H. C., J. Li, F. Kucharski, I.-S. Kang, N. S. Keenlyside, P. Chang, and R. Farneti (2015). "Thermodynamic controls of the Atlantic Niño". In: *Nature communications* 6.1, pp. 1–10.

Oerder, V., F. Colas, V. Echevin, F. Codron, J. Tam, and A. Belmadani (2015). "P eru-C hile upwelling dynamics under climate change". In: *Journal of Geophysical Research: Oceans* 120.2, pp. 1152–1172.

Okumura, Y. M. (2019). "ENSO diversity from an atmospheric perspective". In: *Current Climate Change Reports* 5.3, pp. 245–257.

Pacanowski, R. C. and S. M. Griffies (1999). "The MOM3 Manual". In: *NOAA-Geophysical Fluid Dynamics Laboratory, Princeton, USA*, p. 680.

Pegliasco, C., A. Chaigneau, and R. Morrow (2015). "Main eddy vertical structures observed in the four major Eastern Boundary Upwelling Systems". In: *Journal of Geophysical Research: Oceans* 120.9, pp. 6008–6033.

Pizarro-Koch, M., O. Pizarro, B. Dewitte, I. Montes, M. Ramos, A. Paulmier, and V. Garçon (2019). "Seasonal variability of the southern tip of the Oxygen Minimum Zone in the eastern South Pacific (30-38 S): A modeling study". In: *Journal of Geophysical Research: Oceans* 124.12, pp. 8574–8604.

Pizarro, O., A. J. Clarke, and S. Van Gorder (2001). "El Niño sea level and currents along the South American coast: Comparison of observations with theory". In: *Journal of Physical Oceanography* 31.7, pp. 1891–1903.

Pizarro, O., G. Shaffer, B. Dewitte, and M. Ramos (2002). "Dynamics of seasonal and interannual variability of the Peru-Chile Undercurrent". In: *Geophysical Research Letters* 29.12, pp. 22–1.

Polo, I., A. Lazar, B. Rodriguez-Fonseca, and J. Mignot (2015a). "Growth and decay of the equatorial Atlantic SST mode by means of closed heat budget in a coupled general circulation model". In: *Frontiers in Earth Science* 3, p. 37.

Polo, I., M. Martin-Rey, B. Rodriguez-Fonseca, F. Kucharski, and C. R. Mechoso (2015b). "Processes in the Pacific La Niña onset triggered by the Atlantic Niño". In: *Climate dynamics* 44.1-2, pp. 115–131.

Power, S., T. Casey, C. Folland, A. Colman, and V. Mehta (1999). "Inter-decadal modulation of the impact of ENSO on Australia". In: *Climate Dynamics* 15.5, pp. 319–324.

Power, S., F. Delage, C. Chung, G. Kociuba, and K. Keay (2013). "Robust twenty-first-century projections of El Niño and related precipitation variability". In: *Nature* 502.7472, pp. 541–545.

Rahmstorf, S. (2002). "Ocean circulation and climate during the past 120,000 years". In: *Nature* 419.6903, pp. 207–214.

Ramanathan, V. and W. Collins (1991). "Thermodynamic regulation of ocean warming by cirrus clouds deduced from observations of the 1987 El Nino". In: *Nature* 351.6321, pp. 27–32.

Ren, H.-L. and F.-F. Jin (2013). "Recharge oscillator mechanisms in two types of ENSO". In: *Journal of Climate* 26.17, pp. 6506–6523.

Renault, L., C. Deutsch, J. C. McWilliams, H. Frenzel, J.-H. Liang, and F. Colas (2016a). "Partial decoupling of primary productivity from upwelling in the California Current system". In: *Nature Geoscience* 9.7, pp. 505–508.

Renault, L., M. J. Molemaker, J. C. McWilliams, A. F. Shchepetkin, F. Lemarié, D. Chelton, S. Illig, and A. Hall (2016b). "Modulation of wind work by oceanic current interaction with the atmosphere". In: *Journal of Physical Oceanography* 46.6, pp. 1685–1704.

Richter, I. (2015). "Climate model biases in the eastern tropical oceans: Causes, impacts and ways forward". In: *Wiley Interdisciplinary Reviews: Climate Change* 6.3, pp. 345–358.

Richter, I., S. K. Behera, Y. Masumoto, B. Taguchi, H. Sasaki, and T. Yamagata (2013). "Multiple causes of interannual sea surface temperature variability in the equatorial Atlantic Ocean". In: *Nature Geoscience* 6.1, pp. 43–47.

Richter, I. and S.-P. Xie (2008a). "Muted precipitation increase in global warming simulations: A surface evaporation perspective". In: *Journal of Geophysical Research: Atmospheres* 113.D24.

Richter, I. and S.-P. Xie (2008b). "On the origin of equatorial Atlantic biases in coupled general circulation models". In: *Climate Dynamics* 31.5, pp. 587–598.

Risien, C. M. and D. B. Chelton (2008). "A global climatology of surface wind and wind stress fields from eight years of QuikSCAT scatterometer data". In: *Journal of Physical Oceanography* 38.11, pp. 2379–2413.

Rodríguez-Fonseca, B., I. Polo, J. García-Serrano, T. Losada, E. Mohino, C. R. Mechoso, and F. Kucharski (2009). "Are Atlantic Niños enhancing Pacific ENSO events in recent decades?" In: *Geophysical Research Letters* 36.20.

Rossi, V., C. López, E. Hernández-Garcıa, J. Sudre, V. Garçon, and Y. Morel (2009). "Surface mixing and biological activity in the four Eastern Boundary Upwelling Systems". In: *Nonlinear Processes in Geophysics* 16.4, pp. 557–568.

Rugenstein, M. et al. (2019). "LongRunMIP: Motivation and design for a large collection of millennial-length AOGCM simulations". In: *Bulletin of the American Meteorological Society* 100.12, pp. 2551–2570.

Ruiz-Barradas, A., J. A. Carton, and S. Nigam (2000). "Structure of interannual-to-decadal climate variability in the tropical Atlantic sector". In: *Journal of Climate* 13.18, pp. 3285–3297.

Rykaczewski, R. R., J. P. Dunne, W. J. Sydeman, M. Garcıa-Reyes, B. A. Black, and S. J. Bograd (2015). "Poleward displacement of coastal upwelling-favorable winds in the ocean's eastern boundary currents through the 21st century". In: *Geophysical Research Letters* 42.15, pp. 6424–6431.

Saji, N., B. Goswami, P. Vinayachandran, and T. Yamagata (1999). "A dipole mode in the tropical Indian Ocean". In: *Nature* 401.6751, pp. 360–363.

Samanta, D., K. B. Karnauskas, and N. F. Goodkin (2019). "Tropical Pacific SST and ITCZ biases in climate models: Double trouble for future rainfall projections?" In: *Geophysical Research Letters* 46.4, pp. 2242–2252.

Santer, B. D. et al. (2014). "Volcanic contribution to decadal changes in tropospheric temperature". In: *Nature Geoscience* 7.3, pp. 185–189.

Schuckmann, K. von et al. (2016). "An imperative to monitor Earth's energy imbalance". In: *Nature Climate Change* 6.2, pp. 138–144.

Seager, R., N. Naik, and G. A. Vecchi (2010). "Thermodynamic and dynamic mechanisms for large-scale changes in the hydrological cycle in response to global warming". In: *Journal of Climate* 23.17, pp. 4651–4668.

Seidel, D. J., Q. Fu, W. J. Randel, and T. J. Reichler (2008). "Widening of the tropical belt in a changing climate". In: *Nature geoscience* 1.1, pp. 21–24.

Seidel, D. J. and W. J. Randel (2007). "Recent widening of the tropical belt: Evidence from tropopause observations". In: *Journal of Geophysical Research: Atmospheres* 112.D20.

Shaffer, G., S. Hormazabal, O. Pizarro, and S. Salinas (1999). "Seasonal and interannual variability of currents and temperature off central Chile". In: *Journal of Geophysical Research: Oceans* 104.C12, pp. 29951–29961.

Shaffer, G., O. Pizarro, L. Djurfeldt, S. Salinas, and J. Rutllant (1997). "Circulation and low-frequency variability near the Chilean coast: Remotely forced fluctuations during the 1991–92 El Nino". In: *Journal of Physical Oceanography* 27.2, pp. 217–235.

Sherwood, S. C., S. Bony, and J.-L. Dufresne (2014). "Spread in model climate sensitivity traced to atmospheric convective mixing". In: *Nature* 505.7481, pp. 37–42.

Small, R. J. et al. (2014). "A new synoptic scale resolving global climate simulation using the Community Earth System Model". In: *Journal of Advances in Modeling Earth Systems* 6.4, pp. 1065–1094.

Smith, R. et al. (2010). "The parallel ocean program (POP) reference manual ocean component of the community climate system model (CCSM) and community earth system model (CESM)". In: *LAUR-01853* 141, pp. 1–140.

Smith, R., J. Dukowicz, and R. Malone (1992). "Parallel ocean general circulation modeling". In: *Physica D: Nonlinear Phenomena* 60.1-4, pp. 38–61.

Solomon, S., J. S. Daniel, R. R. Neely, J.-P. Vernier, E. G. Dutton, and L. W. Thomason (2011). "The persistently variable "background" stratospheric aerosol layer and global climate change". In: *Science* 333.6044, pp. 866–870.

Solomon, S., K. H. Rosenlof, R. W. Portmann, J. S. Daniel, S. M. Davis, T. J. Sanford, and G.-K. Plattner (2010). "Contributions of stratospheric water vapor to decadal changes in the rate of global warming". In: *Science* 327.5970, pp. 1219–1223.

Song, F. and G. J. Zhang (2016). "Effects of southeastern Pacific sea surface temperature on the double-ITCZ bias in NCAR CESM1". In: *Journal of Climate* 29.20, pp. 7417–7433.

Staten, P. W., J. Lu, K. M. Grise, S. M. Davis, and T. Birner (2018). "Re-examining tropical expansion". In: *Nature Climate Change* 8.9, pp. 768–775.

Stocker, T. F. (2013). "The ocean as a component of the climate system". In: *International Geophysics*. Vol. 103. Elsevier, pp. 3–30.

Stramma, L., H. W. Bange, R. Czeschel, A. Lorenzo, and M. Frank (2013). "On the role of mesoscale eddies for the biological productivity and biogeochemistry in the eastern tropical Pacific Ocean off Peru". In: *Biogeosciences* 10.11, pp. 7293–7306.

Strub, P. T., V. Combes, F. A. Shillington, and O. Pizarro (2013). "Currents and processes along the eastern boundaries". In: *International Geophysics*. Vol. 103. Elsevier, pp. 339–384.

Sudre, J., C. Maes, and V. Garçon (2013). "On the global estimates of geostrophic and Ekman surface currents". In: *Limnology and Oceanography: Fluids and Environments* 3.1, pp. 1–20.

Sydeman, W., M. Garcıa-Reyes, D. S. Schoeman, R. Rykaczewski, S. Thompson, B. Black, and S. Bograd (2014). "Climate change and wind intensification in coastal upwelling ecosystems". In: *Science* 345.6192, pp. 77–80.

Takahashi, K., A. Montecinos, K. Goubanova, and B. Dewitte (2011). "ENSO regimes: Reinterpreting the canonical and Modoki El Niño". In: *Geophysical Research Letters* 38.10.

Tao, L., Y. Hu, and J. Liu (2016). "Anthropogenic forcing on the Hadley circulation in CMIP5 simulations". In: *Climate dynamics* 46.9-10, pp. 3337–3350.

Taylor, K. E., R. J. Stouffer, and G. A. Meehl (2012). "An overview of CMIP5 and the experiment design". In: *Bulletin of the American meteorological Society* 93.4, pp. 485–498.

Timmermann, A. et al. (2018). "El Niño-Southern Oscillation complexity". In: *Nature* 559.7715, pp. 535–545.

Timmermann, A., S. McGregor, and F.-F. Jin (2010). "Wind effects on past and future regional sea level trends in the southern Indo-Pacific". In: *Journal of Climate* 23.16, pp. 4429–4437.

Tokinaga, H., S.-P. Xie, C. Deser, Y. Kosaka, and Y. M. Okumura (2012). "Slowdown of the Walker circulation driven by tropical Indo-Pacific warming". In: *Nature* 491.7424, pp. 439–443.

Toniazzo, T. (2010). "Climate variability in the south-eastern tropical Pacific and its relation with ENSO: a GCM study". In: *Climate dynamics* 34.7, pp. 1093–1114.

Trenberth, K. E., J. T. Fasullo, and J. Kiehl (2009). "Earth's global energy budget". In: *Bulletin of the American Meteorological Society* 90.3, pp. 311–324.

Ummenhofer, C. C., M. H. England, P. C. McIntosh, G. A. Meyers, M. J. Pook, J. S. Risbey, A. S. Gupta, and A. S. Taschetto (2009). "What causes southeast Australia's worst droughts?" In: *Geophysical Research Letters* 36.4.

Vallès-Casanova, I., S.-K. Lee, G. R. Foltz, and J. L. Pelegrı (2020). "On the spatiotemporal diversity of Atlantic Niño and associated rainfall variability over West Africa and South America". In: *Geophysical Research Letters* 47.8, e2020GL087108.

Vecchi, G. A. and B. J. Soden (2007). "Global warming and the weakening of the tropical circulation". In: *Journal of Climate* 20.17, pp. 4316–4340.

Vecchi, G. A., B. J. Soden, A. T. Wittenberg, I. M. Held, A. Leetmaa, and M. J. Harrison (2006). "Weakening of tropical Pacific atmospheric circulation due to anthropogenic forcing". In: *Nature* 441.7089, pp. 73–76.

Vergara, O., B. Dewitte, M. Ramos, and O. Pizarro (2017). "Vertical energy flux at E NSO time scales in the subthermocline of the S outheastern P acific". In: *Journal of Geophysical Research: Oceans* 122.7, pp. 6011–6038.

Vergara, O., B. Dewitte, I. Montes, V. Garçon, M. Ramos, A. Paulmier, and O. Pizarro (2016). "Seasonal variability of the oxygen minimum zone off Peru in a high-resolution regional coupled model". In: *Biogeosciences* 13.15, pp. 4389–4410.

Vermeer, M. and S. Rahmstorf (2009). "Global sea level linked to global temperature". In: *Proceedings of the national academy of sciences* 106.51, pp. 21527–21532.

Vimont, D. J., M. A. Alexander, and M. Newman (2014). "Optimal growth of central and east Pacific ENSO events". In: *Geophysical Research Letters* 41.11, pp. 4027–4034.

Wang, C. (2019). "Three-ocean interactions and climate variability: A review and perspective". In: *Climate Dynamics* 53.7, pp. 5119–5136.

Wang, C., L. Zhang, S.-K. Lee, L. Wu, and C. R. Mechoso (2014). "A global perspective on CMIP5 climate model biases". In: *Nature Climate Change* 4.3, pp. 201–205.

Wang, D., T. C. Gouhier, B. A. Menge, and A. R. Ganguly (2015). "Intensification and spatial homogenization of coastal upwelling under climate change". In: *Nature* 518.7539, pp. 390–394.

Watanabe, M., H. Shiogama, H. Tatebe, M. Hayashi, M. Ishii, and M. Kimoto (2014). "Contribution of natural decadal variability to global warming acceleration and hiatus". In: *Nature Climate Change* 4.10, pp. 893–897.

Webster, P. J., A. M. Moore, J. P. Loschnigg, and R. R. Leben (1999). "Coupled ocean–atmosphere dynamics in the Indian Ocean during 1997–98". In: *Nature* 401.6751, pp. 356–360.

Wittenberg, A. T. (2009). "Are historical records sufficient to constrain ENSO simulations?" In: *Geophysical Research Letters* 36.12.

Xie, S.-P., C. Deser, G. A. Vecchi, J. Ma, H. Teng, and A. T. Wittenberg (2010). "Global warming pattern formation: Sea surface temperature and rainfall". In: *Journal of Climate* 23.4, pp. 966–986.

Xie, S.-P. and S. G. H. Philander (1994). "A coupled ocean-atmosphere model of relevance to the ITCZ in the eastern Pacific". In: *Tellus A* 46.4, pp. 340–350.

Yeh, S.-W., J.-S. Kug, B. Dewitte, M.-H. Kwon, B. P. Kirtman, and F.-F. Jin (2009). "El Niño in a changing climate". In: *Nature* 461.7263, pp. 511–514.

Ying, J. and P. Huang (2016a). "Cloud–radiation feedback as a leading source of uncertainty in the tropical Pacific SST warming pattern in CMIP5 models". In: *Journal of Climate* 29.10, pp. 3867–3881.

Ying, J. and P. Huang (2016b). "The large-scale ocean dynamical effect on uncertainty in the tropical Pacific SST warming pattern in CMIP5 models". In: *Journal of Climate* 29.22, pp. 8051–8065.

You, Y. and J. C. Furtado (2018). "The South Pacific meridional mode and its role in tropical Pacific climate variability". In: *Journal of Climate* 31.24, pp. 10141–10163.

Yu, X. and M. J. McPhaden (1999). "Dynamical analysis of seasonal and interannual variability in the equatorial Pacific". In: *Journal of physical oceanography* 29.9, pp. 2350–2369.

Zebiak, S. E. (1993). "Air–sea interaction in the equatorial Atlantic region". In: *Journal of Climate* 6.8, pp. 1567–1586.

Zhang, H., A. Clement, and P. Di Nezio (2014a). "The South Pacific meridional mode: A mechanism for ENSO-like variability". In: *Journal of Climate* 27.2, pp. 769–783.

Zhang, H., C. Deser, A. Clement, and R. Tomas (2014b). "Equatorial signatures of the Pacific meridional modes: Dependence on mean climate state". In: *Geophysical Research Letters* 41.2, pp. 568–574.

Zhang, L. and T. Li (2014). "A simple analytical model for understanding the formation of sea surface temperature patterns under global warming". In: *Journal of Climate* 27.22, pp. 8413–8421.

Zhang, X., H. Liu, and M. Zhang (2015). "Double ITCZ in coupled ocean-atmosphere models: From CMIP3 to CMIP5". In: *Geophysical Research Letters* 42.20, pp. 8651–8659.

Zhang, Z., W. Wang, and B. Qiu (2014). "Oceanic mass transport by mesoscale eddies". In: *Science* 345.6194, pp. 322–324.

Zheng, X.-T., S.-P. Xie, Y. Du, L. Liu, G. Huang, and Q. Liu (2013). "Indian Ocean dipole response to global warming in the CMIP5 multimodel ensemble". In: *Journal of Climate* 26.16, pp. 6067–6080.

Zhu, X. and Z. Liu (2009). "Tropical SST response to global warming in the twentieth century". In: *Journal of climate* 22.5, pp. 1305–1312.

Zuo, H., M. A. Balmaseda, S. Tietsche, K. Mogensen, and M. Mayer (2019). "The ECMWF operational ensemble reanalysis–analysis system for ocean and sea ice: a description of the system and assessment". In: *Ocean science* 15.3, pp. 779–808.